Guided elastic waves in soft media

Alexandre Delory

PSL
UNIVERSITÉ PARIS

THÈSE DE DOCTORAT
DE L'UNIVERSITÉ PSL

Préparée à l'École Supérieure de Physique
et de Chimie Industrielles de la ville de Paris

Guided elastic waves in soft media

(Ondes élastiques guidées dans les solides mous)

Soutenue par
Alexandre DELORY
Le 29 novembre 2023

École doctorale n°564
Physique en Île-de-France

Spécialité
Acoustique

Préparée à
l'Institut Langevin (UMR7587)

Composition du jury :

Mathieu PERNOT Directeur de Recherche Inserm, PhysMed	*Président du jury*
Jonathan ASHMORE Professor, University College London	*Examinateur*
Katia BERTOLDI Professor, Harvard University	*Examinateur*
Michel DESTRADE Professor, NUI Galway	*Rapporteur*
Bruno LOMBARD Directeur de Recherche CNRS, LMA	*Rapporteur*
Fabrice LEMOULT Maitre de Conférences ESPCI, Institut Langevin	*Co-encadrant*
Antonin EDDI Chargé de Recherche CNRS, PMMH	*Co-directeur*
Claire PRADA Directrice de Recherche CNRS, Institut Langevin	*Directrice de thèse*

ESPCI PARIS | PSL

Contents

List of figures

Remerciements

Cette thèse n'est en aucun cas le fruit d'une expérience solitaire, mais témoigne plutôt de l'aboutissement d'efforts collectifs et d'un travail d'équipe. Il parait alors évident de commencer cette section en adressant mes remerciements les plus profonds à cette belle équipe encadrante composée d'Antonin Eddi, Claire Prada et Fabrice Lemoult. Chaque réunion s'est déroulée de manière inattendue : les questions fusaient, les débats restaient souvent ouverts et les recrutements CNRS ponctuaient généralement ces moments. Cependant, si c'était à refaire je ne changerais rien, car c'est bien au cours de ces réunions stimulantes que j'ai appris ce que voulait dire être chercheur. Merci d'avoir été, avant tout, une équipe humaine.

Antonin, je te dois beaucoup plus que ce que tu veux bien admettre : ta culture scientifique, ta méthode expérimentale rigoureuse et tes astuces de traitement d'image me resserviront indéniablement. Mais ce que tu m'as enseigné par-dessus tout, c'est d'être capable de laisser parler ses idées, d'explorer et de monter des manips de coin de table avec ce que l'on a sous la main. C'est cette mentalité qui, aujourd'hui, me pousse à dire (peut-être souvent trop vite) « bah viens on fait la manip ».

Claire, merci pour la perspicacité dont tu as toujours fait preuve et pour la pertinence de tes remarques et questions. Tu m'indiquais souvent les points critiques de mon raisonnement, ainsi que les questions que je devais me poser mais que j'avais tendance à éviter car je les savais difficiles. Je te remercie sincèrement car ta porte a (vraiment) toujours été ouverte pour discuter, que ce soit de sujets scientifiques ou d'autres.

Fabrice, difficile de n'écrire que quelques lignes pour te remercier de ton encadrement tout simplement parfait. Tu m'as appris à imaginer, réfléchir, réaliser, présenter et rédiger mes travaux de recherche. Je te dois la plupart des connaissances, des compétences et des techniques qu'il a fallu mettre en œuvre pour mener à bien cette thèse. Tu as d'abord été mon encadrant, puis tu es devenu mon directeur de thèse du fait de ton HDR fraichement obtenue, et aujourd'hui je te considère surtout comme mon mentor.

L'équipe des milieux mous est aussi constituée de deux autres formidables scientifiques que je ne pouvais évidemment pas oublier. Maxime Lanoy, tu as monté la première manip et ma thèse n'aurait pas commencé sans toi. J'espère vivement que notre collaboration perdurera. Daniel Kiefer, tu m'as initié à la résolution numérique, à la rigueur en mécanique, à l'escalade de bloc et aussi donné l'envie de visiter la Bolivie. Merci pour toutes nos interactions scientifiques ou non.

J'en profite pour remercier également Samuel Croquette et Pierre Chantelot qui sont arrivés au laboratoire au cours de ma dernière année de thèse. L'émulation autour des milieux mous ne va faire que croitre au laboratoire, et ce sera grâce à vous et aux idées qui naissent toutes les semaines.

Je suis plus généralement reconnaissant envers l'Institut Langevin d'offrir un environnement académique stimulant, une variété considérable de sujets de physique et des ressources essentielles à la réalisation des recherches. Je remercie les personnels de support, Emmanuel Labbey et David Kho, de gestion, Nathalie Lejeune, Catherine Dupuy et Christelle Jacquet, et de direction, Arnaud Tourin et Yannick De Wilde, sans qui le laboratoire serait tout bonnement à l'arrêt.

Je tiens à remercier chaleureusement l'ensemble des membres du jury d'avoir accepté d'évaluer la qualité de mes travaux de recherche et d'avoir été présents à la soutenance. Merci à Mathieu Pernot de l'avoir présidé et à Jonathan Ashmore et Katia Bertoldi d'avoir examiné mes résultats. Je remercie particulièrement Bruno Lombard et Michel Destrade d'avoir lu en détail et corrigé ce manuscrit écrit dans un anglais approximatif. Cette soutenance a aussi été le moment d'écouter vos

critiques constructives et éclairages en lien avec vos disciplines spécifiques. Ces échanges ont pour sûr contribué à enrichir les réflexions sur les perspectives de ce travail.

Merci à l'AID pour avoir financé à moitié cette thèse et à Bertrand Habert pour avoir suivi, avec excitation, notre travail sur l'onde cochléaire. Merci également à Etienne Reyssat et Stefan Catheline d'avoir pris part à mes 2 comités de thèse.

Mes trois années dans ce laboratoire ne se sont pas seulement déroulées en salle de manip mais aussi dans le bureau R31, très clairement le meilleur bureau de doctorant·e·s. Chacun·e a eu une importance particulière dans mon quotidien de doctorant. J'adresse de profonds et véritables remerciements à Chloë, Yao, Ahmed, Jad, Serena et François pour nos petits-déjeuners de bureau, nos discussions rarement scientifiques, et de manière générale, pour la super ambiance qui régnait au R31. Évidemment, merci aussi aux anciens, Maxime, Paul et Anwesh, et aux plus jeunes, Ariane et Thomas W.

Ensuite, je souhaite remercier ces autres collègues qui sont aussi devenu·e·s des ami·e·s. Je vous remercie car vous avez rempli de rires mon quotidien au laboratoire.

Arthour pour ton humour qui ne sera jamais aussi brillant que ton esprit, Zaza pour ta curiosité envers mes tups et ta mémoire terriblement infaillible, Ul-ul pour ton goût des blagues de mauvais goût, Flav pour ta compétence spéciale qui consiste à changer de sujet avant d'écouter la réponse à tes propres questions, Jérôme pour avoir partagé bien plus que des maxi cornets de frites bi-mensuels.

Merci à Benjamin toujours prêt à discuter de physique mais à condition que ce soit autour d'un cochonnet, à Romain M à qui j'ai fait croire que je comprenais ses questions et qui m'a fait croire qu'il pouvait monter une manip tout seul, à Noet dont je ne sais toujours pas s'il relève du génie ou de l'idiot, à Jeanne pour son humour et ses connaissances socio-politiques et culturelles. Merci à Hussam, Claudia et Maximilian pour nos sorties escalades principalement constituées de rigolades ponctuées de quelques chutes. Merci à Jana pour ta gentillesse, ton sourire et ton honnêteté.

Merci aussi aux ancien·ne·s Camilo, Louis, Samer, Cécile, Kassandra, Loubnan, Clément et aux plus jeunes Thomas L, Romain R, Alioune, Clémence, Inès, Victor, Louise, Zofia, Hafsa, Sylvio, Dimitri, Guyu, Margaux, Florent, Angélique. Merci à Thibaud, Gatien et Quentin d'avoir repris l'organisation des séminaires doctorants. Merci à Emma pour les photos de l'after pot-de-thèse.

Et puis parce que j'ai réalisé une mission doctorale d'enseignement pendant 3 années au CPES2-PSL, je remercie Maika Saint-Jean et Baptiste Lafoux d'avoir partagé le rush de la rentrée scolaire pour préparer les recueils d'exercice d'optique et de thermo.

Merci à mes amis de la promo PC135 et en particulier à mes fidèles comparses Tiago, Vincent et Baška qui ont brillamment défendu leur thèse la même quinzaine que moi, et à mon bibi Yann.

Je souhaite adresser de fervents remerciements à mon groupe d'amis de toujours, qui ont toujours su que je réussirais, constitué des incroyables (par ordre alphabétique) Adrien, Justine, Leatitia, Maxime, Noham, Paul, Simon et Yoann. J'étends ces remerciements à leurs compagnes, compagnons, mais aussi à Florian, Sandra, Matéo et Kelly.

Mes remerciements les plus sincères vont à ma famille pour leur amour indéfectible, leur encouragement et leur compréhension tout au long de ce parcours exigeant. Leur soutien constant, leur foi en mes capacités et leurs sacrifices sont la pierre angulaire de ma persévérance.

Mes derniers remerciements se tournent vers celle avec qui je partage ma vie depuis presque 10 ans, que j'admire beaucoup plus que je n'ose lui dire, et à qui je souhaite exprimer ma plus profonde reconnaissance. Son soutien, son encouragement et sa compréhension ont été les piliers essentiels dans les moments de doute et de travail intense. Marine, merci pour tout.

General introduction

At the heart of natural world, many organisms and systems have evolved towards the use of soft structures. This is not a universal rule but there are many reasons for this adaptation. To just name a few, soft solids offer flexibility, adaptability and sensory feedback. These properties actually rely on two main features. First, biological tissues are mainly composed of water, and are thus assumed to be nearly incompressible. Second, these media still remain solids due to their microstructure, and they exhibit the remarkable ability to withstand substantial elastic deformations.

These unique properties are harnessed by living organisms, notably allowing them to achieve locomotion[1,2] but also enabling the whole morphogenetic chain to happen, through the ability of shaping tissues, and leading to the development of organs and physiological functionalities[3,4]. Similarly, plants leverage this trait to adapt to varying environmental conditions[5,6,7]. Also, their mechanical behaviour plays a crucial role in various physiological processes[8]. For instance, the impact of the local stiffness of tissues during their development[9], the stiffening of a tumor cell[10] or the non-linear softening of arteria[11] are customary mechanisms still under investigation.

To mimic biological tissues, manufactured elastomers seem to be good candidates since they are highly deformable and most of them are nearly incompressible. With recent scientific advances in the fields of gels and polymers[12,13], such elastomers cover a wide range of mechanical properties and can be molded into a wide variety of shapes. For example, in plastic surgery, silicone rubbers have been adopted to reproduce the shapes and mechanical properties of breasts, lips or noses. Nowadays, silicone elastomers seem to be promising materials to build artificial organs[14,15], medical

[1] Josephson (1993): "Contraction dynamics and power output of skeletal muscle"
[2] Huffard et al. (2005): "Underwater bipedal locomotion by octopuses in disguise"
[3] Dervaux and Amar (2008): "Morphogenesis of growing soft tissues"
[4] Heisenberg and Bellaïche (2013): "Forces in tissue morphogenesis and patterning"
[5] Liang and Mahadevan (2011): "Growth, geometry, and mechanics of a blooming lily"
[6] Goriely (2017): *The mathematics and mechanics of biological growth*
[7] Moulia et al. (2021): "Fluctuations shape plants through proprioception"
[8] Levental et al. (2007): "Soft biological materials and their impact on cell function"
[9] Wozniak and Chen (2009): "Mechanotransduction in development: a growing role for contractility"
[10] Kumar and Weaver (2009): "Mechanics, malignancy, and metastasis: the force journey of a tumor cell"
[11] Kalita and Schaefer (2008): "Mechanical models of artery walls"
[12] Kaspar et al. (2021): "The rise of intelligent matter"
[13] Zhao et al. (2021): "Soft materials by design: unconventional polymer networks give extreme properties"
[14] Murray and Thomson (2011): "Synthetic, multi-layer, self-oscillating vocal fold model fabrication"
[15] Vannelli et al. (2015): "Dynamic heart phantom with functional mitral and aortic valves"

devices[16], soft robots[17] and inflatable structures[18], among others.

The evaluation of mechanical properties is of paramount importance and the propagation of elastic waves allows to probe those properties deep inside the medium. For instance, in the human body, ultrasonic waves are used to build medical images of the fœtus and of organs. Because of their above-mentioned incompressible nature, longitudinal waves propagate a lot faster than their transverse counterpart ($V_L \gg V_T$). This specificity has enabled the development of transient elastography[19] which is now clinically used to provide valuable information about the stiffness of tissues, and therefore on the presence and severity of diseases.

Although they permit to probe the material mechanics, elastic waves are by essence dynamical objects. In fact, a consequence of the polymer chains' ability to conform freely is that they rearrange with a characteristic relaxation time. As a result, the material constants are expected to be frequency-dependent and complex-valued: these are the so-called viscoelastic properties of the material, and inevitably concern biological tissues[20,21].

Another main issue is that media of interest generally have finite dimensions. Thus, the presence of interfaces in tissues usually induce guiding phenomena. The wave velocities at play may greatly differ from V_L or V_T, and complex waveguiding phenomena may hamper the ability to retrieve the material properties, notably in elastography.

Guided elastic waves are also naturally involved in physiological processes. At the cellular scale, pressure pulses are observed in lipid monolayers[22], and at the macroscopic scale the vocal cords are the support of stationary waves[23]. Another compelling example is the sound transduction operated by the inner ear of mammalians: the *cochlear wave* is a guided mechanical wave that travels along the basilar membrane[24].

Although guiding is a universal wave phenomenon, the case of elastic waves is particularly fascinating: up to three different polarizations can couple at each reflection[25] and at least two distinct bulk wave velocities are involved. Even in a geometry as simple as a plate, elastic guided waves present original properties. These waves have been extensively studied, especially for non-destructive testing applications[26].

We have just seen that elastic waves in soft solids are impacted by geometry and viscoelasticity. Yet, as mentioned, soft media are highly deformable and the retrieved stiffness in elastography appears to depend on applied stresses[27]. This dependence is known as the acoustoelastic effect[28,29] and refers to the changes in elastic wave velocities with an initial stress. It is for instance at the basis of string instruments (or the vocal cords), where the tension is finely tuned to adjust the pitch of the musical instrument (or the produced sound fundamental frequency). The more deformable the medium, the more significant this effect and this is why the case of soft media is of special interest.

[16] Smith et al. (2023): "Soft devices in neurological surgery"
[17] Marechal et al. (2021): "Toward a common framework and database of materials for soft robotics"
[18] Siéfert et al. (2019): "Bio-inspired pneumatic shape-morphing elastomers"
[19] Sandrin et al. (2003): "Transient elastography: a new noninvasive method for assessment of hepatic fibrosis"
[20] Gennisson et al. (2010): "Viscoelastic and Anisotropic Mechanical Properties of in vivo Muscle Tissue Assessed by Supersonic Shear Imaging"
[21] Deffieux et al. (2015): "Investigating liver stiffness and viscosity for fibrosis, steatosis and activity staging using shear wave elastography"
[22] Griesbauer et al. (2012): "Propagation of 2D Pressure Pulses in Lipid Monolayers and Its Possible Implications for Biology"
[23] Hirano (1974): "Morphological structure of the vocal cord as a vibrator and its variations"
[24] Reichenbach and Hudspeth (2014): "The physics of hearing: fluid mechanics and the active process of the inner ear"
[25] Royer and Dieulesaint (1999): *Elastic waves in solids I: Free and guided propagation*
[26] Su et al. (2006): "Guided Lamb waves for identification of damage in composite structures: A review"
[27] Gennisson et al. (2007): "Acoustoelasticity in soft solids: Assessment of the nonlinear shear modulus with the acoustic radiation force"
[28] Biot (1940): "The Influence of Initial Stress on Elastic Waves"
[29] Destrade and Saccomandi (2007): *Waves in Nonlinear Pre-Stressed Materials*

In summary, the mechanics of soft solids, including guided elastic waves, depends on both frequency and strain. As a consequence, capturing the dynamics of soft structures under significant stress, a common occurrence in our daily environment (vocal cords, tendons, ligaments, muscles and blood vessels), remains a challenge and will be the scope of this manuscript.

In Chapter 1, we recall the key principles of mechanics and linear elasticity in order to explain the propagation of elastic waves. Then, we derive the equations governing the propagation of Lamb waves and present the dispersion diagrams for guided elastic waves in soft plates and strips. Material viscoelasticity is addressed through a semi-analytical method, aligning theoretical predictions with experimental findings.

In Chapter 2, we add a second ingredient, the prestress, and compare our measurements in a highly-deformed soft plate with the predictions derived using the acoustoelastic theory. This latter aspect is enhanced by adding a viscoelastic contribution to the elasticity tensor, yielding complex-valued wavenumbers and attenuation distances that accurately match experimental results.

In Chapter 3, we replace the stretched plate by a strip which supports more propagating modes. After validating the acoustoelastic theory for this geometry, elastography experiments are also performed in such strips. They evidence the limitations of this medical imaging technique: viscoelasticity, guiding geometry, static deformations; and we also explain our approach to characterize both viscoelastic and hyperelastic properties of biological tissues.

In Chapter 4, connections between soft materials and biological tissues are examined by studying the *cochlear wave*. Modeling this membrane as a thin strip, the study explores how geometrical gradients influence the local dispersion of this mode and how they enable frequency discrimination.

In Chapter 5, we use the stress as a time modulation tool for flexural waves in a strip. A space-time interface is observed and characterized. Its interaction with flexural waves is then studied by measuring the frequency and wavenumber changes at the interface.

Chapter 1

Fundamentals of guided elastic waves in soft media

Objectives

In this chapter, we present in detail the experimental and theoretical framework required for the investigation of guided waves in soft waveguides. First, an experimental platform designed to track the in-plane displacement of a thin plate is proposed. The corresponding theoretical background (Rayleigh-Lamb equation) is uncovered. Then, an equivalence between Lamb modes and in-plane guided waves in a thin strip is made and the strip configuration is investigated as well. Unique wave features such as a backward mode, a zero group velocity point (ZGV) and a Dirac cone in the $k \to 0$ limit are reported. Finally, it is demonstrated how rheology impacts such guided waves dispersion.

- Designing an experimental setup to observe in-plane motion in soft waveguides
- Theoretical introduction to linear elastodynamics and guided waves in a plate
- Experimental observation of fundamental modes and their dispersion in a plate
- Analogy between in-plane guided waves in a strip and Lamb modes in a plate
- Description of the Spectral Collocation Method used for numerical predictions
- Experimental dispersion curves of in-plane guided modes in a strip are obtained
- Revealing the elastomer rheology impact on guided waves properties

Contents

To begin with, we review the basic concepts of mechanics and linear elasticity. Then, we enter the field of linear elastodynamics, taking into account the time variable in the equation of motion. By looking for plane wave solutions, we calculate the velocities of elastic waves that propagate in an infinite elastic medium, *i.e.* shear waves (transverse) and pressure waves (longitudinal). And we finish these theoretical reminders by describing Lamb waves, where two parallel plane interfaces are added. These new boundary conditions lead us to the Rayleigh-Lamb equation, and we draw the dispersion diagram for guided elastic waves in a soft plate.

These theoretical considerations are then supported by experimental measurements, in which we first take care to explain each stage of our experimental method and post-processing. In particular, we demonstrate the simplicity and versatility of this method for measuring in-plane displacements in such a plate, and their corresponding dispersion curves.

In the last part of this chapter, we introduce the thin strip geometry that will be used throughout this PhD thesis. We detail the different families of modes that propagate in such a waveguide. We notably show that the dispersion diagram of in-plane guided waves is analogous to that of a plate, provided we adapt some parameters such as the longitudinal velocity. We discuss the richness of these guided modes, but we also see that our theory still lacks an essential ingredient: the material rheology. This notion is therefore introduced and we develop a semi-analytical method to obtain dispersion curves. It enables fast calculations and fine-tuning of theoretical predictions with our experimental results. Finally, we modify the boundary conditions to validate our approach and highlight once again how the richness of these guided waves emerges.

The following is largely duplicated from a work published as Delory et al. (2022)[30].

1 Theoretical Aspects

The propagation of elastic waves in isotropic solids is a well-documented topic. In this first section, we quickly run through the basics of linear elasticity and Lamb waves but comprehensive developments can be found in textbooks[31,25].

1.1 Linear elasticity

The background of the linear elasticity theory is provided because it will serve as a foundation for that of non-linear elasticity in Chapter 2. Linear elasticity theory is a branch of continuum mechanics that describes the behaviour of solid materials under the influence of external forces and the assumption of infinitesimal strain. It assumes that the material's response is proportional to the applied stresses. Let us discuss some of its main aspects and assumptions.

1.1.1 Configurations

Let $\mathcal{B}_r$, described by position $\mathbf{X}$, be the reference configuration of the solid at rest, and $\mathcal{B}$ the deformed configuration described by position $\mathbf{x}$, as indicated in figure 1.1. Deformation in the material is represented by the mapping $\boldsymbol{\chi} : \mathcal{B}_r \to \mathcal{B}$ which takes points $\mathbf{X}$ in $\mathcal{B}_r$ to points $\mathbf{x}$ in $\mathcal{B}$ such that:

$$\mathbf{x} = \boldsymbol{\chi}(\mathbf{X}), \quad \mathbf{X} \in \mathcal{B}_r. \tag{1.1}$$

In the following, $\mathbf{X}$ and $\mathbf{x}$ have Cartesian coordinates X_i and x_j, respectively with $i, j \in \{1, 2, 3\}$. Let us define some quantities of interest. First, like the displacement:

$$\mathbf{u}(\mathbf{X}) = \mathbf{x} - \mathbf{X}. \tag{1.2}$$

[30] Delory et al. (2022): "Soft elastomers: A playground for guided waves"
[31] Auld (1973): *Acoustic Fields and Waves in Solids*
[25] Royer and Dieulesaint (1999): *Elastic waves in solids I: Free and guided propagation*

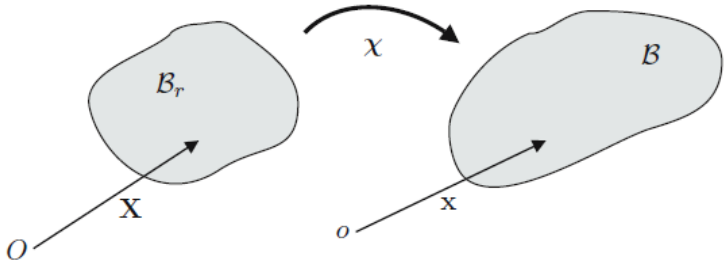

FIGURE 1.1: **Reference and deformed configurations** – Material particles are labelled by the position vector $\mathbf{X}$ in $\mathcal{B}_r$ and $\mathbf{x}$ in $\mathcal{B}$. They are related through the deformation mapping $\boldsymbol{\chi}$. (*Reproduced from* DESTRADE and SACCOMANDI (2007)[29]).

Distances in $\mathcal{B}$ are related to those in $\mathcal{B}_r$ by the deformation gradient tensor $\mathbf{F}$:

$$\mathbf{F} = \frac{\partial \mathbf{x}}{\partial \mathbf{X}} = \nabla \mathbf{x} = \nabla \mathbf{u} + \mathbf{1} \tag{1.3}$$

where ∇ is the gradient operator, and $\mathbf{1}$ is the second-order unit tensor. With these definitions, we can introduce a strain tensor and a stress tensor.

1.1.2 Linearized stress and strain tensors

First, we choose how to quantify deformation in a solid. One has many options, but we stick to a simple and natural one, given by the Green-Lagrange strain tensor:

$$\mathbf{E} = \frac{1}{2}\left(\mathbf{F}^{\mathrm{T}} \cdot \mathbf{F} - \mathbf{1}\right) \quad \text{or} \quad \mathbf{E} = \frac{1}{2}\left[(\nabla \mathbf{u})^{\mathrm{T}} + \nabla \mathbf{u} + (\nabla \mathbf{u})^{\mathrm{T}} \cdot \nabla \mathbf{u}\right] \tag{1.4}$$

where "$\cdot$" is the dot product. This strain tensor is obviously a non-linear function of displacement $\mathbf{u}$. By assuming infinitesimal deformations $|\mathbf{u}| \ll 1$, we define its linearized form known as the infinitesimal strain tensor $\boldsymbol{\epsilon}$, which is symmetric $\boldsymbol{\epsilon} = \boldsymbol{\epsilon}^{\mathrm{T}}$:

$$\boldsymbol{\epsilon} = \frac{1}{2}\left[(\nabla \mathbf{u})^{\mathrm{T}} + \nabla \mathbf{u}\right] \tag{1.5}$$

Similarly, we also need to make a choice to describe stresses in a solid. A natural choice for incremental deformations is the Cauchy stress tensor $\boldsymbol{\sigma}$ but other stress tensors, introduced in Chapter 2, could be selected as well. This stress tensor relates forces in the deformed configuration to areas in the deformed configuration. At this point, only incremental deformations are considered and there is no need to distinguish reference and deformed configurations. One should also note that $\boldsymbol{\sigma}$ must be symmetric $\boldsymbol{\sigma} = \boldsymbol{\sigma}^{\mathrm{T}}$ to satisfy the balance of angular momentum.

1.1.3 A famous linear constitutive law: generalized Hooke's law

At the heart of linear elasticity is Hooke's law[32,33], which states that deformation in a material is directly proportional to stresses applied to it, as long as the material remains within its elastic limit, that is to say deformation remains infinitesimal. Mathematically, generalized Hooke's law is written as:

$$\boldsymbol{\sigma} = \mathbf{C} : \boldsymbol{\epsilon} \tag{1.6}$$

[32] HOOKE (1678): *Lectures de potentia restitutiva, or of spring, explaining the power of springing bodies*
[33] LANDAU et al. (1986): *Theory of elasticity: volume 7*

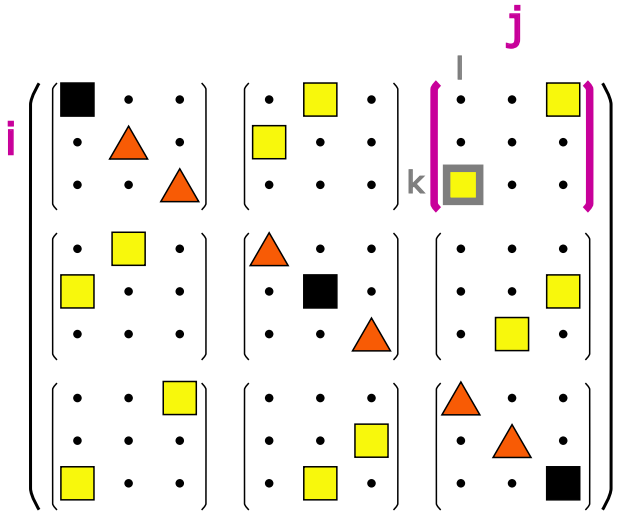

FIGURE 1.2: **Isotropic stiffness tensor** – Representation of the fourth-order stiffness tensor as a 3x3 matrix of 3x3 matrices. On the given example, the grey contoured yellow square is the value of $C_{1331} = \mu$, while black squares are given by $\lambda_L + 2\mu$ and orange triangles by λ_L.

where $\mathbf{C}$ is a fourth-order stiffness tensor and ":" is a double-dot product operation. $\mathbf{C}$ has 81 coefficients. They are not independent because of fundamental symmetries. First, the Cauchy stress tensor is symmetric $\boldsymbol{\sigma} = \boldsymbol{\sigma}^{\mathrm{T}}$, directly leading to $C_{jikl} = C_{ijkl}$. Second, $\boldsymbol{\epsilon}$ also being symmetric implies that, if $C_{ijlk} \neq C_{ijkl}$, then only the symmetric part $(C_{ijkl} + C_{ijlk})/2$ ultimately appears in the Cauchy stress tensor in equation (1.6) and the symmetry $C_{ijlk} = C_{ijkl}$ can be assumed without loss of generality. Finally, and this will be the object of further discussions with the introduction of hyperelasticity in Chapter 2, the material is elastic and stresses can be derived from an elastic potential energy[33]. This leads to a definition for the stiffness tensor where the symmetry $C_{klij} = C_{ijkl}$ naturally appears. In the end, the stiffness tensor should satisfy the following *major* symmetries, which reduce the number of independent components from 81 to 21:

$$C_{jikl} = C_{ijkl} \quad ; \quad C_{ijlk} = C_{ijkl} \quad \text{and} \quad C_{klij} = C_{ijkl}. \tag{1.7}$$

As long as the symmetry $C_{ijlk} = C_{ijkl}$ is satisfied, Hooke's law may be rewritten $\boldsymbol{\sigma} = \mathbf{C} : \boldsymbol{\epsilon} = \mathbf{C} : \nabla\mathbf{u}$.

1.1.4 Isotropic material

Assuming the material is isotropic, the number of independent components finally reduces from 21 to 2, namely the Lamé parameters, and the stiffness tensor rewrites:

$$C_{ijkl} = \lambda_L \delta_{ij}\delta_{kl} + \mu\left(\delta_{ik}\delta_{jl} + \delta_{il}\delta_{kj}\right) \tag{1.8}$$

where δ_{ij} is the kronecker delta (1 if $i = j$, 0 otherwise). To represent a fourth-order tensor, we display a 3x3 matrix of 3x3 matrices as depicted in figure 1.2. Usually, *major* symmetries lead to the so-called Voigt notation where the elasticity tensor can be represented as a 6x6 matrix. But here, we prefer to represent the 81 coefficients. For now, the stiffness tensor is the simplest but this representation will prove more useful later on. For historical reasons, people usually refer to the Lamé constants λ_L and μ. However, note that any pair of parameters can be used to describe the mechanical properties of an isotropic elastic solid. For example, it is also possible to use the Young modulus $E = \frac{\mu(3\lambda_L+2\mu)}{\lambda_L+\mu}$, the bulk modulus $\kappa = \lambda_L + \frac{2}{3}\mu$ or the Poisson ratio $\nu = \frac{\lambda_L}{2(\lambda_L+\mu)}$. The case

[33] LANDAU et al. (1986): *Theory of elasticity: volume 7*

of nearly incompressible media corresponds to the limit $\nu \to \frac{1}{2}$ *i.e.* $\lambda_L \gg \mu$ in terms of the Lamé constants, or $E \to 3\mu$.

1.1.5 Equation of motion

When invoking the infinitesimal assumption, reference and deformed configurations can logically be considered to be the same, so that $\mathbf{u}(\mathbf{X})$ simply identifies as $\mathbf{u}(\mathbf{x})$, and so that operators applied in the reference or deformed configurations are similar. Also, the mass density ρ in both configurations is considered the same. In the following of this chapter, only $\mathbf{x}$ coordinates are used.
By using an Eulerian point of view and applying Cauchy momentum equation, in absence of any external forces, one has:

$$\rho \frac{\partial^2 \mathbf{u}}{\partial t^2} = \nabla \cdot \boldsymbol{\sigma}. \tag{1.9}$$

Inserting Hooke's law in this equation of motion leads to a wave equation:

$$\nabla \cdot [\mathbf{C} : \nabla \mathbf{u}] = \rho \frac{\partial^2 \mathbf{u}}{\partial t^2} \qquad \text{or} \qquad C_{jikl} \frac{\partial^2 u_k}{\partial x_j \partial x_l} = \rho \frac{\partial^2 u_i}{\partial t^2}\,, \tag{1.10}$$

And assuming the material is isotropic, the stiffness tensor $\mathbf{C}$ can be replaced to obtain:

$$\rho \frac{\partial^2 \mathbf{u}}{\partial t^2} = (\lambda_L + \mu) \nabla \nabla \cdot \mathbf{u} + \mu \nabla \cdot \nabla \mathbf{u} \tag{1.11}$$

At this stage, it's noteworthy that the theory of linear elasticity is an idealization and has limitations. It assumes small deformations, linear stress-strain relationships, and neglects factors like material non-linearity or viscoelasticity. However, within these assumptions, linear elasticity still provides a valuable theoretical framework to describe elastic waves in solids. To start with, we focus on plane waves in an infinite media.

1.2 Bulk waves

In equation (1.11), the three components of the displacement field are coupled. In order to decouple the equations, it is common to introduce the scalar potential ϕ and vector potential $\boldsymbol{\Psi}$ as:

$$\mathbf{u} = \nabla \phi + \nabla \times \boldsymbol{\Psi}$$

where $\times$ is a cross-product. The $\nabla\phi$ component corresponds to an irrotational vector field while the $\nabla \times \boldsymbol{\Psi}$ component is associated to a divergence free field, that is a deformation without any volume change. These two potentials are independent and satisfy the following decoupled wave equations:

$$\frac{\partial^2 \phi}{\partial t^2} - \frac{\lambda_L + 2\mu}{\rho} \Delta \phi = 0 \tag{1.12}$$

$$\frac{\partial^2 \boldsymbol{\Psi}}{\partial t^2} - \frac{\mu}{\rho} \Delta \boldsymbol{\Psi} = 0 \tag{1.13}$$

These d'Alembert equations demonstrate the propagation of two different types of waves with distinct polarizations and velocities. On one hand, equation (1.12) corresponds to a longitudinal wave propagating at velocity $V_L = \sqrt{(\lambda_L + 2\mu)/\rho}$ with a displacement parallel to the propagation direction. On the other hand, equation (1.13) stands for transverse (or shear) waves propagating at velocity $V_T = \sqrt{\mu/\rho}$ with displacements perpendicular to the propagation direction.

The special case of incompressible media – Throughout this manuscript, selected soft elastomers are platinum-catalyzed silicone rubbers Smooth-On Ecoflex® with different shore hardness between 00-05 and 00-50. Ecoflex is a nearly incompressible material that has been widely used in academic in the last few years. To check its incompressibility, we measured V_L at 3 MHz with a pulse echo method in a bulk sample of our material Ecoflex® 00-30 and found $V_L = 1008$ m/s while V_T is about 5 m/s (Young's modulus of about 75 kPa). The high contrast between these two velocities confirms its incompressible nature as:

$$\nu = \frac{{V_L}^2 - 2{V_T}^2}{2\left({V_L}^2 - {V_T}^2\right)} = 0.4999 \sim \frac{1}{2}$$

Further investigations of Ecoflex will be performed later in this chapter and in this manuscript. For now, those are the only two needed parameters to assess the behaviour of elastic guided waves in a plate or in a strip.
Now that we have investigated plane waves in a bulk material and experimentally determined the corresponding velocities V_T and V_L, let's add boundary conditions to shape a plate and examine its influence on the propagation of elastic waves.

1.3 Lamb waves

Before considering two parallel free planes, we first consider a single free interface.

1.3.1 Reflection at a free interface

Consider an incident plane wave with a wavevector in the (x_1, x_2)-plane, impinging on a medium interface at $x_2 = 0$ (Fig. 1.3a). As elastic waves have three polarizations, the reflection on the interface may give rise to three different plane waves. The so-called shear horizontal (*SH*) wave, with displacement along the x_3 direction ($u_1 = u_2 = 0$), can only be generated as a reflection of a shear horizontal wave as sketched in figure 1.3(a). On the contrary, longitudinal and shear vertical waves with displacements in the plane (x_1, x_2) are coupled through reflections on the interface.
Adding a second interface parallel to the first one leads to complex waveguiding. As sketched in figure 1.3(b), separation between *SH* waves and the two others remains valid in this configuration. The next two sections describe the two families of modes that can propagate in a soft plate of thickness $2h$.

1.3.2 *SH* guided waves

The case of the shear-horizontal guided wave is relatively simple because its dispersion curves (*i.e.* the evolution of the time-frequency as a function of the spatial-frequency, or wavenumber) map those of well-known acoustic waveguides. Indeed, as all displacements occur in the x_3-direction, the problem becomes a scalar wave problem. Applying translational invariance in the x_1-direction, one seeks monochromatic solutions of the form:

$$\mathbf{u}(\mathbf{x}, \omega) = \begin{pmatrix} 0 \\ 0 \\ u_3(x_2, \omega) \end{pmatrix} e^{ikx_1}$$

Assuming that interfaces at $x_2 = \pm h$ are free to move, the stress component σ_{32} at these interfaces vanishes:

$$\sigma_{32}(x_2 = \pm h) = \mu \left.\frac{\partial u_3}{\partial x_2}\right|_{x_2 = \pm h} = 0$$

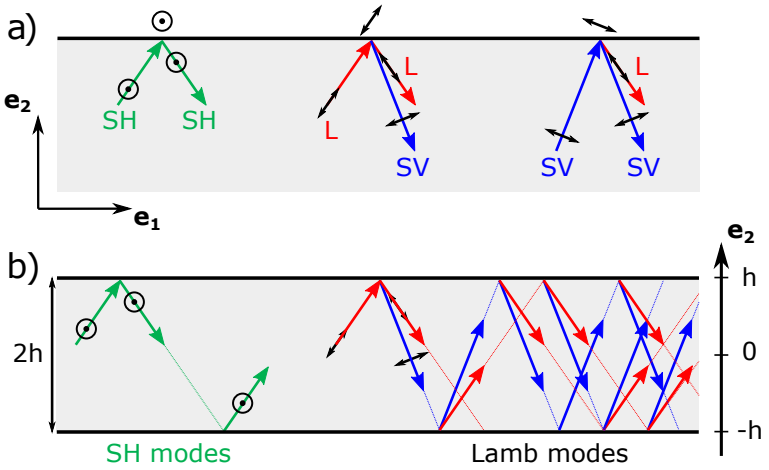

FIGURE 1.3: **Reflection on a free interface and mode coupling** – (a) Reflection of a shear horizontal (*SH*) wave on an interface does not generate out-of-plane displacements while longitudinal (*L*) and shear vertical (*SV*) waves couple. (b) When multiple reflections occur, *SH* waves remain independent while *L* and *SV* waves couple leading to a new family of modes: namely Lamb waves.

Solving wave equation (1.11) for shear waves together with these boundary conditions provides an analytical form for guided shear horizontal waves inside the plate:

$$u_3(x_2,\omega) = C\cos\left(\frac{n\pi}{2h}(x_2-h)\right)$$

where C is a scalar constant. And the dispersion relation simply writes:

$$k^2 = \left(\frac{\omega}{V_T}\right)^2 - \left(\frac{n\pi}{2h}\right)^2 \tag{1.14}$$

Such a dispersion relation (figure 1.4) exhibits a non-dispersive mode, denoted SH_0, propagating at all frequencies at V_T, as well as dispersive propagating modes above their respective cut-off frequencies $f_{c_n} = nV_T/4h$. In an Ecoflex sample of thickness 3 mm, with a shear velocity around 5 m/s, the first cut-off frequency is at 833 Hz.

1.3.3 Lamb waves

Due to the coupling at each reflection, the cases of longitudinal waves and shear vertical waves are more complicated. However, calculation steps to establish the dispersion relation and solutions remain similar. It was initially introduced by Lamb a century ago[34]. Here, it is preferable to start back from the scalar and vector potentials ϕ and $\mathbf{\Psi}$. Applying some geometrical arguments, their expressions can be simplified. First, the invariance by translation along x_1 implies a dependence on x_1 of the form e^{ikx_1}. Second, component of displacement u_3 is zero and other components should not depend on x_3. Third, $x_2 = 0$ is a symmetry plane so solutions should either be symmetric or anti-symmetric with respect to this plane. Considering all these simplifications and solving equations (1.12) and (1.13), analytical formulations for potentials write[25]:

$$\begin{cases} \phi(\mathbf{r},\omega) &= \phi_0\cos(px_2+\alpha)e^{ikx_1} \\ \mathbf{\Psi}(\mathbf{r},\omega) &= \psi_3\sin(qx_2+\alpha)e^{ikx_1}\mathbf{e_3} \end{cases} \tag{1.15}$$

[34] LAMB (1917): "On waves in an elastic plate"
[25] ROYER and DIEULESAINT (1999): *Elastic waves in solids I: Free and guided propagation*

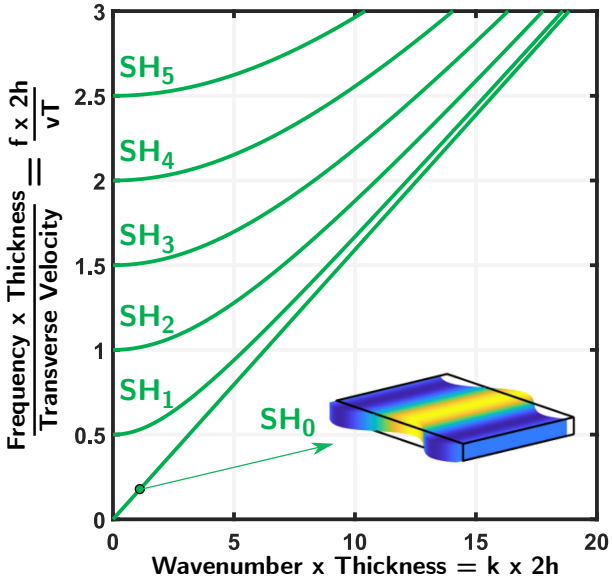

FIGURE 1.4: **Theoretical dispersion curves of SH waves** – The SH_0 mode is non dispersive with a velocity V_T and its polarisation is mostly transverse, as expected. Higher modes are dispersive and appear at cut-off frequencies corresponding to every multiple of $\frac{V_T}{4h}$.

with $p^2 = (\omega/V_L)^2 - k^2$ and $q^2 = (\omega/V_T)^2 - k^2$. Symmetrical solutions correspond to $\alpha = 0$ and anti-symmetrical ones to $\alpha = \pi/2$. From these potentials, displacements are now:

$$\mathbf{u}(\mathbf{x},\omega) = \begin{pmatrix} u_1(x_2,\omega) \\ u_2(x_2,\omega) \\ 0 \end{pmatrix} e^{ikx_1}$$

with two non-zero components being:

$$\begin{cases} u_1(x_2,\omega) &= ik\phi_0 \cos(px_2+\alpha) + q\psi_3 \cos(qx_2+\alpha) \\ u_2(x_2,\omega) &= -p\phi_0 \sin(px_2+\alpha) - ik\psi_3 \sin(qx_2+\alpha) \end{cases} \tag{1.16}$$

The dispersion relation of these modes is deduced from boundary conditions. Assuming free boundaries at both interfaces $x_2 = \pm h$, stresses σ_{12} and σ_{22} must each cancel there, which implies:

$$\begin{cases} (k^2 - q^2)\phi_0 \cos(ph+\alpha) &= 2ikq\psi_3 \cos(qh+\alpha) \\ (k^2 - q^2)\psi_3 \sin(qh+\alpha) &= 2ikp\phi_0 \sin(ph+\alpha) \end{cases} \tag{1.17}$$

Non-trivial solutions for ϕ_0 and ψ_3 are found when the determinant of this system vanishes. Under these circumstances, u_1 and u_2 are described with a single scalar coefficient C as:

$$\begin{cases} u_1(x_2,\omega) = & qC\left[\frac{2k^2}{k^2-q^2} \cos(qh+\alpha)\cos(px_2+\alpha) - \cos(ph+\alpha)\cos(qx_2+\alpha)\right] \\ u_2(x_2,\omega) = & ikC\left[\frac{2pq}{k^2-q^2} \cos(qh+\alpha)\sin(px_2+\alpha) + \cos(ph+\alpha)\sin(qx_2+\alpha)\right] \end{cases} \tag{1.18}$$

And the dispersion relation, known as the Rayleigh-Lamb equation, is:

$$(k^2-q^2)^2 \sin(qh+\alpha)\cos(ph+\alpha) + 4k^2pq \sin(ph+\alpha)\cos(qh+\alpha) = 0 \tag{1.19}$$

Unfortunately, the Rayleigh-Lamb equation (1.19) does not have general analytical solutions and must be solved numerically. Many options are available to solve for this dispersion relation for the

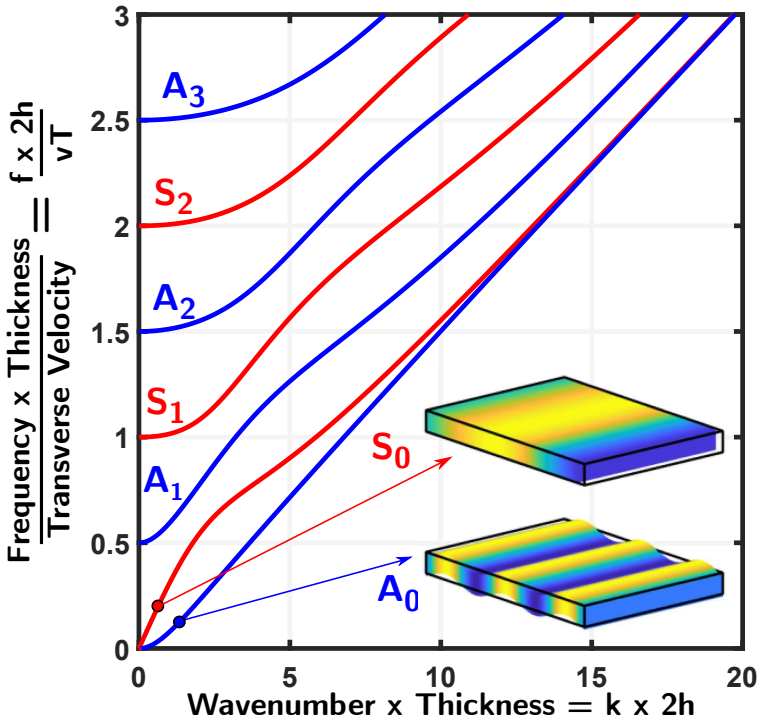

FIGURE 1.5: **Theoretical dispersion curves of Lamb waves in a nearly incompressible material** – Dispersion curves of symmetric (red) and anti-symmetric (blue) Lamb modes. In the low frequency range, the S_0 mode is non dispersive with a velocity $V_P = 2V_T$ its polarization is mostly longitudinal. On the contrary, the A_0 mode has a quadratic dispersion and mainly has an out-of-plane displacement. Higher modes exhibit cut-off frequencies every multiple of $\frac{V_T}{4h}$.

nearly-incompressible soft plate considered here. A Muller algorithm[35] or a commercial software such as Disperse[36] can be used to find the roots of this equation. Similarly, a finite element software can also be used such as COMSOL Multiphysics. Or alternatively, a spectral collocation method (SCM) implemented in Matlab by KIEFER (2022)[37] allows to find the dispersion curves of all guided waves in a plate (including *SH* modes) given the appropriate stiffness tensor. This approach was selected because it has shown great performance[38] and because Daniel A. Kiefer joined the laboratory as a post-doc at the end of my first PhD year, leading to fruitful interactions.
The dispersion curves displayed in figure 1.5 highlight families of symmetric and anti-symmetric modes. Below the first cut-off frequency of $V_T/4h \approx 833$ Hz, only two modes exist: anti-symmetric A_0 and symmetric S_0 modes. While A_0 mode has a parabolic dispersion curve in the low frequency limit, S_0 mode is rather non-dispersive.

Displacements of these modes, given by equations (1.18), can also be simplified in the long wavelength limit ($kh \to 0$). On one side, taking the limit for the S_0 mode gives:

$$\begin{cases} u_1(x_2,\omega) &= -\dfrac{qC}{\nu} + o(k) \\ u_2(x_2,\omega) &= i\dfrac{qC}{1-\nu}kx_2 + o(k) \end{cases} \tag{1.20}$$

Displacement u_1 is homogeneous across the plate and is far greater than displacement u_2. In a sense, in this low frequency limit and long wavelength approximation, S_0 mode is seen as a longitudinal

[35] MULLER (1956): "A method for solving algebraic equations using an automatic computer"
[36] PAVLAKOVIC et al. (1997): "Disperse: A General Purpose Program for Creating Dispersion Curves"
[37] KIEFER (2022): *GEW dispersion script*
[38] KIEFER (2022): *Elastodynamic quasi-guided waves for transit-time ultrasonic flow metering*

mode. Its phase velocity, known as the plate velocity, is given by:

$$V_P = 2V_T\sqrt{1-\left(\frac{V_T}{V_L}\right)^2} = \sqrt{\frac{2}{1-\nu}}\,V_T \quad \xrightarrow[\nu\to\frac{1}{2}]{} \quad 2V_T \tag{1.21}$$

The surprising feature is that, in the incompressible limit, the phase velocity of S_0 simplifies to $V_P = 2V_T$. It is thus independent of the longitudinal velocity V_L despite its apparent longitudinal polarization. This is all the more striking as V_T happens to be several orders of magnitude smaller than V_L.

On the other side, for A_0, one finds:

$$\begin{cases} u_1(x_2,\omega) &= -iC'kx_2 + o(k) \\ u_2(x_2,\omega) &= C' + o(k) \end{cases} \tag{1.22}$$

where the new constant C' has been introduced without losing generality. Displacement u_2 is homogeneous across the thickness, and u_1 is relatively negligible ($kx_2 \to 0$). This mode, generally named flexural mode, is mostly a transverse vertical mode. It has a really unique property: its dispersion is quadratic[25] in the long wavelength limit ($kh \to 0$) and reads:

$$\omega_{A_0} = \frac{V_P}{\sqrt{3}}k^2h. \tag{1.23}$$

In this section, we have explored the linear elasticity theory and described the main steps involved in obtaining the Rayleigh-Lamb equation (1.19). We now present experimental results in a plate of Ecoflex.

2 Experimental method

The soft plate preparation and experimental platform are described. Then, stroboscopic image acquisition and post-processing operations are explained and the resulting wave-fields are discussed.

2.1 Sample preparation

As illustrated in figure 1.6, rubber is obtained by mixing a monomer (A) and its cross-linking agent (B) in equal quantities. The liquid can be vacuumed for air bubbles removal. Next, the mix is poured onto a homemade mould fabricated using plastic sheets and a laser cutter (Trotec Engraver Speedy 100). The mould simply consists of a flat surface with rigid walls forming a 60-centimeter-side square. A 3 mm-thick Ecoflex plate requires about 500 mL of each liquid. The mixture is then left for curing at room temperature for several hours (usually overnight) until a translucent soft material is obtained. Anticipating image processing operations, dark pigments are seeded during the curing stage. A good contrast is obtained by using small black carbon powder from a local art shop. The seeding operation can be performed after pouring half of the total volume ($t = 10$ minutes) and before pouring the other half (Fig. 1.6). In the end, one gets a single layer of pigment located halfway through the plate. In this study, the grain density is approximately of one grain per square millimeter.

2.2 Setup

The experiment consists in shaking the plate and imaging its in-plane motion. To this end, the soft plate is clamped at its top and bottom extremities into a metallic structure (Fig. 1.7) which dimensions can be adjusted in order to reduce static tension, except from gravity.

[25] Royer and Dieulesaint (1999): *Elastic waves in solids I: Free and guided propagation*

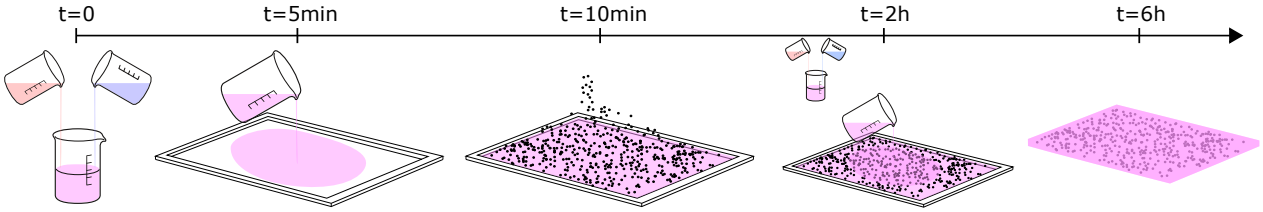

FIGURE 1.6: **Ecoflex sample preparation** – At time $t = 0$, the monomer and its cross-linking agent are mixed in equal proportions and a first layer is poured in the sample mould. At $t = 10$ min, the sample is sprinkled with black carbon grains dedicated to displacement tracking. At $t = 2$ hours, a second layer is poured and cures for 6 hours until complete cross-linking.

The excitation is performed by a shaker (Tira Vib 51120), driven by an external arbitrary wave generator (Keysight AWG 33220) which is itself connected to a power amplifier (Tira Analog Amplifier BAA 500). Typical excitation frequencies span from 1 to 300 Hz. The shaker is connected to a 30 cm long plastic line clip in the back of the soft plate (black line source in figure 1.7). Another similar plastic line clip clamps the plate with magnets. Such a line clamp is designed to ensure the generation of plane-like waves. The shaker and pinching clamp can be rotated to promote specific polarization and propagation directions. The set-up essentially captures displacements parallel to the (x_1, x_3)-plane. The motion is captured by a CCD camera (Basler acA4112-20um) with a 4112x3008-pixels sensor (Fig. 1.7). Note that it is necessary to use a global shutter: all pixels are exposed simultaneously and capture a full snapshot of the scene. A 85-mm zoom lens mounted on the camera and placed 3 m away from the object provides a clean field of view of roughly 30 cm wide square. Narrow angle lenses drastically reduce optical distortions. Moreover, it is crucial to carefully align the camera sensor plane with the plate to avoid any perspective correction. For an optimal contrast, the system is back-lighted thanks to a wide LED panel placed behind the plate.

2.3 Monochromatic excitation and stroboscopy

Given the chosen region of interest, the maximum acquisition frame rate of the camera is roughly 130 Hz (highly dependent on the number of recorded lines). This means that Shannon's criterion[39] is not fulfilled for frequencies higher than 65 Hz. However, in the linear regime, there is no need for a higher speed camera since the stroboscopic effect can be exploited. To that end, the acquisition period of the camera T_{cam} is set slightly greater than the excitation period $T_{\text{excitation}}$, *i.e.* $T_{\text{cam}} = T_{\text{excitation}} + \delta t$. Actually, we can set $T_{\text{cam}} = n\,T_{\text{excitation}} + \delta t$ with $n \in \mathbb{N}$ so that the accumulated phase shift $2\pi\delta t/T_{\text{excitation}}$ remains small. The final movie provides the illusion that the successive snapshots belong to a single wave period (sketch on figure 1.8). We refer to this quantity as the pseudo-period.

For the following post-processing steps, it is preferable to work with a given amount of images per movie. The measurements are performed setting this quantity to $N = 60$ frames over one pseudo-period. This means that the acquisition frame rate has to be determined for each different excitation frequency. If the maximum frame rate of the camera is too low, one can always, as just mentioned, reduce the sampling frequency by waiting for several excitation periods between successive camera triggers. For example, at 100 Hz, an acquisition sampling rate of precisely 24.8963 Hz would yield 60 frames regularly spaced within one pseudo-period (the 61st should be the same as the first image), and successive shots occur roughly every 4 periods. Note that the exposure time of the camera should always remains much smaller than the excitation period. The image would be blurred otherwise. Our measurements are performed with a typical exposure time of 150 μs. The image

[39] SHANNON (1949): "Communication in the Presence of Noise"

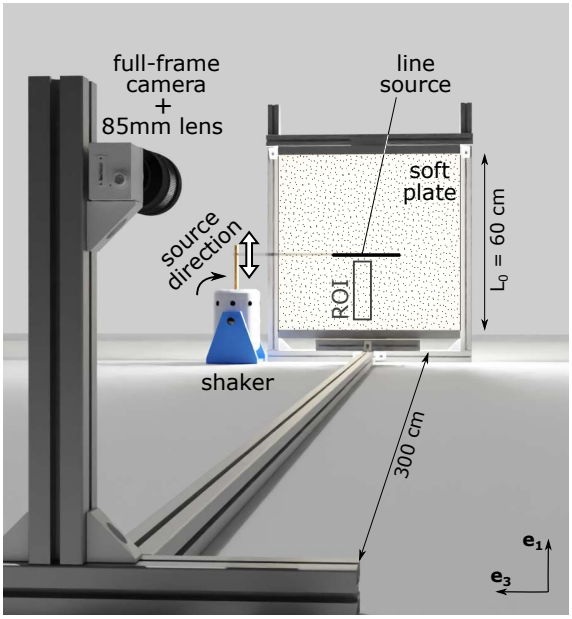

FIGURE 1.7: **Experimental set-up using a line source** – A thin plate of Ecoflex with dimensions 60 cm x 3 mm x 60 cm is held in a vertical position. Vibrations are generated by a shaker driven monochromatically. The experiment is recorded using a CCD camera located 3 m away from the plate.

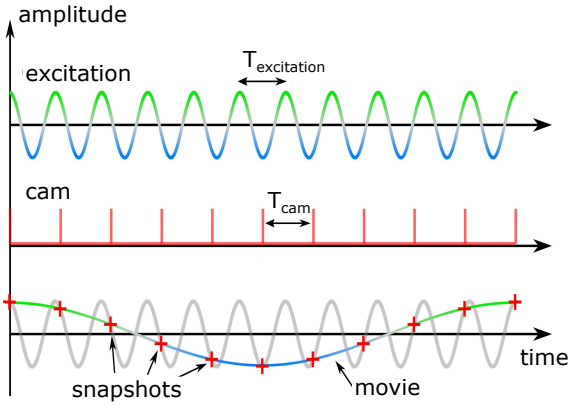

FIGURE 1.8: **Principle of the stroboscopic imaging** – As the recording framerate is lower than the excitation frequency, one full cycle is reconstructed from the measurements, depicted by the red crosses, taken over several cycles of excitation. The sampling rate has to be precisely defined with respect to the driving frequency.

quality is seriously hampered above approximately 300 Hz.

In addition to these N frames, a reference image should be captured as the sample is at rest for image processing purposes.

2.4 Extraction of the complex displacement maps

Next, each of the N frames is compared to a reference thanks to an open source Digital Image Correlation (DIC) algorithm[40,41], implemented for Matlab, which provides instantaneous displacement (Fig. 1.9). The correlation is computed on small image regions, called *macropixels*. Each macropixel yields one displacement vector (u_1, u_3). By repeating the operation for all the macropixels of a single frame, two displacement maps are obtained (Fig. 1.9e and f). The macropixel size is set manually. It should be large enough to contain several seeds while remaining smaller than the wavelength. Here, macropixels extending over 25 pixels $\times$ 25 pixels of the original image are chosen, *i.e.* a size of 2.5 mm. Sometimes, the algorithm fails to find a realistic solution for a given macropixel. In that case, one can always spatially interpolate missing information or apply spatial convolution filter to smooth the displacement maps. Note that the DIC algorithm enables sub-pixel resolution. For example, displacements down to 5 μm are measured when a single image pixel corresponds to 100 μm on the plate.

Knowing the displacement maps gives the opportunity to build a magnified version of the deformed image as in figure 1.9(c). This can be very useful for visualizing wave propagation. For

[40] WILDEMAN (2018): "Real-time quantitative Schlieren imaging by fast Fourier demodulation of a checkered backdrop"
[41] WILDEMAN (2021): *DICflow*

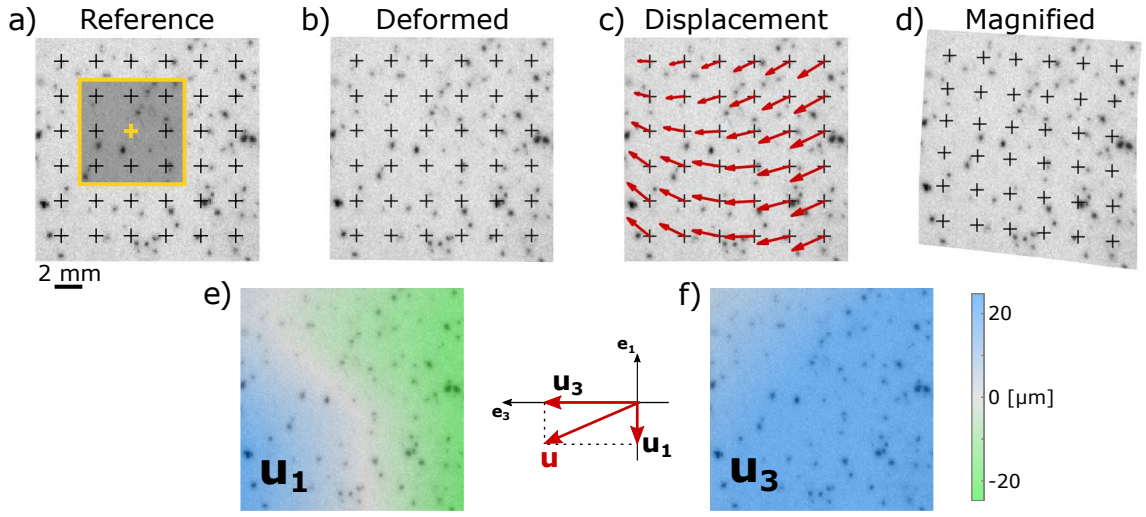

FIGURE 1.9: **Principle of displacement extraction through Digital Image Correlation (DIC) algorithm** – (a) Example of a reference image. Black seeds provide a *texture* enabling DIC analysis. Displacement components are computed for each position (crosses) by applying the DIC algorithm over the shaded area. (b) As the shaker is turned on, the image is deformed. Displacements are barely noticeable by eye (typically 10 μm). The DIC algorithm computes correlations between the deformed and reference images. (c) Output of the DIC algorithm. A displacement vector is computed for each macropixel. (d) This displacement is used to build a magnified ($\times 50$) distorted image where displacements appear clearly. (e-f) Vertical (resp. horizontal) displacement maps.

convenience, a separate colored representation of the two displacement components is preferred in figure 1.9(e) and (f). At this stage, for a given excitation pulsation ω, a series of N displacement matrices $\mathbf{u}^{(n)}(\mathbf{x})$ are obtained, corresponding to times $t_n = nT/N$, where $n \in [0, N-1]$ refers to the frame index. From this series, $\mathrm{i}\omega t_n = 2\mathrm{i}\pi n/N$ and the complex monochromatic displacement is computed as follow, within one phase factor:

$$\mathbf{u}(\mathbf{x},\omega) = \frac{1}{N}\sum_{n=0}^{N-1} \mathbf{u}^{(n)}(\mathbf{r}) e^{\frac{2in\pi}{N}} \tag{1.24}$$

Data contained in 60 memory-consuming frames of thousands of pixels has been reduced to a single complex matrix of a few hundreds points.

2.5 First observations

With the set-up in figure 1.7, field maps are acquired in an area of 17 cm $\times$ 2.4 cm below the line source (dashed area in the same figure). Figure 1.10 gathers real parts of the extracted displacements for an excitation frequency of 120 Hz. Three different vibration orientations (vertical, horizontal and 45°) are investigated while the source (a 30-cm-wide clamp) is maintained horizontal. In the left part of figure 1.10, for which the vibration is vertical, u_3 cancels everywhere in the measured area: the motion is purely vertical (x_1-direction). Also, u_1 exhibits a periodic pattern along the x_1 direction and a flat profile along the x_3 direction. This measurement corresponds to a plane wave-like pattern (with a wavelength λ of roughly 10 cm) with both displacement and wavevector being parallel to x_1. The plate thus supports an in-plane guided elastic wave that appears as longitudinal. This is the so-called S_0 mode that we discussed earlier. Similarly, the horizontal excitation in x_3-direction of the clamp (middle column in figure 1.10) generates a plane wave-like propagation with a

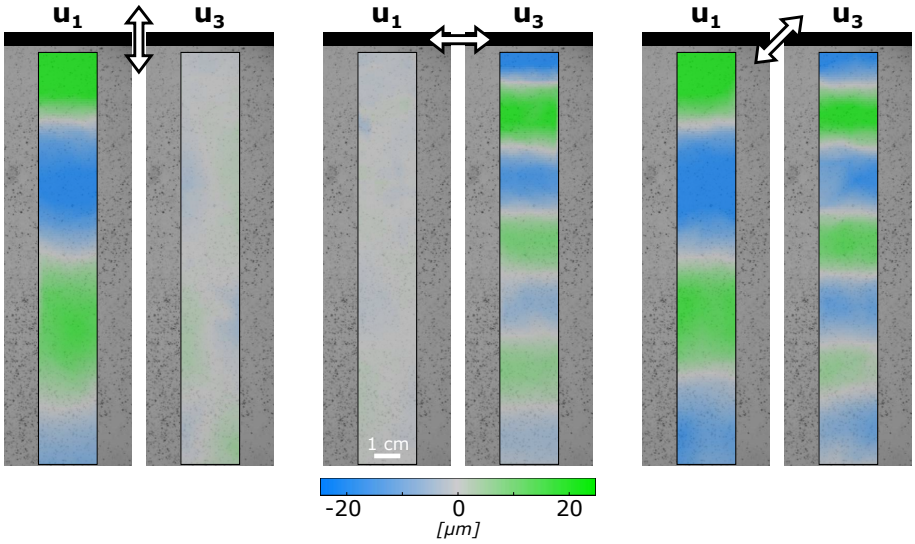

FIGURE 1.10: **Measurement of in-plane waves in a soft plate** – Displacement fields in both vertical (u_1) and horizontal (u_3) directions measured for three excitation directions with a forcing frequency $f = 120$ Hz. The source oscillates vertically (left), horizontally (middle) or at 45° (right) as indicated by the white arrows. Magnitude of in-plane displacements are indicated by the colorbar.

polarization parallel to x_3, that can be qualified as a transverse wave. Interestingly, its wavelength is exactly half the wavelength of its longitudinal counterpart. This is actually not surprising because the SH_0 mode is indeed generated and we have already seen there is a factor of 2 between the velocities, thus a factor of 2 between wavelengths. The versatility of this experimental platform is highlighted in the right panel of figure 1.10. Instead of selectively exciting each type of plane wave, a motion of the clamp along a 45° tilted direction excites simultaneously the two waves: with one measurement several modes are retrieved.

Finally, a systematic extraction of the two aforementioned plane waves for frequencies ranging from 50 to roughly 300 Hz is performed. For each frequency, the maps are averaged in the x_3-direction, meaning projected onto a plane wave. Then, the maximum of the spatial Fourier transform along x_1 provides the wavenumber $k = \frac{2\pi}{\lambda}$ (with λ the wavelength) of the mode. This way, a dispersion diagram is constructed for two polarizations in figure 1.11. Both dispersion curves appear to be straight lines passing through the origin. It corresponds to non-dispersive modes *i.e.* propagating at a constant phase velocity. The factor 2 between the wavelengths here nicely appears as a factor 2 between the slopes: the pseudo-longitudinal mode S_0 travels twice faster (12 m/s) than the transverse one SH_0 (6 m/s). From here, we recover a transverse velocity $V_T = 6$ m/s which roughly match the value of 5 m/s initially given.

For the highest frequencies, the experimental points slightly move off the linear behaviour. As will be discussed in section 3.6, the rheology of the polymer is the origin of both this deviation and the mismatch between 5 and 6 m/s, which remains anecdotal at this stage.

Before adding lateral edges to shape a strip, let us discuss the flexural wave in such a soft plate. In equation (1.22), the displacement of the flexural mode A_0 is derived in the long wavelength limit ($k \times 2h \ll 1$). From this, it appears that the A_0 mode is mainly out-of-plane, i.e. polarized along the x_2 axis. However, one can also see that, for $k > 0$, there is always an additional small displacement along the direction of propagation x_1. This being said, one can guess that our experimental setup also enables the detection of this flexural mode. We rotate the shaker so that a plane wave polarized along x_2 and propagating along x_1 is generated. By applying the same methods as before, the displacement component u_1 is extracted and the dispersion curve of this flexural wave is obtained

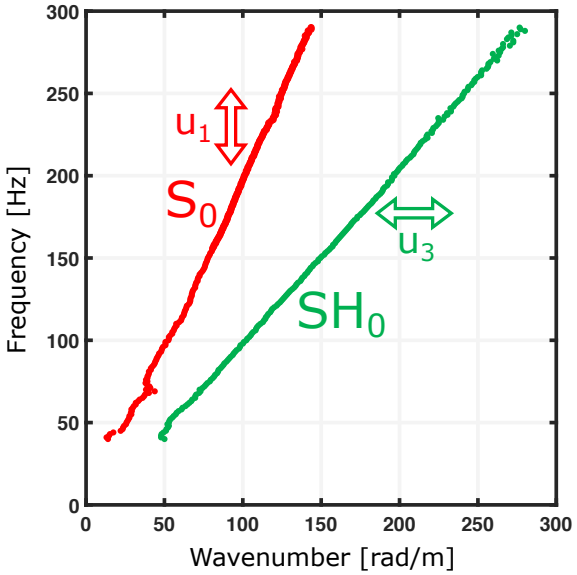

FIGURE 1.11: **Experimental dispersion curves of in-plane modes in a 3-mm-thick soft plate** – A vertically polarized (blue) and a horizontally polarized (green) non dispersive modes are retrieved. The vertically polarized mode propagates twice faster than the horizontally polarized one.

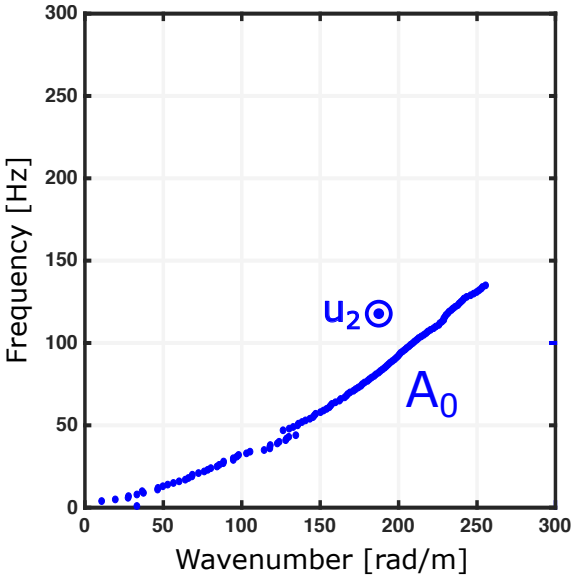

FIGURE 1.12: **Experimental dispersion curves of the flexural mode in a 3-mm-thick soft plate** – The quadratic behaviour of A_0, first anti-symmetric Lamb mode, or flexural mode, in a plate is retrieved.

in figure 1.12.

3 From a plate to a strip

In this section, a different geometry is considered: a thin rectangular waveguide made of the same nearly incompressible material. First, an analogy is made between this geometry and the previously described plate geometry. Notably, the dispersion of in-plane modes propagating in this strip is shown to be similar to that of Lamb waves propagating in an isotropic plate with a longitudinal wave velocity being exactly twice the shear wave velocity. Then, experimental results, already reported by LANOY et al. (2020)[42], are presented. The procedure used to separate modes in order to obtain their profiles as well as their phase velocities is thoroughly described.

The theory of elastic modes propagating in rectangular waveguides is not straightforward. As this geometry involves three coupled polarizations, obtaining the full dispersion diagram can be challenging[43]. Thanks to the Rayleigh-Lamb approximation[44,45], the problem drastically simplifies as then, one deals with the in-plane modes of a strip with a large aspect ratio. This section addresses this problem in the specific case of a soft solid.

[42] LANOY et al. (2020): "Dirac cones and chiral selection of elastic waves in a soft strip"
[43] KRUSHYNSKA and MELESHKO (2011): "Normal waves in elastic bars of rectangular cross section"
[44] CROSS and LIFSHITZ (2001): "Elastic wave transmission at an abrupt junction in a thin plate with application to heat transport and vibrations in mesoscopic systems"
[45] LAURENT et al. (2020): "In-plane backward and Zero-Group-Velocity guided modes in rigid and soft strips"

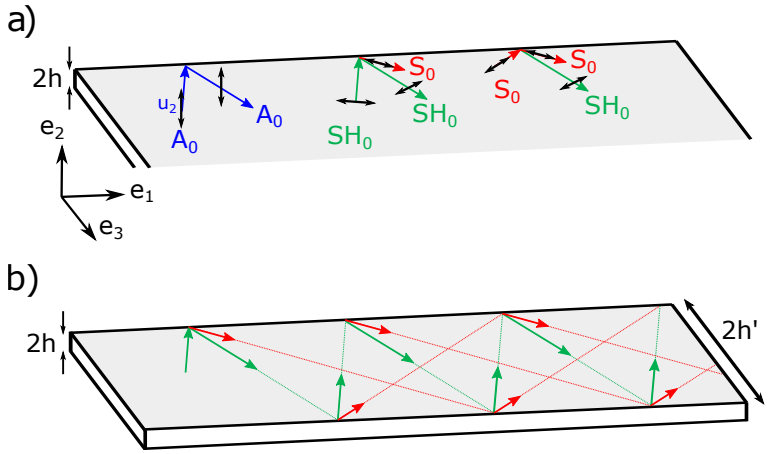

FIGURE 1.13: **Mode coupling in a strip** – (a) Reflection of A_0 on the edge only generates A_0 while S_0 and SH_0 modes couple. (b) Multiple reflections lead to S_0 and SH_0 in-plane mode coupling in a similar manner to shear and longitudinal waves couple in an infinite plate, as in figure 1.3.

3.1 Reflection at a free interface

As described in the previous section, only three modes propagate in a plate at low frequencies: the first shear horizontal mode SH_0 (Fig. 1.4) and the first symmetric S_0 and anti-symmetric A_0 Lamb modes (Fig. 1.5). They have uniform profiles across the plate and can roughly be considered as linearly polarized. In particular, S_0 can be seen as a pseudo-longitudinal wave propagating at the constant plate velocity V_P. Besides, as shown in equation (1.16), for nearly incompressible materials $V_P = 2V_T$. A_0 mode is essentially polarized in x_2-direction. As a consequence, it is unaffected by a reflection on the strip edge, as shown in figure 1.13(a). On the contrary, SH_0 and S_0, which are polarized in the (x_1, x_3)-plane, can couple at the edge. Adding a second edge enables to form a strip of width $2h'$ in figure 1.13(b). Before discussing this coupling between SH_0 and S_0 modes, let us first discuss the easier case of guided flexural modes in a strip.

3.2 Flexural modes in a strip

In the same way that SH modes are guided between two parallel planes in a plate (Fig. 1.3), flexural modes are guided independently in a strip of width $2h'$. To obtain their dispersion curves in figure 1.14, the procedure is similar to the one employed for figure 1.4 but using equation (1.23), and simply reads:

$$\omega = \omega_{A_0}\left(\sqrt{k^2+\left(\frac{n\pi}{2h'}\right)^2}\right) = \frac{V_P}{\sqrt{3}}\left[k^2+\left(\frac{n\pi}{2h'}\right)^2\right]h. \tag{1.25}$$

Dispersion curves of such modes are presented in figure 1.14. They have been obtained using COMSOL Multiphysics. A cuboid with dimensions $a = 0.1$ mm, $2h = 2.7$ mm, $2h' = 40$ mm is considered with material parameters $\rho = 1070$ kg/m^3, $V_T = 5.3$ m/s and $V_L = 1000$ m/s. Floquet periodicity with wavenumber k is assumed between faces at $x_1 = 0$ and $x_1 = a$, *i.e.* $\mathbf{u}(\pi/a, x_2, x_3) = \mathbf{u}(0, x_2, x_3)\, e^{ika}$. The resulting eigenvalue problem is solved to obtained frequencies $f(k)$ and the procedure is repeated for $0 \leq k \leq \pi/a$. The quadratic dispersion of A_0 in a plate is clearly revealed in this dispersion diagram for two reasons. First, the branches themselves are parabolic. Second, the cutoff frequencies are no longer equidistant but evolve as n^2. Additionally, we see two families of modes on this diagram, depending on their symmetry with respect to the $(x_3 = 0)$-plane. The first symmetrical flexural mode is actually identical to the A_0 mode in a plate, as indicated by equation (1.25), and thus appears as a plane wave polarized in the x_2 direction.

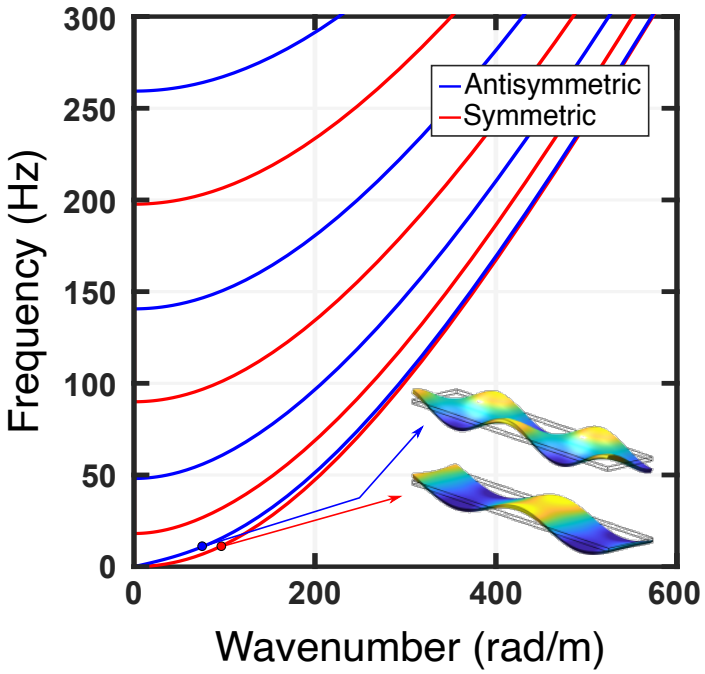

FIGURE 1.14: **Flexural modes in a strip** – Dimensions of this strip are $2h = 2.7$ mm, $2h' = 40$ mm and $V_T = 5.3$ m/s. The quadratic dispersion of A_0 in a plate is clearly revealed. Two families of modes exist, depending on their symmetry with respect to the $(x_3 = 0)$-plane. The two first modes are often referred to as the flexural (symmetric) and torsional (antisymmetric) modes of the strip.

Table 1.1: Analogy between Lamb waves in a plate and in-plane guided waves in a thin strip

	Guide dimension	Longitudinal velocity	Transverse velocity	Symmetry plane
Plate	Thickness $2h$	V_L	V_T	$x_2 = 0$
Strip	Width $2h'$	$V'_L = V_P$	$V'_T = V_T$	$x_3 = 0$

In addition, the first anti-symmetrical flexural mode corresponds to an upward displacement on one of the strip's lateral edges (*e.g.* $x_3 = -b/2$) and an opposite displacement on the other edge ($x_3 = +b/2$). This is in fact a torsional wave and, almost unexpectedly, behaves in a manner similar to the mode described above. Higher-order modes have additional nodes in their transverse profile (along the x_3 direction).
Now that we have discussed flexural waves, we describe the coupling of SH_0 and S_0 modes.

3.3 In-plane guided waves: analogy with Lamb waves

In a strip, the coupling of SH_0 and S_0 at both edges gives rise to complex in-plane guided modes. As shown in the section III of reference[44], this coupling is similar to the one of shear and compression bulk waves in a plate. These observations enable to build an analogy between Lamb waves in a plate and in-plane guided waves in a thin strip. In other words, the dispersion diagram for low frequency in-plane guided waves in a strip is equivalent to the one for guided waves in a plate. In the following descriptions, the symbol " $'$ " will be added to the notations when dealing with the strip configuration. The plate thickness $2h$ is replaced by the strip width $2h'$, the longitudinal wave

[44] CROSS and LIFSHITZ (2001): "Elastic wave transmission at an abrupt junction in a thin plate with application to heat transport and vibrations in mesoscopic systems"

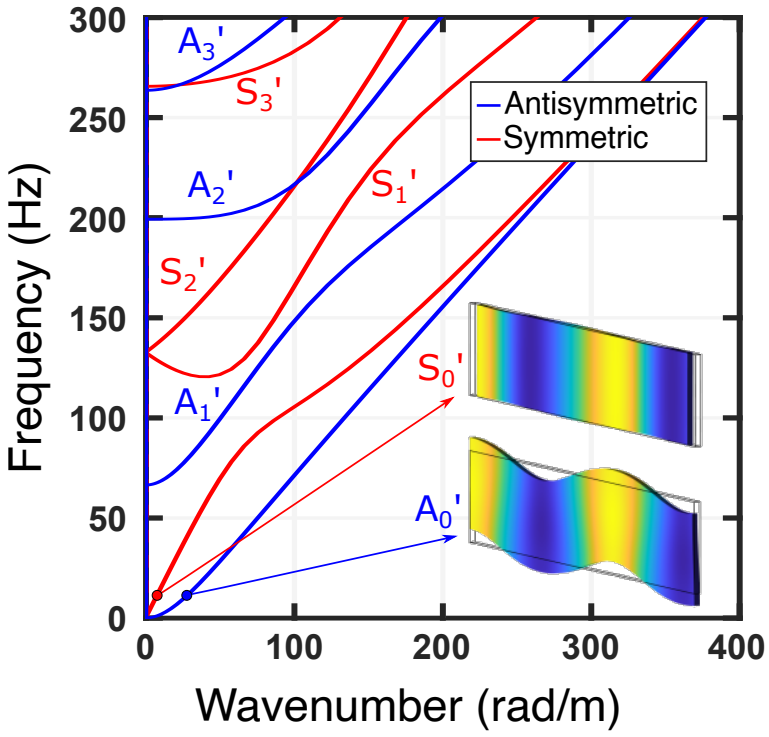

FIGURE 1.15: **Theoretical dispersion curves of in-plane modes in a soft strip** – Dispersion curves of symmetric (red and labeled S') and anti-symmetric (blue, A') modes without damping, in a strip with dimensions $2h = 2.7$ mm, $2h' = 40$ mm and transverse velocity $V_T = 5.3$ m/s. The first two modes are represented. Again, the polarization of the first symmetrical mode (S'_0) is mostly longitudinal while the first anti-symmetrical one (A'_0) rather corresponds to a flexural motion but in its width. From these curves, one can extract the bar velocity (mode S'_0 at low frequencies), and can evidence a Zero Group Velocity point (S'_1) and a backward branch, as well as a Dirac cone with a finite group velocity at $k=0$ and $f_c=V_T/2h'$.

propagating at V_L is replaced by the linearly polarized in-plane wave S_0 propagating at velocity V_P (that is $V'_L = V_P$), and the SV wave propagating at V_T is replaced by the transversely polarized in-plane wave SH_0 propagating at V_T (that is $V'_T = V_T$), as summarized in table 1.1.
This amounts to solving for Lamb waves in a material of equivalent Poisson's ratio:

$$\nu' = \frac{\nu}{1+\nu} \tag{1.26}$$

where ν is the Poisson's ratio of the strip material. In the mechanical computing community, this is known as the plane-stress formulation which perfectly matches this idea of equivalence between the strip and the plate that would be the plane-strain equivalent[46].

For incompressible materials, the equivalent Poisson ratio is $\nu' = 1/3$, and the knowledge of V_T is sufficient to obtain the full dispersion diagram of the in-plane guided waves in the low frequency range. Like for Lamb waves, solutions are separated into two families of modes that are either symmetrical S' or anti-symmetrical A' with respect to the $(x_3 = 0)$-plane.

The dispersion curves of the in-plane modes propagating in a soft strip are thus obtained by finding the roots of the Rayleigh-Lamb equation (1.19). Note that these solutions can also be recovered using COMSOL Multiphysics. Solutions are displayed in figure 1.15 in normalized units. Several interesting properties are highlighted in the following section.

[46] UGURAL and FENSTER (2003): *Advanced strength and applied elasticity*

3.4 Dispersion relation: key physical features

As we have just described a method to compute dispersion curves of guided waves in a soft strip, we can now explore some of its physical content. Many features of in-plane guided modes are worth highlighting. We focus on in-plane modes, not only because we can observe them with our experimental set-up, but also because the physics involved is particularly rich.

Bar velocity – The first symmetrical mode, denoted S_0', is approximately non dispersive for frequencies below the first cut-off frequency of $\sim$ 66 Hz. As with the first symmetric S_0 Lamb mode, S_0' can be seen as longitudinally polarized since it corresponds to compression in the strip. Its phase velocity can be calculated as a pseudo-plate velocity V_P', deduced from equation (1.21) and has a remarkably simple formulation:

$$V_P' = \sqrt{\frac{2}{1-\nu'}} V_T = \sqrt{2(1+\nu)} V_T \tag{1.27}$$

In the incompressible limit, it simplifies to $V_P' = \sqrt{3} V_T$. Interestingly, although polarized longitudinally at low frequencies, the S_0' velocity does not depend on the longitudinal velocity.

Furthermore, V_P' also corresponds to the well known bar velocity, associated to the propagation of compression waves along any bar or rod regardless of their cross-section. It can be obtained from the following intuitive reasoning. As it corresponds to longitudinal compression-extension of the waveguide, the relevant elastic modulus is the Young's modulus E and the associated velocity is $\sqrt{E/\rho}$. After injecting the expression $E = 2\,(1+\nu)\,\mu$, one immediately gets equation (1.27). For an incompressible material, the Young's modulus simplifies to $E = 3\mu$ and the bar velocity to $\sqrt{3} V_T$.

A flexural wave, but in the width – In contrast, the first anti-symmetrical mode, denoted A_0', is highly dispersive in the low frequency regime. Actually, when we study its associated displacement in figure 1.15, we see that it is a flexural motion, but along its width. Using the appropriate Poisson's ratio in equation (1.23) and h' rather than h, it is straightforward to derive the dispersion of the A_0' mode in the low-frequency limit, as:

$$\omega_{A_0'} = \frac{V_P'}{\sqrt{3}}\, k^2 h' = V_T\, k^2 h'. \tag{1.28}$$

When increasing the frequency, the wavelength becomes comparable to the strip width $2h'$, while still remaining very large compared to the thickness $2h$, and the two modes A_0' and S_0' merge to give rise to an edge mode propagating along the lateral edge of the strip.

Zero Group Velocity and Negative Phase Velocity – Similarly to Lamb modes, the second symmetrical mode S_1' has a remarkable behavior. Indeed, the corresponding branch exhibits a local minimum for a finite wavenumber. At this specific location, the group velocity $V_g = \mathrm{d}\omega/\mathrm{d}k$ vanishes. This is the signature of a Zero Group Velocity (ZGV) point. For small wave numbers, the S_1' branch has a negative slope. This indicates that the group velocity is opposite to the phase velocity. Causality imposes that the energy travels from the source to the receiver. As a consequence the group velocity should always remain positive. In practice, the negative slope section cannot be measured and experiments rather reveal its symmetric branch with respect to the $k=0$ axis. This is discussed and displayed in the following sections.

Dirac cones: finite group velocity at $k \to 0$ − In the small wavenumber limit ($k \to 0$), branches usually presents a horizontal slope (for example the Lamb modes in the plate of figure 1.5) and dispersion curves $\omega(k)$ are quadratic around their cut-off pulsations ω_c. As shown by Mindlin (2006)[47], this expansion does not hold for Lamb modes when there is a coincidence between a shear and a longitudinal cut-off frequency of the same symmetry. In these particular cases, the dispersion law is linear in the limit $k \to 0$ and approximates to the first order in k as:

$$\omega(k) = \omega_c + V_g k + o(k) \tag{1.29}$$

Such coincidences occur for symmetrical modes S_{2m+1} and S_{2n}, when the bulk velocity ratio V_L/V_T is equal to $2n/(2m+1)$, and for anti-symmetrical modes A_{2m+1} and A_{2n} when $V_L/V_T = (2m+1)/2n$. For example, recent experiments conducted in a cooled aluminum plate ($V_L/V_T = 2$) by Stobbe and Murray (2017)[48] illustrate this linear dispersion near $k=0$. For modes S_1 and S_2, linear slopes of the $\omega(k)$ curve can be derived by developing equation (1.19) to the first order and were found[47] to be $V_g = \pm 2V_T/\pi$.

The Lamb wave approximation for in-plane modes in a thin soft strip (*i.e.* $\nu' = 1/3$) reveals a coincidence frequency for symmetrical modes S_1' and S_2'. As a result, these two modes cross linearly at the normalized frequency $2fh'/V_T = 1$ in figure 1.15. This linear crossing is also referred to as a Dirac cone[49,50]. While for ordinary cut-offs the displacement is either pure S_0 or pure SH_0, both polarizations are involved when there is a coincidence.

3.5 Experimental measurements in a soft strip

Let us now experimentally assess the dispersion curves of in-plane guided waves in a soft strip. The soft plate is replaced by a soft strip using a new mould. The final strip dimensions are 60 cm, $2h = 3$ mm and $2h' = 40$ mm in x_1, x_2 and x_3 directions respectively. The line source is replaced by a point-like clamp, obtained by attaching a small magnet to the shaker and pinching the strip with a second magnet. The source is slightly off-centered ($x_3 \neq 0$) and vibrates in the x_1-direction. The setup[42] is reported in figure 1.16. Here again, the strip is shaken monochromatically for frequencies ranging from 1 to 200 Hz. The camera captures the motion by following the stroboscopic sketch pictured in figure 1.8. Finally, displacement components u_1 and u_3 are extracted by applying the DIC algorithm. Examples of the obtained field maps at 110 Hz are represented in figure 1.17. The wave pattern is quite different from the one obtained in the plate. This is due to the superposition of several modes with different propagation constants and spatial profiles. Separating and identifying them requires two additional post-processing steps schematized in figure 1.17. First, symmetrical and anti-symmetrical parts are extracted by respectively summing or subtracting displacement maps with their flipped counterpart in x_3-direction. Concatenating these field maps yields two bigger matrices $\mathbf{u}$, in top of figure 1.17, one for each symmetry. Then, a Singular Value Decomposition (SVD) is performed on each matrix. This amounts to the following matrix decomposition:

$$\mathbf{u} = \mathrm{V}\Sigma\mathrm{W} \tag{1.30}$$

where V and W are unitary matrices providing displacement profiles along the x_3 and x_1 coordinates, respectively, and Σ is a diagonal matrix providing singular values, *i.e.* the mode prominence in the overall measurement. The i-th column of V is noted V_i, and the i-th line of W is noted W_i. As a selection criterion, all modes associated with singular values of at least 10% of the maximum singular

[47] Mindlin (2006): *An Introduction to the Mathematical Theory of Vibrations of Elastic Plates*
[48] Stobbe and Murray (2017): "Conical dispersion of Lamb waves in elastic plates"
[47] Mindlin (2006): *An Introduction to the Mathematical Theory of Vibrations of Elastic Plates*
[49] Maznev (2014): "Dirac cone dispersion of acoustic waves in plates without phononic crystals"
[50] Huang et al. (2011): "Dirac cones induced by accidental degeneracy in photonic crystals and zero-refractive-index materials"
[42] Lanoy et al. (2020): "Dirac cones and chiral selection of elastic waves in a soft strip"

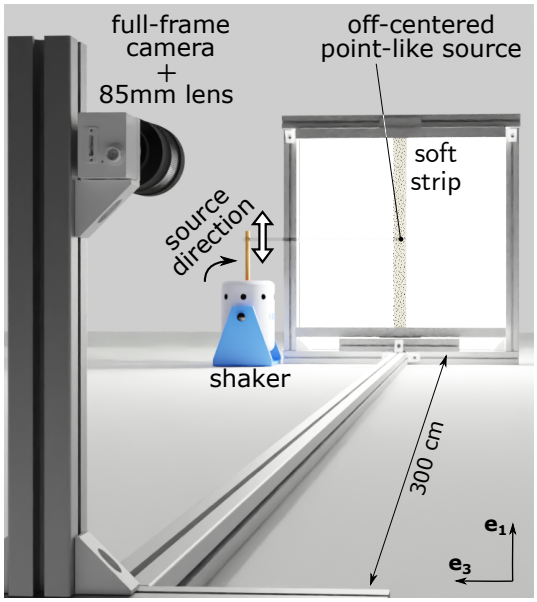

FIGURE 1.16: **Experimental set-up using a point-like source** – A thin strip ($L = 60$ cm, $2h' = 40$ mm, $2h = 3$ mm) is held vertically. A shaker generates in-plane displacements propagating in the strip.

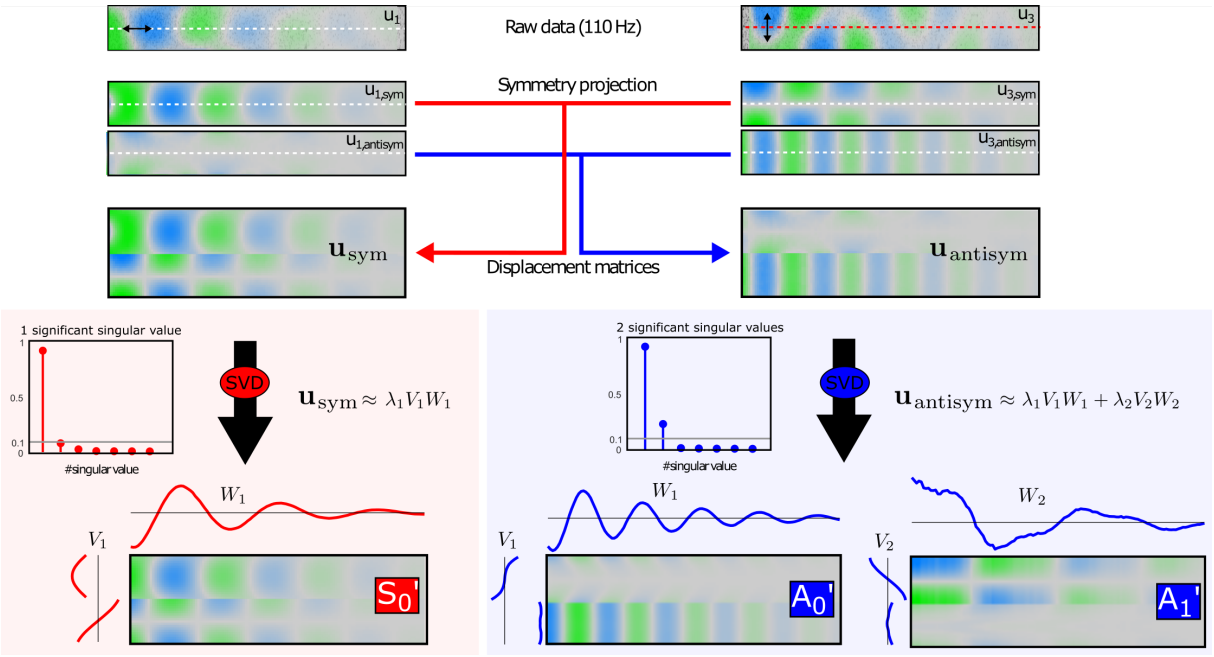

FIGURE 1.17: **Mode separation via Singular Value Decomposition (SVD)** – At 110 Hz, in-plane displacement components u_1 and u_3 (top left) are projected onto their symmetrical and anti-symmetrical parts (top right). Data are then concatenated into a single complex matrix $\mathbf{u}_{\text{sym}}$ (resp. $\mathbf{u}_{\text{antisym}}$) on which the SVD is directly applied. After extracting most significant modes (singular values above a 10% threshold), we obtain one symmetrical (S_0') and two anti-symmetrical (A_0' and A_1') modes.

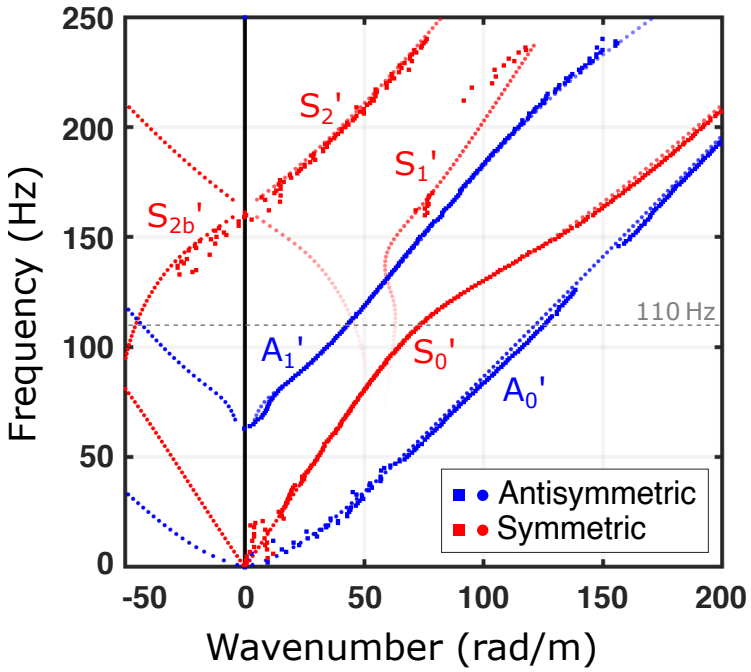

FIGURE 1.18: **Dispersion curves of in-plane modes in a free strip ($2h' = 39$ mm)** – Experimental (squares) and theoretical (circles) dispersion curves with damping (the more transparent the curve the more attenuated the mode). Dirac cone (linear crossing of the $k=0$ axis) and backward modes (negative wavenumbers) are unambiguously evidenced, while the ZGV point has disappeared. Predictions are also drawn by symmetry and corresponds to modes propagating in direction $-\mathbf{e}_1$.

value are considered as meaningful. The other ones are rejected. At 110 Hz (see figure 1.17), three modes have a relevant contribution: two symmetrical modes and one anti-symmetrical. Other selection criteria could be used, such as SVD entropy:

$$S = \left\lceil -\sum_i \frac{\lambda_i}{\sum_j \lambda_j} \ln\left(\frac{\lambda_i}{\sum_j \lambda_j}\right) \right\rceil$$

but it has not shown better peformance than a simple threshold so we stick to the first described criterion. In any case, the selection criterion is often chosen low enough to ensure that all modes are available at the end. Since W gives the displacement profile along the propagation direction (x_1), its Fourier transform yields the wavenumbers of the contributing modes.

These steps are repeated for all frequencies and dispersion curves are represented as symbols in figure 1.18. As stated earlier, in experiments, one measures negative phase velocities rather than negative group velocities. This is why the horizontal axis covers negative values.

3.6 Influence of rheology

Overall, the experimental dispersion curves in figure 1.18 relatively resemble theoretical ones in figure 1.15 and most of the discussed key features are visible. Indeed, the bar velocity of the strip (S'_0 mode at low frequency) matches the expected value of $\sqrt{3}V_T \sim 10$ m/s (where V_T is deduced from the SH_0 velocity measurement presented in figure 1.10). At 150 Hz, S'_2 crosses the $k=0$ axis with a linear slope: this is the Dirac cone. Note that, below the Dirac frequency, the measured points have negative wavenumbers: this is a signature of negative phase velocities. The continuity in the measured points naturally leads to label this backward branch S'_{2b} ("b" for backward). This

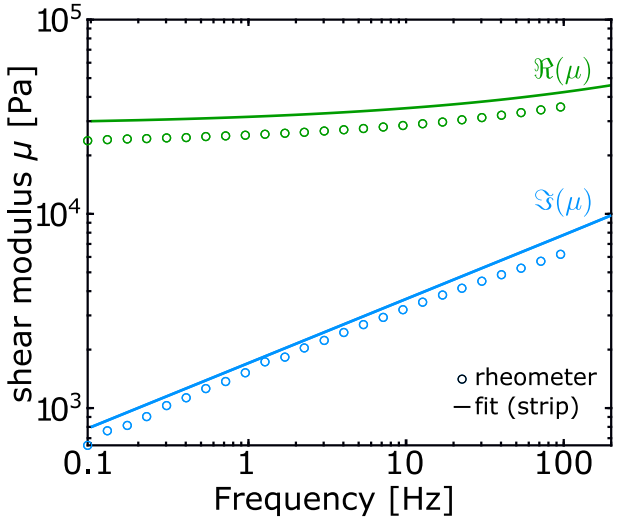

FIGURE 1.19: **Rheology of Ecoflex** – Measurement of the complex shear modulus of Ecoflex 00-30 in the range $0.1 - 100$ Hz with a conventional plane-plane rheometer (circles). Re(μ) is the storage modulus of the rubber while Im(μ) is its loss modulus. Lines correspond to the values extracted from the dispersion curves (see text and figure 1.18).

may appear in contradiction with the dispersion curves for a lossless material shown in figure 1.15 where the backward mode belongs to the S_1' branch. However, when the complex wavenumbers are displayed for Lamb modes [51], it clearly appears that the backward branch is connected to S_2' mode even when the cone does not exist[47], thus this notation is adopted in several papers[52,53,54,45].

However, there are two main differences between theory in figure 1.15 and experiment in figure 1.18. First, the Dirac cone should exactly be at $f_c = V_T/2h'$ but it does not match the value deduced from the measured bar velocity nor the value deduced from the asymptotic behaviour at high frequencies of A_0' and S_0'. Second, and more surprisingly, the ZGV point is not visible in the experiment. These two differences can be explained by examining the elastomer rheology that we measured independently with a conventional rheometer (Anton-Paar MCR501) which operates in the plate-plate configuration. To this end, a different sample of Ecoflex 00-30 is cured in the rheometer itself. Both the real (storage modulus) and imaginary (loss modulus) parts of the measured shear modulus for frequencies ranging from 0.1 to 100 Hz are displayed as symbols in figure 1.19. In such a logarithmic scale, the loss modulus appears to vary linearly with a slope of almost 1/3, while the storage modulus slowly increases. As the slope is not an integer, we opt for a fractional derivative model. One of the simplest model which also satisfies the Kramers-Kronig relations is the fractional derivative Kelvin-Voigt model[55,56,57], also suggested for Ecoflex by other works[58,59], which takes

[51] MINDLIN and MEDICK (1959): "Extensional Vibrations of Elastic Plates"
[47] MINDLIN (2006): *An Introduction to the Mathematical Theory of Vibrations of Elastic Plates*
[52] PRADA et al. (2005): "Laser-based ultrasonic generation and detection of zero-group velocity Lamb waves in thin plates"
[53] PHILIPPE et al. (2015): "Focusing on plates: controlling guided waves using negative refraction"
[54] GÉRARDIN et al. (2016): "Negative reflection of Lamb waves at a free edge: Tunable focusing and mimicking phase conjugation"
[45] LAURENT et al. (2020): "In-plane backward and Zero-Group-Velocity guided modes in rigid and soft strips"
[55] MERAL et al. (2009): "Surface response of a fractional order viscoelastic halfspace to surface and subsurface sources"
[56] KEARNEY et al. (2015): "Dynamic viscoelastic models of human skin using optical elastography"
[57] ROLLEY et al. (2019): "A flexible rheometer design to measure the visco-elastic response of soft solids over a wide range of frequency"
[58] YASAR et al. (2013): "Wideband MR elastography for viscoelasticity model identification"
[59] LIU et al. (2014): "Ultra wideband (0.5–16 kHz) MR elastography for robust shear viscoelasticity model identification"

the form:

$$\mu(\omega) = \mu_0\left[1 + (\mathrm{i}\omega\tau)^n\right] \tag{1.31}$$

The Kelvin-Voigt model is a commonly used viscoelastic model, and its fractional derivative counterpart $(\mathrm{i}\omega)^n$ with $0 < n < 1$ originates from so-called memory effects, where no relaxation times and Prony series decomposition are needed because the relaxation function is given by a power-law decay as detailed in [60,61,62]. This viscoelastic model tends to apply for soft solid mechanics[63] and is recommended to model the behaviour of soft tissues[64].

At this stage, it is worth mentioning that the analogy presented in section 3.3 was initially built in order to enable the derivation of those dispersion curves. However, it is difficult to implement frequency-dependent parameters in either COMSOL Multiphysics, or in the Muller algorithm that is used to find roots of the Rayleigh-Lamb equation.

As already mentioned earlier, with the arrival of Daniel A. Kiefer at the laboratory, we adapted the Spectral Collocation Method (SCM) implemented in Matlab for plates[37,38] to the geometry of a rectangular waveguide. This is published in Delory et al. (2023)[65] and detailed in Appendix A. As it allows to use frequency-dependent parameters and because its implementation rapidly provides accurate solutions for the waves of interest, we have used the SCM to perform parametric studies all along this thesis.

So the frequency-dependent complex shear modulus, given by equation (1.31), is injected in the stiffness tensor for the SCM. The latter is being run with several sets of parameters (μ_0, τ, n) until a satisfying agreement between theory and experiment is reached. The final set of parameters is $\mu_0 = 26$ kPa, $\tau = 260$ μs and $n = 0.33$. It corresponds fairly well to the measured rheology (Fig. 1.19) but slightly overestimates $\mathrm{Re}(\mu)$. This discrepancy can be attributed to temperature changes or to differences between the two samples due to preparation or ageing.

Theoretical dispersion curves in figure 1.18 are calculated with these parameters. The imaginary part of the wavenumber is rendered by transparency. The frequency dependence of $\mathrm{Re}(\mu)$ induces a frequency dependence of the velocity V_T which allows to fit the entire S_0', A_0' and A_1' branches. Factoring viscoelasticity in also explains the lowered Dirac frequency. As for the absence of ZGV points, it is solely due to the viscous damping. While for a lossless material, the S_1' branch and the symmetrical of S_{2b}' with respect to the $k = 0$ axis connect at the ZGV point, here, the losses separate those two branches, as already evidenced in the work of Simonetti and Lowe (2005)[66].

Fundamental aspects of this system and its properties have now been identified. We now examine what happens if we impose a zero displacement at the lateral edges of the strip, *i.e.* we switch from Neumann to Dirichlet boundary conditions.

3.7 Investigating Dirichlet boundary conditions

In this section, the experiment is modified in order to investigate the role of boundary conditions, as shown in figure 1.20. In the Dirichlet configuration, the dispersion is simpler. In section 1.3.3, the analytical Lamb problem is derived assuming free boundary conditions (Neumann configuration). Here, the case of fixed boundaries (Dirichlet configuration) is investigated. In practice, these conditions can be implemented by clamping the strip in a rigid frame as shown in figure 1.21.

[60] Mainardi (2010): *Fractional Calculus and Waves in Linear Viscoelasticity*
[61] Machado et al. (2011): "Recent history of fractional calculus"
[62] Meral et al. (2010): "Fractional calculus in viscoelasticity: An experimental study"
[63] Sharma et al. (2023): "Characterizing Viscoelastic Polyvinyl Alcohol Phantoms for Ultrasound Elastography"
[64] Parker et al. (2019): "Towards a consensus on rheological models for elastography in soft tissues"
[37] Kiefer (2022): *GEW dispersion script*
[38] Kiefer (2022): *Elastodynamic quasi-guided waves for transit-time ultrasonic flow metering*
[65] Delory et al. (2023): "Guided elastic waves in stretched viscoelastic strip"
[66] Simonetti and Lowe (2005): "On the meaning of Lamb mode nonpropagating branches"

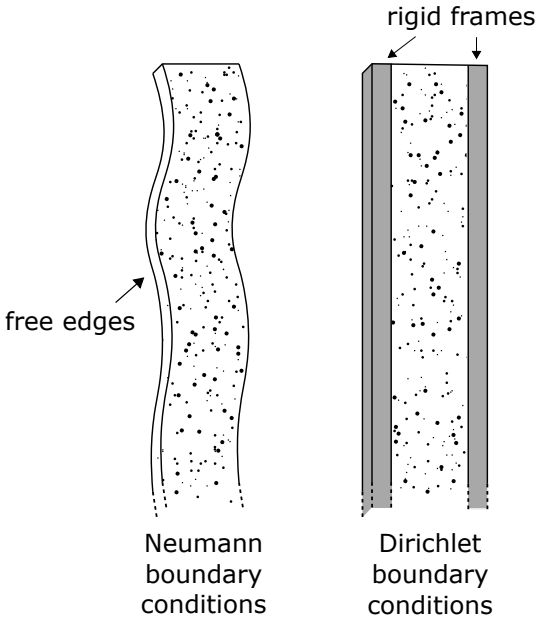

FIGURE 1.20: **Boundary conditions** – We study the Neumann (free edges) and Dirichlet (fixed edges) boundary conditions.

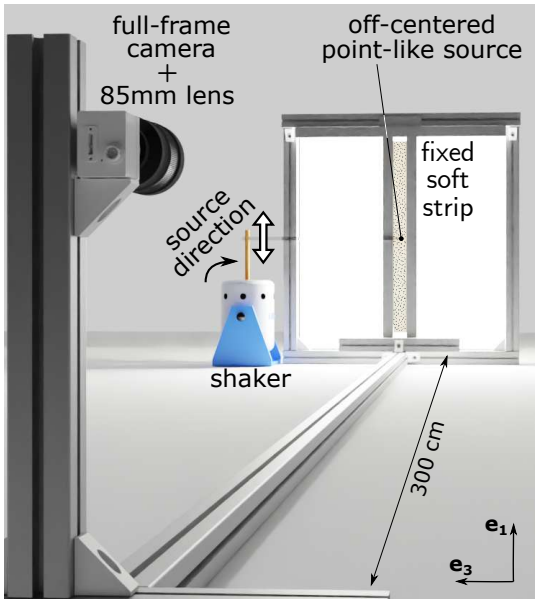

FIGURE 1.21: **Experimental set-up for a fixed strip** – A thin strip ($L = 60$ cm, $2h' = 47$ mm, $2h = 3$ mm) is clamped at its lateral edges and held vertically.

3.7.1 Theory

From a theoretical point of view, switching from Neumann to Dirichlet boundaries amounts to replacing the zero strain condition in equations (1.17) by a zero displacement condition:

$$\begin{cases} ik\phi_0 \cos(p'h'+\alpha) + q\psi_3 \cos(qh'+\alpha) &= 0 \\ -p'\phi_0 \sin(p'h'+\alpha) + ik\psi_3 \sin(qh'+\alpha) &= 0 \end{cases} \tag{1.32}$$

The equivalent Rayleigh-Lamb equation for rigid boundaries then writes:

$$k^2 \sin(qh'+\alpha)\cos(p'h'+\alpha) + qp' \sin(p'h'+\alpha)\cos(qh'+\alpha) = 0 \tag{1.33}$$

Dispersion curves can be obtained by searching the roots of this equation, or by implementing those new boundary conditions in the SCM.

The analogy with Lamb waves is first used to obtain theoretical dispersion curves displayed in figure 1.22. Compared to figure 1.15, one important feature is the absence of propagation at low frequency (A'_0 and S'_0 have disappeared). Indeed, rigid walls imply that no static in-plane deformation can be solution to the problem. However, cut-off modes (A'_1, S'_1, A'_2, *etc.*.) still exist. Note that the negative sloped branch, Dirac cone and ZGV exist for anti-symmetric modes rather than symmetric ones.

The Dirac cone appears here for anti-symmetric modes at the same frequency $f_c = V_T/2h$ as for the Neumann configuration. And the Taylor expansion of p and q at this frequency can be derived and substituted into the dispersion relation (1.33), leading to the same expression for the group velocity $V_g = \pm\frac{2}{\pi}V_T$.

3.7.2 Measurements in a clamped soft strip

The experiment is performed under the same conditions as before. The strip is held along its edges between two steel plates, and the width is adjusted to avoid buckling or static tension. The

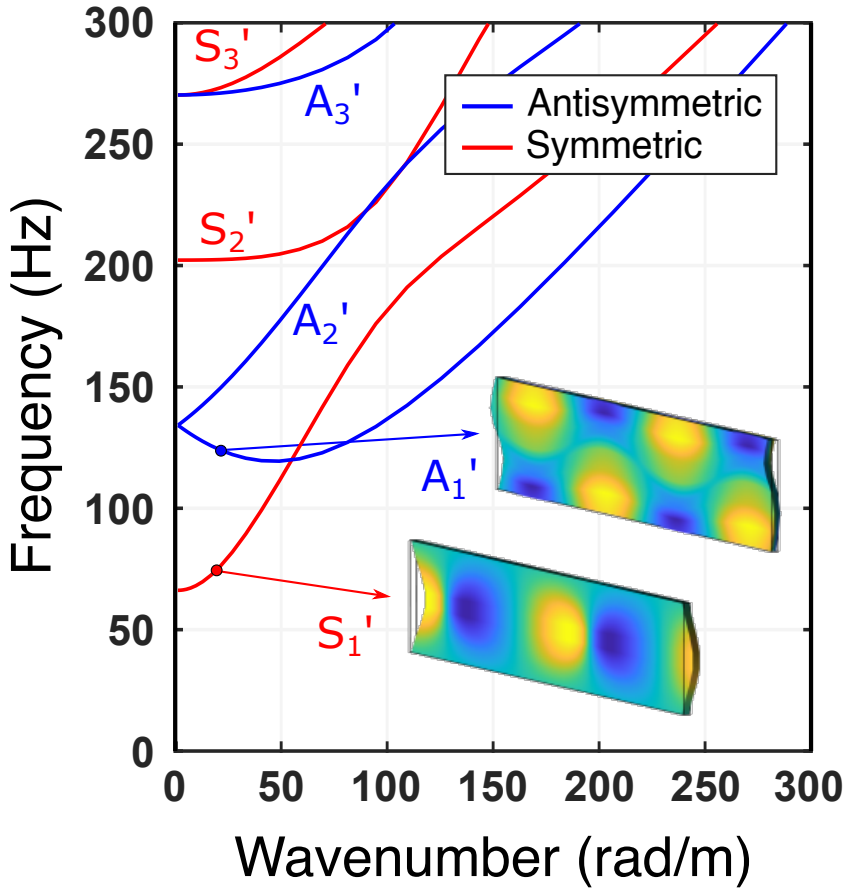

FIGURE 1.22: **Theoretical dispersion curves of in-plane modes in a clamped soft strip** – Dispersion curves of symmetric (red and labeled S') and anti-symmetric (blue, A') modes without damping in a strip with dimensions $2h = 3$ mm, $2h' = 47$ mm and transverse velocity $V_T = 6$ m/s. The polarization of the first symmetrical mode (S'_1) is mostly longitudinal while the first anti-symmetrical one (A'_1) is mostly transverse (along x_3). Note that these first two modes already have a non-zero cut-off frequency. These curves evidence a Zero Group Velocity point (A'_1) and a backward branch, as well as a Dirac cone with a finite group velocity at $k=0$ and $f_c=V_T/2h'$.

excitation clamp is again slightly off-centered and vibrates in the x_1-direction from 50 to 200 Hz. The image analysis allows to extract the experimental dispersion curves represented as symbols in figure 1.23. The three modes expected in this frequency range are well detected and similar observations as for the free strip can be made. First, data points around 130 Hz show a linear crossing of the $k=0$ axis, which evidences the existence of a Dirac cone for anti-symmetric modes. Second, points measured below this cut-off frequency correspond to negative wavenumbers, which is the signature of a backward mode. Here again, the continuity of the points across the Dirac cone logically leads to attribute the backward modes to the branch A'_2, unlike what is indicated for the lossless medium theoretical curves represented in figure 1.22. We should not forget that $k \leftrightarrow -k$ symmetry exists, so the symmetrical branch backward modes in the $k < 0$ region actually joins the A'_2 branch in the $k > 0$ region. This part of the curve is thus referred to as A'_{2b}. Just like for the Neumann configuration, theory provides a convincing agreement provided that rheology is taken into account. The value of $\mathrm{Re}(\mu)$ has an effect on the asymptotic slopes, while the value of $\mathrm{Im}(\mu)$ again affects the Dirac frequency. In addition, the ZGV point is accurately defined only when $\mathrm{Im}(\mu) = 0$. In this lossy material, two modes with almost opposite wavenumbers coexist, which almost corresponds to a ZGV point. The absence of actual ZGV point is evidenced by the

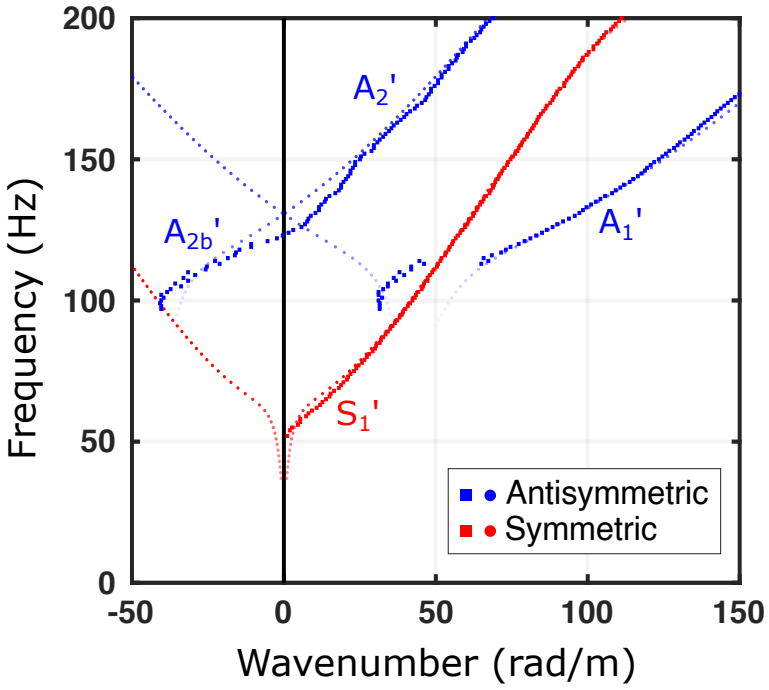

FIGURE 1.23: **Dispersion curves of in-plane modes in the clamped strip** ($2h' = 50.6$ **mm**) – Experimental (squares) and theoretical (circles) dispersion curves (the more transparent the more attenuated). The A'_2 Dirac cone (linear crossing of the $k=0$ axis) and backward A'_{2b} modes (negative wavenumbers) are unambiguously evidenced.

disconnection between branches A'_1 and the symmetric of A'_{2b} with respect to $k = 0$ axis, just as in the Neumann configuration. This is a direct consequence of increasing losses near this point as rendered by the theoretical points transparency.

4 Conclusion

In this chapter, we introduced the linear elasticity theory and briefly described elastic waves in bulk media. We studied the coupling of the three existing polarizations when reflecting on a plane interface, leading naturally to waves in a plate, consisting of two parallel plane interfaces. We first described this problem analytically and obtained the Rayleigh-Lamb equation. Instead of using usual root-finding algorithms, we showed that the resolution could be performed using a Spectral Collocation Method (SCM), a numerical tool for calculating dispersion curves of guided elastic waves in a plate (both *SH* and Lamb modes).

We then introduced a simple yet versatile experimental platform to generate and observe these guided waves, which we could even call a "playground". In particular, we measured the three fundamental modes, *i.e.* SH_0, S_0 and A_0, in Ecoflex, a commercial silicone elastomer. Soft elastomers enable large displacements and slow propagation, which drastically facilitates the experimental procedure. We verified that the longitudinal plate velocity V_P is indeed given by twice the transverse velocity V_T.

Next, we focused on the geometry studied in depth later in this PhD thesis: the so-called strip geometry. An analogy with Lamb waves allowed us to obtain an approximate dispersion diagram for in-plane guided waves, but once again SCM provided an accurate solution. This strip geometry greatly enriches the physics at stake, and key features of the dispersion curves were discussed. Namely, a Dirac cone appears as a direct consequence of the incompressibility nature of

soft elastomers. Finally, still using this strip geometry, we demonstrated the importance of rheology and its impact on cut-off frequencies, asymptotic slopes and the ZGV point disappearance. We have also been able to apply all these methods to another configuration where the strip edges are fixed, and consistent results were obtained.

One question that came up was: what influence could weight might have on the propagation of these guided waves? We naturally wondered how these dispersion diagrams would change if the elastomers were pulled before applying our experimental method. The following chapter indeed investigates the effect of prestress on the velocities of SH_0 and S_0 modes in a plate. Then, in chapter 3, we look at the full dispersion diagrams in prestressed strips with either free or fixed edges.

Appendix A: Solving the full 3D problem using a Spectral Collocation Method

We briefly recall the theory underlying elastic guided waves in a strip, going back to equation (1.10). The infinite strip has a rectangular cross-section Ω in the (x_2, x_3)-plane, the thickness (respectively the width) is given in direction x_2 (resp. x_3). We are interested in plane guided waves propagating in the x_1-direction, which lead to a wave field of the form:

$$\mathbf{u}(k, x_2, x_3, \omega)\, \mathrm{e}^{\mathrm{i}(kx_1 - \omega t)}\,. \tag{1.34}$$

Here, our method to compute the dispersion curves with Matlab is based on a SCM. The mathematical background of the method is treated in References[67,68]. For a general overview on implementing spectral collocation to compute guided waves in plates (one-dimensional cross-section) refer to Reference[69]. Lastly, a very concise derivation for anisotropic plates is presented in Reference[70].

The computational method consists of three fundamental steps: (i) derive the boundary-value problem that describes plane guided waves, (ii) replace differential operators by spectral differentiation matrices to obtain a discrete approximation of the guided wave problem, and (iii) use standard numerical methods to solve the resulting algebraic eigenvalue problem.

Step (i) consists of inserting equation (1.34) into the equation of motion (1.10). After rearranging the terms this yields (in symbolic tensor notation):

$$\begin{aligned}\Big[&(\mathrm{i}k)^2\mathbf{c}_{11} + \mathrm{i}k(\mathbf{c}_{21} + \mathbf{c}_{12})\partial_2 + \mathrm{i}k(\mathbf{c}_{31} + \mathbf{c}_{13})\partial_3 + \\ &+\mathbf{c}_{22}\partial_2^2 + (\mathbf{c}_{32} + \mathbf{c}_{23})\partial_3\partial_2 + \mathbf{c}_{33}\partial_3^2 + \omega^2\rho\mathbf{1}\Big] \cdot \mathbf{u} = \mathbf{0} \quad \text{on} \quad \Omega\,,\end{aligned} \tag{1.35}$$

where we have defined the second order tensors $\mathbf{c}_{ij} := \mathbf{e}_i \cdot \mathbf{C} \cdot \mathbf{e}_j$ with $i, j \in \{1, 2, 3\}$. A more detailed derivation for a plate can be found in Kiefer et al. (2023)[70].

Boundary conditions are needed in addition to equation (1.35). The strip is free (homogeneous Neumann boundary condition) on the boundary $\partial\Omega$. Writing $\mathbf{e}_n$ for the unit normal to the strip cross-section, *i.e.* either $\mathbf{e}_2$ or $\mathbf{e}_3$, the homogeneous Neumann boundary condition reads:

$$\mathbf{e}_n \cdot \mathbf{C} : \nabla\mathbf{u} = [\mathrm{i}k\mathbf{c}_{n1} + \mathbf{c}_{n2}\partial_2 + \mathbf{c}_{n3}\partial_3] \cdot \mathbf{u} = \mathbf{0} \quad \text{on} \quad \partial\Omega_{\mathrm{N}}\,. \tag{1.36}$$

The equation of motion (1.35) together with the boundary condition in equation (1.36) constitute the boundary-value problem that describes guided waves in the strip. Note that for a given value of ω, it constitutes a quadratic differential eigenvalue problem with eigenvalue k and eigenfunction $\mathbf{u}(x_2, x_3)$.

The discretization is performed in step (ii). To this end, the domain $\Omega = [0, h] \times [0, b]$ is discretized as suggested by Weideman and Reddy (2000)[68] using Chebyshev spectral collocation. The first and second order differentiation matrices $D^{(10)}$ and $D^{(20)}$ of size $N \times N$ along the x_2-coordinate are computed using DMSUITE[68]. We proceed similarly for differentiation along the x_3-coordinate, yielding matrices $D^{(01)}$ and $D^{(02)}$ of size $P \times P$. Next, the differentiation matrices

[67] Trefethen (2000): *Spectral Methods in MATLAB*
[68] Weideman and Reddy (2000): "A MATLAB Differentiation Matrix Suite"
[69] Adamou and Craster (2004): "Spectral methods for modelling guided waves in elastic media"
[70] Kiefer et al. (2023): "Computing zero-group-velocity points in anisotropic elastic waveguides: Globally and locally convergent methods"
[70] Kiefer et al. (2023): "Computing zero-group-velocity points in anisotropic elastic waveguides: Globally and locally convergent methods"
[68] Weideman and Reddy (2000): "A MATLAB Differentiation Matrix Suite"
[68] Weideman and Reddy (2000): "A MATLAB Differentiation Matrix Suite"

in the (x_2, x_3)-plane are obtained as Kronecker products[A], denoted by "$\otimes$", between the former one-dimensional differentiation matrices. Concretely, this yields the matrices:

$$\begin{aligned} D_{23} &= D^{(01)} \otimes D^{(10)}\,, & D_2 &= I_P \otimes D^{(10)}\,, & D_{22} &= I_P \otimes D^{(20)}\,, \\ D_3 &= D^{(01)} \otimes I_N\,, & D_{33} &= D^{(02)} \otimes I_N\,, & I_\mathrm{d} &= I_P \otimes I_N\,, \end{aligned} \tag{1.37}$$

where I_Q denotes the identity matrix of size $Q \times Q$.

Next, partial derivatives in equations (1.35) and (1.36) are replaced by differentiation matrices given in equation (1.37). When doing so, the multiplication of the differentiation matrices with second order constitutive tensors $\mathbf{c}_{ij}$ needs to be interpreted again as Kronecker products. This finally yields:

$$\begin{aligned} \Big[&(\mathrm{i}k)^2 \mathbf{c}_{11} \otimes I_\mathrm{d} + \mathrm{i}k(\mathbf{c}_{21} + \mathbf{c}_{12}) \otimes D_2 + \mathrm{i}k(\mathbf{c}_{31} + \mathbf{c}_{13}) \otimes D_3 + \\ &+ \mathbf{c}_{22} \otimes D_{22} + (\mathbf{c}_{32} + \mathbf{c}_{23}) \otimes D_{23} + \mathbf{c}_{33} \otimes D_{33} + \omega^2 \rho \mathbf{1} \otimes I_\mathrm{d}\Big]\, u = 0\,, \end{aligned} \tag{1.38}$$

where u denotes the $3NP \times 1$ vector of u_1, u_2, u_3 displacements at the NP collocation points. Hence, equation (1.38) represents a linear system of size $3NP \times 3NP$.

The discrete boundary conditions are obtained similarly and the Neumann boundary condition from equation (1.36) becomes:

$$[\mathrm{i}k\mathbf{c}_{n1} \otimes I_\mathrm{d} + \mathbf{c}_{n2} \otimes D_2 + \mathbf{c}_{n3} \otimes D_3]\, u = 0\,. \tag{1.39}$$

Lastly, the boundary conditions need to be incorporated into equation (1.38). This is done by replacing the corresponding rows of (1.38) with the ones from (1.39), as appropriate. Denoting final matrices with the mentioned replacements as L_2, L_1, L_0 and M, this finally leads to:

$$[(\mathrm{i}k)^2 L_2 + \mathrm{i}k L_1 + L_0 + \omega^2 M]u = 0\,. \tag{1.40}$$

The above represents an algebraic eigenvalue problem for the eigenpair (ω^2, u) parameterized by k, as is common in commercial software. Alternatively, it can be solved for the eigenpair (k, u) that is parameterized in ω, which is particularly useful for frequency-dependent material parameters. Choosing different values for ω and solving the quadratic eigenvalue problem with conventional methods (e.g., `polyeig` in Matlab) yields the desired dispersion curves $k(\omega)$. Note that wavenumbers k are complex valued, while ω remains a real quantity. This is handled naturally by the eigenvalue solver and presents no difficulty.

In order to test the implementation, we first consider a purely elastic and isotropic material. In this case, we compute the propagating waves by prescribing real-valued k and computing the eigenpair (ω^2, u). Computations of the free strip in the range $\omega/2\pi < 300\,\mathrm{Hz}$ yield converged results with $N = 8$ and $P = 14$ and compare well to solutions obtain with COMSOL Multiphysics, while being much faster, as depicted in figure 1.24. As we are able to rapidly obtain accurate solutions for the waves of interest, we have stuck to the very fast SCM to perform parametric studies all along this thesis.

To switch to the configuration of a strip with fixed lateral edges, one should modify equation (1.36) in:

$$\mathbf{u} = \mathbf{0} \quad \text{on} \quad \partial\Omega_\mathrm{D}\,. \tag{1.41}$$

and the equation (1.39) in:

$$\mathbf{1} \otimes I_\mathrm{d}\, u = 0\,. \tag{1.42}$$

[A] The Kronecker product $A \otimes B$ of the $m \times n$-matrix $A = [A_{ij}]$ with the $p \times q$-matrix B yields the block matrix $[A_{ij}B]$ of size $mp \times nq$.

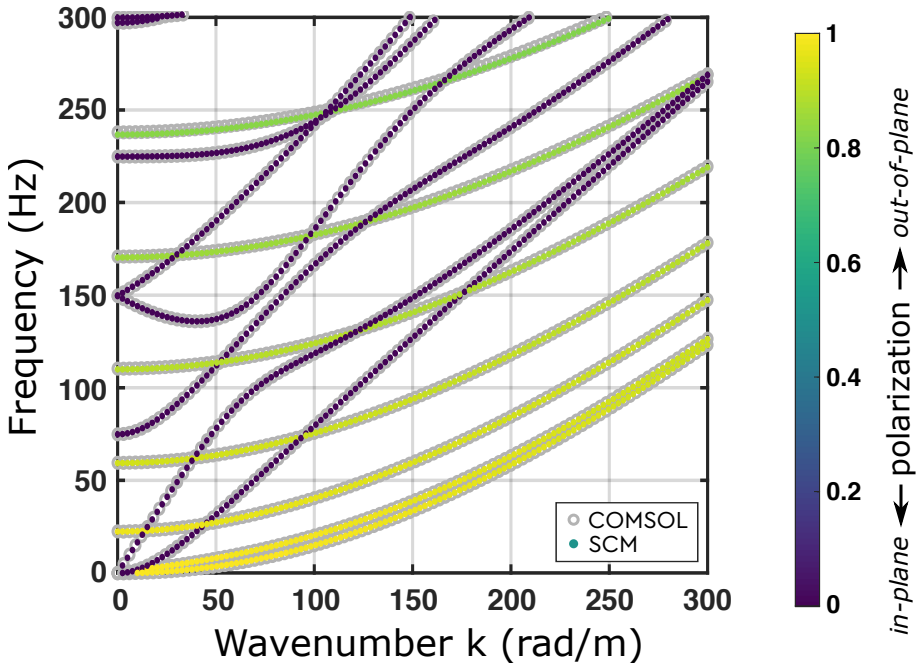

FIGURE 1.24: **Comparison of the SCM with solutions obtained with COMSOL Multiphysics** — Numerically computed dispersion curves for in-plane guided waves in a soft elastic strip of size $h = 3\,\text{mm} \times b = 40\,\text{mm}$. Both the in-plane and out-of-plane solutions coincide for a free strip.

At this point, there is one remaining subtlety to clarify. By implementing these boundary conditions, the collocation points located at the corner, *e.g.* with coordinates $(x_2 = \pm h/2, x_3 = \pm b/2)$ should satisfy both Neumann and Dirichlet boundary conditions. In practice, its numerical implementation is hard and we have decided to eliminate the Dirichlet degree of freedoms. However, different solutions are still obtained depending on the parity of N. To obtain the right dispersion curves of in-plane (respectively out-of-plane) modes in the fixed strip, compared to COMSOL results, one should consider N to be even (resp. odd).

Likewise, we saw that using the Lamb waves analogy in figure 1.22, the Dirac cone must exist for anti-symmetric modes in a fixed strip. However, when we solve the 3D problem using the SCM (N even) or COMSOL, the Dirac cone does not appear rigorously this time but there is instead a slight mismatch between cutoff frequencies. At this stage, it is difficult to identify the actual origin of this mismatch. Knowing that it does not appear in the case of a free strip, we can assume that this is due to the combination of both the Neumann and Dirichlet boundary conditions. A slight phase shift must occur when S_0 and SH_0 modes are reflected at the lateral edges, leading to a shift in cut-off frequencies. However, we did not attempt to further understand the origin of this mismatch. At the end, this is indeed smoothed by viscoelasticity as in figure 1.23 and further illustrated later in figure 3.19 in chapter 3.

Chapter 2

Acoustoelastic effect in a soft plate

Objectives

In this chapter, we study the propagation of guided elastic waves in a highly-stretched Ecoflex plate. The plate is subjected to a nearly-uniaxial stress with an elongation reaching 120% and we measure in-plane displacements of the shear horizontal mode SH_0 and plate mode S_0 coexisting in the low frequency limit. An induced anisotropy is observed and characterized by tracking the evolution with stress of the phase velocities in the principal directions. Velocity changes in a prestressed elastic medium are already well studied and referred to as the acoustoelastic effect. It is based on a nonlinear elasticity framework which is described and particular attention is given to the choice of tensors to be used. Based on our experimental results, we evidence the limits of the acoustoelastic theory to predict those phase velocities in a prestressed elastomer. Taking into account the rheology, a fractional derivative viscoelastic part is added; and this provides accurate predictions up to 80% elongation.

- In-plane guided waves are measured in a highly-stretched plate of Ecoflex
- *Major* symmetries are broken and the induced anisotropy is fully characterized
- Limits of the acoustoelastic theory are evidenced
- An experiment-driven fractional viscoelastic model is used to adapt the theory
- The visco-hyperelastic fractional model properly estimates complex wavenumbers up to an elongation of 80%

Contents

In this chapter, we investigate, experimentally and theoretically, the propagation of guided elastic wave in a highly elongated soft plate (elongation reaching 120%). Such high deformations are commonly reached in tensile tests but rarely in experiments which involve wave propagation. First, the stress-induced anisotropy is observed and quantified. We perform systematic measurements of guided wave velocities along or transversely to the stress direction at different stretch ratios ($1 \leq \lambda_1 \leq 2.2$). They reveal different behaviours for the two fundamental modes propagating in a plate at low-frequency, that is to say the first shear horizontal mode SH_0 and the first symmetric Lamb mode, the so-called plate mode S_0. Such changes in velocities in an elastic medium is referred to the acoustoelastic effect[28,71]. The description of this effect requires a non-linear elasticity framework which is first described and particular attention is given to the choice of tensors. The theory here relies on the use of an hyperelastic constitutive law where stress tensors are derived from a strain energy density function W. Usual hyperelastic models are described, both in their compressible and incompressible forms. Then hyperelasticity is combined with an incremental approach, also known as a small-on-large analysis, leading to a wave equation for incremental displacements, provided an equivalent elastic tensor is used. Then, each *major* symmetry is broken and the Voigt notation can no longer be used. From this equivalent elasticity tensor, it is straightforward to derive predictions for bulk wave velocities but a little more work needs to be done to obtain predictions for guided waves velocities in a plate. Using the work of Rogerson and collaborators[72,73,74], we are still able to build analytical hyperelastic predictions for investigated velocities. Although, similarly to Li et al. (2022)[75], we can recover the applied static stress in the plate, no hyperelastic model could correctly describe the evolution of velocities as a function of elongation. To rightfully predict those changes, we add a dissipative stress tensor to the hyperelastic stress tensor. The chosen viscoelastic contribution is a fractional derivative term since we identified a fractional Kelvin-Voigt model in chapter 1. From this new term, we compute how the equivalent elasticity tensor is modified. Now that tensor components have a non-zero imaginary part, the obtained wavenumbers are complex-valued and predictions for attenuation distances can also be constructed. In the end, this model not only correctly predicts the changes in phase velocities, but also the attenuation distances of those two modes. The following is largely duplicated from our work published in Delory et al. (2023)[76].

1 First observations in a stretched plate

In this first section, we observe elastic waves propagating in a soft plate when it is highly deformed. The experimental setup is recalled, as well as the measurement of the full in-plane displacement field. Two guided modes are observed and identified in view of what was discussed in chapter 1. Then, the setup is used to evaluate the anisotropy induced by the initial stress and demonstrate how the different velocities depend on this prestress.

1.1 Experimental method

The experiment is similar to the one presented in figure 1.7 in chapter 1. The same 3 mm thick plate made of Ecoflex is held vertically and clamped at its bottom and top edges to rigid bars, as shown in figure 2.1(a). This configuration allows us to apply a static and large stretch in the plate, as demonstrated in figure 2.1(b). At first, the plate is undeformed and in a natural configuration.

[28] Biot (1940): "The Influence of Initial Stress on Elastic Waves"
[71] Toupin and Bernstein (1961): "Sound Waves in Deformed Perfectly Elastic Materials. Acoustoelastic Effect"
[72] Rogerson and Fu (1995): "An asymptotic analysis of the dispersion relation of a pre-stressed incompressible elastic plate"
[73] Nolde et al. (2004): "Dispersion of Small Amplitude Waves in a Pre-Stressed, Compressible Elastic Plate"
[74] Rogerson and Prikazchikova (2009): "Generalisations of long wave theories for pre-stressed compressible elastic plates"
[75] Li et al. (2022): "Non-destructive mapping of stress and strain in soft thin films through sound waves"
[76] Delory et al. (2023): "Guided elastic waves in a highly-stretched soft plate"

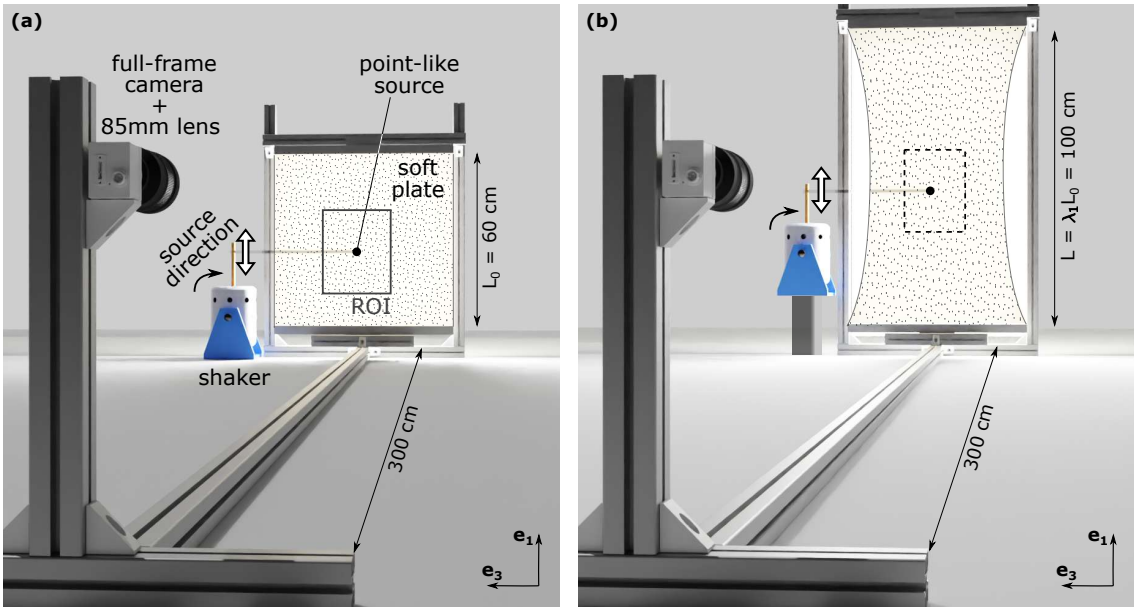

FIGURE 2.1: **Experimental setup to measure velocities in a deformed plate**– (a) A thin plate of Ecoflex00-30, with dimensions 60 cm x 3 mm x 60 cm in directions x_1, x_2, x_3, is held in a vertical position and clamped to a frame on its top and bottom edges. Sinusoidal vibrations in the (x_1, x_3)-plane are generated by a shaker and displacements are extracted using a CCD camera located 3 m away from the plate. (b) Same experimental configuration but the frame is adjusted to impose large deformations, reaching stretch ratio $\lambda_1 > 2$ along the vertical axis.

After applying a nearly-uniaxial stress, the plate is in a deformed configuration characterized by stretch ratios $(\lambda_1, \lambda_2, \lambda_3)$ in the three principal directions.

To observe wave propagation, we assume that the deformation under uniaxial stress is uniform along the plate. We first need to evaluate the validity of this assumption. If the applied stress is uniaxial, then stretch ratios equal $\left(\lambda_1, \lambda_1^{-0.5}, \lambda_1^{-0.5}\right)$ by symmetry and incompressibility.

However due to boundaries, this assumption does not hold. To quantify this discrepancy from uniaxial tension, the same plate is stretched using a user-controlled static stress by adding weights to the bottom clamp. Results are shown in figure 2.2 for the undeformed plate ($\lambda_1 = 1$) and for a plate submitted to a stress of 65 kPa resulting in a stretch ratio of $\lambda = 1.75$. Image processing enables us to extract the displacement of a mesh of black dots so that stretch ratios are computed and displayed in figure 2.2(a) and (b). We can see the effect of the edges on the λ_3 map. Overall, the deformation remains almost homogeneous and this will not be a problem in the following as the regions of interest (black or white rectangles) are centered on the region of the plate where the deformation can be considered homogeneous. However, by repeating this experiment, we tracked the evolution of λ_1 and λ_3. We found in figure 2.2(c) that a good fit corresponds to $\lambda_3 = \lambda_1^{-0.41} \neq \lambda_1^{-0.5}$, and we have thus quantified the discrepancy with uniaxial tension. A last observation is this apparent vertical gradient in λ_1. It can be explained since the undeformed plate is not in its natural configuration, but is submitted to its own weight. It is well known that, due to its own weight, deformation in the upper part of the plate is higher than in the lower part. Actually, the bottom of the plate should exactly be undeformed. Then, applying a constant static tension in the plate (by opposition to the weight which is not a constant stress) induces a higher apparent stretch ratio in the bottom of the plate since the upper part of the plate was already slightly deformed in the reference configuration (as opposed to the natural configuration). This small contribution was not corrected here because it is negligible in the region of interest given by white (or black) rectangles. More details about this

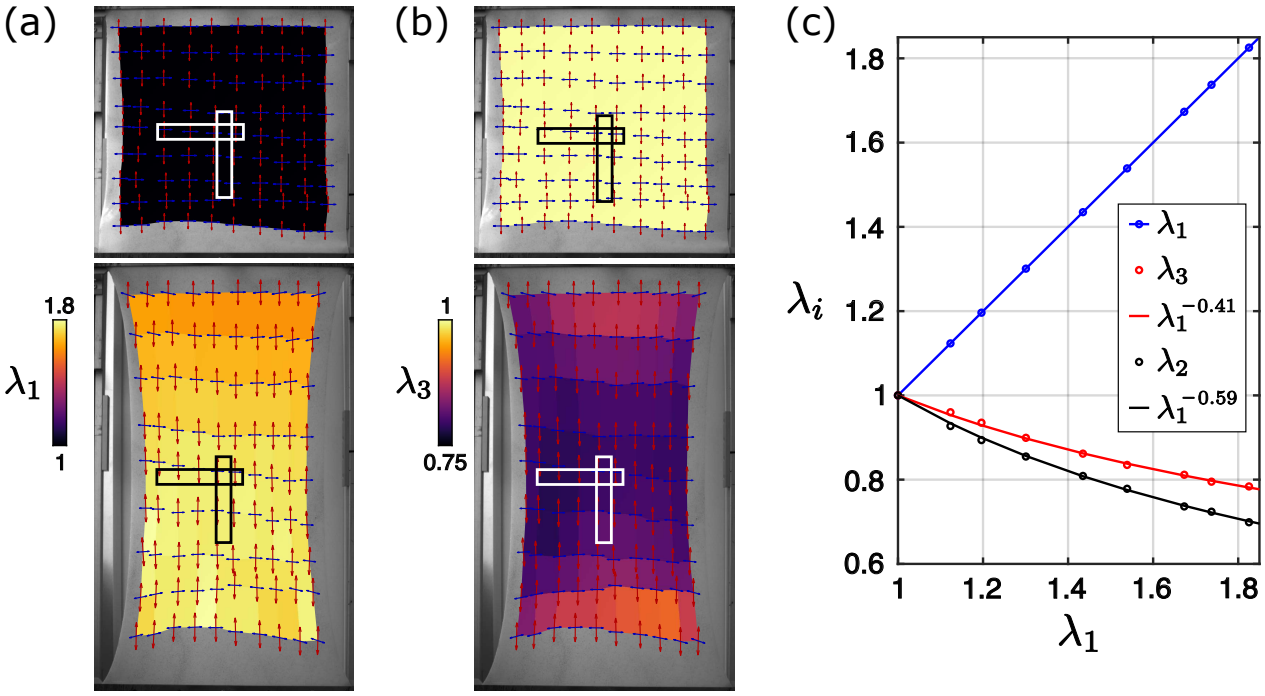

FIGURE 2.2: **Mapping the static deformation in the stretched plate** – Displacements of a mesh of black dots is extracted between the undeformed plate at rest and the deformed plate submitted to a 65 kPa stress. Stretch ratios λ_1 (a) and λ_3 (b) are displayed. Due to boundaries, the deformation is not homogeneous everywhere but is in the region of interest (black or white rectangles). The gap to uniaxial tension is quantified by relating λ_3 as a function of λ_1 in (c).

static deformation can be found in Appendix A.

Regarding the wave generation, in both configurations, we use a point-like source made of two magnets pinching the plate in its center and driven monochromatically with a shaker so that it generates displacements in the (x_1, x_3)-plane. The source polarisation is changed by rotation of the shaker. The excitation frequency ranges from 50 to 300 Hz. Again a 60-frame video is recorded and DIC is applied to retrieve in-plane wave field components (u_1, u_3).

1.2 The initial stress induces anisotropy for elastic waves

An example of acquired frame is displayed in figure 2.3(a) for the undeformed plate. Typical displacement maps obtained when vibrating the source at 200 Hz are also shown as a colour code. Given a source vibrating in x_1-direction (respectively x_3), the displacement $\mathrm{Re}\,[u_1(\omega)]$ (respectively $\mathrm{Re}\,[u_3(\omega)]$) is displayed in figure 2.3(b) (respectively 2.3c). As a first observation one can notice that a 90° source rotation involves a rotation of 90° of the displacement map. This demonstrates that the material is isotropic at rest and no privileged direction exists in the undeformed case. By carefully looking at the wave pattern along the two main directions one can notice the existence of two distinct wavelengths, one being twice larger than the other. This effect is confirmed by applying a spatial Fourier Transform on these wave-fields. After normalization and summation in intensity of the two, the spatial spectrum of the measured waves evidences two concentric circles in figure 2.3(d), revealing two isotropic guided modes, with radii again showing this factor of 2.

Given the theoretical framework detailed in chapter 1, only three modes can propagate in this plate at this frequency: the first shear horizontal mode SH_0 and the first two Lamb modes S_0 and A_0. As already indicated in figures 1.11 and 1.12, SH_0 and S_0 are polarized in the (x_1, x_3)-plane while A_0 is a flexural mode and mainly polarized in x_2-direction at this frequency. Given the source

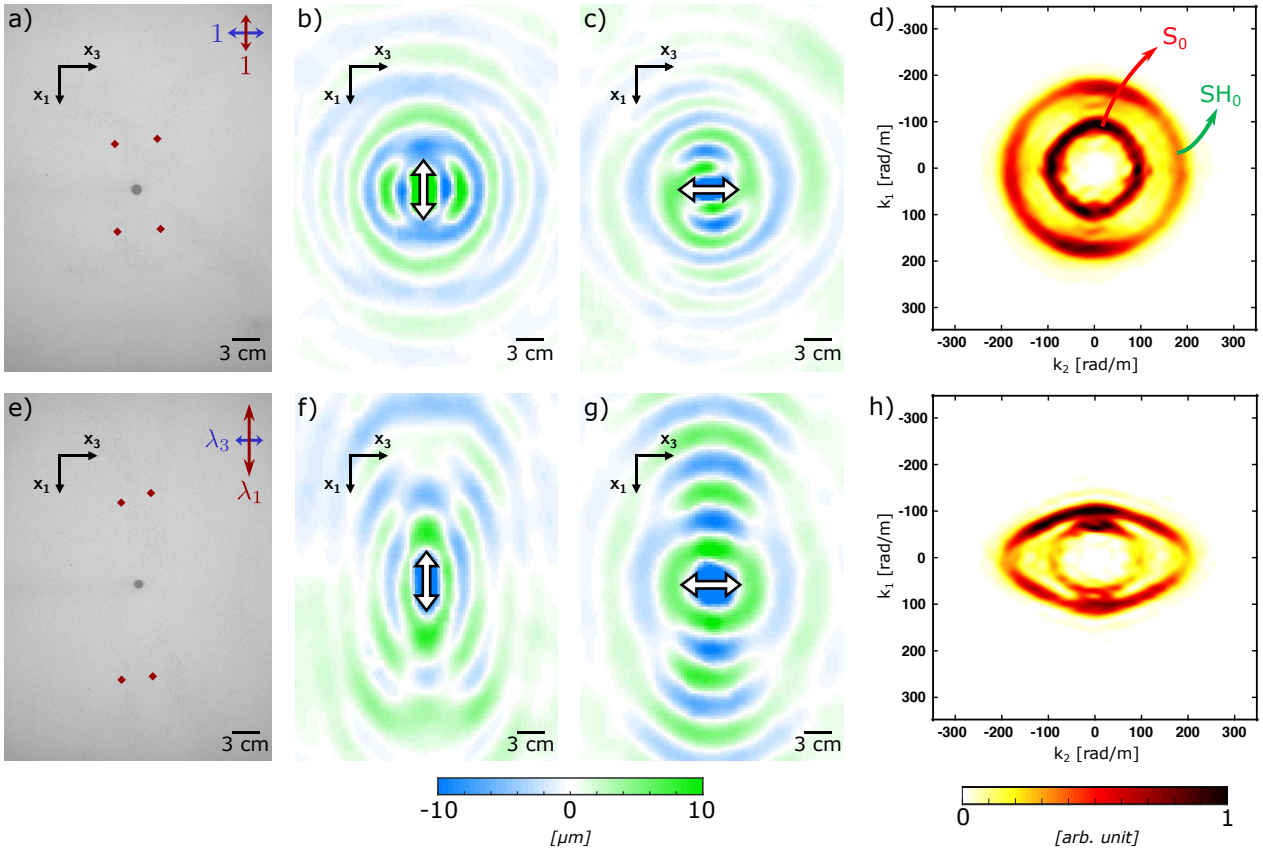

FIGURE 2.3: **Experimental 2D displacement maps in an undeformed and a deformed plate at 200 Hz** – (a)-(e) Typical pictures obtained for the initial and the deformed plate. 4 red dots are here to measure $\lambda_1 = 2.01$ and $\lambda_3 = 0.74$. (b)-(f) 2D map of the displacement u_1 with a source vibrating along x_1. (c)-(g) 2D map of the displacement along u_3 with a source vibrating along x_3. (d)-(h) Isofrequency contours for the initial and deformed plate. The spatial Fourier transforms of the two previous maps are normalized, squared and summed.

polarization, A_0 cannot be observed in this experiment and only SH_0 and S_0 are visible. Let us recall that those 2 modes are nearly non-dispersive, and propagate respectively at V_T and $V_P = 2V_T$ for an incompressible solid. The two circles are thus labeled accordingly in figure 2.3(d).

The same procedure is then repeated after applying a static load to the plate. The stretch ratios in x_1 and x_3 directions are measured by manually tracking red diamonds displacements in figure 2.3(e). Here, stretch ratios $\lambda_1 = 2.01$ and $\lambda_3 = 0.74$ are measured in the plate center.

Comparing field maps for two different vibrating directions in figure 2.3(f) and (g) now reveals that the system is no longer invariant by rotation: the initial deformation leads to anisotropic propagation. Again, this effect is nicely caught in the spatial Fourier domain of figure 2.3(h) where circles are now replaced with ellipses. It appears that prestress does not affect similarly SH_0 and S_0 since ellipses have different aspect ratios.

1.3 Static prestrain dependence of SH_0 and S_0 phase velocities

To systematically track the induced anisotropy, a new set of measurements is performed. The point source is replaced by a line source to generate plane waves as done in chapter 1 and shown in the left part of figure 2.4. Measurements are repeated for different frequencies and static stretch ratio λ_1. As displayed in figure 1.10, shaking the line source in the (x_1, x_3)-plane, with a 45°

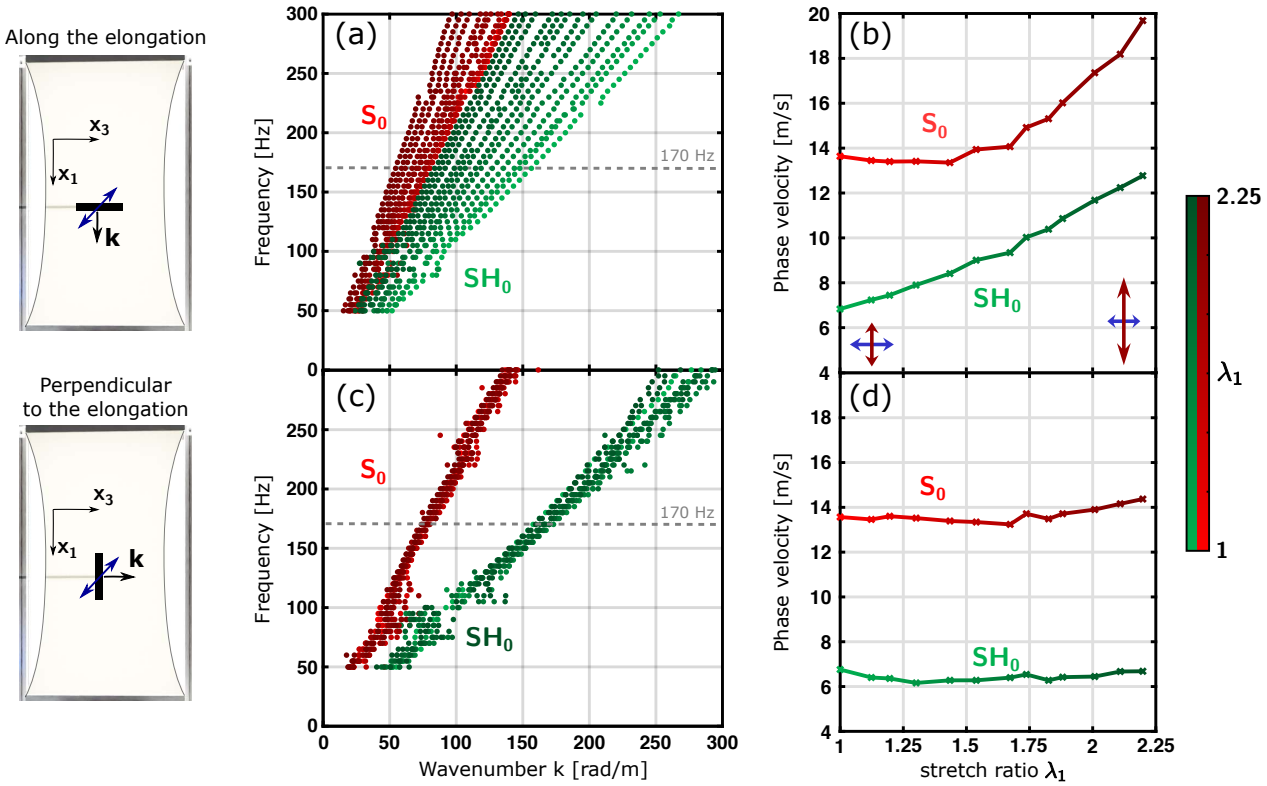

FIGURE 2.4: **Experimental dispersion curves and phase velocities at 170 Hz in a stretched plate** – Measurement in the top part (respectively bottom part) are obtained for plane waves propagating in x_1-direction (resp. x_3-direction). (a)-(c) Dispersion curves of waves propagating in directions x_1 and x_3. The stretch ratio λ_1 is given by the darkness, as represented on the colorbar. (b)-(d) Phase velocities of SH_0 and S_0 at 170 Hz extracted and plotted as functions of λ_1.

angle between displacement and propagation directions allows the combined observations of SH_0 and S_0 in one single experiment. Dispersion curves obtained for different stretch ratios λ_1 are plotted in figure 2.4(a) (resp. 2.4b) for plane waves propagating in x_1-direction (resp. x_3-direction). The higher the stretch ratio, the darker the curves. The behaviour depends on the propagation direction: while the slopes are increasing in the parallel direction (x_1-direction), they barely vary in the perpendicular direction (x_3-direction). Note that at the frequency $f \sim 100$ Hz, an accident occurs due to a mechanical resonance of the clamp fixed to the shaker and holding the line source. This small "anti-crossing" has no influence on the measured dispersion relation above 150 Hz. From now on, phase velocities are extracted at an intermediate frequency of 170 Hz and plotted as a function of the stretch ratio λ_1 in figure 2.4(b) and (d) for parallel and perpendicular directions (numerical values are available in Appendix C). The velocity of SH_0 appears to vary linearly with λ_1 in the parallel direction, while the evolution is more complex for S_0 mode. In addition, velocities of both SH_0 and S_0 remain almost constant in the perpendicular direction.

In this section, the experimental setup has allowed the observation of SH_0 and S_0 in a soft plate and the factor of 2 between their velocities. The phase velocities dependence with the stretch ratio λ_1 was observed by systematic measurements at different frequencies in a highly-stretched plate. Those variations are also referred to as the acoustoelastic effect, which is detailed in the next section.

2 Theoretical aspects underlying the acoustoelastic effect

The acoustoelastic effect is the change in velocities of elastic waves due to an initial stress. It relies on non-linear elasticity since the initial stress usually induces large deformations compared to incremental motions describing waves propagating in the material. In our experiment, the non-linearity first appears as a non-linear geometrical effect but we will see that a mechanical non-linearity must also be thought out by using a hyperelastic model. Numerous experimental and theoretical works have been devoted to explaining this phenomenon, and its main characteristics are recalled. More details can be found in the works of Ogden, Destrade and Saccomandi[77,29,78]. In order to understand the experimental observations made in the previous section, we apply the acoustoelastic theory to guided waves in a plate. Firstly, the acoustoelastic effect is used to make predictions for bulk waves. We demonstrate symmetry breaking in the equivalent elasticity tensor, and that it is responsible for the induced anisotropy observed in figure 2.3 and 2.4. Secondly, phase velocities of guided waves SH_0 and S_0 are derived using the acoustoelastic theory and compared to experimental data.

2.1 Nonlinear elasticity

In chapter 1, basics of linear elasticity have been introduced using Hooke's law, the most common constitutive law in elastic solids. In this context, the Cauchy stress $\boldsymbol{\sigma}$ is linearly related to the linearized strain tensor $\boldsymbol{\epsilon}$ and a wave equation is obtained and recalled here using Einstein summation notation:

$$C_{jikl}\frac{\partial^2 u_k}{\partial X_j \partial X_l} = \rho\frac{\partial^2 u_i}{\partial t^2} \tag{2.1}$$

In the framework of non-linear elasticity, the strain tensor $\boldsymbol{\epsilon}$ should be replaced by the Green-Lagrange strain tensor:

$$\begin{aligned}\mathbf{E} &= \frac{1}{2}\left[\mathbf{F}^{\mathrm{T}}\cdot\mathbf{F}-\mathbf{1}\right]\\ &= \frac{1}{2}\left[\nabla\mathbf{u}+(\nabla\mathbf{u}_s)^{\mathrm{T}}+(\nabla\mathbf{u}_s)^{\mathrm{T}}\cdot\nabla\mathbf{u}_s\right]\end{aligned} \tag{2.2}$$

where $\mathbf{u}_s(\mathbf{X}) = \mathbf{x}-\mathbf{X}$ is now the static displacement matching the initial deformation visible in figure 2.1(b). See figure 1.1 in chapter 1 for the definitions of $\mathbf{x}$ and $\mathbf{X}$ coordinates. Before discussing the choice for a stress tensor, we derive the Green-Lagrange strain tensor for a simple uniaxial case. If no rotations are present in the static deformation, then stretch ratios $(\lambda_1,\lambda_2,\lambda_3) = (\lambda,\lambda^{-0.5},\lambda^{-0.5})$ are simply the diagonal coefficients of the deformation gradient $\mathbf{F}$. Inserting this into equation (2.2), simply leads to:

$$E_{ij} = \frac{{\lambda_i}^2-1}{2}\delta_{ij} \tag{2.3}$$

It should be noted that other strain tensors could also be adopted. Similarly, different stress measures exist and one should ensure that the selected tensors are conjugate[77,79].

A geometrical non-linearity is therefore evidenced in equation (2.2), but the mechanical non-linearity must also be thought out. Typically, it is common to use a hyperelastic law for soft media like elastomers. This constitutive law is detailed in the following part and basically relies on a strain energy density function W.

[77] Ogden (1997): *Non-Linear Elastic Deformations*
[29] Destrade and Saccomandi (2007): *Waves in Nonlinear Pre-Stressed Materials*
[78] Saccomandi and Ogden (2004): *Mechanics and Thermomechanics of Rubberlike Solids*
[77] Ogden (1997): *Non-Linear Elastic Deformations*
[79] Mihai and Goriely (2017): "How to characterize a nonlinear elastic material? A review on nonlinear constitutive parameters in isotropic finite elasticity"

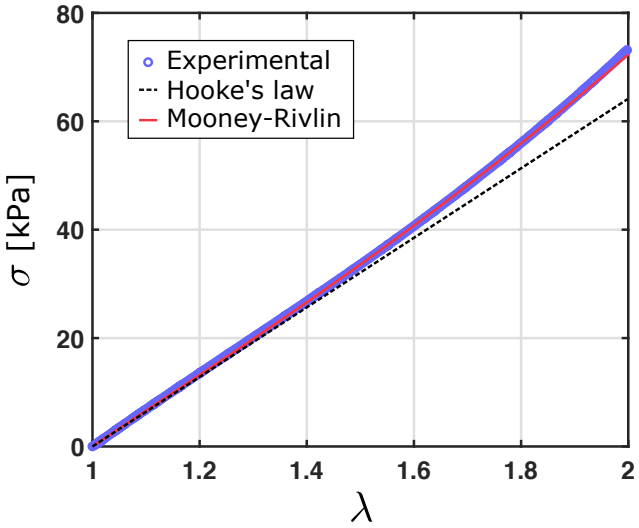

FIGURE 2.5: **Experimental tensile test of Ecoflex** – The Cauchy stress σ is plotted as a function of the stretch ratio λ. Predictions using a linear (Hooke's law, in black) and a nonlinear (Mooney-Rivlin, in red) model.

But just before that, we can explore this non-linearity with a simple uniaxial tensile test. Using an Instron instrument, we measure the force as a function of the stretch ratio λ on an Ecoflex sample. Results of the tensile tests are shown in figure 2.5. The Cauchy stress σ is derived as the measured force divided by the deformed cross-section area, and plotted as a function of the stretch ratio λ. Hooke's law is the linear prediction (black dashed line) and simply reads $\sigma = E_0\,(\lambda - 1)$. The Mooney-Rivlin prediction (red line) is explained later but we must first introduce the notion of hyperelasticity. This term is justified since the slope increases with λ.

2.2 Hyperelastic constitutive law

The hyperelastic constitutive law relies on the use of a strain energy density function W which contains all mechanical properties. From this energy function, the stress–strain relationship can be derived. Depending on the selected strain tensor, the appropriate stress tensor should be considered. The following is largely inspired by the book of OGDEN (1997)[77] and works of Destrade and Saccomandi[29,80,81,78]. The simplest equation writes:

$$\mathbf{P} = \frac{\partial W}{\partial \mathbf{F}} \qquad \text{or} \qquad P_{ij} = \frac{\partial W}{\partial F_{ij}} \tag{2.4}$$

where $\mathbf{P}$ is the first Piola–Kirchhoff stress tensor and relates forces in the present configurations with areas in the reference configuration. This definition is widely used under the name of "engineering stress", because it is typically what you get with a classical tensile test.

This simple case is in fact asymmetric and may not appear natural. For instance, it is also possible to relate forces in the reference configuration with areas in the reference configuration, and this is the second Piola–Kirchhoff stress tensor $\mathbf{S}$,

$$\mathbf{S} = \frac{\partial W}{\partial \mathbf{E}} \qquad \text{or} \qquad S_{ij} = \frac{\partial W}{\partial E_{ij}} \tag{2.5}$$

[77] OGDEN (1997): *Non-Linear Elastic Deformations*
[29] DESTRADE and SACCOMANDI (2007): *Waves in Nonlinear Pre-Stressed Materials*
[80] DESTRADE et al. (2010): "Third- and fourth-order constants of incompressible soft solids and the acousto-elastic effect"
[81] DESTRADE et al. (2012): "Large Acoustoelastic Effect"
[78] SACCOMANDI and OGDEN (2004): *Mechanics and Thermomechanics of Rubberlike Solids*

Here, $\mathbf{S}$ and $\mathbf{E}$ are conjugate. Note that the nominal stress tensor $\mathbf{N} = \mathbf{P}^{\mathrm{T}}$ and $\mathbf{F}$ are also conjugate. A couple of strain and stress tensors are said conjugate when the stress power density can be derived as follows:

$$\text{stress power density} = \mathrm{Tr}\left(\mathbf{S} \cdot \frac{\partial \mathbf{E}}{\partial t}\right) = \mathrm{Tr}\left(\mathbf{N} \cdot \frac{\partial \mathbf{F}}{\partial t}\right) \tag{2.6}$$

Finally, the Cauchy stress tensor $\boldsymbol{\sigma}$ relates forces in the deformed configuration with areas in the deformed configuration. To write $\boldsymbol{\sigma}$, one needs to perform the so-called push-forward operation of the second Piola–Kirchhoff stress tensor $\mathbf{S}$, that is to say:

$$\boldsymbol{\sigma} = \frac{1}{J}\mathbf{F} \cdot \mathbf{S} \cdot \mathbf{F}^{\mathrm{T}} = \frac{1}{J}\mathbf{F} \cdot \frac{\partial W}{\partial \mathbf{E}} \cdot \mathbf{F}^{\mathrm{T}} \qquad \text{or} \qquad \sigma_{il} = \frac{1}{J} F_{ij} \frac{\partial W}{\partial E_{jk}} F_{lk} \tag{2.7}$$

with $J = \det(\mathbf{F})$ gives the relative change of volume in the material.

Isotropic solid – For an isotropic solid, W should be invariant under a permutation of the stretch ratios $(\lambda_1, \lambda_2, \lambda_3)$ so that W must be a function of the principal invariants of the left (or right) Cauchy-Green tensor $\mathbf{B} = \mathbf{F} \cdot \mathbf{F}^{\mathrm{T}}$:

$$\begin{aligned} I_1 &= \mathrm{Tr}(\mathbf{B}) = \lambda_1^2 + \lambda_2^2 + \lambda_3^2 \\ I_2 &= \frac{1}{2}\left(\mathrm{Tr}(\mathbf{B})^2 - \mathrm{Tr}\left(\mathbf{B}^2\right)\right) = \lambda_2^2\lambda_3^2 + \lambda_1^2\lambda_3^2 + \lambda_1^2\lambda_2^2 \\ I_3 &= \det(\mathbf{B}) = \lambda_1^2\lambda_2^2\lambda_3^2 = J^2 \end{aligned} \tag{2.8}$$

When dealing with anisotropic material, additional invariants should be considered [82,83,84]. For the rest of this thesis, we will stick to isotropic solids. When considering this symmetry, it is possible to rewrite principal Cauchy stress tensor components as:

$$\sigma_i = \frac{\lambda_i}{J}\frac{\partial W}{\partial \lambda_i} \tag{2.9}$$

The incompressible approach – The literature is very rich when it deals with incompressible hyperelastic models because most of the studied materials likely to be hyperelastic are also nearly incompressible, such as rubbers and biological tissues[85,86]. Since there are no volume change in such materials, $J \to 1$. In that case of an incompressible hyperelastic model $W(I_1, I_2)$, it is important to keep the incompressibility condition in the stress tensor. This is achieved by using a Lagrange multiplier p and by rewriting the Cauchy stress tensor as:

$$\boldsymbol{\sigma} = -p\,\mathbf{1} + \frac{1}{J}\mathbf{F} \cdot \frac{\partial W}{\partial \mathbf{E}} \cdot \mathbf{F}^{\mathrm{T}}. \tag{2.10}$$

The Lagrange multiplier is named p here since the term $-p\,\mathbf{1}$ is similar to a hydrostatic pressure. We now explore some hyperelastic models proposed in the literature.

2.3 Some examples of hyperelastic models

Before going deeper in the acoustoelastic effect, it is essential to describe some hyperelastic models. Let us begin with incompressible models *i.e.* when $J \to 1$ and $W = W_{\text{incompressible}}(I_1, I_2)$.

[82] Balzani et al. (2006): "A polyconvex framework for soft biological tissues. Adjustment to experimental data"

[83] Peyraut et al. (2010): "A closed form solution for the uniaxial tension test of biological soft tissues"

[84] Mukherjee et al. (2022): "Representing the stress and strain energy of elastic solids with initial stress and transverse texture anisotropy"

[85] Wex et al. (2015): "Isotropic incompressible hyperelastic models for modelling the mechanical behaviour of biological tissues: a review"

[86] Chagnon et al. (2015): "Hyperelastic Energy Densities for Soft Biological Tissues: A Review"

Neo-Hookean – Knowing the strain energy density W is a function of invariants I_1 and I_2, the simplest functions that come to mind are polynomial functions. First, we can write W as a linear function of I_1; this is the neo-Hookean model:

$$W_{\text{NH}} = \frac{\mu}{2}\left(I_1 - 3\right). \tag{2.11}$$

Here, the shear modulus μ naturally appears when comparing to isotropic Hooke's law at infinitesimal strains. Despite its obvious simplicity, this model has some physical meaning in view of molecular chain statistics. Actually, in elastomers or rubber, the elasticity of the polymeric network is mainly due to entropic changes during deformation, leading Treloar (2005)[87] to write $W = \frac{1}{2}nk_BT\left(I_1 - 3\right)$ with n the chain density, k_B the Boltzmann constant and T the material temperature.

Mooney-Rivlin – Given that W can also depend on the invariant I_2, another idea is to write the strain energy density as a sum of two terms linear in I_1 and I_2; this is the Mooney-Rivlin model[88]:

$$W_{\text{MR}} = \frac{\mu}{2}\left[(1-\alpha)\left(I_1 - 3\right) + \alpha\left(I_2 - 3\right)\right]. \tag{2.12}$$

Again, the coefficients should match Hooke's law at infinitesimal strains. The physical interpretation of this model is not straightforward and is still a current issue in this research field[89]. Note that taking $\alpha = 0$ brings us back the neo-Hookean model. Moreover, the Cauchy stress tensor from equation (2.10) then simplifies:

$$\boldsymbol{\sigma} = -p\mathbf{1} + \mu\Big[(1-\alpha)\mathbf{B} - \alpha\mathbf{B}^{-1}\Big] \tag{2.13}$$

Other polynomials models – Beyond models with linear functions of I_1 and I_2, it makes sense to consider polynomial functions of I_1 and I_2; this is the generalized Rivlin model:

$$W_{\text{generalized Rivlin}} = \sum_{p,q=0}^{N} C_{pq}(I_1 - 3)^p\ (I_2 - 3)^q. \tag{2.14}$$

where C_{pq} are material constants and p, q integers. Previous models in equations (2.11) and (2.12) are special cases of this generalized model. In the following of this thesis, we stick to the two simple neo-Hookean and Mooney-Rivlin hyperelastic models.

Additional models – Of course, it is possible to consider more complex functions of I_1 and I_2, such as exponential (Fung (1993)[90]) or logarithmic (Gent (1958)[91]) functions of I_1. Another famous model, developed by Ogden, uses the modified invariants $I_\alpha = \left(\lambda_1^\alpha + \lambda_2^\alpha + \lambda_3^\alpha\right)/\alpha$ where $\alpha \in \mathbb{R}^*$. For a complete review about these hyperelastic models, see References[92,93,79].

[87] Treloar (2005): *The Physics of Rubber Elasticity*
[88] Rivlin (1948): "Large elastic deformations of isotropic materials IV. Further developments of the general theory"
[89] Anssari-Benam et al. (2021): "On the central role of the invariant I_2 in nonlinear elasticity"
[90] Fung (1993): *Biomechanics*
[91] Gent (1958): "On the relation between indentation hardness and Young's modulus"
[92] Boyce and Arruda (2000): "Constitutive Models of Rubber Elasticity: A Review"
[93] Marckmann and Verron (2006): "Comparison of hyperelastic models for rubber-like materials"
[79] Mihai and Goriely (2017): "How to characterize a nonlinear elastic material? A review on nonlinear constitutive parameters in isotropic finite elasticity"

From incompressible to compressible hyperelastic models – As indicated above, those are hyperelastic models to be used in the incompressible approach. However, as seen later in this work, we found it is important to keep the compressible part directly in the strain energy density. We thus need to write compressible versions of the neo-Hookean and Mooney-Rivlin models. There are different ways to extend those incompressible models[94] but the simplest is to write:

$$W_{\text{compressible}}\left(I_1, I_2, J\right) = W_{\text{incompressible}}\left(\bar{I}_1, \bar{I}_2\right) + W_{\text{vol}}(J) \tag{2.15}$$

with $\bar{I}_1 = \dfrac{I_1}{J^{2/3}}$ and $\bar{I}_2 = \dfrac{I_2}{J^{4/3}}$. In fact, these invariants are normalized so that $\bar{I}_3 = \dfrac{I_3}{J^{6/3}} = 1$. Once again, a choice has to be made for the volumetric contribution. To keep it simple, we use a quadratic function, that is to say:

$$W_{\text{vol}}(J) = \frac{\kappa}{2}\left(J-1\right)^2 \quad \text{with} \quad \kappa = \lambda_L + \frac{2}{3}\mu, \tag{2.16}$$

and the bulk modulus κ appears here to ensure Hooke's law in the limit of infinitesimal strains.

Compressible neo-Hookean and Mooney-Rivlin – The two models of interest read:

$$W_{\text{nH, compressible}} = \frac{\mu}{2}\left(\frac{I_1}{J^{2/3}} - 3\right) + \frac{\kappa}{2}\left(J-1\right)^2 \tag{2.17}$$

$$W_{\text{MR, compressible}} = \frac{\mu}{2}\left[(1-\alpha)\left(\frac{I_1}{J^{2/3}} - 3\right) + \alpha\left(\frac{I_2}{J^{4/3}} - 3\right)\right] + \frac{\kappa}{2}\left(J-1\right)^2. \tag{2.18}$$

Note that the compressible form of the Mooney-Rivlin hyperelastic model is also called the Blatz-Ko model[95]. We have selected the strain tensor, stress tensor and compressible hyperelastic models. We can now build predictions for tensile test curves by computing the Cauchy stress tensor as a function of the stretch ratios. For example, for the Mooney-Rivlin model,

$$\sigma = \frac{E_0}{3}\left(1 - \alpha + \frac{\alpha}{\lambda}\right)\left(\lambda^2 - \frac{1}{\lambda}\right)$$

and a fitting procedure provides $E_0 = 67$ kPa and $\alpha = 0.15$ in figure 2.5. It matches our tensile tests up to $\lambda = 2$.

We are interested in the propagation of guided waves in a deformed material. To assess the behaviour of those waves, we need to use an incremental approach, *i.e.* perform a small-on-large analysis.

2.4 Incremental displacements

To describe waves in a prestressed body, the incremental approach described by Ogden and Destrade[77,29] is used. Once again, details are omitted but the main ideas are recalled. This approach requires to introduce a new configuration named $\mathcal{B}'$ whose coordinates are $\mathbf{x}'$ (figure 1.1). We look for the wave equation that governs the incremental displacement $\mathbf{u}'(\mathbf{x}, t) = \mathbf{x}' - \mathbf{x}$. Here, an important feature is that $\mathbf{u}'$ is a function of the coordinates in the deformed configuration $\mathbf{x}$ and not of the initial one $\mathbf{X}$ as in equation (2.1). In view of this feature, a misleading starting point would be to write $\mathbf{u}_{\text{tot}} = \mathbf{u}_\mathbf{s} + \mathbf{u}'$ where $\mathbf{u}_\mathbf{s}$ is a large static displacement (the uniaxial deformation for instance) since those functions depend on different coordinates. First, we define $\mathbf{x}' = \boldsymbol{\chi}'\left(\mathbf{X}\right)$ where

[94] Pence and Gou (2015): "On compressible versions of the incompressible neo-Hookean material"
[95] Blatz and Ko (1962): "Application of Finite Elastic Theory to the Deformation of Rubbery Materials"
[77] Ogden (1997): *Non-Linear Elastic Deformations*
[29] Destrade and Saccomandi (2007): *Waves in Nonlinear Pre-Stressed Materials*

$\boldsymbol{\chi}'$ is "close" to $\boldsymbol{\chi}$. For sake of simplicity, rather than writing the following using the strain tensor $\mathbf{E}$ and the stress tensor $\boldsymbol{\sigma}$, we use the deformation gradient $\mathbf{F}$ and the first Piola-Kirchhoff $\mathbf{P}$. The equation of motion reads:

$$\nabla_{\mathbf{X}} \cdot \mathbf{P}' = \rho_r \frac{\partial^2 x'}{\partial t^2} \tag{2.19}$$

where $\mathbf{P}' = \dfrac{\partial W}{\partial \mathbf{F}'}(\mathbf{F}')$ and $\mathbf{F}' = \nabla_{\mathbf{X}} \mathbf{x}'$ and ρ_r is the mass density in the reference configuration. Then, we introduce incremental deformation gradient and stress tensor:

$$\begin{aligned} \mathbf{F}_{\text{incr}} &= \mathbf{F}' - \mathbf{F} \\ \mathbf{P}_{\text{incr}} &= \mathbf{P}' - \mathbf{P} = \frac{\partial W}{\partial \mathbf{F}'}(\mathbf{F}') - \frac{\partial W}{\partial \mathbf{F}}(\mathbf{F}) \end{aligned} \tag{2.20}$$

And now, to describe waves that are infinitesimal strains superimposed on a much bigger static deformation, we linearize $\mathbf{P}_{\text{incr}}$ to write:

$$\mathbf{P}_{\text{incr}} = \frac{\partial^2 W}{\partial \mathbf{F} \partial \mathbf{F}} \colon \mathbf{F}_{\text{incr}} \tag{2.21}$$

where the term $\dfrac{\partial^2 W}{\partial \mathbf{F} \partial \mathbf{F}}$ is a fourth-order tensor. And the equation of motion for $\mathbf{u}'$ reads:

$$\frac{\partial^2 W}{\partial F_{ji} \partial F_{kl}} \frac{\partial^2 u'_k}{\partial X_j \partial X_l} = \rho_r \frac{\partial^2 u'_i}{\partial t^2}, \tag{2.22}$$

the incremental displacement $\mathbf{u}'$ being here rewritten as a function of $\mathbf{X}$ and not $\mathbf{x}$. To write it in the deformed configuration, with $\mathbf{x}$ coordinates, we need to perform a push-forward operation. It gives the same wave equation as in (2.1) but with a different elasticity tensor $\mathbf{C^0}$:

$$C^0_{jikl} \frac{\partial^2 u'_k}{\partial x_j \partial x_l} = \rho \frac{\partial^2 u'_i}{\partial t^2} \tag{2.23}$$

By applying the chain rule to $\dfrac{\partial^2 W}{\partial F_{ji} \partial F_{kl}}$, we can express $\mathbf{C^0}$ in terms of the successive derivatives of λ_i, rather than $\mathbf{F}$, and this simplifies after the push-forward operation as:

$$\begin{aligned} C^0_{iijj} &= \frac{\lambda_i \lambda_j}{J} W_{ij} \\ C^0_{ijji} &= \frac{\lambda_i^2}{J} \frac{\lambda_i W_i - \lambda_j W_j}{\lambda_i^2 - \lambda_j^2} && (i \neq j, \lambda_i \neq \lambda_j) \\ C^0_{ijji} &= \frac{C^0_{iiii} - C^0_{iijj} + \lambda_i W_i / J}{2} && (i \neq j, \lambda_i = \lambda_j) \\ C^0_{ijij} &= \frac{\lambda_i \lambda_j}{J} \frac{\lambda_j W_i - \lambda_i W_j}{\lambda_i^2 - \lambda_j^2} && (i \neq j, \lambda_i \neq \lambda_j) \\ C^0_{ijij} &= \frac{C^0_{iiii} - C^0_{iijj} - \lambda_i W_i / J}{2} && (i \neq j, \lambda_i = \lambda_j) \end{aligned} \tag{2.24}$$

where $W_i = \dfrac{\partial W}{\partial \lambda_i}$ and $W_{ij} = \dfrac{\partial^2 W}{\partial \lambda_i \partial \lambda_j}$.

Here, formulas are slightly different from the ones found in the books of Ogden (1997)[77] or Destrade and Saccomandi (2007)[29] because the dot products convention is different. To go from their definition to the one presented in this thesis, there is a simple permutation to accomplish for the last 2 indices. In the end, the wave equation (2.23) to be solved is the same.

[77] Ogden (1997): *Non-Linear Elastic Deformations*
[29] Destrade and Saccomandi (2007): *Waves in Nonlinear Pre-Stressed Materials*

Incompressible case – The equations for the elasticity tensor $\mathbf{C^0}$ remain valid using an incompressible hyperelastic model but the equation of motion (2.23) is rewritten and longitudinal waves are no longer solutions:

$$C^0_{jikl}\frac{\partial^2 u'_l}{\partial x_j \partial x_k} - \frac{\partial p'}{\partial x_i} = \rho \frac{\partial^2 u'_i}{\partial t^2} \tag{2.25}$$

with p' an incremental Lagrange multiplier.

In this part, we have introduced the basics of non-linear elasticity and hyperelasticity. In particular, we have detailed how to take into account the geometrical non-linearity *i.e.* using the strain tensor $\mathbf{E}$ instead of $\boldsymbol{\epsilon}$, and also the mechanical non-linearity by using a hyperelastic constitutive law based on a strain energy density function W. Finally, a wave equation for incremental displacements is valid upon using a new elasticity tensor $\mathbf{C^0}$. In the following section, this tensor is computed in order to get bulk wave velocities.

2.5 Bulk waves

The representation given in figure 1.2 is used to display the fourth-order tensor $\mathbf{C^0}$. In figure 2.6(a), the isotropic elastic tensor C_{ijkl} has 3 different coefficients: the two Lamé coefficients λ_L (orange) and μ (yellow), and a third coefficient which depends on these two constants $\lambda_L + 2\mu$ (black). Given the fact that a stress is applied along a particular direction in our experiments, one would be tempted to consider a transverse isotropic material where x_1 (the uniaxial tension direction) would be the symmetry axis. The elasticity tensor for such an anisotropic medium remains as sparse as the one of the isotropic material but now contains 6 distinct coefficients as depicted in figure 2.6(b). Note that a transverse isotropic material respect the *major* symmetries.

We now consider a uniaxial tension for a nearly-incompressible material $\lambda_2 = \lambda_3 = \lambda_1^{-0.5}$. Using the neo-Hookean hyperelastic model, Lamé constants are sufficient to describe the modified elasticity tensor $\mathbf{C^0}$, as seen in the energy density W in equation (2.17). It contains 7 different coefficients as shown in figure 2.6(c). Very interestingly, *major* symmetries are now broken: $C^0_{ijkl} \neq C^0_{jikl}$, $C^0_{ijkl} \neq C^0_{ijlk}$ and even $C^0_{ijkl} \neq C^0_{klij}$. This may be surprising because we have seen in chapter 1 that the stiffness tensor derives from a potential, as explained in equations (2.4) and (2.5). But in fact, the push-forward operation breaks this symmetry. Therefore, Voigt notation is no longer valid and no "usual" anisotropic model can be used. The Mooney-Rivlin model brings an additional constant α and there are now 9 different coefficients in $\mathbf{C^0}$, as shown in figure 2.6(d).

From the knowledge of $\mathbf{C^0}$ and the propagation equation (2.23), bulk wave velocities for any plane wave can be retrieved. Depending on the considered hyperelastic model, two transverse waves may have degenerated velocities. The results are summed up in the bottom part of figure 2.6. The linear isotropic, transverse isotropic and two hyperelastic models are considered. For each model, bulk waves velocities propagating in the (x_1, x_3) plane are derived and the corresponding slownesses are plotted for different values of λ_1 below the corresponding elasticity tensor in figure 2.6. In the undeformed case, circles indicate an isotropic media. The longitudinal velocity being very large compared to the transverse one in a nearly-incompressible medium, longitudinal slowness curves appear as centered single points.

In the transverse isotropic model, the shear wave propagating and polarized in the (x_1, x_3)-plane (red) must remain isotropic because of the *major* symmetry $C_{1331} = C_{3113}$, while the shear wave polarized in x_2-direction (blue) is anisotropic. In fact, this is exactly what the transverse isotropy model is about: there is a symmetry axis (x_1 here), and any shear wave that either propagates or is polarized along this axis, propagates at the same velocity. Or, put another way, any plane that contains this symmetry axis is an isotropy plane.

Taking into account the hyperelasticity, slowness curves become ellipses and shear waves are degenerated for a neo-Hookean model. This degeneracy is explained by the fact that the neo-

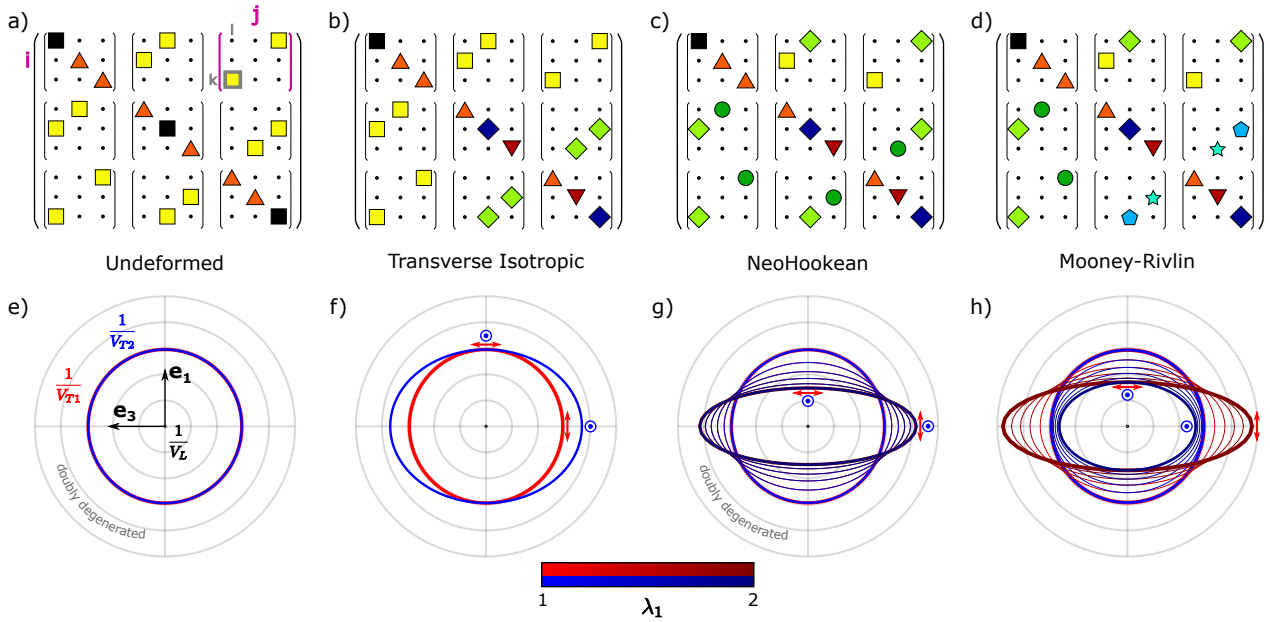

FIGURE 2.6: **Elasticity tensors and slowness curves for various models assuming a uniaxial tension** – The elasticity tensor C^0_{ijkl} is represented as a 3x3 matrix (i,j) of 3x3 matrices (k,l), and the slowness curves of bulk waves propagating in the (x_1,x_3) plane are plotted: V_{T1} in red (respectively V_{T2} in blue) is the velocity of the shear wave polarized in the (x_1,x_3) plane (resp. along the x_2 axis). An equal radial spacing of 0.02 s/m is applied. First, a linear isotropic model (a,e) with $\lambda_L = 1$ GPa and $\mu = 46$ kPa and a transversely isotropic solid (b,f) are considered. To plot the slowness curves in (f), the following elastic constants are used: $C_{44}/C_{55} = 0.8^2$, $C_{55} = C_{66}$, $C_{11} = C_{22}$ and $C_{23} = C_{12}$ (Voigt notation). Then, a neo-Hookean hyperelastic model (c,g) using the same mechanical constants λ_L and μ predicts degenerated shear waves, while a Mooney-Rivlin hyperelastic model (d,h) uses an additional constant $\alpha = 0.5$. For each hyperelastic model, different stretch ratios $1 \leq \lambda_1 \leq 2$ are considered.

Hookean model only takes into account geometric non-linearities but not mechanical non-linearities. Note that the shear wave propagating and polarized in the (x_1,x_3)-plane is no longer isotropic. For the Mooney-Rivlin model, transverse velocities are now distinct. In particular, the shear wave polarized in the (x_1,x_3)-plane propagates slower in the perpendicular direction in a deformed plate, as for the neo-Hookean model, while the shear wave polarized in the x_3-direction propagates faster.

In this part, we derived bulk wave velocities in a material subjected to a uniaxial tension. In our experiment, we assess the velocities of SH_0 and S_0, that are guided waves in a plate.

3 Guided elastic waves in a stretched plate

Combining wave equation (2.23) and boundary conditions leads to guided waves. To find their dispersion curves, we can use the Spectral Collocation Method (SCM) developped in chapter 1, as illustrated in figures 1.4 and 1.5. This method allows us to insert any elasticity tensor, even if fundamental symmetries (Voigt notation) are broken. But before doing so, we present analytical results from the work of Rogerson and collaborators[72,73,74] both for compressible and incompressible prestressed elastic plates.

[72] ROGERSON and FU (1995): "An asymptotic analysis of the dispersion relation of a pre-stressed incompressible elastic plate"
[73] NOLDE et al. (2004): "Dispersion of Small Amplitude Waves in a Pre-Stressed, Compressible Elastic Plate"
[74] ROGERSON and PRIKAZCHIKOVA (2009): "Generalisations of long wave theories for pre-stressed compressible elastic plates"

3.1 Analytical predictions for SH_0 and S_0 velocities

Incompressible case – In equation (1.14), the velocity of SH_0 is equal to the bulk shear velocity. Here, it reads, for a propagation direction i and a polarization direction j (no summation),

$$\rho {V_{T,i}}^2 = C^0_{ijji} = \lambda_i^2 \frac{\lambda_i W_i - \lambda_j W_j}{\lambda_i^2 - \lambda_j^2} \tag{2.26}$$

When the plate is subjected to a uniaxial stress in x_1-direction, one should consider $(i = 1, j = 3)$ for the parallel velocity $V_{T,\parallel}$, and $(i = 3, j = 1)$ for the perpendicular one $V_{T,\perp}$.

It is more complex to obtain the plate velocity and one should solve Lamb waves as discussed in chapter 1. Rogerson and Fu (1995)[72] obtained the S_0 velocity analytically in the low-frequency limit, also referred to as the plate velocity, for an incompressible elastic plate. It reads for propagation direction i, as

$$\rho {V_{P,i}}^2 = C^0_{i22i} + 3C^0_{2ii2} = \left(\lambda_i^2 + 3\lambda_2^2\right) \frac{\lambda_i W_i - \lambda_2 W_2}{\lambda_i^2 - \lambda_2^2} \tag{2.27}$$

When the plate is subjected to a uniaxial stress in x_1-direction, one should consider $(i = 1)$ for the parallel velocity $V_{P,\parallel}$, and $(i = 3)$ for the perpendicular one $V_{P,\perp}$.
Let us apply equations (2.26) and (2.27) to a Mooney-Rivlin hyperelastic model where W is given by equation (2.12), with $\lambda_1 = \lambda$ and $\lambda_2 = \lambda_3 = \lambda^{-0.5}$:

$$\begin{aligned}
\rho {V_{T,\parallel}}^2 &= \mu \left[(1-\alpha)\,\lambda^2 + \alpha\lambda\right] \\
\rho {V_{T,\perp}}^2 &= \mu \left[\frac{1-\alpha}{\lambda} + \frac{\alpha}{\lambda^2}\right] \\
\rho {V_{P,\parallel}}^2 &= \mu \left(1 - \alpha + \frac{\alpha}{\lambda}\right)\left(\lambda^2 + \frac{3}{\lambda}\right) \\
\rho {V_{P,\perp}}^2 &= 4\mu \left(\frac{1-\alpha}{\lambda} + \alpha\lambda\right)
\end{aligned} \tag{2.28}$$

Compressible case – In the next chapter, we use the SCM, based on the equation for compressible materials. As explained in chapter 1, we rather work with a compressible material by keeping $\lambda_L = 1$ GPa as a material constant. If a compressible material is used, then the equations (2.17) and (2.18) should be used instead. The derivation is similar for the SH_0 velocity, and it reads for a propagation direction i and a polarization direction j as

$$\rho {V_{T,i}}^2 = C^0_{ijji} = \frac{\lambda_i^2}{J} \frac{\lambda_i W_i - \lambda_j W_j}{\lambda_i^2 - \lambda_j^2} \tag{2.29}$$

To derive the plate velocity, it is again possible to use the work of Rogerson and collaborators[73,74], and it reads for propagation direction i, as

$$\rho {V_{P,i}}^2 = C^0_{iiii} - {C^0_{ii22}}^2 / C_{2222} \tag{2.30}$$

Here we want to apply these formulas to a Mooney-Rivlin hyperelastic model, but an obvious question is: how to take the incompressible limit to recover the results given in previous paragraph? For the SH_0 mode, the limit is straightforward and considering $J \to 1$ provides the expressions in equation (2.28). However, for S_0, additional work needs to be done. In particular, the incompressible

[72] Rogerson and Fu (1995): "An asymptotic analysis of the dispersion relation of a pre-stressed incompressible elastic plate"
[73] Nolde et al. (2004): "Dispersion of Small Amplitude Waves in a Pre-Stressed, Compressible Elastic Plate"
[74] Rogerson and Prikazchikova (2009): "Generalisations of long wave theories for pre-stressed compressible elastic plates"

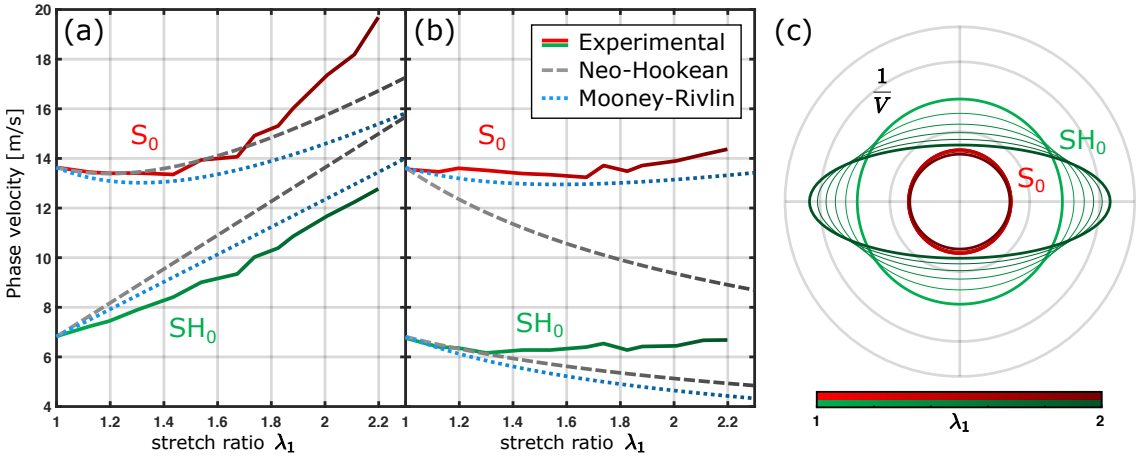

FIGURE 2.7: **Hyperelastic model predictions for SH_0 and S_0 velocities** – Neo-Hookean model predictions (dashed grey lines) and Mooney-Rivlin ones (dotted blue lines) are presented for propagation in the parallel (a) or perpendicular (b) directions. Both models use the same shear modulus $\mu = 46$ kPa but the Mooney-Rivlin also involves an additional constant $\alpha = 0.32$. (c) Slowness curves are plotted for the Mooney-Rivlin model using previous fitting parameters.

limit consists in taking $J \to 1$ but also $\lambda_L \to \infty$ which is problematic when the term $\lambda_L (J-1)$ appears. To solve it, we need another equation, namely the free boundary condition $\sigma_2 = 0$. This provides a non-zero value for $\lambda_L (J-1)$ so that $J \neq 1$ indeed, even if the material is assumed incompressible $(J-1) \to 0$ still. Then, this value of J is re-injected in previous expressions for velocities by considering $\lambda_2 = J/(\lambda_1 \lambda_3)$. Actually, to solve numerically for Lamb dispersion curves using the SCM, we systematically replace J and λ_2 in the full elasticity tensor as explained above.

In this last theoretical part, guided waves in prestressed plates were solved to obtain analytical hyperelastic predictions for SH_0 and S_0 velocities. In the following, we compare those predictions with the quantitative measurements presented in figure 2.4(b) and (d). Here we should recall that $\lambda_3 = \lambda_1^{-0.41}$ in our experiment (not exactly a uniaxial test as illustrated in figure 2.2).

3.2 Limitations of the classic acoustoelastic theory

Analytical hyperelastic predictions for SH_0 and S_0 velocities are superimposed on experimental data in figure 2.7(a) and (b). Grey lines corresponds to neo-Hookean predictions while blue lines correspond to Mooney-Rivlin ones. The transverse velocity in the undeformed plate, at $\lambda_1 = 1$ directly provides $\mu = \rho {V_T}^2 = 46$ kPa. No fitting is needed for the neo-Hookean model. However, for the Mooney-Rivlin model, the coefficient $\alpha = 0.32$ is obtained using a least-square procedure involving the four velocities for $1 \leq \lambda_1 \leq 1.8$. For slowness curves in figure 2.7(c), the tensor of a compressible Mooney-Rivlin model is first derived using Mathematica [96] and used as an input in the SCM. Those slowness curves should be compared to experimental isofrequency contours displayed in figure 2.3(d) and (h).

Although the parallel velocity of SH_0 is almost rightfully modelled as a linear function of the stretch ratio λ_1, it appears that neither the neo-Hookean model nor the Mooney-Rivlin one can predict the slope. Additionally, the greatest differences appear in the perpendicular direction. Both models predict that the perpendicular velocity of SH_0 decreases with λ_1 while it remains almost unchanged in the measurements. Following these observations, we tested various existing

[96] WOLFRAM RESEARCH (2021): *Mathematica 12.2.0.0*

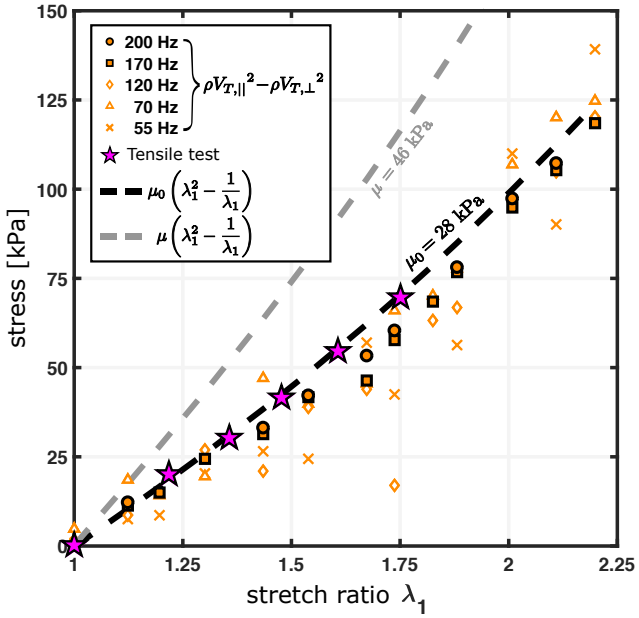

FIGURE 2.8: **Applied static stress is measured with different methods** – The observable $\rho V_{T,||}^2 - \rho V_{T,\perp}^2$ is plotted in orange symbols for different frequencies. It is compared to an independent static measurement (magenta stars) similar to a tensile test. Two theoretical predictions assuming a neo-Hookean model and a uniaxial tension are plotted in black ($\mu_0 = 28$ kPa) and grey ($\mu = 46$ kPa) dashed line.

hyperelastic models [80,93], with unknown mechanical constants to be determined during the least-square procedure, but none of them were able to capture both the parallel velocity slope and the perpendicular velocity of SH_0. In particular, raising the perpendicular velocity increases the slope in the parallel direction too. A key point here is to use both directions to make comparisons. If we restricted our attention to waves propagating only in the uniaxial direction, then good fittings would be possible for various hyperelastic models like Mooney-Rivlin, Gent or Ogden. But in our experiments, we have assessed propagation in both directions and thus highlighted the inadequacies of the current acoustoelastic effect modelling.

3.3 A second evidence of the impact of rheology

Another limit of those hyperelastic predictions appears when comparing those dynamic results to static measurements. In figure 2.8, the static stress in the plate is plotted as a function of λ_1 (magenta stars) during a homemade tensile test. A static shear modulus $\mu_0 = 28$ kPa can be deduced using the initial slope given by the Young modulus $E = 3\mu_0$. Assuming a neo-Hookean model and a uniaxial tension, the principal stresses are $\sigma_1 = \mu_0\left(\lambda_1^2 - 1/\lambda_1\right), \sigma_2 = \sigma_3 = 0$ and σ_1 is plotted as a black dashed line in figure 2.8. This value is markedly different from the one used in figure 2.7: $\mu = 46$ kPa, which was fixed to match the transverse velocity in the undeformed plate. This points out the frequency dependence of the shear modulus: $\mu(\omega) \neq \mu_0$, which needs to be taken into account. Once again, we come across proof of the importance of rheology when studying these nearly-incompressible materials.

The static stress surprisingly can be estimated from dynamic experiments thanks to a model-

[80] DESTRADE et al. (2010): "Third- and fourth-order constants of incompressible soft solids and the acousto-elastic effect"
[93] MARCKMANN and VERRON (2006): "Comparison of hyperelastic models for rubber-like materials"

independent observable, as explained by Li et al. (2022)[75] and Zhang et al. (2023)[97]. This property is as follows:

$$\rho {V_{T,||}}^2 - \rho {V_{T,\perp}}^2 = \sigma_1 - \sigma_3 \tag{2.31}$$

It's not difficult to prove this equation, starting from equation (2.26), and using equation (2.9), one can show

$$\rho {V_{T,||}}^2 - \rho {V_{T,\perp}}^2 = C^0_{1331} - C^0_{3113} = \lambda_1 W_1 - \lambda_3 W_3 = \sigma_1 - \sigma_3.$$

In figure 2.8, this quantity is plotted as a function of λ_1 in various orange symbols for different frequencies. The data points follow the static measurements and this implies very interesting applications: the static and local stress in a plate can be probed through dynamic perturbations[75,97]. All the more remarkable, it seems to remain true for all the measured frequencies.
As just mentioned, the measured static shear modulus μ_0 differs from $\rho {V_T}^2$ at all frequencies. This observation highlights the frequency dependence of the shear modulus μ, as already discussed in chapter 1. We recall the chosen viscoelastic model:

$$\mu(\omega) = \mu_0 \left[1 + (\mathrm{i}\omega\tau)^n\right] \tag{2.32}$$

with $\tau = 210$ µs and $n = 0.27$. These parameters may slightly vary from a sample to another and were adjusted as explained in the following section. Now that we have identified a missing ingredient in the classic acoustoelastic effect, we explain how to incorporate it in the model.

3.4 The proposed nonlinear viscoelastic model

From the last observations, it appears that material rheological properties are essential in the problem and must be taken into account. To do so, the constitutive law needs to be redesigned to factor in both the rheology of the material when it is undeformed and its hyperelasticity when it is deformed.

Following the work of Antman (2004)[98] and Destrade et al. (2009)[99], the Cauchy stress tensor is written as the sum of a static and a dynamic part, rather than an elastic and a dissipative part. The static part is still given by the hyperelastic theory, and the dynamic part writes:

$$\boldsymbol{\sigma}_{\text{dynamic}} = 2\nu\mathbf{D} + \beta\left(\mathbf{B}\cdot\mathbf{D} + \mathbf{D}\cdot\mathbf{B}\right) \tag{2.33}$$

where ν, β are material constants to be determined and $\mathbf{D} = 1/2\left[\mathbf{L} + \mathbf{L}^{\mathrm{T}}\right]$ with $\mathbf{L} = \dfrac{\partial \mathbf{F}}{\partial t}\cdot\mathbf{F}^{-1}$.

The tensor $\mathbf{D}$ may look familiar as it is written in the same way as $\boldsymbol{\epsilon}$ but with an extra time derivative [B].

To match the previously assessed viscoelastic model, recalled in equation (2.32), the time derivative in the tensor $\mathbf{L}$ should be replaced by a fractional derivative one. As in a recent theoretical study [100], it becomes:

$$\mathbf{L} = \frac{\partial^n \mathbf{F}}{\partial t^n}\cdot\mathbf{F}^{-1}. \tag{2.34}$$

[75] Li et al. (2022): "Non-destructive mapping of stress and strain in soft thin films through sound waves"
[97] Zhang et al. (2023): "Noninvasive measurement of local stress inside soft materials with programmed shear waves"
[75] Li et al. (2022): "Non-destructive mapping of stress and strain in soft thin films through sound waves"
[97] Zhang et al. (2023): "Noninvasive measurement of local stress inside soft materials with programmed shear waves"
[98] Antman (2004): *Nonlinear Problems of Elasticity*
[99] Destrade et al. (2009): "Small amplitude waves and stability for a pre-stressed viscoelastic solid"
[B] By considering $\beta = 0$ and adding the incompressibility condition, i.e. a term $-p\mathbf{1}$ in the Cauchy stress tensor, the classic formula for stresses in a Newtonian fluid is recovered.
[100] Zhang et al. (2022): "Propagation and attenuation of Lamb waves in functionally graded fractional viscoelastic soft plates with a pre-deformation"

First, this definition is actually not objective[101]. To overcome this issue, the tensor $\mathbf{D}$ should be replaced by

$$\mathbf{D} = \frac{1}{2}\mathbf{F} \cdot \frac{\partial^n \mathbf{I} - \mathbf{C}^{-1}}{\partial t^n} \cdot \mathbf{F}^{\mathrm{T}}. \tag{2.35}$$

Second, note that equation (2.33) is established for incompressible solids. However, by assuming that the longitudinal (or extensional) viscosity is much lower compared to the usual shear viscosity in this elastomer, then equation (2.33) should remain valid.

The extra term is derived in Appendix B, and it reads at a given frequency as

$$C^{\omega}_{ijkl} = C^{0}_{ijkl} + (\delta_{ik}\delta_{jl} + \delta_{il}\delta_{kj}) \left(\nu + \beta \frac{\lambda_i^2 + \lambda_j^2}{2} \right) (\mathrm{i}\omega)^n \tag{2.36}$$

This equation is an important result of this approach and is the only thing we need to build predictions for the velocities of interest. In fact, this stiffness tensor contains all the information on both the material and the prestress.

First, considering $(\nu, \beta) \to 0$, we recover hyperelastic predictions C^0_{ijkl}. Second, in an undeformed plate, $(\lambda_i) \to 1$, the rheology described in equation (2.32) must be recovered, leading to $\nu + \beta = \mu_0 \tau^n$. This condition is satisfied rewriting $\beta = \beta' \mu_0 \tau^n$ and $\nu = (1 - \beta')\mu_0 \tau^n$ so there is only one remaining unknown constant in this fractional viscous part β'. Of course, if the material rheology is unknown, one can still use constants (ν, β).

From this, it is straightforward to derive SH_0 and S_0 velocities using C^{ω}_{ijkl} instead of C^0_{ijkl}. Note that this change does not involve any additional symmetry-breaking or the appearance of formerly null terms. However, material constants now include an imaginary part so we should specify that measured velocities are indeed phase velocities. Doing so leads to predictions depicted in figure 2.9. Compared to hyperelastic predictions in figure 2.7, both the parallel and perpendicular velocities of SH_0 are now well captured. The same remark holds for S_0 velocities.

Now that a dissipative part has been added in the stress tensor, one can also build predictions for attenuation distances L. Displacement maps are studied more thoroughly and a linear regression of $\log |\mathbf{u}(\omega)|$ allowed a measurement of attenuation distances L that are comparable to the total propagation distance.

The fitting of complex wavenumbers $k = \frac{\omega}{V} - \mathrm{i}L^{-1}$ for $1 \leq \lambda_1 \leq 1.8$ provides $\alpha = 0.29$ and $\beta' = 0.29$. Here, phase velocities have a greater weight than attenuation distances in the least-square loss function since $\mathrm{Re}\,[k] > \mathrm{Im}\,[k]$. Moreover, slowness curves plotted in figure 2.9(e) are from now on similar to the experimental isofrequency contours presented in figure 2.3(d) and (h). Those corrections were possible thanks to the viscoelastic part in the Cauchy stress tensor, and particularly the frequency-dependence of the new elasticity tensor C^{ω}_{ijkl}, obtained with the fractional derivative model. Once again, we have highlighted the importance of rheology in these experiments.

We have also checked that the static stress prediction is still in agreement with experimental data presented in figure 2.8. Regardless of the distance between experimental data for L and its predictions, it is important to note that the attenuation distance of SH_0 in the parallel direction (orange curve in figure 2.9(c)) is multiplied by almost 4 when the stretch ratio is multiplied by 2. This originates from the combination of a geometrical scaling and velocity increase. Said differently, the SH_0 wave propagates much further in the stretching direction as if it is less sensitive to viscosity.

One should also remark that phase velocities curves in figure 2.9(a) and (b) are no longer well captured for a stretch ratio $\lambda \geq 1.8$. In fact, a Mooney-Rivlin model remains a weakly non-linear hyperelastic model. When performing static measurements such as tensile tests, it is common to use other hyperelastic models. Here, it is our choice to avoid adding new material constants in the Cauchy stress tensor especially since the dynamic part in equation (2.33) could also become more

[101] Berjamin and Destrade (2023): *Models of fractional viscous stresses for incompressible materials*

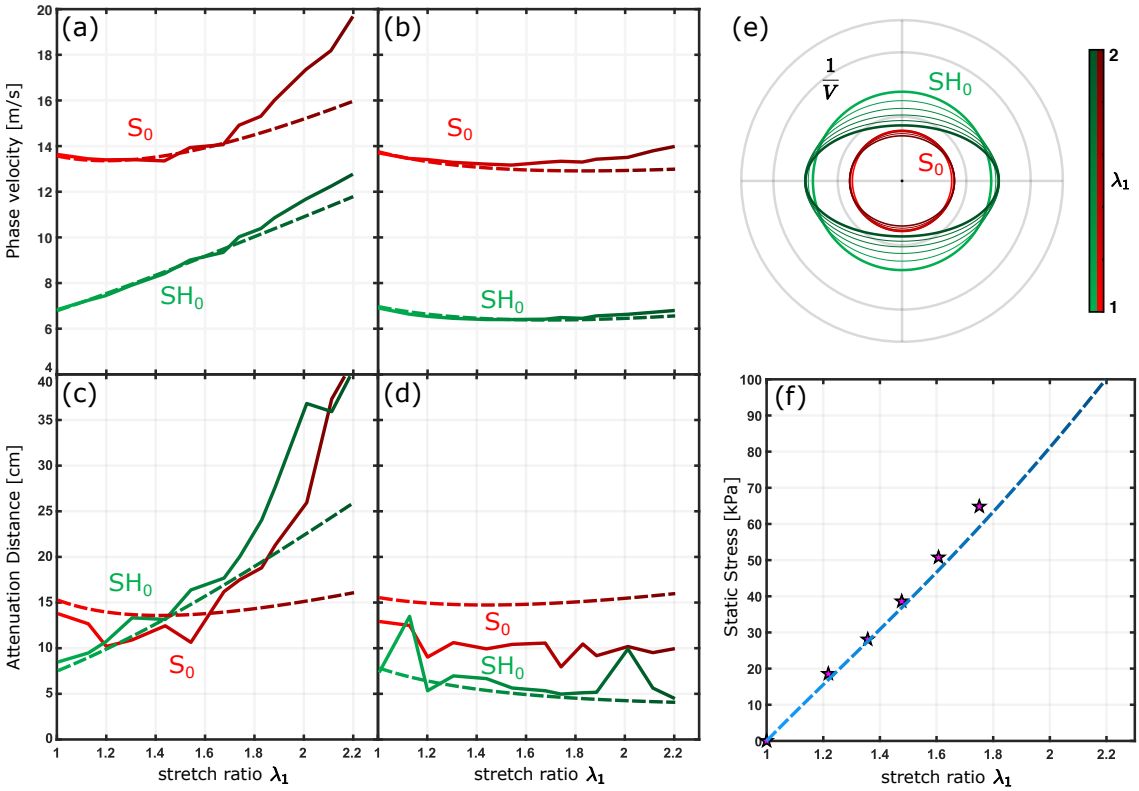

FIGURE 2.9: **Visco-hyperelastic Mooney-Rivlin model predictions for all experimental data at 170 Hz** – Experimental measurements of SH_0 and S_0 phase velocities V are plotted for the parallel (a) and perpendicular (b) directions. Measurements of attenuation distances L are also added in (c) and (d). The fitting of complex wavenumbers in both directions for $1 \leq \lambda_1 \leq 1.8$ provides $\alpha = 0.29$ and $\beta' = 0.29$. Slowness curves (e) and static stress (f) are plotted using previous fitting parameters.

complex and would be written:

$$\boldsymbol{\sigma}_{\text{dynamic}} = 2\nu\mathbf{D} + \beta\left(\mathbf{B}\cdot\mathbf{D} + \mathbf{D}\cdot\mathbf{B}\right) + \gamma\left(\mathbf{B}^2\cdot\mathbf{D} + \mathbf{D}\cdot\mathbf{B}^2\right) + \quad \ldots \tag{2.37}$$

Finally, one practical question remains. By considering the complex-evaluated elasticity tensor C^{ω}_{ijkl}, equation (2.31) is no longer exactly true and there is a mismatch between the quantity $\rho {V_{T,||}}^2 - \rho {V_{T,\perp}}^2$ and the applied static stress. However, knowing that $\mathrm{Re}\,[k] > \mathrm{Im}\,[k]$ and in view of the experiments presented in figure 2.8, this quantity still remains a good estimation of the applied stress. For an exact solution, we suggest to use $\rho\frac{\omega^2}{k^2_{T,||}} - \rho\frac{\omega^2}{k^2_{T,\perp}}$ where $k = \frac{\omega}{V} - \mathrm{i}L^{-1}$ are the measured complex wavenumbers, but attenuation distances are still difficult to measure experimentally.

4 Conclusion

In this chapter, we performed an experiment in a highly-stretched plate and observed induced anisotropy for two fundamental guided modes SH_0 and S_0 with in-plane polarization. To quantify this anisotropy, we repeated the experiment for several applied prestresses and monitored the evolution of their velocities. This change in velocities is actually well known and is named the acoustoelastic effect. We then explained this effect by first introducing the framework of nonlinear elasticity. In nearly-incompressible materials such as the one used in this thesis, it is common to

use a hyperelastic constitutive law, which relies on the use of a strain energy density function W. By combining this constitutive law with an incremental approach, we were able to obtain the main results of the acoustoelastic effect, notably the derivation of an equivalent fourth-order elasticity tensor $\mathbf{C^0}$. In such a tensor, the usual symmetries allowing Voigt notation are broken and none of the usual anisotropic elasticity tensors were able to explain the induced anisotropy. From here, analytical predictions of velocities at play where constructed. In fact, these predictions could not fully explain our experimental observations and they evidence the limit of the classical acoustoelastic theory for soft elastomers. We demonstrated that no hyperelastic model can rightfully fit those experimental data. So, we had to push our thinking further, and material rheology once again emerged as the solution for fully explaining the behavior of such materials.

We took viscoelasticity into account by rewriting the Cauchy tensor and thus the equivalent elasticity tensor. A fractional viscoelastic model identified from previous rheological measurements leads us to propose additional terms including fractional derivative. Finally, with only 2 fitting parameters, we were able to construct accurate predictions up to an elongation of 80% for all phase velocities and attenuation distances. In the same time, static stress measurements confirm that it can approximately be estimated using the material-independent quantity in equation (2.31). A generalization of this method is accessible to other rheological models by adjusting the viscous stress tensor. In the same way, these measurements are of practical interest for rheological characterization of soft materials since this method captures the influence of applied stresses on measured viscoelastic properties. Finally, our framework bridges the gap between elastic wave physics and rheology, but also paves the way for robust quantitative elastography. This will be thoroughly discussed in the next chapter, as well as the influence of prestress on dispersion curves of guided waves in a strip.

Appendix A: Static deformation in the plate

The same plate is stretched using a user-controlled static stress by roping weights to the bottom clamp. Here the results are shown for the undeformed plate ($\lambda_1 = 1$) and for a plate submitted to a stress of 65 kPa resulting in a stretch ratio of $\lambda = 1.75$, in figure 2.10. Some basic image processing allowed us to extract the displacement of a mesh of black dots, and the deformation gradient $\mathbf{F} = \mathbf{1} + \nabla\mathbf{u}$ is computed in the deformed plate. In figure 2.10(a) (resp. 2.10b), the first (resp. second) element of the diagonal F_{11} (resp. F_{33}) is plotted. If an uniaxial tension is assumed, then $\mathbf{F}$ should be homogeneous and diagonal with $(\lambda_1, \lambda_2, \lambda_3) = \left(\lambda_1, \lambda_1^{-0.5}, \lambda_1^{-0.5}\right)$ on its diagonal. However due to boundaries, this assumption does not hold and $\mathbf{F}$ is not diagonal. To quantify this gap to uniaxial tension, we have also plotted the angle atan (F_{13}/F_{11}) describing the proper rotation tensor in the polar decomposition of $\mathbf{F}$ in the right part of figure 2.10. When this angle is null, deformation is purely stretching. Here we rather observe that boundaries, especially corners, induce some deformations that are not purely stretching, because the top and bottom clamps are fixing the plate width to its initial length. However, because of symmetries of this static tension, $\mathbf{F}$ turns out to be almost diagonal in some regions of the plate as centered axis $x_1 = 0$ and $x_3 = 0$, where the angle tends to zero. Those are the regions, white (or black) rectangles in figure 2.10, where we have chosen to study in-plane guided waves and where we have measured stretch ratios λ_1 and $\lambda_3 = \lambda_1^{-0.41}$. A last observation is this apparent vertical gradient in F_{11}. It can be explained since the undeformed plate is not in its natural configuration, but is submitted to its own weight. It is well known that, due to its own weight, deformation in the upper part of the plate will be higher than in the lower part. Actually, the bottom of the plate should exactly be undeformed. Then, applying a constant static tension in the plate (by opposition to the weight which is not a constant stress) induces a higher apparent stretch ratio in the bottom of the plate since the upper part of the plate was already slightly deformed in the reference configuration (as opposed to the natural configuration). This small contribution was not corrected here because it is negligible in the region of interest given by white (or black) rectangles.

Appendix B: Method to derive the additional dynamic term in the equivalent stiffness tensor C^{ω}_{ijkl}

For this demonstration, we use the notation from Refs.[29,99]. Assuming a small monochromatic displacement superimposed on a large static one, the coordinates are written in the perturbed configuration $\mathcal{B}'$:

$$\begin{aligned} x_1' &= \lambda_1 X_1 + u_1(X_1, X_2, X_3, \omega) = x_1 + u_1'(x_1, x_2, x_3, \omega) \\ x_2' &= \lambda_2 X_2 + u_2(X_1, X_2, X_3, \omega) = x_2 + u_2'(x_1, x_2, x_3, \omega) \\ x_3' &= \lambda_3 X_3 + u_3(X_1, X_2, X_3, \omega) = x_3 + u_3'(x_1, x_2, x_3, \omega) \end{aligned}$$

Let's derive the deformation gradient:

$$F_{ij} = \frac{\partial x_i'}{\partial X_j} = \lambda_i \delta_{ij} + \frac{\partial u_i}{\partial X_j} = \lambda_i \delta_{ij} + \lambda_j \frac{\partial u_i'}{\partial x_j} \tag{2.38}$$

Other essential tensors such as the inverse of the deformation gradient $\mathbf{F}^{-1}$, the usual symmetrical part of the spatial velocity gradient $\mathbf{D}$ or the left Cauchy-Green tensor $\mathbf{B}$ are then derived and

[29] Destrade and Saccomandi (2007): *Waves in Nonlinear Pre-Stressed Materials*
[99] Destrade et al. (2009): "Small amplitude waves and stability for a pre-stressed viscoelastic solid"

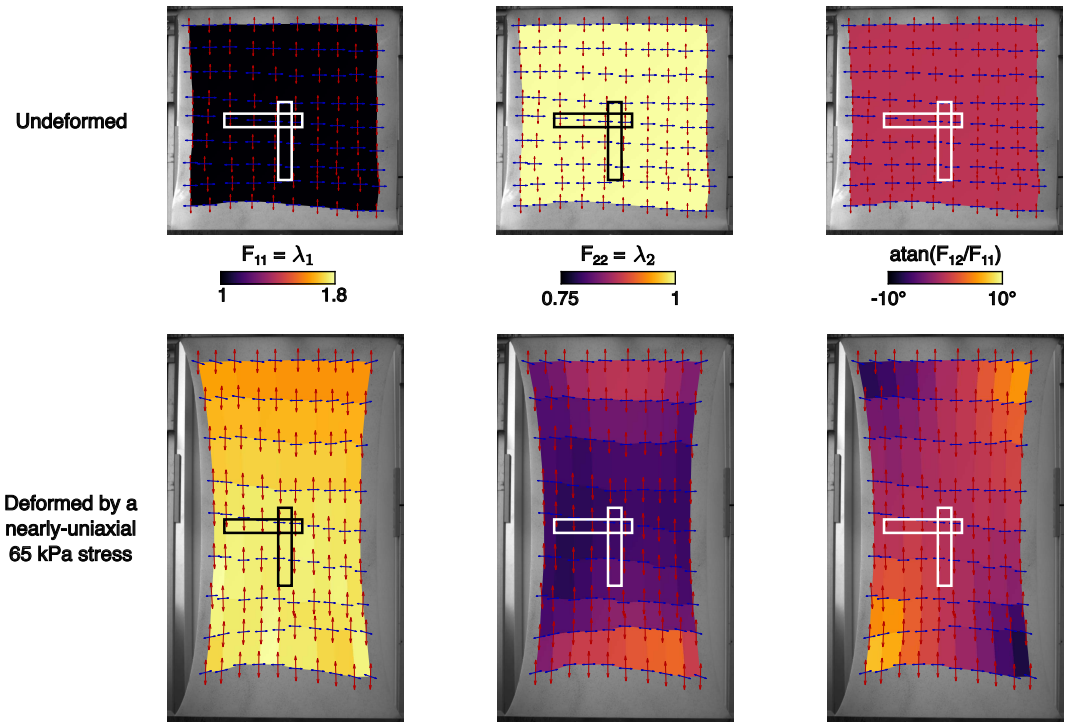

FIGURE 2.10: **Mapping the static deformation in the stretched plate** – Displacements of a mesh of black dots is extracted between the undeformed plate at rest (top) and the deformed plate submitted to a 65 kPa stress (bottom). Diagonal terms of $\mathbf{F}$ are stretch ratios λ_1 (left) and λ_3 (center). Due to boundaries, the angle of rotation (right) is not null everywhere. The region of interest are given by white (or black) rectangles.

approximated to the first order in u:

$$\begin{aligned}\left[\mathbf{F}^{-1}\right]_{ij} &= \frac{\delta_{ij}}{\lambda_i} - \frac{1}{\lambda_i}\frac{\partial u'_i}{\partial x_j} \\ 2D_{ij} &= \left(\frac{\partial u'_i}{\partial x_j} + \frac{\partial u'_j}{\partial x_i}\right)(\mathrm{i}\omega)^n \\ B_{ij} &= \lambda_i^2\delta_{ij} + \lambda_i^2\frac{\partial u'_j}{\partial x_i} + \lambda_j^2\frac{\partial u'_i}{\partial x_j}\end{aligned}$$

with $(\mathrm{i}\omega)^n$ appearing because of the fractional derivative. Using these expressions, the new dynamic contribution can be rewritten:

$$\left[\sigma_{\text{dynamic}}\right]_{ij} = \frac{1}{2}\frac{\partial u'_i}{\partial x_j} + \frac{\partial u'_j}{\partial x_i}\left(\nu + \beta\frac{\lambda_i^2+\lambda_j^2}{2}\right)(\mathrm{i}\omega)^n. \tag{2.39}$$

Using the equation of motion

$$C^0_{jikl}\frac{\partial^2 u'_l}{\partial x_j \partial x_k} + \frac{\partial\left[\sigma_{\text{dynamic}}\right]_{ij}}{\partial x_j} = \rho\frac{\partial^2 u'_i}{\partial t^2}, \tag{2.40}$$

leads to the use of an equivalent elasticity tensor:

$$C^\omega_{jikl} = C^0_{jikl} + (\delta_{ik}\delta_{jl} + \delta_{il}\delta_{jk})\left(\nu + \beta\frac{\lambda_i^2+\lambda_j^2}{2}\right)(\mathrm{i}\omega)^n. \tag{2.41}$$

Finally, let's notice that the additional term is invariant under the permutation of the two first indices. And, to be consistent with our numerical approach (SCM), one still needs to permute the two last indices but the extra term does not change indeed.

Appendix C: Experimental phase velocities and attenuation distances of SH_0 and S_0 at 170 Hz, used in fitting procedures

Table 2.1: Phase velocities V (m/s) and attenuation distances L (cm) of SH_0 and S_0 modes in parallel and perpendicular directions as functions of the stretch ratio λ_1 at 170 Hz.

λ_1	$V_{T,\parallel}$	$V_{T,\perp}$	$V_{P,\parallel}$	$V_{P,\perp}$	$L_{T,\parallel}$	$L_{T,\perp}$	$L_{P,\parallel}$	$L_{P,\perp}$
1	6.83	6.72	13.64	13.52	8.69	7.26	13.99	12.85
1.123	7.23	6.46	13.45	13.27	9.68	13.42	12.88	12.42
1.196	7.44	6.36	13.40	13.23	10.95	5.25	10.40	8.94
1.301	7.90	6.27	13.41	13.10	13.53	6.88	11.11	10.53
1.435	8.41	6.22	13.35	13.03	13.36	6.58	12.66	9.85
1.539	9.01	6.22	13.94	12.98	16.59	5.55	10.85	10.33
1.673	9.34	6.23	14.07	13.10	17.89	5.24	16.41	10.48
1.737	10.02	6.30	14.92	13.15	20.26	4.80	17.71	7.87
1.825	10.39	6.27	15.31	13.10	24.24	5.02	19.01	10.38
1.881	10.86	6.38	16.02	13.24	27.92	5.08	21.52	9.09
2.008	11.68	6.45	17.36	13.32	36.03	9.83	26.16	10.10
2.109	12.24	6.53	18.19	13.60	36.13	5.54	37.51	9.43
2.199	12.77	6.61	19.69	13.80	40.78	4.38	41.76	9.87

Chapter 3

Elastography in a deformed viscoelastic strip

Objectives

In the previous chapters, we first described the physics of guided elastic waves in a soft strip, and we then developed a material model that takes into account both the viscoelastic and prestress effects. In this chapter, we measure, predict and understand how the behavior of guided elastic waves in a strip are modified when it is subjected to large initial deformations. Notably, we discuss the effectiveness of widely used 1D models to describe our observations. Then, in a second step, we study this strip using elastography with a commercial ultrasound system. Elastography is a medical imaging technique commonly used to map the elasticity of biological tissues. We highlight the limits of this technique due to waveguiding, viscoelasticity and prestress. We fully explain our measurements and we believe that our method will pave the way for robust quantitative elastography of elongated tissues.

- Dispersion curves are measured in a strip subjected to a uniaxial stress
- Near-perfect predictions are built combining SCM with the equivalent stiffness tensor
- Simple 1D models provide a good understanding of the fundamental modes velocities
- Elastography experiments provide a wide range of values from 2 to 6 m/s
- Dispersion curves of the generated shear waves are obtained with a spatio-temporal Fourier transform and well explained

Contents

The study of guided elastic waves in plates made of soft material is motivated by the similarities that these materials share with biological tissues, and because elastic waves enable a better understanding and description of their dynamics. Indeed, elastic waves are guided in plate geometries at different scales in the human body. Just to give a few examples, they propagate in the myocardium[102] and biofilms[103], and on a smaller scale, pressure pulses are observed in lipid monolayers[22].

Elastic waves are also guided in other geometries in the human body. For instance, they propagate in artery walls[104,105,106] but are also stationary in vocal cords[23]. One of the most important geometry is the strip, which can be found widely, from the Achilles' tendon in the foot[107] to the basilar membrane in the inner ear[108,24] where the sound transduction occurs. This last example is discussed in Chapter 4 where we fully describe the *cochlear wave*, a guided mechanical wave that travels along this basilar membrane.

As mentioned previously, soft materials are highly deformable and each of the examples cited above are media that are often subjected to prestress, which modifies their dynamics. For instance, to produce sounds, we adjust the tension of our vocal cords in order to control the resulting pitch.

In light of Chapter 2 on the effect of prestress on elastic guided waves in a plate, we can already understand the dynamics of many of the cited examples. The strip is a geometry that is of particular interest, and we naturally wonder how prestress could affect guided elastic waves there.

Additionally, in chapters 1 and 2, we have often pointed out the impact that this work could have in elastography, without really explaining what this technique is about, and without proving it either.

In this chapter, we first measure the dispersion curves of in-plane guided elastic waves in a free strip subjected to a uniaxial tension. To build predictions, we use our semi-analytical method, based on the implementation of the equivalent stiffness tensor $\mathbf{C}^{\omega}$ (see Chapter 2) in the Spectral Collocation Method (see Chapter 1). The resulting predictions are compared with our experimental measurements and found to match almost perfectly without using any fitting procedure. By zooming in on the fundamental modes A_0' and S_0', we note two completely different behaviours. We show that when the strip is deformed, their behaviour can be predicted using 1D models and that their polarization is a key factor in understanding the impact of prestress. The approach is also validated in the case of a strip with fixed lateral edges submitted to a planar tension, and we discuss in greater depth how the Dirac cone evolves with stretching.

In the second part of this chapter, we use elastography to probe velocities in a strip. The elastography technique is first introduced, along with its relevance to clinical applications. We then show that this medical imaging method is not always quantitative and discuss these limitations in detail. By applying large deformations to the viscoelastic strip in different orientations, we measure a wide range of phase velocities. Firstly, the generated shear waves are fully explained. Then, using our semi-analytical method, we build predictions for their dispersion curves. Finally, we are also able to capture the change of velocities with the prestress. Our work thus tackles the main

[102] Nenadic et al. (2011): "Lamb wave dispersion ultrasound vibrometry (LDUV) method for quantifying mechanical properties of viscoelastic solids"

[103] Liou et al. (2019): "Nondestructive characterization of soft materials and biofilms by measurement of guided elastic wave propagation using optical coherence elastography"

[22] Griesbauer et al. (2012): "Propagation of 2D Pressure Pulses in Lipid Monolayers and Its Possible Implications for Biology"

[104] Couade et al. (2010): "Quantitative assessment of arterial wall biomechanical properties using shear wave imaging"

[105] Astaneh et al. (2017): "Arterial waveguide model for shear wave elastography: implementation and in vitro validation"

[106] Maksuti et al. (2017): "Influence of wall thickness and diameter on arterial shear wave elastography: a phantom and finite element study"

[23] Hirano (1974): "Morphological structure of the vocal cord as a vibrator and its variations"

[107] Brum et al. (2014): "In vivo evaluation of the elastic anisotropy of the human Achilles tendon using shear wave dispersion analysis"

[108] Robles and Ruggero (2001): "Mechanics of the mammalian cochlea"

[24] Reichenbach and Hudspeth (2014): "The physics of hearing: fluid mechanics and the active process of the inner ear"

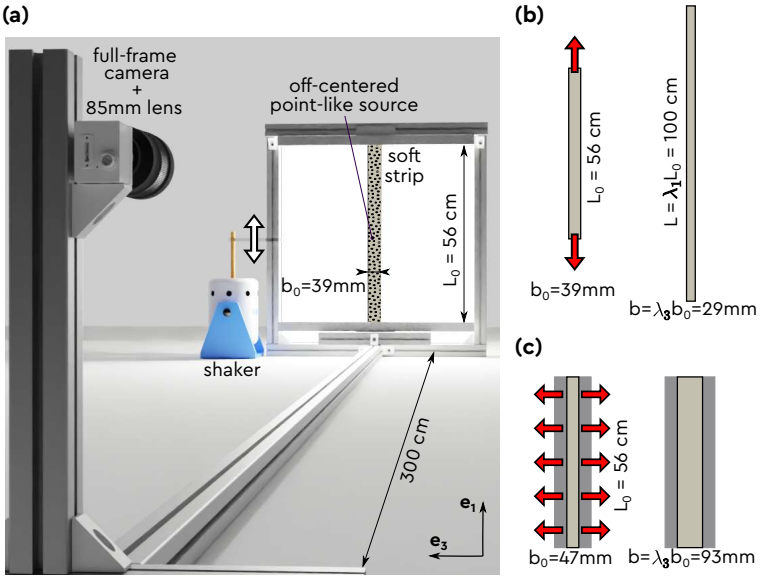

FIGURE 3.1: **Experimental setup to measure elastic guided waves in deformed strips** – (a) A thin strip of Ecoflex00-30, with dimensions 60 cm x 3 mm x 4 cm in directions x_1, x_2, x_3, is held in a vertical position and clamped to a frame on its top and bottom edges. Sinusoidal vibrations in the (x_1, x_3)-plane are generated by a shaker and displacements are extracted using a CCD camera located 3 m away from the plate. (b,c) The frame is adjusted to impose large deformations in a strip with free (respectively fixed) lateral edges, reaching stretch ratio $\lambda_1 > 2$ (resp. $\lambda_3 > 2$) along the vertical (resp. horizontal) axis.

limitations, and we hope that our method will be a step towards quantitative elastography.

The following is largely duplicated from our works published as DELORY et al. (2023)[65] and DELORY et al. (2023)[109].

1 Guided elastic waves in a stretched free strip

Going back to the strip geometry, we use the experimental setup and method described in figure 2.1 and replace the plate with a strip. It is recalled here in figure 3.1(a). The free strip is submitted to a uniaxial tension $(\lambda_1, \lambda_2, \lambda_3) = (\lambda, \lambda^{-0.5}, \lambda^{-0.5})$ in figure 3.1(b), and the fixed strip is submitted to a plane-strain tension $(\lambda_1, \lambda_2, \lambda_3) = (1, \lambda^{-1}, \lambda)$ in figure 3.1(c). Note that the fixed strip indeed has free top and bottom edges leading to a deviation from this planar tension configuration $(\lambda_1, \lambda_2, \lambda_3) = (\lambda^{-0.08}, \lambda^{-0.92}, \lambda)$ in the measured portion.

1.1 Dispersion curves for a free strip subjected to a uniaxial tension

Let us first focus on the configuration with a free strip and present our experimental results for this configuration.

1.1.1 Experimental measurements

At each frequency, the total in-plane displacement field is decomposed using a singular value algorithm as illustrated previously in figure 1.17 and shown again here in figure 3.2(a). This procedure has already been explained in Chapter 1. At 200 Hz in an undeformed free strip, five in-plane guided

[65] DELORY et al. (2023): "Guided elastic waves in stretched viscoelastic strip"
[109] DELORY et al. (2023): "Exploring the limits to quantitative elastography: supersonic shear imaging in stretched soft strips"

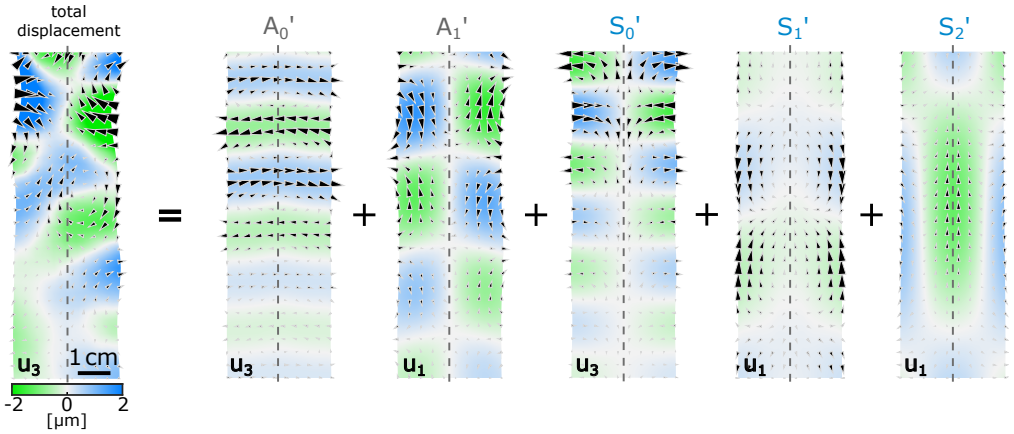

FIGURE 3.2: **Field decomposition at 200 Hz** – The experimental in-plane total displacement field at 200 Hz is decomposed in eigenmodes with a singular value decomposition algorithm. A_0' is referred to as the flexural mode, while the S_0' mode to as the compressional mode.

modes coexist with different symmetries, shapes and wavenumbers (or wavelengths). Applying a spatial Fourier transform enables the extraction of their wavenumbers, and thus their dispersion curves.

To build predictions for such dispersion curves, we implement the equivalent stiffness tensor $\mathbf{C}^{\omega}$ in the Spectral Collocation Method (SCM). This equivalent stiffness tensor is derived in Chapter 2 and brings together all the mechanical properties of the material, including viscoelasticity, and the prestress features, namely the stretch ratios $(\lambda_1, \lambda_2, \lambda_3)$.

All the experimental and numerical results are compiled in the dispersion diagram of figure 3.3, which showcases the experimental points (top row) and the corresponding numerical outcomes (bottom row). These were acquired from the same soft strip subjected to varying degrees of longitudinal static stretching, ranging from $\lambda = 1$ (depicted in dark blue) to $\lambda = 1.8$ (depicted in yellow), and encompassing frequencies up to 250 Hz. For enhanced clarity, symmetric and anti-symmetric modes are presented in separate diagrams and are labeled S_n' and A_n' as in figure 1.18.

As one can notice, the theory effectively captures our experimental observations. No fitting procedure was performed since all the mechanical parameters are known thanks to the experiment carried out on the plate made of the same elastomer (see Chapter 2). It is noteworthy that the SCM provides the dispersion curves of out-of plane strip modes presented in figure 1.25. This method also provides all evanescent modes, so that some solutions have been discarded and the transparency encodes for the imaginary part of the wavenumbers.

First, slopes (*i.e.* group velocity) globally increase and it seems that cut-off frequencies have also increased. This is not clearly visible for the A_1' mode since it is difficult to define properly a cut-off frequency in a viscoelastic solid where the transition between an evanescent mode and a propagating one is smoothed by the intrinsic losses in the material. This remark also holds for the zero-group velocity point that should exist in such a strip but without losses[66]. More detailed information about the effect of viscoelasticity on this ZGV point are presented in Appendix A. The off-centered polarized source vibrates along x_1, and the input energy in the S_1' mode remains very low such that its dispersion curve is barely visible. Besides that, our semi-analytical approach markedly fits the full dispersion curves, for all the modes, across several hundreds of Hz, and for stretch ratio up to $\lambda = 1.8$.

[66] SIMONETTI and LOWE (2005): "On the meaning of Lamb mode nonpropagating branches"

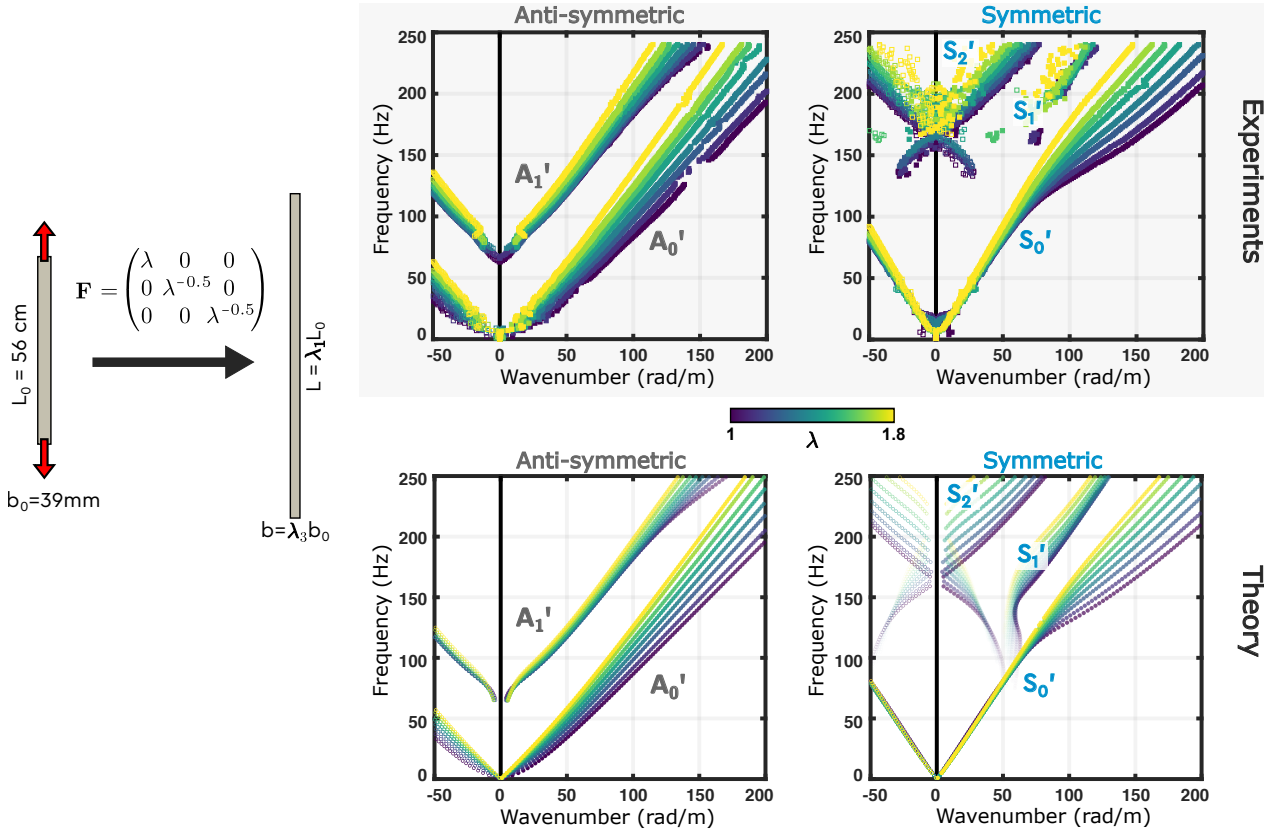

FIGURE 3.3: **Dispersion in a soft strip subjected to a uniaxial stress** – The deformation gradient $\mathbf{F}$ and the geometry are recalled for a free strip subjected to a uniaxial tension. Experimental dispersion curves of antisymmetric and symmetric modes in the elongated strip for several values of the stretch ratio $1 \leq \lambda \leq 1.8$ are shown in the top line. The theoretical predictions (bottom line) are obtained using the SCM (see text).

1.1.2 Polarization as a determining criterion

Of particular interest is the uneven impact of longitudinal stretching on these branches. S'_0 is a compressional mode below 100 Hz (see figure 1.15 in Chapter 1) and seems nearly immune to it, a characteristic shared with A'_1. Conversely, the other modes, like the flexural mode A'_0, exhibit greater sensitivity to stretching, notably in their slopes but also, in the case of S'_1 and S'_2, in their cut-off frequencies.

A striking result is the bifurcation in the behaviour of S'_0. Note how the branches spread out above 100 Hz. This feature provides a valuable hint towards understanding the governing mechanism. Indeed, at low frequencies S'_0 is essentially polarized in the longitudinal direction, which is why it is commonly called the compressional mode. However, its dominant polarization switches as the frequency increases. On the displacement map acquired at 200 Hz, displayed in figure 3.2(a), S'_0 indeed appears essentially polarized in the transverse direction. This is because when the frequency is increased, the wavelength becomes comparable to the strip width. When the wavelength is small enough, the wave no longer feels the width of the strip and behaves like an edge wave propagating along the lateral edge of the strip.

This bifurcation strongly suggests that polarization is a determining criterion. This conclusion is further supported by the fact that, on the one hand, both A'_0 and S'_2 are essentially polarized in the transverse direction (as depicted in figure 3.2) and turn out to be significantly influenced by the degree of stretching. On the other hand, A'_1 is characterized by longitudinal polarization and

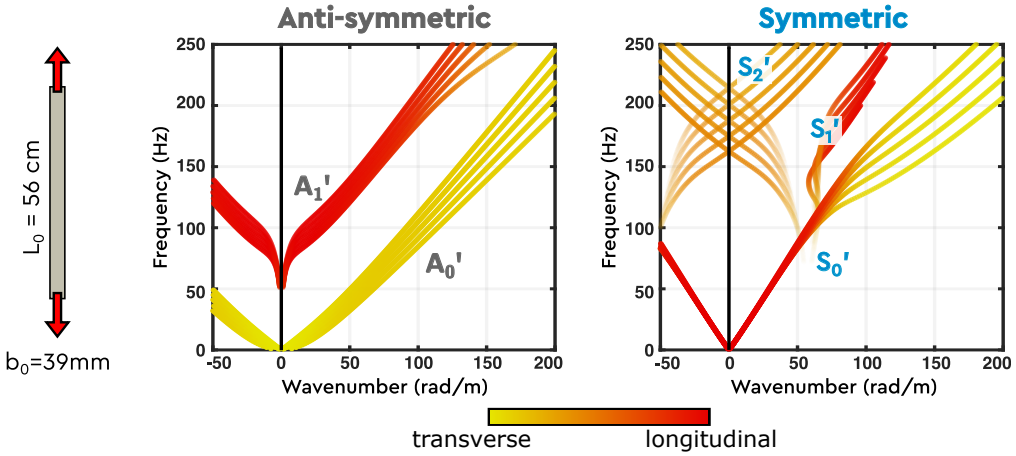

FIGURE 3.4: **Role of the polarization for a free strip** – Theoretical dispersion curves for the free strip subjected to a uniaxial tension. The color indicates the dominant polarization (yellow = transverse, red = longitudinal).

proves resilient to stretching. To support this hypothesis, we display again the theoretical dispersion curves but with a colormap rendering their polarization.

Practically, the SCM is used to solve equation (1.40) at a fixed angular frequency ω to obtain the eigenpair $(k, \mathbf{u})$. By studying $\mathbf{u}$, one can discriminate the in-plane eigenmodes (from their out-of-plane counterparts) and their corresponding symmetry. One can also study their main polarization by evaluating mean values of $|u_1|^2$ and $|u_3|^2$ over the cross-section and compute the inverse tangent of the ratio $\int |u_1|^2 / \int |u_3|^2$. Then, it is possible to quantify whether a given mode is mostly polarized in the direction x_1 (longitudinal in red) or in the direction x_3 (transverse in yellow).

The first obvious observation is on the polarization of the S_0' mode for a free strip. For low frequencies, it appears red and all curves are superimposed. When increasing the frequency, the branch gradually becomes orange, then yellow. It indicates the gradual change from a pure longitudinal polarization to a more mixed polarization. Interestingly, the stretching starts to affect the dispersion diagram when the polarization becomes more transverse to the stretching direction. In contrast, the A_0' mode in a free strip is highly dependent on the applied stress, especially for low frequencies where curves are yellow (transverse *i.e.* in-plane flexion in the strip width). Similar qualitative observations can be made for the other modes. The redder the curves, the closer they remain, so the less effect the prestress has. Conversely, the yellower they are, the greater the impact of prestress.

1.1.3 Discussion about the Dirac cone in a free strip

Finally, let us take a close look at the S_1' and S_2' branches in figure 3.3. We see that their two cut-off frequencies coincide. This results in a degenerate crossing at $k = 0$: the so-called Dirac cone already assessed in Chapter 1. The mixed polarization of these modes close to the Dirac cone nicely appears as orange curves in figure 3.4. When there is no coincidence, the mode is either purely longitudinal or purely transverse on the $k = 0$ axis, so this mixed polarization is a typical feature of the Dirac cone.

Here, we observe that this cone is robust to extensional stress, since it remains orange with an increasing prestress. Our measurements also demonstrate that the crossing frequency can be controlled by adjusting the amount of static stretch.

In an undeformed strip, such a crossing appears because of the coincidence of the two cut-off frequencies $f = 2\dfrac{V_T}{2b} = \dfrac{V_P}{2b}$. In the case of a strip subjected to uniaxial tension, we know how these

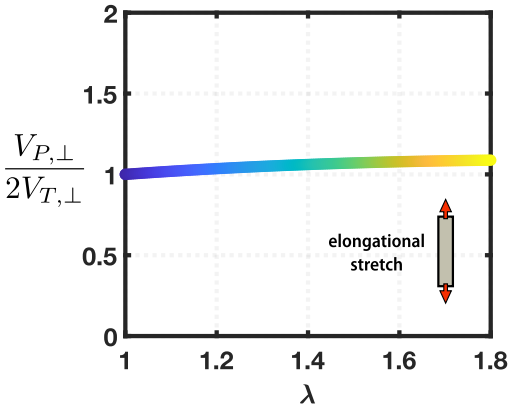

FIGURE 3.5: **Cut-off frequencies** – Evolution of the ratio $V_{P,\perp}/2V_{T,\perp}$ with the applied deformation in the case of a uniaxial stress.

velocities evolve with the stretch ratio (see Chapter 2). More specifically, we need to know how the velocities evolve in the x_3 direction, and to derive the ratio $V_P/2V_T$. If this ratio equals 1, then cut-off frequencies perfectly coincide. This ratio is plotted as a function of λ in figure 3.5.

Our method allows us to obtain complex valued wavenumbers, and by also plotting their imaginary part, one can notice that this linear crossing is in fact two straight lines passing each other side by side with non-zero imaginary parts. Details about the effect of viscoelasticity on this Dirac cone are presented in Appendix A.

By increasing the stretch ratio, cut-off frequencies do not strictly coincide. In a purely elastic material, one expects the Dirac cone to be broken (see Appendix A). Actually, in viscoelastic media, the branches still pass each other side by side but with an increasing imaginary part, and the Dirac cone is still present. We remember that, strictly speaking, there is no linear crossing of theses curves in the complex plane, but there is one when the solutions are projected onto the real wavenumber axis.

In the end, small discrepancies with theoretical predictions are visible around this Dirac cone because it is experimentally hard to assess the behaviour at the $k = 0$ axis, especially when the imaginary part of the wavenumber starts to outweigh its real part. Discrepancies also appear at the highest stretch ratio $\lambda = 1.8$ because the material model is no longer valid up to this stretch ratio value. In a plate in Chapter 2, we have seen that the SH_0 and S_0 phase velocities are not captured at such high deformations.

Let us now take a look at the two fundamental modes A'_0 and S'_0. In the low-frequency limit, their wavenumbers k tend to zero *i.e.* their wavelengths become very large compared with the strip width and thickness. This naturally raises the question of whether their behaviour can be understood from one-dimensional models.

1.2 Discussion around the physics of beams

This strip is similar in many aspects to a beam, wire or string. Flexural waves in these objects have been extensively studied. To name just a few applications, these waves propagate in power transmission lines, railway rails, bridges, musical instruments and so on. In particular, it can be very useful to know how these flexural waves are modified when such structures are loaded. And reciprocally, these modifications being understood, these waves can be used to probe prestresses in these structures. It may therefore be entirely relevant to link our measurements in a strip to these 1D models, so that we can export our understanding of the 3D theory to these applied cases.

Usually, such 1D models require the use of geometrical parameters and of the Young modulus E. A number of questions naturally arise. What is the Young modulus to be considered when the strip is deformed? And just as important, what is it when the deformation is dynamic, *i.e.* elastic waves propagating at ω?

1.2.1 The Young modulus

As already demonstrated in figure 2.5 in Chapter 2, the static response of the material deviates from the simple Hookean model when carrying out a simple tensile test and a Mooney-Rivlin is needed. The principal component of the Cauchy stress tensor along x_1, for such a Mooney-Rivlin solid subjected to a uniaxial tension, reads:

$$\sigma = \frac{E_0}{3}\left(1-\alpha+\frac{\alpha}{\lambda}\right)\left(\lambda^2-\frac{1}{\lambda}\right) \tag{3.1}$$

with E_0 the static Young modulus and α a dimensionless Mooney-Rivlin parameter. As visible on the curve $\sigma(\lambda)$ previously presented in figure 2.5, the slope increases with λ, leading us to think that one should derive an effective elongation-dependent Young modulus. However, the desired equivalent Young modulus is not simply the derivative of the Cauchy stress tensor $\boldsymbol{\sigma}$ with respect to the stretch ratio λ, but rather that of the first Piola–Kirchhoff stress tensor $\mathbf{P}$[110], also introduced in Chapter 2. In our case, one simply has $P = \sigma/\lambda$ for its principal component along x_1. This amounts to considering the deformed material as Hookean with the following elongation-dependent Young modulus:

$$E(\lambda, \omega = 0) = \frac{E_0}{3}\left[(1-\alpha)\left(1+\frac{2}{\lambda^3}\right)+\frac{3\alpha}{\lambda^4}\right] \tag{3.2}$$

Note that this expression is only valid in the static regime ($\omega = 0$).

When increasing the frequency, one should use the fractional Kelvin-Voigt model, as justified in chapters 1 and 2:

$$E(\lambda = 1, \omega) = E_0\left[1+(\mathrm{i}\omega\tau)^n\right]. \tag{3.3}$$

This time, this expression is valid in the absence of external deformation ($\lambda = 1$).

In summary, the Young modulus depends on both frequency and strain, which are usually examined separately. However, drawing conclusions about E for any couple of parameters (λ, ω) is not straightforward due to their interdependence. So far, there has been no unified framework to account for both simultaneously. For now, we just assume their independence, and write:

$$E(\lambda, \omega) = E(\lambda, \omega = 0)\left[1+(\mathrm{i}\omega\tau)^n\right]. \tag{3.4}$$

Now that we have proposed an expression of this Young modulus, we can study the compressional mode and flexural mode. To illustrate the behaviour of these modes at low frequencies, we plot their phase velocities in figure 3.6 for frequencies ranging from 0 to 100 Hz and for stretch ratio λ ranging from 1 to 1.8.

1.2.2 Compressional mode

As mentioned in Chapter 1, we should take a close look at the S_0' mode. We see in figure 3.4 that its polarization is mainly longitudinal, which naturally recalls the compressional mode propagating in a beam.

[110] Zhao and Chang (2021): "Elastic wave velocities in finitely pre-stretched soft fibers"

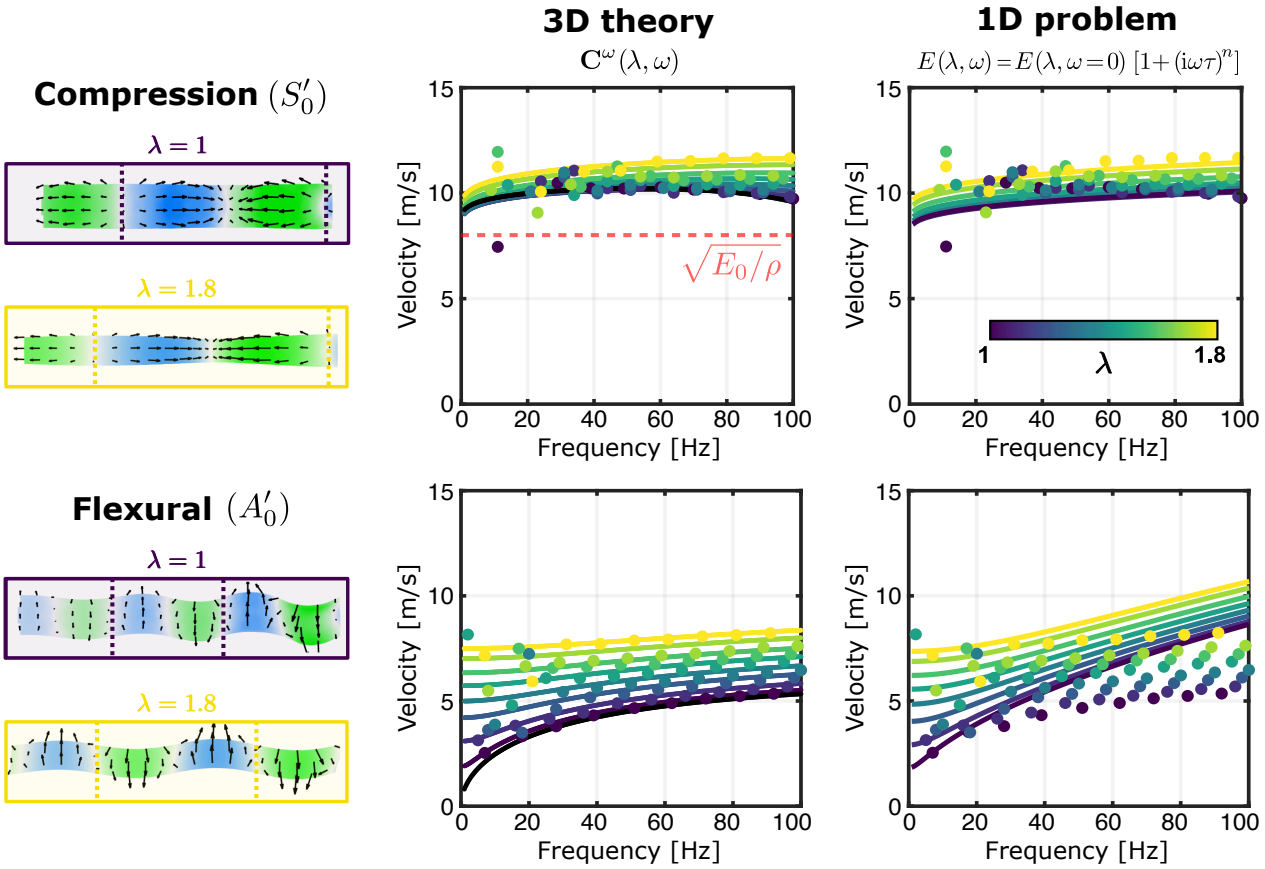

FIGURE 3.6: **Velocities of fundamental modes in a stretched free strip** – Left: profiles of the displacements at 50 Hz for $\lambda = 1$ (blue frame) and $\lambda = 1.8$ (yellow frame). Dashed lines indicate the wavelength. Middle: Phase velocity for static elongations varying from $\lambda = 1$ (blue) to $\lambda = 1.8$ (yellow). Measured points are compared with theoretical predictions (lines). Right: Same as in the middle, but theoretical predictions are built using 1D models.

Anyone studying this system, in civil engineering for instance, would write the equation governing the compressional dynamics (see for instance equation (25.1) in reference[33]):

$$E\frac{\partial^2 u_1}{\partial {x_1}^2} - \rho\frac{\partial^2 u_1}{\partial t^2} = 0, \tag{3.5}$$

Estimating the phase velocity from the static Young modulus E_0 leads to a velocity of $V_c^0 = \sqrt{E_0/\rho} = 8$ m/s (indicated by a red dashed line in figure 3.6) which significantly underestimates the observations. In addition, this approach assumes a constant velocity *i.e.* a non-dispersive propagation, which is not accurate here.

A better estimation can be obtained by replacing the Young modulus with that of equation (3.3) to arrive at

$$V_c(\lambda=1,\omega) = \left[\mathrm{Re}\left(\sqrt{\frac{\rho}{E(\lambda=1,\omega)}}\right)\right]^{-1} = \frac{V_c^0}{\mathrm{Re}\left[(1+(\mathrm{i}\omega\tau)^n)^{-1/2}\right]} \tag{3.6}$$

Because we take into account the rheology, this amounts to a frequency-dependent phase velocity. At 50 Hz, this expression yields a velocity of roughly 10 m/s, in much better agreement with our

[33] LANDAU et al. (1986): *Theory of elasticity: volume 7*

measurements. Also, this velocity slowly grows in power law with frequency, partly explaining the observed dispersion.

Regarding the dependence on elongation, our experiments indicate that V_c is almost independent of λ, as already observed in figure 3.3. To capture this effect accurately, it is necessary to incorporate the hyperelastic prediction for the Young modulus from equation (3.2). However, this alone is not enough since wave equation (3.5) is written with undeformed coordinates and a push-forward operation is required to obtain the correct Young modulus. This operation is described in Chapter 2 and amounts to transitioning from a Lagrangian (material coordinates) to an Eulerian (laboratory coordinates) description. In the present simple uniaxial configuration, it corresponds[110] to replacing the Young modulus in equation (3.2) by $\lambda^2 E$. Overall, the compressional velocity is

$$V_c(\lambda,\omega) = \left[\mathrm{Re}\left(\sqrt{\frac{\rho}{\lambda^2 E(\lambda,\omega)}}\right)\right]^{-1} \tag{3.7}$$

These predictions, plotted in the right part of figure 3.6, are quite good since they give the right trends, such as the evolution with frequency below 50 Hz, but also the evolution with stretch ratio. Overall, equation (3.7) effectively captures the small variations observed in the experimental points of figure 3.6, using simple physical arguments.

However, they are not as accurate as the 3D theoretical predictions. At $\lambda = 1$ the velocity starts decreasing for frequencies higher than 50 Hz, which is not supported by this approach. In fact, the wavelength becomes comparable to the strip width, and the one-dimensional model inevitably fails. At this point, the full 3D model is needed to understand the velocity of this mode at higher frequencies. Actually, this is the edge mode previously mentioned and highlighted by the change of polarization of S_0' in figure 3.4.

1.2.3 Flexural mode

In a beam, flexural modes are the most studied. Here, we need to distinguish between the two types of bending that exist in a rectangular cross-section beam. Generally speaking, it's the bending in the thickness h (the smallest dimension) that is studied. But instead we have been looking at the bending in the width $b \gg h$ (the large dimension). Actually, the type of bending is not important. We will see that, for wavelengths large compared with (h, b), the applied tension controls identically their dispersion.

Unlike the compression dynamics, flexural dynamics displays a remarkable sensitivity to the application of a static stress. At 10 Hz, our measurements indicate that the velocity goes from 2 m/s at $\lambda = 1$ up to 7 m/s at $\lambda = 1.8$. Interestingly, the static stress triggers a bifurcation in the dispersion behaviour. For instance, as illustrated in figure 3.6, when $\lambda \approx 1$ (dark blue symbols), the flexural wave is highly dispersive. Its velocity grows from 0 m/s in the quasi-static limit to around 5 m/s at 100 Hz. In contrast, for $\lambda = 1.8$, the velocity becomes nearly independent of frequency *i.e.* the propagation is non-dispersive. This is characteristic of the transition from a flexural beam regime to a string-like regime, governed by the tension in the material. This was employed by Li et al. (2022)[75] to map stresses in thin films since this bifurcation also appears for the first anti-symmetric mode propagating in a plate.

This effect can be captured by getting back to the simple Euler-Bernoulli model [111]:

$$\frac{EI}{A}\frac{\partial^4 u_3}{\partial {x_1}^4} - \sigma\frac{\partial^2 u_3}{\partial {x_1}^2} + \rho\frac{\partial^2 u_3}{\partial t^2} = 0, \tag{3.8}$$

[110] Zhao and Chang (2021): "Elastic wave velocities in finitely pre-stretched soft fibers"
[75] Li et al. (2022): "Non-destructive mapping of stress and strain in soft thin films through sound waves"
[111] Doyle (1989): *Wave propagation in structures*

with σ the applied tension, $A = bh$ the strip cross-sectional area and $I = hb^3/12$ the second moment of area. Note that this moment corresponds to the bending in the plane (e_1, e_3), *i.e.* in the width, and is necessarily different from the one classically studied with bending in the thickness ($I_{\text{classical}} = bh^3/12$). Assuming a propagative solution with wavenumber k, one obtains the following dispersion relation:

$$\frac{2EI}{A}k^2 = -\sigma \pm \sqrt{\sigma^2 + \frac{4EI}{A}\rho\omega^2}. \tag{3.9}$$

From this expression, it is possible to identify a non-dimensional parameter $\gamma = A\sigma^2/4\rho EI\omega^2$ which measures the competition between tension and bending, and evidences the existence of the two aforementioned regimes. When the strip is not stretched, $\sigma = 0$ and γ cancels. The phase velocity of flexural waves reads

$$V_f\left(\lambda = 1, \omega\right) = \sqrt{\omega}\left[\frac{EI}{\rho A}\right]^{\frac{1}{4}}. \tag{3.10}$$

The $\sqrt{\omega}$ dependence is the signature of a strongly dispersive regime, depicted by the dark blue line in figure 3.6. It corresponds to the quadratic dispersion of the A_0' mode, described in equation (1.28). Obviously, this velocity should saturate at some point; otherwise these waves would become infinitely fast. This highlights a limitation of the Euler-Bernoulli model, which becomes invalid at higher frequencies because it assumes that the displacement should remain purely transverse. This is all the more apparent in figure 3.6, where the dark blue line of the 1D model rapidly deviates from experimental measurements as frequency increases. Besides, just like in the previous section, the question arises of which expression one should consider regarding the Young modulus E. Similarly, including the complex rheology of equation (3.3) yields to a more quantitative expression of the velocity.

As the tension σ is increased with λ varying from 1.1 to 1.8, the non-dimensional parameter γ grows from 0.1 to 8, and a change of the strip behavior is reached. Now, the flexion is completely governed by the tension, and the velocity simply writes:

$$V_f\left(\lambda, \omega\right) = \sqrt{\sigma/\rho} \tag{3.11}$$

This dispersion is intimately linked with the wave speed in a string[112], which is given by $\sqrt{\frac{T}{\rho_L}}$ with T the tension in the string, and ρ_L its linear density. In such a string, the wave is actually a flexural wave, and $T = \sigma \times A$ with A the deformed cross-section area, and $\rho_L = \rho \times A$. The velocity of this wave in a string finally rewrites $\sqrt{\frac{\sigma}{\rho}}$. This expression reflects the relatively non-dispersive dynamics observed in the low-frequency regime, but above all it reflects the increase of the velocity with λ in the limit $\omega \to 0$.

Finally, if we are not in one of these two regimes ($\gamma = 0$ or $\gamma \gg 1$), then we need to calculate the phase velocity $V_f(\lambda, \omega)$ starting from equation (3.9) replacing σ and E using equation (3.1) and (3.4). Predictions are then plotted in figure 3.6. Our conclusions are the same when we solve the problem outside asymptotic regimes. Predictions are quite good in the string-like regime at low frequencies, but quickly fail with an increasing frequency.

1.2.4 Limits of one-dimensional models

These 1D models provides an efficient picture of the strip behaviour in the low frequency regime. When the frequency increases, the wavelength decreases and they inevitably fail because these 1D models of flexion and compression do not take into account the finite size of the strip. Lastly, they

[112] Melde (1860): "Ueber die Erregung stehender Wellen eines fadenförmigen Körpers"

do not offer the possibility to clearly evidence the respective roles of rheology and stretching, which happens to be crucial here.

Finally, let's take a look at this interdependence. In Chapter 2, we build a Cauchy stress tensor with an additional dynamic term:

$$\boldsymbol{\sigma}_{\text{dynamic}} = \mu_0 \tau^n \left[2\left(1-\beta'\right)\mathbf{D} + \beta'\left(\mathbf{B}\cdot\mathbf{D} + \mathbf{D}\cdot\mathbf{B}\right)\right] \tag{3.12}$$

It features a dependence on both λ (in tensor $\mathbf{B}$) and ω (in tensor $\mathbf{D}$), and underscores the interdependence between these two variables. In fact, variable separation would be possible only if the second coefficient β' canceled. Instead, for our elastomer, a value of $\beta' = 0.29$ was determined in Chapter 2. To the best of our knowledge, this interdependence is not physically explained yet, but simply originates from a general representation[98,99]. It remains to be established whether this independence is a strong assumption or not.

To validate our 3D theory, we imagine another configuration where the strip has fixed lateral edges and is subjected to a planar tension, quite different from the uniaxial tension we have just studied.

1.3 Validating the approach by studying the case of a strip with fixed edges

This alternative configuration, wherein a soft strip is clamped at its lateral edges, also supports the existence of a Dirac cone (see figure 1.22) and fundamental modes are no longer solutions (the clamping process suppresses rigid body motions). By adjusting the distance between the clamps, we are able to induce a transverse stretch as illustrated in figure 3.1(c) and 3.7. Indeed, it allows to implement other boundary conditions and predeformation (transverse tension), and thus to validate our approach.

Measured dispersion curves are presented in figure 3.7. Once again, the theory effectively renders the experimental data. While the slopes remain nearly unchanged, cut-off frequencies decrease with λ, which is quite different from the case of the free strip in figure 3.3. It is still experimentally difficult to measure the Dirac cone for the A_2' branch in a deformed strip, as noticeable in figure 3.7.

Globally, note that all tendencies are covered anyway by our semi-analytical method and small discrepancies mainly appear at high stretch ratios, as in the case of the free strip. In this configuration, which corresponds to a planar stress, we obtain that the first and second non-zero cut-off frequencies gradually diverge as the stretching increases, as pictured by the dashed line in figure 3.8. As a result, we anticipate a clear disruption of the Dirac cone, contrary to what we discussed about the free strip. The linear crossing, which is its signature, occurs in the initial state (blue symbols), but splits in two separate branches as λ increases (yellow symbols). This trend is apparent in the experimental curve and becomes more evident in the theoretical plots. Again, more details are presented in Appendix A about this Dirac cone in a fixed strip. Notably, the influence of viscoelasticity and prestress are discussed.

Again, we display the theoretical dispersion curves of in-plane guided elastic waves in fixed strip, but with a colormap rendering their polarization. Results are shown in figure 3.9. As aforementioned, cut-off frequencies become sufficiently different (see figure 3.8) so that the cone splits into two parts. The mixed polarization (orange) for the undeformed case gives rise to two different branches with clear orthogonal polarizations (yellow and red) for stretched cases.

One should again keep in mind that the wavenumber is complex and its imaginary part is omitted in this representation. See Appendix A to learn more about such a representation. One can notably see in Appendix A that a small loop exists in the imaginary plane and makes the transition between

[98] Antman (2004): *Nonlinear Problems of Elasticity*
[99] Destrade et al. (2009): "Small amplitude waves and stability for a pre-stressed viscoelastic solid"

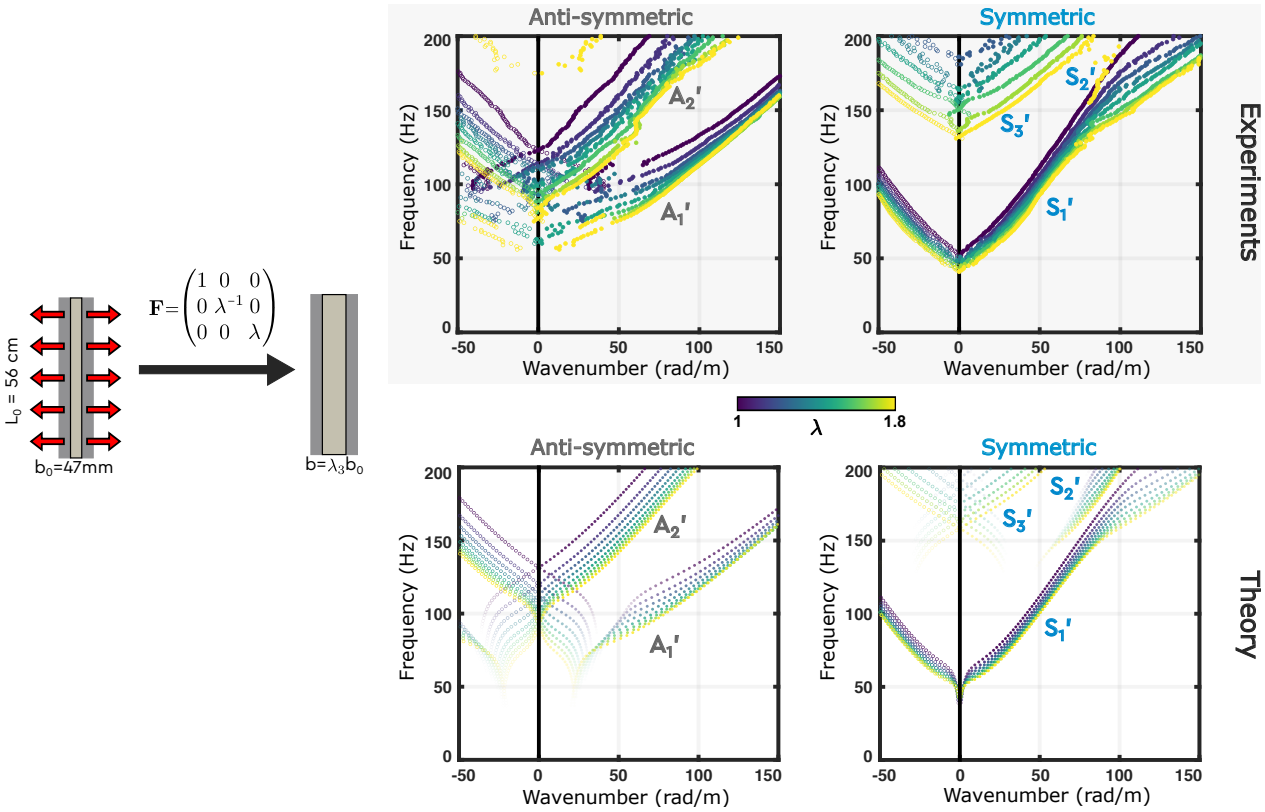

FIGURE 3.7: **Dispersion in a fixed strip subjected to a transverse stress** – The deformation gradient $\mathbf{F}$ and the geometry are recalled for a fixed strip subjected to a transverse and planar stress. Experimental dispersion curves of antisymmetric and symmetric modes in the elongated strip for several values of the stretch ratio $1 \leq \lambda \leq 1.8$ are shown in the top line. The theoretical predictions (bottom line) are obtained using SCM (see text).

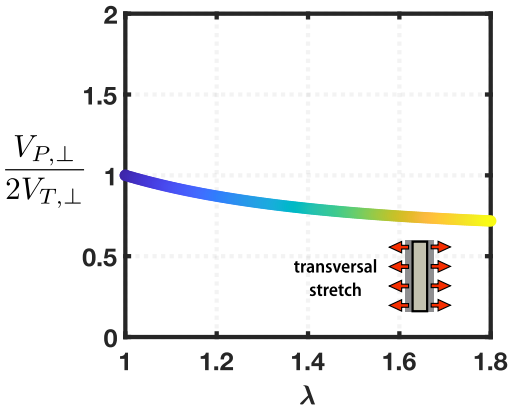

FIGURE 3.8: **Cut-off frequencies** – Evolution of the ratio $V_{P,\perp}/2V_{T,\perp}$ with the applied deformation in the case of a transverse and planar tension.

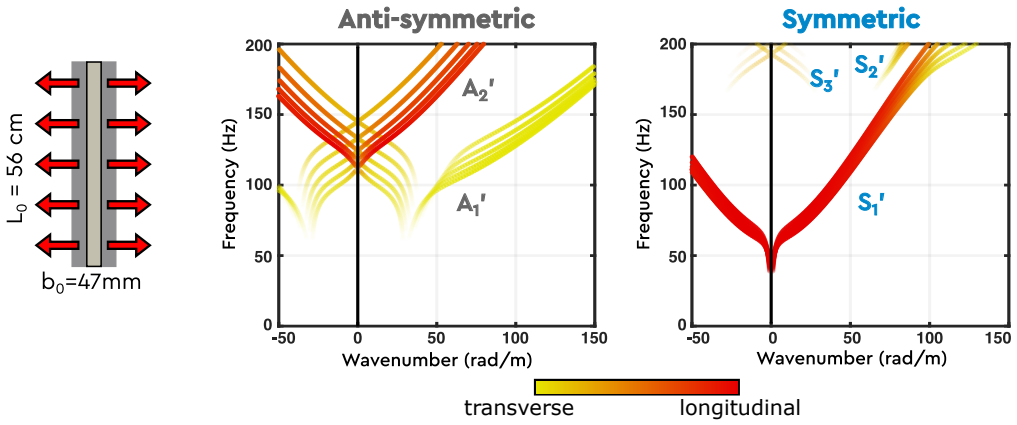

FIGURE 3.9: **Role of the polarization for a fixed strip** – Theoretical dispersion curves for the fixed strip subjected to a planar stress. The color indicates the dominant polarization (yellow = transverse, red = longitudinal).

the two modes at different cut-off frequencies. This loop increases in size as stretching is increased, confirming that the cone is indeed broken.

This configuration provides a demonstration that the three-dimensional model can readily be extended to various sets of boundary conditions and to different kinds of static deformations. Also, this illustrates how the application of an external static stretch serves as a mean to tailor the dispersion, and consequently, enables the tuning of the overall strip dynamics.

2 Introduction to elastography

We now have a good understanding of how prestress affects the dynamics of a soft strip, and we know that this is an important and common geometry in the human body. To study the elasticity and dynamics of these biological tissues, it is now common to use elastography, which measures the speed of elastic waves in the medium of interest. However, in view of what we have just discussed, we are entitled to wonder which velocities are measured using this technique. So, in the second part of this chapter, we will carry out measurements in a similar soft strip, and try to understand the measured velocities. But first, we describe the elastography.

2.1 What is elastography?

Elastography refers to a non-invasive medical imaging technique used to map the elasticity of tissues. To measure their elasticity, physicians have not always used elastography but rather a technique called palpation. The Ebers Papyrus (1500 BC) is the oldest medical writing mentioning palpation, notably methods of abdominal palpation to probe for the presence of abdominal masses. Since then, it has been used by several civilizations at different times, as illustrated in figure 3.10. This technique consists of manually deforming the tissue of interest, and analyzing the amount of force needed. The mechanical behavior of the tissue is therefore statically probed, in much the same way as a modern indentation test.

The four methods of clinical observation are inspection, palpation, auscultation and percussion[113]. Elastography is a contemporary equivalent of palpation and provides information on mechanical properties of tissues by measuring their deformation when subjected to external mechanical forces, such as compression or shear waves. This technique is particularly useful in the field of di-

[113] AVICENNA (1025): *The Canon of Medicine*

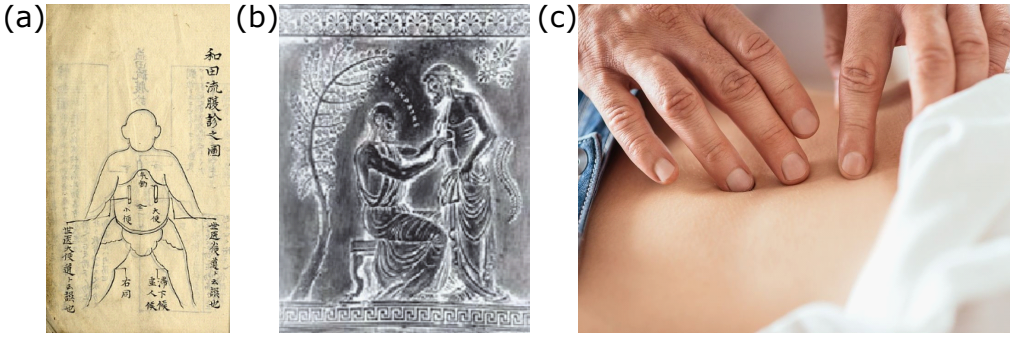

FIGURE 3.10: **Palpation** – Some illustrations of the palpation as a medical technique to statically probe the mechanical properties of tissues, at different times. (a) From "Doctor Murai Kinzan's teachings (alias Genshinkan, 1733-1815)" in Collection W. Michel (Fukuoka, Japon). (b) Liver hand palpation from SANDRIN et al. (2011)[135]. (c) From "L'importance de la palpation abdominale et des fascias au cœur de la formation techniques manuelles" in Formation Pole Thérapeutes.

agnostic imaging, as it can provide valuable information about the presence and severity of diseases such as liver fibrosis[114,19,115,21,116], breast lesions[117,118,119,120], prostate cancer[121], thyroid nodules[122], heart problems[123,124,125,126,127], tendinopathies[128,129,130] and other musculoskeletal disorders[131,132,133,134].

Elastography exploits either ultrasound imaging, magnetic resonance imaging (MRI) or optical coherence tomography (OCT) to record a movie from which the displacement can be extracted. For each imaging technique, several methods exist to measure the stiffness[136].

Ultrasound elastography – Ultrasound imaging, also known as sonography, is a non-invasive medical imaging technique using high-frequency pressure waves (propagating at the longitudinal velocity V_L in solids) to create real-time detailed images of the internal structures of the body. During an ultrasound exam, a transducer (or ultrasound probe array) emits sound waves that

[114] SANDRIN et al. (2002): "Shear modulus imaging with 2-D transient elastography"
[19] SANDRIN et al. (2003): "Transient elastography: a new noninvasive method for assessment of hepatic fibrosis"
[115] ASBACH et al. (2010): "Viscoelasticity-based Staging of Hepatic Fibrosis with Multifrequency MR Elastography"
[21] DEFFIEUX et al. (2015): "Investigating liver stiffness and viscosity for fibrosis, steatosis and activity staging using shear wave elastography"
[116] KENNEDY et al. (2018): "Quantitative Elastography Methods in Liver Disease: Current Evidence and Future Directions"
[117] BERCOFF et al. (2003): "In vivo breast tumor detection using transient elastography"
[118] SINKUS et al. (2005): "Viscoelastic shear properties of in vivo breast lesions measured by MR elastography"
[119] BARR and ZHANG (2012): "Effects of Precompression on Elasticity Imaging of the Breast"
[120] BARR (2019): "Future of breast elastography"
[121] CORREAS et al. (2013): "Ultrasound elastography of the prostate: State of the art"
[122] CANTISANI et al. (2015): "Strain US Elastography for the Characterization of Thyroid Nodules: Advantages and Limitation"
[123] ELGETI and SACK (2014): "Magnetic Resonance Elastography of the Heart"
[124] SINKUS (2014): "Elasticity of the Heart, Problems and Potentials"
[125] HANSEN et al. (2015): "Shear wave elastography for lipid content detection in transverse arterial cross-sections"
[126] KHAN et al. (2018): "Cardiovascular magnetic resonance elastography: A review"
[127] PRUIJSSEN et al. (2020): "Vascular Shear Wave Elastography in Atherosclerotic Arteries: A Systematic Review"
[128] PRADO-COSTA et al. (2018): "Ultrasound elastography: compression elastography and shear-wave elastography in the assessment of tendon injury"
[129] FARRON et al. (2009): "Measurement of Tendon Strain During Muscle Twitch Contractions Using Ultrasound Elastography"
[130] MIFSUD et al. (2023): "Elastography in the assessment of the Achilles tendon: a systematic review of measurement properties"
[131] WINN et al. (2016): "Sonoelastography in the musculoskeletal system: Current role and future directions"
[132] PALUCH et al. (2016): "Use of Ultrasound Elastography in the Assessment of the Musculoskeletal System"
[133] TALJANOVIC et al. (2017): "Shear-Wave Elastography: Basic Physics and Musculoskeletal Applications"
[134] DAVIS et al. (2019): "Clinical utilization of shear wave elastography in the musculoskeletal system"
[136] ORMACHEA and PARKER (2020): "Elastography imaging: the 30 year perspective"

bounce off organs and tissues, and the returning echoes are captured and processed to generate images.

This imaging technique, used in this work, finds many clinical applications and is the most widespread as a basis for elastography[137,138,139]. There is a wide choice of different methods for deforming the medium. This can be done statically or dynamically, locally or globally, directly using ultrasound or with any other physical object. In particular, acoustic radiation force methods have proved particularly effective to probe elasticity in real-time and in-depth, as detailed by Doherty et al. (2013)[140]. In figure 3.11, different types of ultrasound elastography using an acoustic radiation force to deform the tissue of interest are presented.

In this work, we use supersonic shear imaging (SSI), a technique that originated in our laboratory almost 20 years ago[141,142]. SSI is an ultrasound shear-elastography method where shear waves are generated using an acoustic radiation force[140]. This acoustic radiation force, also referred to as a *push*, is repeated at different depths in the tissue at a velocity which is greater than the generated shear waves. This first justifies the *supersonic* feature, and second allows the generation of plane shear waves in the tissue to be imaged. In this work, the Aixplorer^{TM} system is used. It is not the most recent commercialized system but it supports a "research" mode which allows access to the raw data acquired by the ultrasound probe array. The induced displacement is assessed and the propagation velocity of plane shear waves V_T is measured. In an incompressible material, it is well known that the Young modulus can be deduced from this velocity using the simple relation $E = 3\rho {V_T}^2$.

Before discussing this simple hypothesis, let us first briefly describe other ways to realize elastography experiments.

Optical Coherence Elastography – During the last decade, great progress has also been made in optical coherence elastography (OCE) as detailed in the recent reviews[143,144], and find noteworthy applications in ophthalmology[145,146]. It is based on Optical Coherence Tomography (OCT), which is a non-invasive medical imaging technique that uses light waves to create high-resolution, cross-sectional images of transparent biological tissues. It roughly works by measuring the reflections of a light beam, and using the time delay of these reflections to create micrometer-scale images of tissue structures. It can approximately be described as the optical equivalent to medical ultrasound. Then, to probe the elasticity of these tissues, an external mechanical force is applied and the deformation is extracted by comparing images. A schematic drawing of a typical optical setup is represented in figure 3.12(a). There, it is a Spectral Domain OCT where a source with a wide frequency spectrum is used in order to simultaneously generate images at different depths. But many other optical setup exist, as well as many ways to apply an external mechanical force. Each combination is chosen based on the typical size and timescale studied, as illustrated in figure 3.12(a)

[137] Gennisson et al. (2013): "Ultrasound elastography: principles and techniques"
[138] Shiina (2014): "Ultrasound elastography: Development of novel technologies and standardization"
[139] Sigrist et al. (2017): "Ultrasound Elastography: Review of Techniques and Clinical Applications"
[140] Doherty et al. (2013): "Acoustic radiation force elasticity imaging in diagnostic ultrasound"
[141] Bercoff et al. (2004): "Supersonic shear imaging: a new technique for soft tissue elasticity mapping"
[142] Deffieux (2008): "Palpation par force de radiation ultrasonore et échographie ultrarapide : Applications à la caractérisation tissulaire in vivo"
[140] Doherty et al. (2013): "Acoustic radiation force elasticity imaging in diagnostic ultrasound"
[143] Zvietcovich and Larin (2022): "Wave-based optical coherence elastography: the 10-year perspective"
[144] Leartprapun and Adie (2023): "Recent advances in optical elastography and emerging opportunities in the basic sciences and translational medicine [Invited]"
[145] Kirby et al. (2017): "Optical coherence elastography in ophthalmology"
[146] Lan et al. (2023): "In vivo corneal elastography: A topical review of challenges and opportunities"

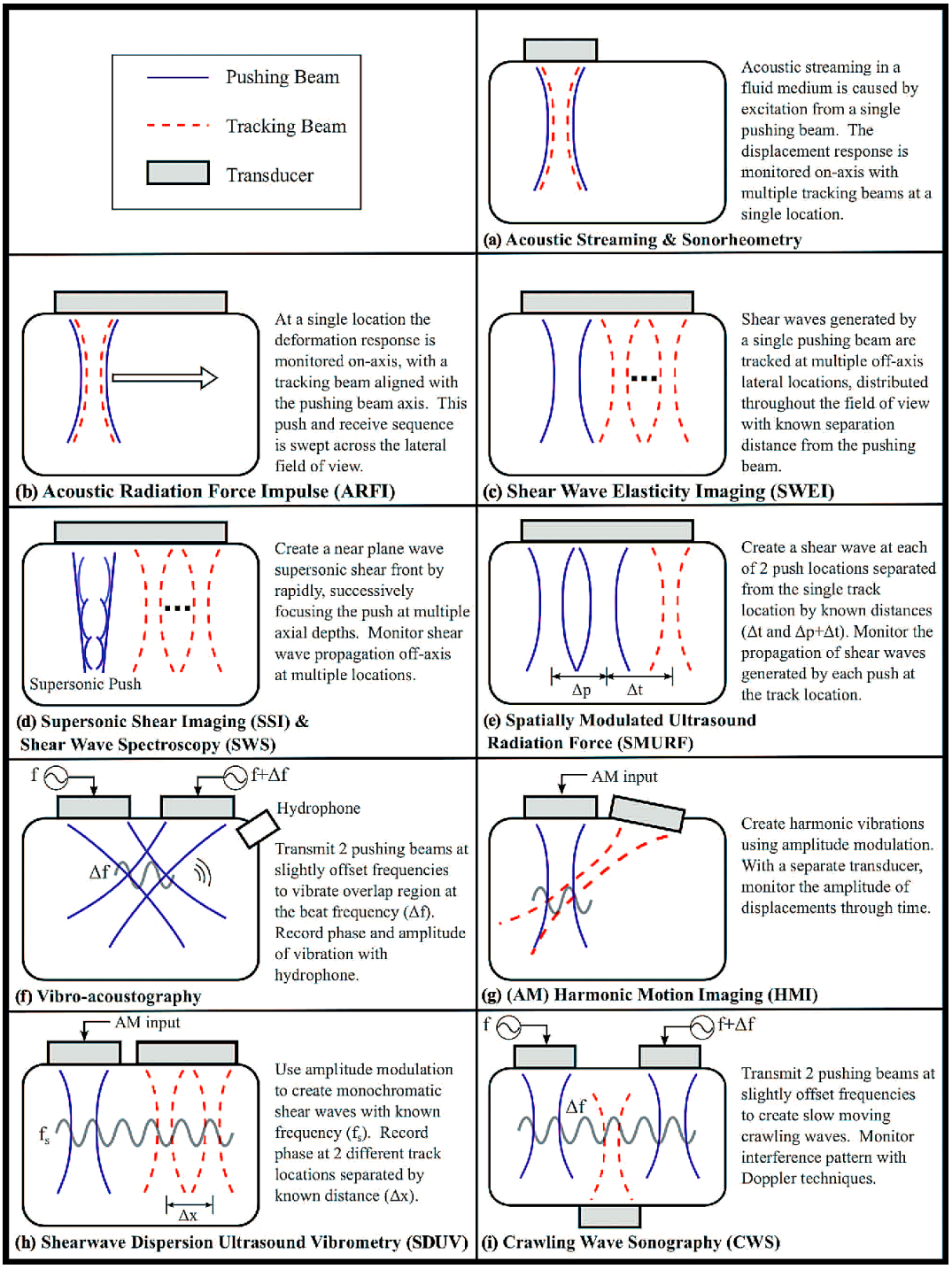

FIGURE 3.11: **Ultrasound Elastography** – Different types of ultrasound elastography using an acoustic radiation force to deform the tissue under study.
Adapted from DOHERTY et al. (2013)[140].

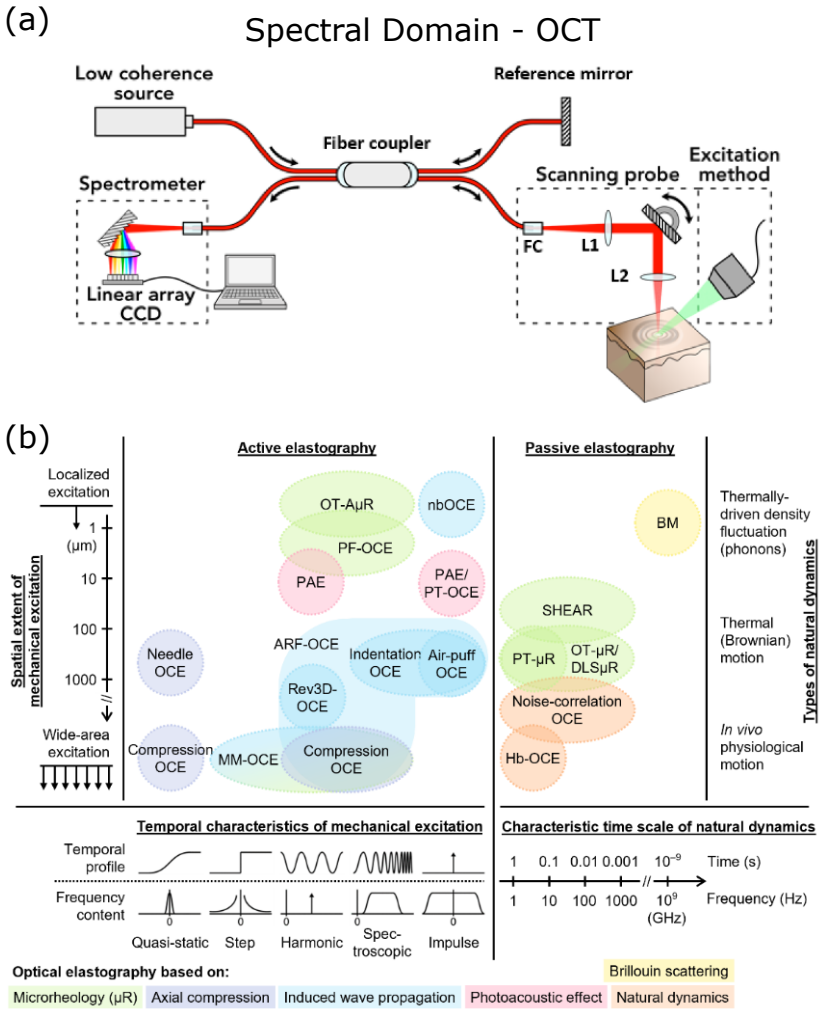

FIGURE 3.12: **Optical Coherence Elastography (OCE)** – (a) Typical experimental setup for the Spectral Domain Optical Coherence Tomography imaging technique, with an additional external mechanical excitation. (b) Range of techniques used in OCE to map elasticity of biological tissues. *Adapted from* ZVIETCOVICH and LARIN (2022)[143] *and from* LEARTPRAPUN and ADIE (2023)[144].

Magnetic Resonance Elastography – Similarly, magnetic resonance elastography (MRE) has proved its worth [147,148] and likewise finds clinical applications in large tissues[136] such as breast[118], heart [123,126,149] and brain[150]. It is much less common since Magnetic Resonance Imaging (MRI) instruments are rarer, more expensive and the image acquisition time is important. Just like UE or OCE, MRE involves the application of mechanical vibrations to the body, and MRI technology to capture images of how these vibrations deform tissues.

[147] LOW et al. (2016): "General review of magnetic resonance elastography"
[148] SACK (2023): "Magnetic resonance elastography from fundamental soft-tissue mechanics to diagnostic imaging"
[136] ORMACHEA and PARKER (2020): "Elastography imaging: the 30 year perspective"
[118] SINKUS et al. (2005): "Viscoelastic shear properties of in vivo breast lesions measured by MR elastography"
[123] ELGETI and SACK (2014): "Magnetic Resonance Elastography of the Heart"
[126] KHAN et al. (2018): "Cardiovascular magnetic resonance elastography: A review"
[149] MARLEVI et al. (2020): "Combined spatiotemporal and frequency-dependent shear wave elastography enables detection of vulnerable carotid plaques as validated by MRI"
[150] HISCOX et al. (2016): "Magnetic resonance elastography (MRE) of the human brain: technique, findings and clinical applications"

2.2 Current limitations in quantitative elastography

Let us return to the hypothesis that states the Young modulus verify $E = 3\rho {V_T}^2$, with V_T the measured velocity and ρ the material density, which is assumed to be 1000 kg/m^3 in practice. Actually, this equation only holds under certain strong assumptions that are rarely valid, thus limiting the robustness of quantitative elastography. These limitations can be attributed to four different causes. First, the viscoelasticity of a tissue lead to frequency-dependent mechanical parameters, including the deduced Young modulus[124,151,147,150,116]. Second, tissues like muscles are inherently anisotropic and V_T strongly depend on the propagation direction[128,130]. Third, most tissues have boundaries and act as waveguides for shear waves, leading to strong dispersion[145,126,152,153]. Last, surrounding fluids or other external factors may apply a prestress in the tissue of interest, again leading to changes in the measured velocity[123,125,122,154,120].

Besides, it is common that biological tissues combine several of the above-mentioned aspects as highlighted in several reviews involving different imaging modalities[139,155,136,156,157,134,143,144,146]. These limits have been known for some time and are still the subject of active research.

Viscoelasticity is the most tackled issue[115,20,58,107,21,158,159,63] and the waveguiding geometry is also widely studied, in particular for clinical applications involving arterial and myocardium walls[104]

[124] Sinkus (2014): "Elasticity of the Heart, Problems and Potentials"
[151] Kennedy et al. (2014): "A Review of Optical Coherence Elastography: Fundamentals, Techniques and Prospects"
[147] Low et al. (2016): "General review of magnetic resonance elastography"
[150] Hiscox et al. (2016): "Magnetic resonance elastography (MRE) of the human brain: technique, findings and clinical applications"
[116] Kennedy et al. (2018): "Quantitative Elastography Methods in Liver Disease: Current Evidence and Future Directions"
[128] Prado-Costa et al. (2018): "Ultrasound elastography: compression elastography and shear-wave elastography in the assessment of tendon injury"
[130] Mifsud et al. (2023): "Elastography in the assessment of the Achilles tendon: a systematic review of measurement properties"
[145] Kirby et al. (2017): "Optical coherence elastography in ophthalmology"
[126] Khan et al. (2018): "Cardiovascular magnetic resonance elastography: A review"
[152] Pelivanov et al. (2019): "Does group velocity always reflect elastic modulus in shear wave elastography?"
[153] Ramier et al. (2019): "Measuring mechanical wave speed, dispersion, and viscoelastic modulus of the cornea using optical coherence elastography"
[123] Elgeti and Sack (2014): "Magnetic Resonance Elastography of the Heart"
[125] Hansen et al. (2015): "Shear wave elastography for lipid content detection in transverse arterial cross-sections"
[122] Cantisani et al. (2015): "Strain US Elastography for the Characterization of Thyroid Nodules: Advantages and Limitation"
[154] Li et al. (2017): "Guided waves in pre-stressed hyperelastic plates and tubes: Application to the ultrasound elastography of thin-walled soft materials"
[120] Barr (2019): "Future of breast elastography"
[139] Sigrist et al. (2017): "Ultrasound Elastography: Review of Techniques and Clinical Applications"
[155] Bilston (2018): "Soft tissue rheology and its implications for elastography: Challenges and opportunities"
[136] Ormachea and Parker (2020): "Elastography imaging: the 30 year perspective"
[156] Caenen et al. (2022): "Assessing cardiac stiffness using ultrasound shear wave elastography"
[157] Crutison et al. (2022): "The combined importance of finite dimensions, anisotropy, and pre-stress in acoustoelastography"
[134] Davis et al. (2019): "Clinical utilization of shear wave elastography in the musculoskeletal system"
[143] Zvietcovich and Larin (2022): "Wave-based optical coherence elastography: the 10-year perspective"
[144] Leartprapun and Adie (2023): "Recent advances in optical elastography and emerging opportunities in the basic sciences and translational medicine [Invited]"
[146] Lan et al. (2023): "In vivo corneal elastography: A topical review of challenges and opportunities"
[115] Asbach et al. (2010): "Viscoelasticity-based Staging of Hepatic Fibrosis with Multifrequency MR Elastography"
[20] Gennisson et al. (2010): "Viscoelastic and Anisotropic Mechanical Properties of in vivo Muscle Tissue Assessed by Supersonic Shear Imaging"
[58] Yasar et al. (2013): "Wideband MR elastography for viscoelasticity model identification"
[107] Brum et al. (2014): "In vivo evaluation of the elastic anisotropy of the human Achilles tendon using shear wave dispersion analysis"
[21] Deffieux et al. (2015): "Investigating liver stiffness and viscosity for fibrosis, steatosis and activity staging using shear wave elastography"
[158] Zampini et al. (2021): "Measuring viscoelastic parameters in Magnetic Resonance Elastography: a comparison at high and low magnetic field intensity"
[159] Jugé et al. (2023): "Ex vivo bovine liver nonlinear viscoelastic properties: MR elastography and rheological measurements"
[63] Sharma et al. (2023): "Characterizing Viscoelastic Polyvinyl Alcohol Phantoms for Ultrasound Elastography"

[,160,105,106,161,156]. Additionally, several works focus on guided waves in a viscoelastic medium[102,162].

However, the influence of prestress is still not very well understood. As can be guessed at this point, the retrieved stiffness depends on applied stresses[163,27,157], since elastic wave velocities change with prestress. It is also worth mentioning recent experimental works by Zhang et al. (2023)[97], who use a customized ultrasound sequence focusing consecutive pushes along a horizontal line (in addition to vertical in SSI) to map stresses in a prestressed soft material by measuring changes in velocities along two directions. While the geometry, anisotropy and prestress are treated, the viscoelasticity is not accounted for.

A comprehensive review by Li and Cao (2017)[164] describes theoretically each of these aforementioned limits and how they arise in elastography. A particularly interesting aspect is the treatment of acoustoelasticity in intrinsically anisotropic media.

Here, using a simple silicone strip immersed in water and simple ultrasound sequence, we suggest solutions to overcome the issues raised by viscoelasticity, waveguide geometry and prestress. Some anisotropy is naturally considered since prestress leads to extrinsic anisotropy for the propagation of shear waves in soft media, as shown in Chapter 2.

3 Elastography experiments

Given the former chapters on guided elastic waves in a strip, we now well understand the role of geometry, viscoelasticity and prestress. Earlier in this chapter, we saw that SCM allows us to quantitatively predict the dispersion curves of guided waves in such a strip. Then it is straightforward to compare elastography measurements with theoretical predictions.

Elastography experiments are first described, and by applying large deformations to the viscoelastic strip in different orientations, we obtain a wide range of phase velocities. Firstly, the generated shear waves are fully explained. Then, we build predictions for their dispersion curves. Finally, we also capture the change of velocities with stretching. Our work thus tackles the main above-mentioned limitations, and we hope that our method is a step towards quantitative elastography.

3.1 Experimental setup

A simple silicone strip, really similar to the one studied earlier in this chapter, is positioned in a water tank and used as a waveguide for the elastic waves. We then place an ultrasound probe over the strip and look at the velocity map returned by the Aixplorer^{TM} ultrasound system. The experimental setup is illustrated in figure 3.13.

Here, we prepared a strip with thickness $h = 2.7$ mm, width $b = 4$ cm and length $L_0 = 60$ cm. This time, it is made of Ecoflex-0020 which is softer than Ecoflex-0030 previously used. Whatever

[104] Couade et al. (2010): "Quantitative assessment of arterial wall biomechanical properties using shear wave imaging"
[160] Caenen et al. (2015): "A versatile and experimentally validated finite element model to assess the accuracy of shear wave elastography in a bounded viscoelastic medium"
[105] Astaneh et al. (2017): "Arterial waveguide model for shear wave elastography: implementation and in vitro validation"
[106] Maksuti et al. (2017): "Influence of wall thickness and diameter on arterial shear wave elastography: a phantom and finite element study"
[161] Marais et al. (2019): "Arterial Stiffness Assessment by Shear Wave Elastography and Ultrafast Pulse Wave Imaging: Comparison with Reference Techniques in Normotensives and Hypertensives"
[156] Caenen et al. (2022): "Assessing cardiac stiffness using ultrasound shear wave elastography"
[102] Nenadic et al. (2011): "Lamb wave dispersion ultrasound vibrometry (LDUV) method for quantifying mechanical properties of viscoelastic solids"
[162] Thu-Mai Nguyen et al. (2011): "Assessment of viscous and elastic properties of sub-wavelength layered soft tissues using shear wave spectroscopy: Theoretical framework and in vitro experimental validation"
[163] Catheline et al. (2003): "Measurement of elastic nonlinearity of soft solid with transient elastography"
[27] Gennisson et al. (2007): "Acoustoelasticity in soft solids: Assessment of the nonlinear shear modulus with the acoustic

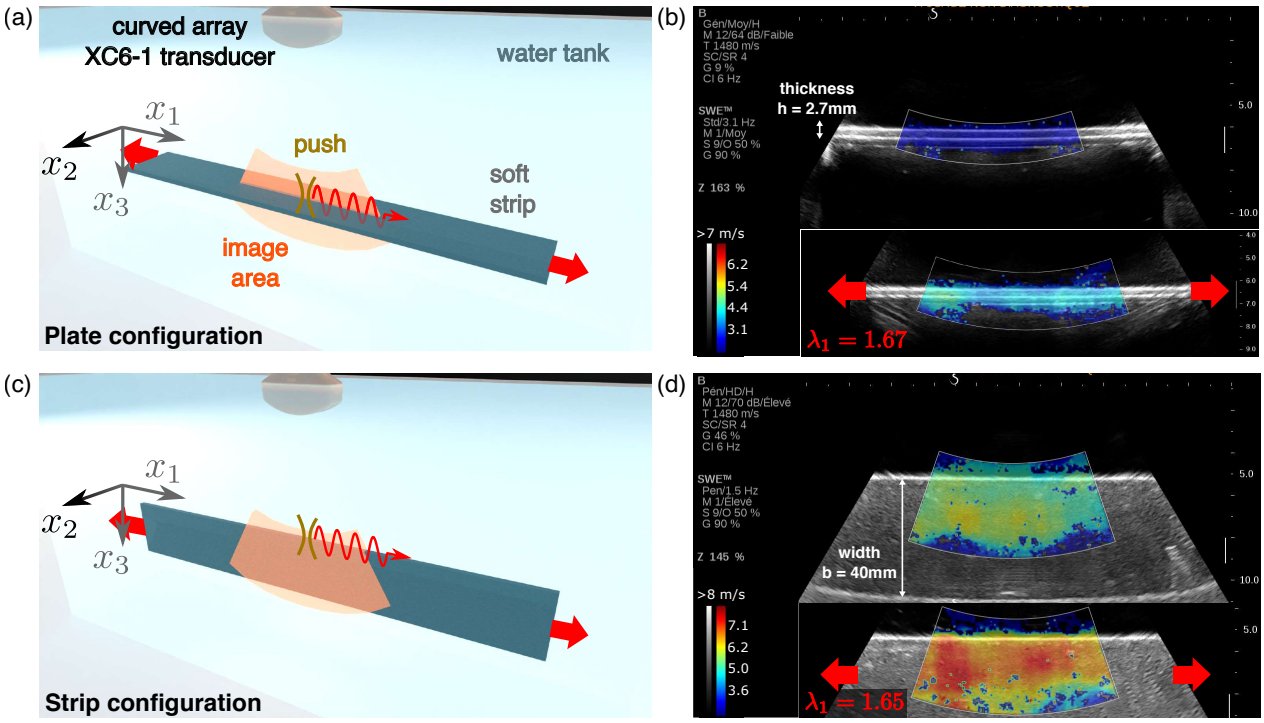

FIGURE 3.13: **Elastic waves are guided in two different orientations** — Using the Supersonic Shear Imaging technique, shear waves are generated in an Ecoflex-0020 strip in two different orientations. In the plate orientation (respectively strip), the imaging plane (x_1, x_3) cuts the strip along its thickness (a) (resp. along its width (c)). Typical results from the Aixplorer^{TM} are shown in (b) (resp. (d)) for an undeformed strip. The B-mode image is represented with a grayscale while the map of velocities is rendered using a colormap. The results for a stretched strip are in the corresponding inset.

the Ecoflex series (0005 to 0050), silicone is often used to prepare phantoms for ultrasonic imaging since it is soft just enough to mimic biological tissues (Young modulus of ~ 50 kPa) and is preferred to agar gels for practical reasons (e.g. it doesn't age). As seen in Chapter 2, its properties are well known, both statically thanks to tensile tests (figure 2.5), and dynamically thanks to rheological measurements (figure 1.19).

Elastography experiments are performed using an Aixplorer Multiwave ultrasound system and a curved array XC6-1 transducer from Supersonic Imaging. A default SSI ultrasound sequence is used with 5 push lines, each composed of 4 push depths. After each push line, the transducer switches to the imaging mode (framerate of 1,750 frames per second) to follow in real-time the generated shear wave[141,142].

The strip can be placed and studied in two different orientations as described in figure 3.13. In both cases, the transducer array is parallel to the strip axis x_1 and each push line generates a displacement along x_3. In the plate (respectively strip) orientation depicted in figure 3.13(a) (resp. 3.13(c)), the imaging plane cuts the strip along its thickness (resp. width), as seen in the

radiation force"

[157] CRUTISON et al. (2022): "The combined importance of finite dimensions, anisotropy, and pre-stress in acoustoelastography"

[97] ZHANG et al. (2023): "Noninvasive measurement of local stress inside soft materials with programmed shear waves"

[164] LI and CAO (2017): "Mechanics of ultrasound elastography"

[141] BERCOFF et al. (2004): "Supersonic shear imaging: a new technique for soft tissue elasticity mapping"

[142] DEFFIEUX (2008): "Palpation par force de radiation ultrasonore et échographie ultrarapide : Applications à la caractérisation tissulaire in vivo"

grayscale B-mode image in figure 3.13(b) (resp. 3.13(d)) and an out-of-plane (resp. in-plane) displacement is generated.

At this point, we may already guess which type of waves and which velocity is going to be measured, but here we are taking a more naive approach and trying to imagine that we do not really know the sample *a priori*.

Turning on the shear wave velocity measurement, the scanner provides the velocity of the measured shear waves within the strip. They are displayed as a color code in figure 3.13(b) and (d). Surprisingly, the measured velocities in these are different. In the plate orientation, a velocity of ~ 3 m/s is measured, while in the strip, it is a velocity of $\lesssim 5$ m/s. Also, none of these two values correspond to the bulk shear velocity of the same elastomer that would be around 5.3 m/s. This comes from the fact that the strip acts as a waveguide and not as the bulk material. This is a first illustration of the fact that the velocity alone might no be a sufficient parameter to retrieve the stiffness of the considered material.

Now, the very same sample is submitted to a uniaxial stress along its length with an elongation of $\sim 65\%$. The shear wave measurements are repeated in the two orientations. The measured velocities are shown as insets in figure 3.13(b) and (d). Both of them have increased to reach ~ 4 m/s (respectively 6.5 m/s) for the plate (resp. strip) orientation. This is a second illustration of the limitation in the quantitativeness of elastography.

As a summary of this part, shear wave elastography measurements with a commercial scanner have given 4 different shear velocities for the same sample under different experimental conditions (orientation and initial stress). This is confusing for a medical application that was developed for bringing quantitative stiffness measurements. From a physics point of view, waveguiding and acoustoelasticity are the key ingredients to explain these deviations, and the objective of the next parts is to extract the material parameters out of these measurements.

3.2 Waveguiding and dispersion

Experiment – Let us first take a closer look at the measured displacements to extract the dispersion curves of the observed waves. This is the so-called shear-wave spectroscopy technique[165] that allows to capture the frequency dependence of wave velocities. Then, comparing them to our predictions, we are able to identify these waves, to plot their dispersion curves and, equally important, to understand how they are generated.

Again, the two orientations are investigated, but we now use the Aixplorer$^{\text{TM}}$ in research mode. Basically, it allows to extract the full beamformed sequence of images after the line of shear pushes is realized. The displacement field $u_3(x_1, x_3, t)$ is obtained by taking the phase of the correlation between 2 consecutive complex IQ images. Each sequence of images is acquired 5 times and the results are averaged in order to improve the signal-to-noise ratio.

For the plate orientation, the displacement is homogeneous along the thickness (direction x_3) so that we average it along the thickness and a mean displacement map $\overline{u_3}(x_1, t)$ is obtained for each push line. The result for the push in the middle of the scanned area is represented in figure 3.14(a).

For the strip orientation, the post-processing is slightly different since the displacement is not homogeneous anymore along x_3. There are several reasons for explaining this effect. In fact, the longitudinal velocity used for imaging was taken equal to those of water, that is to say 1480 m/s, but sound propagates at around 1000 m/s in our material. This implies two additional difficulties. Firstly, the $x_3 = ct$ axis is properly computed between the transducer and the first strip edge at $x_3 = -b/2$, but in the strip, this axis is wrongly estimated and the beamforming procedure is biased. This is indeed clear in figure 3.13(d) where the second edge (at $x_3 = +b/2$) appears curved at the bottom of the B-mode image. Secondly, the push focusing must also be degraded when going

[165] Deffieux et al. (2009): "Shear Wave Spectroscopy for In Vivo Quantification of Human Soft Tissues Visco-Elasticity"

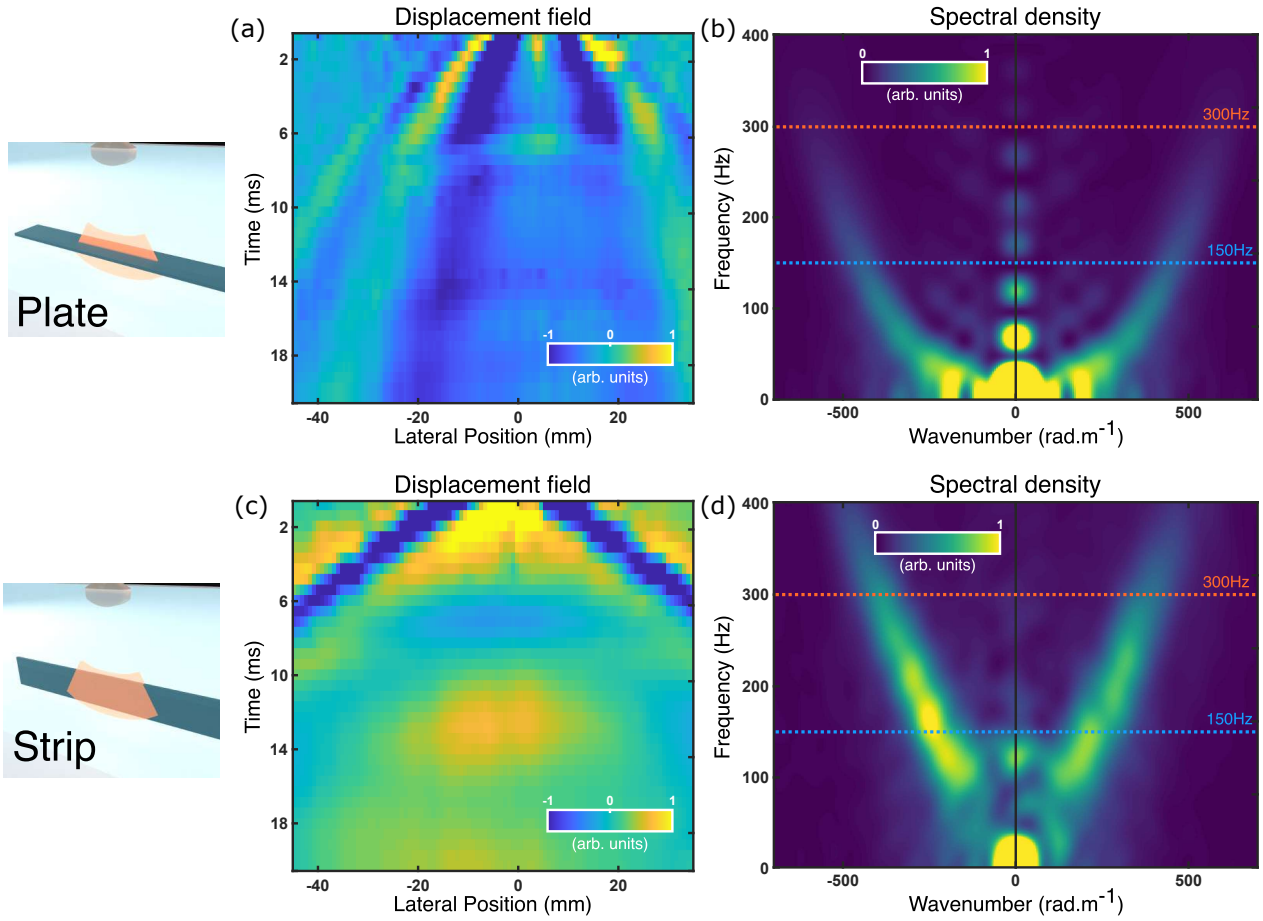

FIGURE 3.14: **Spectroscopy shear-wave elastography in both orientations** — For a given push, a displacement field is obtained and averaged over 4 or 5 consecutive acquisitions in the plate orientation (a) or in the strip orientation (c). The 2D spatio-temporal Fourier transform is applied to get the dispersion curves of guided elastic waves in the plate orientation (b) and in the strip orientation (d). They are summed over 5 different push locations.

deeper in the strip. In conclusion, only the top strip edge displacement can be studied in an unbiased manner. The spatio-temporal displacement map corresponding to this top edge displacement is thus represented in figure 3.14(c).

Both these maps evidence a localized displacement at the central position at time $t = 0$ (top line) which then travels symmetrically toward the left and right directions with increasing time t. The first comment when comparing the two spatio-temporal displacement maps is relatively obvious: the two orientations give different results. And, as a confirmation of the previously measured velocity, the shear wave reaches earlier the edges of the scanned area in the strip orientation compared to the plate one. A more trained observer can also discern additional phenomena. In the strip orientation, the wave follows a line as a signature of a non-dispersive propagation. Whereas in the plate orientation a more quadratic behaviour is observed. This dispersive behaviour can also be revealed by looking at the differences in the shape of the wavepacket for early times compared to the late ones; for example short wavelengths seem to travel faster than the long ones which have not reached the left edge of the presented image. As a last observation from these maps, we notice the existence of echoes at the abscissa of the push at respectively 8 ms and 13 ms for the plate and strip orientations.

Despite providing more insights on the discrepancy between these two orientations, we are still

in the observation stage and can only conclude that these two shear waves behave differently. More concretely, for an imaging application, we cannot yet retrieve the material elastic parameters.

In order to evidence the waveguiding phenomenon within the strip at the origin of these observations, we propose to extract some dispersion curves. By applying a spatial and temporal Fourier transform on the displacement maps, a frequency versus wavenumber map of the same data can be obtained. The magnitudes of such a representation are presented in figure 3.14(b) and (d). For the sake of completeness, because we performed several pushes at different positions along the x_1 axis, the presented maps are actually the summation of the normalized maps obtained for each of these 5 realizations. Therefore the presented results are not local but correspond to an average over the entire scanned area.

Again, the two maps exhibit different behaviours. Perhaps the most obvious is the shape of these curves. While the strip orientation gives a linear dispersion curve, the plate orientation rather provides a convex one. In accordance to observations in figure 3.14(a) and (b), this is another way of evidencing the dispersive nature of the propagation in this orientation: phase velocities are frequency dependent. Next, intensities are not equally distributed with the frequency in the two maps. In the plate orientation, intensities are high in the low-frequency range and fades rapidly as frequency increases, almost disappearing around 300 Hz. On the contrary, energy is found at higher frequencies in the strip orientation, with a maximal intensity around 150 Hz (putting aside the zero-frequency spot). Lastly, we also notice some spots for multiple frequencies on the $k = 0$ axis, in both orientations. These spots reflect the above mentioned echoes. Indeed, in a waveguide, those back-and-forth usually materialize as cut-off frequencies in the full dispersion diagram.

Theoretical predictions – To have a better insight on the propagation at play, we compare these results with theoretical predictions. To that end, let us use COMSOL Multiphysics to search for the dispersion curves of guided elastic waves in a strip immersed in water. We wish we could use the SCM but it does not yet allow the implementation of a fluid-coupling interface. A strip of thickness $h = 2.7$ mm and width $b = 4$ cm is considered with a density of 1.07 g/cm^3, a longitudinal velocity of 1000 m/s and a transverse velocity of 5.31 m/s. The relevant dispersion curves corresponding to the two orientations are presented in figure 3.15. In-plane (resp. out-of-plane) guided modes are represented in the $k < 0$ (resp. $k > 0$) region. They are very similar to those we saw in Chapter 1 in figure 1.14 and 1.15, but present some differences because of the coupling with water. This coupling is further discussed in Chapter 4. In the meantime, we provide a comparison in appendix B.

In the plate orientation, the dispersion curve that corresponds to the experimental one is displayed as a thick red line in figure 3.15. Its convex behaviour is a well known observation for a bending mode, and indeed, the mode displacements shown as insets for two different frequencies reveal such a flexural motion of the strip. This is in total agreement with the SSI scenario envisioned previously where the strip was pushed down and a flexural motion was imposed. Note that the effect of the strip's width begins to be felt since the displacement profile becomes progressively inhomogeneous around 100 Hz.

Alternatively, the pushes in the strip orientation generates in-plane displacements in the strip. Many modes can propagate in such a strip and comparing the theoretical dispersion curves with the experimental one, as well as their displacement profiles, we deduce that the generated mode is the first anti-symmetrical mode, or a combination of the first anti-symmetrical mode and the first symmetrical mode. The dispersion curve of this mode is plotted as a thick blue line in figure 3.15 with negative wavenumbers.

Again, the displacement profile of this mode at 10 and 300 Hz is compatible with an excitation at the top end of the strip. At 10 Hz, this mode is in fact dispersive since it is really similar to a bending of the strip, but this time in its width. This is the mode we referred to earlier in this chapter as A_0', the fundamental flexural mode, not to be confused with the flexural mode observed

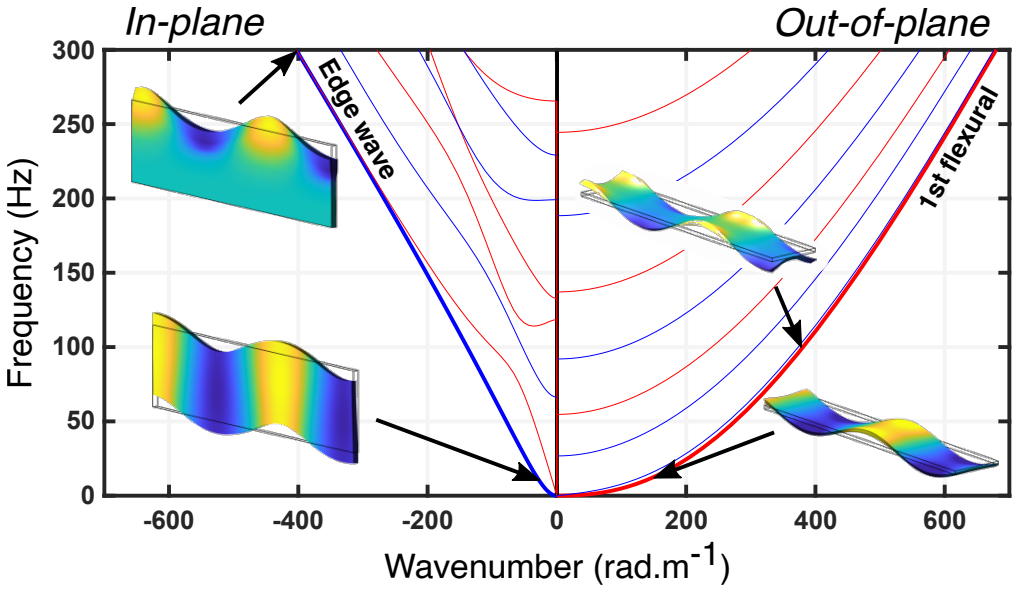

FIGURE 3.15: **Simplified dispersion diagram for a strip in water** — A purely elastic strip is considered with thickness $h = 2.7$ mm, width $b = 4$ cm and transverse velocity $V_T = 5.31$ m/s. Two dispersion curves from COMSOL are plotted, for the first out-of-plane (or flexural) mode for positive wavenumbers, and the first antisymmetric (with respect to the strip axis) in-plane mode for negative wavenumbers. Other dispersion curves are also plotted in thin lines and are there to recall that other modes exist, and to give the value of their cut-off frequency. Displacements u_3 are displayed for both modes at 10 Hz. The flexural mode is also displayed at 100 Hz where the effect of lateral boundaries begins to show, while the in-plane mode is displayed at 300 Hz where it has been summed with its symmetric counterpart to emphasize its edge wave nature. The strip axis is not to scale.

in the plate orientation, which corresponds to a flexural motion in the thickness. When increasing the frequency, the wavelength decreases and most of the mode's energy is now confined to the edge. Catching that most of the energy is present at frequencies greater than 100 Hz in the experiment, it is most likely an edge wave that propagates along the strip edge, with a fast amplitude decay along x_3 axis.

Regarding the echoes observed in figure 3.14(a) and (c) at $x_1 = 0$ and corresponding spots on the $k = 0$ axis in figure 3.14(b) and (d), such a simulation permits to attribute them to the cut-off frequencies of higher order modes. In fact, there is a last subtlety to mention. The first cut-off frequency in the in-plane mode diagram does not appear in figure 3.14(d). It corresponds to a shear wave propagating back-and-forth in the x_3 direction. However, the displacement generated is itself in the x_3 direction, so no such shear wave can be generated in our experiment. In contrast, the second cut-off frequency corresponds to a wave of longitudinal appearance (the S_0 mode propagating at V_P in a plate) and is generated precisely because it corresponds to a displacement and propagation in the x_3 direction.

Finally, there is one more aspect of the problem that needs to be addressed: the viscoelasticity. This has an effect on the dispersion curves shown in figure 3.15. Theoretically, the edge mode is not dispersive. However, by extracting the experimental phase velocity V_ϕ of this mode, we obtain 4 m/s at 150 Hz and 4.8 m/s at 300 Hz. There is of course small dispersion intrinsic to this mode, but the difference also originates from the viscoelasticity of the medium, *i.e.* its frequency dependent material properties. Here, we know it can be implemented using equation (3.3).

A difficulty then naturally arises, as COMSOL Multiphysics does not allow the use of frequency-

dependent parameters, so we can no longer search for dispersion curves using this method. To overcome this, we need to distinguish between the two orientations and solve two different problems. For the plate orientation, the dispersion of the first flexural mode in a strip is almost identical to the one in a plate (see Appendix B for details). This is easy to understand given equation (1.25) for $n = 0$. So we can solve the simpler problem of a plate immersed in water to calculate the dispersion of the first anti-symmetric mode. In fact, a SCM can also be used to calculate the dispersion curves of guided elastic waves in a plate, and unlike the case of the strip, the coupling with water can be added[166]. For the strip orientation, the problem is not easily solvable since a similar method for a strip immersed in water is not yet available. So we would like to use our method for a free strip *i.e.* not immersed in water. In such scenario which neglects the presence of water, the dispersion curves are slightly modified.

In order to quantify the error, we performed COMSOL simulations comparing the dispersion curves with/without water in the dispersive case (see Appendix B). The velocity is decreased bya factor of 1.15 when the coupling of water is added. Later we will thus increase wavenumbers by a factor of 1.15 for emulating the presence of water when computing the solutions in the absence of water. Note that this factor also appears when modelling surface waves at the interface between an incompressible elastic media and air or water[145,152,143]:

$$V_{\text{air/solid interface}}/V_{\text{water/solid interface}} = V_{\text{Rayleigh}}/V_{\text{Scholte}} = 1.13. \tag{3.13}$$

These two methods are used to build predictions for the phase velocities of the two modes of interest. Viscoelasticity is not a problem, but rather an asset that we can take advantage of, as it also seems possible to perform an inverse problem and recover the complex shear modulus $\mu(\omega)$ from the measurements. Please note that this is *a priori* not straightforward since the dispersion also originates from the waveguiding, especially for the flexural mode in the plate orientation, but this can still be overcome using the previously described methods.

In summary, this theoretical part has permitted to evidence the two guided modes that are excited in the plate and strip orientations. Their dispersion curves can be predicted for all frequencies. Overall, these results exhibit both the effect of the guiding geometry and the frequency dependence of the parameters. The measured phase velocity V_ϕ at 150 or 300 Hz would lead to different values for the Young modulus $E = 3\rho {V_\phi}^2$, as indicated in figure 3.16(c). But thanks to our theoretical modelling we can actually predict the right dispersion and recover better material characterization than by considering a bulk propagation.

3.3 Stretching and acoustoelastic effect

Knowing the nature of the generated waves and their dispersion curves, we now focus on the effect of a stretching of the strip. Here, we aim at showing that one can predict the shear wave propagation by knowing the material parameters, or reciprocally, measuring the same tissue under different loads provides more data and better characterization of the material.

Experiment – The idea is now to deform the strip before measuring the propagation of shear guided waves. Experimentally, we impose a new length to the strip by stretching its two extremities in the x_1 direction. The deformation is characterized in terms of the stretch ratios along the principal directions $(\lambda_1, \lambda_2, \lambda_3)$. Assuming an incompressible material and a uniaxial elongation along x_1, we again have $\lambda_2 = \lambda_3 = 1/\sqrt{\lambda_1}$. The same research mode on the ultrasound scanner is

[166] Kiefer et al. (2019): "Calculating the full leaky Lamb wave spectrum with exact fluid interaction"
[145] Kirby et al. (2017): "Optical coherence elastography in ophthalmology"
[152] Pelivanov et al. (2019): "Does group velocity always reflect elastic modulus in shear wave elastography?"
[143] Zvietcovich and Larin (2022): "Wave-based optical coherence elastography: the 10-year perspective"

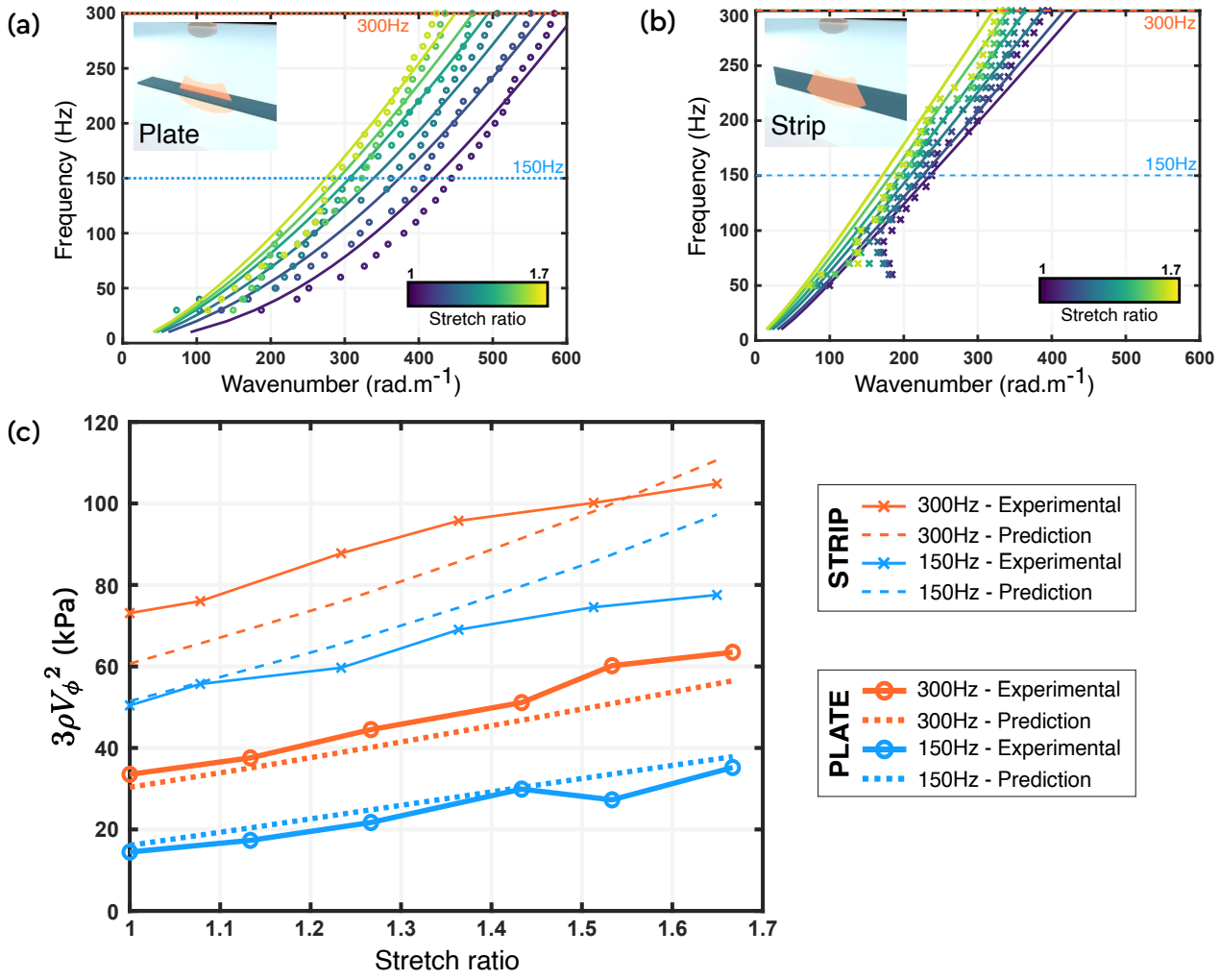

FIGURE 3.16: **Comparison of the measured dispersion curves for various stretch ratios** — For each stretch ratio, wavenumbers are extracted from the dispersion curve at certain frequencies and plotted as circles for the plate orientation (a) and squares for the strip orientation (b). Predictions are added with a full line and match both the dependence in frequency and stretching. Additionally, by looking for an appropriate Young modulus E, one should compute the quantity $3\rho {V_\phi}^2$. The multiple values, obtained with a single sample, range from 15 to 105 kPa.

used for tracking the shear wave propagation, and the experiment is repeated for several values of λ_1 ranging from 1 (undeformed) to 1.67 (insets of figure 3.13(b) and (d)). For each stretch ratio and each orientation of the strip, the spatio-temporal displacement maps are extracted again by correlation between two consecutive images. The spatio-temporal Fourier transform is applied to obtain the frequency versus wavenumber representation of the same data. Eventually, the maximum for each frequency is detected in order to draw a line plot of the extracted dispersion relation.

The results of all the treated experiments are condensed as symbols in figure 3.16(a) and for the plate orientation and 3.16(b) for the strip orientation. The color coding stands for the stretch ratio λ_1. The dark blue points correspond to the same data as in the previous section and in figure 3.14. Frequencies above 300 Hz are discarded since there is almost no signal above in the plate orientation and the same for frequencies below 50 Hz in the strip orientation.

In both scenarii, applying a static stress tends to increase the slopes of dispersion curves: the higher the stretching, the higher the frequency for a given wavenumber. Said differently, the velocity

of the wave guided along the stretched direction is increased. This is in agreement with our previous measurements in figure 3.3.

To better assess this evolution, the phase velocities V_ϕ are extracted at 150 and 300 Hz and the quantity $3\rho {V_\phi}^2$, homogeneous to a Young modulus, is plotted (symbols) as a function of the stretch ratio in figure 3.16(c). This plot now evidences a linear growth of the velocity with the stretch ratio, and the growths are similar for the two orientations. But the main point that comes out of this figure is that a large range of velocities are obtained for the same experimental sample. The standard technique that consists in defining the Young modulus directly from the measured velocity would lead to values varying from 15 to 105 kPa. One would easily recognize that it is not satisfying for a quantitative modality.

But because these observations make physical sense, the idea would be to take advantage of all these measurements to better characterize the medium under investigation. The corollary question is: are we able to quantitatively predict those curves?

Theory – On top of all the guiding phenomena discussed previously, one needs to incorporate the stretching to the theoretical model. This has already been done earlier in this chapter. The model developed in Chapter 2, and the resulting equivalent stiffness tensor, are reemployed. For the theoretical predictions presented in figure 3.16 the same tricks as in the previous section were used, *i.e.* solving the problem of a plate immersed in water to get the dispersion curve of the first flexural wave in a strip; and increasing wavenumbers by a factor of 1.15 to get the edge wave dispersion.

For all the predictions, we considered a strip of Ecoflex-0020, of thickness $h = 2.7$ mm and width $b = 4$ cm. We use rheological parameters $\mu_0 = 15$ kPa, $\tau = 1000$ µs and $n = 0.33$; and hyperelastic parameters $\alpha = 0.29$ and $\beta' = 0.29$. These parameters are chosen after manual adjustment of the dispersion curves by fixing the values for α and β' since they were already assessed for a plate made of this material and also showed good predictions in a strip. Note that the values are different from those used in figure 3.3 and 3.7, because the material is not Ecoflex-0030 but 0020.

Comparison – For the plate (respectively strip) orientation, predictions are depicted as full lines in figure 3.16(a) (resp. (b)) and thick dotted (resp. thin dashed) lines in figure 3.16(c). We can see that the predictions provided by our approach are very satisfactory in figure 3.16(a) and (b). Similarly, the increase in velocities with elongation are also well understood, whether in the plate or strip orientation, at an intermediate frequency of 150 Hz or at a higher frequency of 300 Hz. Just as surprisingly, their slopes are just as well predictable.

In the end, we see that with a simple strip, the elasticity of the medium can be quantified using Young moduli ranging from 15 to 105 kPa. This is a very wide range of values, and these experiments clearly highlight the limits to quantitativeness in elastography. But more importantly, we are able to fully explain this broad field of values.

Based on these few measurements, we can imagine the implementation of an inverse problem that would enable to probe both the rheological and hyperelastic parameters of the material under study. To go even further, ultrasound images can be used to monitor the evolution of the geometric parameters (h, b) with the prestress. These measurements should be carried out in conjunction with the evolution of cut-off frequencies, which also provide direct information on these geometric parameters.

Some differences still persist in figure 3.16. Firstly, and most obviously, this is because the exact problem is not solved in either orientations, errors in figure 3.16(b) are probably mainly due to the oversimplified modeling using the 1.15 factor. Secondly, errors can also be attributed to the non-linear material model since it has only been validated for Ecoflex-0030 and not for 0020, and also because the involved hyperelastic model remains a weakly non-linear elasticity model.

4 Conclusion

In this chapter, we first investigated the in-plane dynamics of stretched soft strips by monitoring the propagation of elastic waves within the strips. Our experiments, supported by a semi-analytical model, reveal that static stretching strongly impacts the dynamics of the strip. Interestingly, we observe that certain vibration modes seem nearly immune to the external stretching, while others display a high sensitivity. We find that this sensitivity is essentially governed by the displacement's polarization.

Everything can be well explained by incorporating both the rheology and the hyperelastic constitutive law of the material. Our method indeed solves the full 3D waveguiding phenomenon, but simple 1D models also improve the understanding of the effect of stretching on the in-plane compression and flexion of the strip.

Then, because in biological tissues and organic matter, flexible structures under tension play a pivotal role, we performed ultrasound elastography experiments to showcase their current limits for quantitative evaluation of stretched organs.

The influence of frequency, geometry and static deformation in elastography are thus captured using a single material and a simple experimental method. We show that neglecting these effects may lead to a wide range of incorrect Young moduli and provide solutions to the understanding of generated guided waves in SSI. The procedure used in this chapter can be adapted to other material models, including anisotropic ones, but also to any geometry with a rectangular cross-section. A generalization to other guiding geometry should also be performed. Besides, the inverse problem should be tackled in order to estimate both the hyperelastic and viscoelastic properties from the measured dispersion curves.

Appendix A: The effect of viscoelasticity and prestress on the Dirac cone and on the ZGV in free and fixed strips

Free strip – To better understand the effect of prestress on the Dirac cone in a free strip, we display in figure 3.17 the dispersion curves for in-plane guided elastic waves in 3 dimensions, *i.e.* with coordinates $(\mathrm{Re}\,(k)\,,\mathrm{Im}\,(k)\,,\omega)$. First, we consider the strip to be purely elastic. In practice, we calculate the equivalent stiffness tensor $\mathbf{C}^{\omega}$ and use only its real part for the SCM calculation. Again, symmetrical and anti-symmetrical modes are found with respect to the (e_1, e_3) plane. Of particular interest is to notice the saddle shape of the ZGV point. Below this point frequency, two evanescent modes exist, with a non-zero real part, and merge to give two propagative modes for higher frequencies. The Dirac cone is found in the $\mathrm{Im}\,(k) = 0$ plane.

We first look at the effect of viscoelasticity on these two unique physical features, zooming in on their region of existence at the bottom of figure 3.17. Three curves are found depending on the input tensor in the SCM: elastic $\mathrm{Re}\,(\mathbf{C}^{\omega})$, partially viscoelastic $\mathrm{Re}\,(\mathbf{C}^{\omega}) + \mathrm{i}\,\mathrm{Im}\,(\mathbf{C}^{\omega})\,/10$ or viscoelastic $\mathbf{C}^{\omega}$. On the left of figure 3.17 is the zoom on the Dirac cone. As expected, adding viscoelasticity globally increases the imaginary part of wavenumber solutions, including those around the Dirac cone, but does not significantly change their real parts. The Dirac cone is no longer two crossing lines but rather two straight lines with non-zero imaginary parts, as visible in the top view. The greater the viscoelasticity, the further the straight lines cross. For each branch, when decreasing the frequency, the branch needs to join the ZGV branch and its (absolute) imaginary part thus increases. Note that its imaginary part is not too important and this is why we could assess it experimentally in figure 3.3. Additionally, one can see that adding viscoelasticity also modifies the behaviour of the ZGV point. Actually, even a slight viscoelastic part makes it disappear, as visible on the right part of figure 3.17. Branches do not longer merge but avoid each other and this time, the real part is quite impacted. This also explains why it is so hard to measure it in figure 3.3: its imaginary part quickly increases when decreasing the frequency below the ZGV point frequency.

Globally, viscoelasticity breaks degeneracies in the dispersion diagram, whether it is a Dirac cone (linear crossing) or a ZGV point (saddle shape). The influence of prestress should also be thought out. To avoid overloading the display in figure 3.18, We zoom in on the Dirac cone, for several stretch ratio values ($1 \leq \lambda \leq 1.8$) indicated by the colorbar, for both a purely elastic material and a viscoelastic one.

When considering a uniaxial stress in a free strip, cut-off frequencies almost coincide, as indicated in figure 3.5. It appears quite convincingly in the left part of figure 3.18, where small purely imaginary loops appear between the two cut-off frequencies, since they are no longer strictly equal for $\lambda > 1$. Note that these loops remains very small, with a maximum imaginary part of 10 rad/m, compared to the imaginary part of branches around the Dirac cone in a viscoelastic material (20 rad/m in the top view of figure 3.17). As a result, when adding viscoelasticity, the induced additional imaginary contribution remain quite low and it seems that branches simply avoid each other a little more and that the Dirac cone still exist for $1 \leq \lambda \leq 1.8$. In fact, its imaginary part increases anyway, which is why it becomes difficult to measure it when the stretch ratio increases.

Fixed strip – Let us focus on the Dirac cone in a fixed strip. Here, we do not plot the full 3D dispersion diagram but directly zoom in on the Dirac cone and the ZGV in figure 3.19 for $\lambda = 1$ in a purely elastic material and a viscoelastic one. We recover what we have already seen at the end of Chapter 1. In the case of a fixed strip, given predictions in figure 3.8 for $\lambda = 1$ and given the analogy with Lamb's waves, one predicts a coincidence in cut-off frequencies, and thus the existence of a Dirac cone. The only expected difference is the symmetry of the modes at the origin of this Dirac cone. In the case of the free strip, these are symmetrical modes, whereas in the case of the fixed strip, they are anti-symmetrical ones. However, when solving the full 3D problem, it

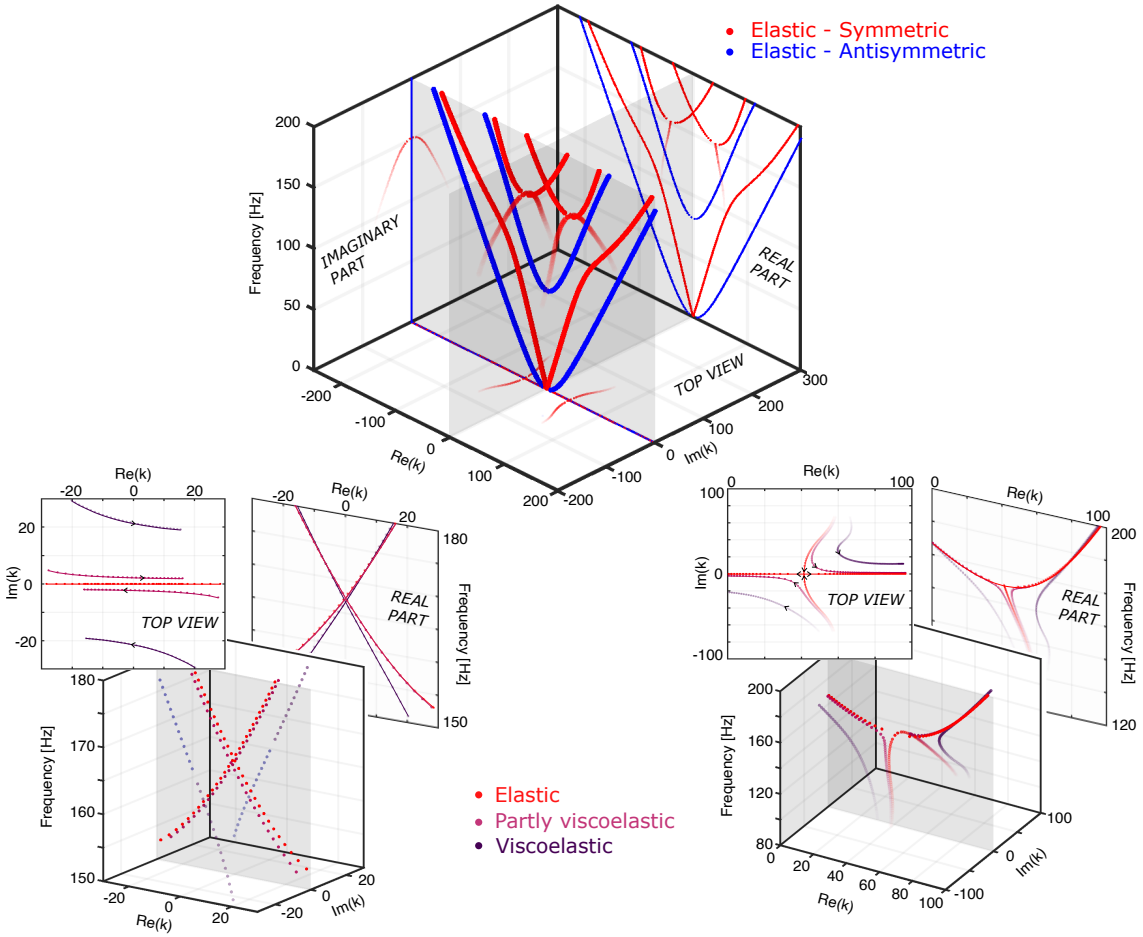

FIGURE 3.17: **Effect of viscoelasticity on Dirac cone and ZGV in a free strip** — Dispersion curves are represented in 3D with complex-valued wavenumbers (rad/m). Full dispersion curves of a purely elastic material are plotted (top). The Dirac cone (left) and ZGV (right) are degeneracies and are zoomed in to reveal the effect of the viscoelasticity.

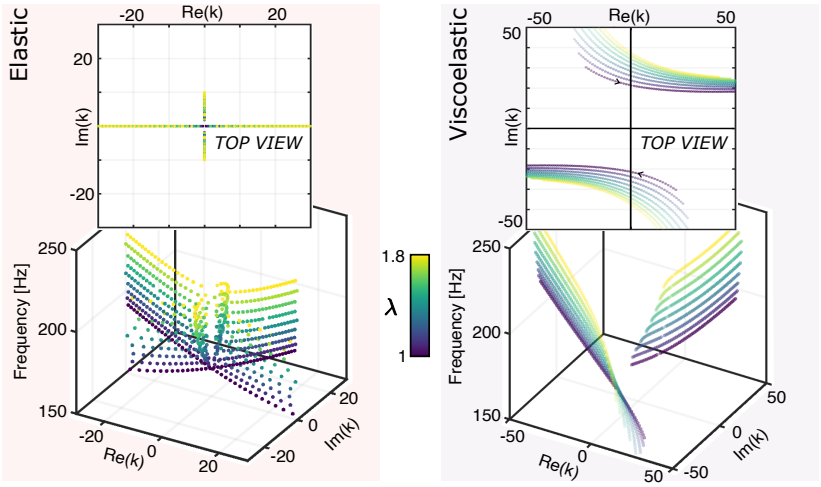

FIGURE 3.18: **Effect of prestress on the Dirac cone in a free strip** — We zoom in on the Dirac cone to reveal the mismatch in cut-off frequencies in a purely elastic material (left) with an increasing stretch ratio. On the contrary, in a viscoelastic material (right), the linear crossing still appears but branches are further apart in the top view.

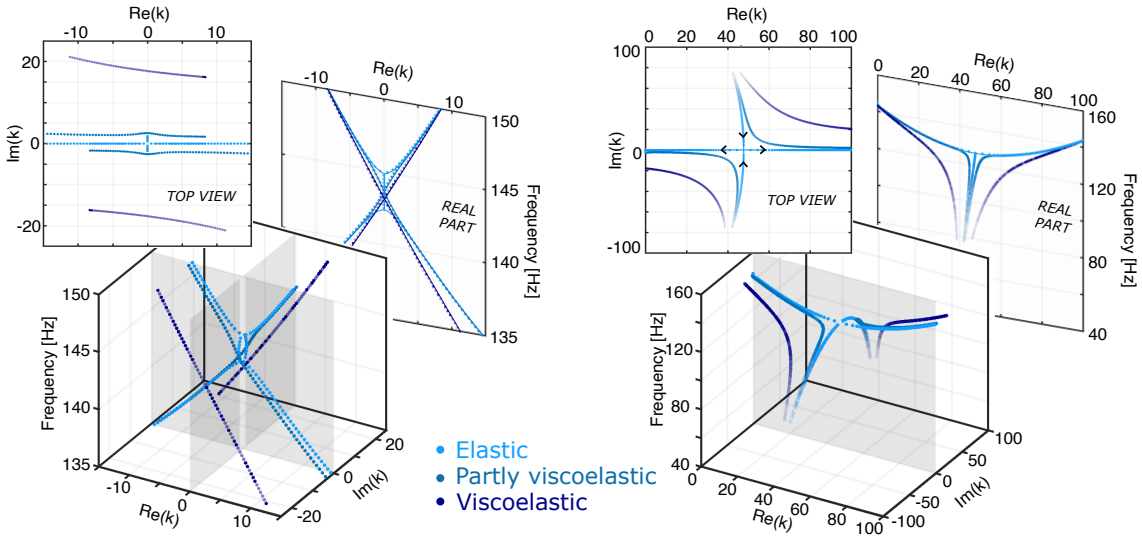

FIGURE 3.19: **Effect of viscoelasticity on Dirac cone and ZGV in a fixed strip** — Dispersion curves are represented in 3D with complex-valued wavenumbers (rad/m). The Dirac cone (left) and ZGV (right) are degeneracies and are zoomed in to reveal the effect of the viscoelasticity. The Dirac cone does not exist in a purely elastic material for $\lambda = 1$, but appears to exist in a viscoelastic material.

appears that, despite the coincidence in cut-off frequencies, the Dirac cone does not exist in a purely elastic material for $\lambda = 1$ and a small imaginary loop indeed exists, as illustrated in the left part of figure 3.19. When taking the viscoelasticity into account, this small imaginary loop is smoothed out and the Dirac cone appears again. This is particularly visible in the top view. For the ZGV point, the conclusions are the same as in the case of a free strip.

Again, the influence of prestress should also be thought out. We zoom in on the Dirac cone, for several stretch ratio values ($1 \leq \lambda \leq 1.8$) indicated by the colorbar, for both a purely elastic material and a viscoelastic one in figure 3.20.

When considering a planar tension in a fixed strip, cut-off frequencies gradually diverges when increasing the stretch ratio, as indicated in figure 3.8. It appears quite convincingly in the left part of figure 3.20, where the small initial imaginary loop for $\lambda = 1$ quickly expands to reveal frequency gaps of several tens of Hz. As a result, when adding viscoelasticity, even though the imaginary part of these branches were initially important for $\lambda = 1$, they still significantly rise in the top view in the right part of figure 3.20. The large frequency gap actually reveals when simply looking at the real part of these branches. This explains why the Dirac cone is measured experimentally only for very low stretch ratios.

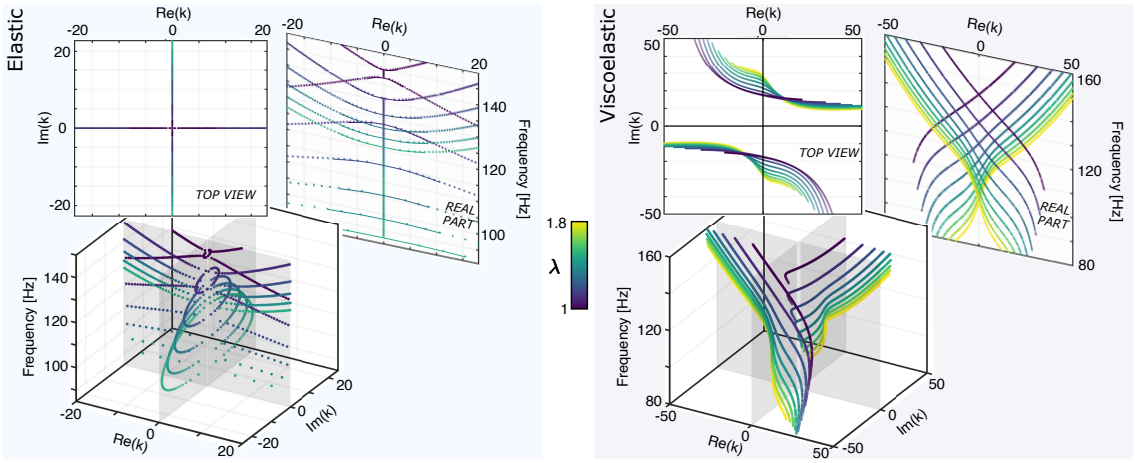

FIGURE 3.20: **Effect of prestress on the Dirac cone in a fixed strip** — We zoom in on the Dirac cone to reveal the increasing mismatch in cut-off frequencies with the stretch ratio in both a purely elastic material (left) and a viscoelastic material (right). Contrary to the case of a free strip, the linear crossing does not appear when only plotting its real part.

Appendix B: The influence of water on the dispersion curves of guided elastic waves in a free strip

We solve for the full dispersion diagram of a soft strip using eigenfrequency analysis from COMSOL finite-element software (figure 3.21). The strip has the same dimensions as previously, thickness $h = 2.7$ mm and width $b = 4$ cm. But it is not easy to take into account both the 3D geometry, the viscoelasticity and the prestress. In particular, when taking into account the viscoelasticity and the prestress using an equivalent elasticity tensor as described in Chapter 2, it becomes hard to implement adequate boundary conditions, and to solve for wavenumber k and not frequency. This leads us to perform simulations using a simple homogeneous, isotropic and purely elastic material with a transverse velocity $V_T = 5.31$ m/s.

In figure 3.21, dispersion curves of a strip in air or immersed in water are compared. The coupling with water has a significant effect on flexural modes that displace an additional quantity of water, adding inertia and lowering the dispersion curves (more details in Chapter 4). On the other side, the effect is less important on the in-plane guided modes but still remain important. Notably, the edge wave velocity is decreased by a factor of 1.15 for such a material.

Lastly, the dispersion curves of elastic guided waves in a plate are added. By looking at the first flexural mode that can propagate in a plate (black full line on the right part of figure 3.21), one notices that it coincides with the first flexural mode that can propagate in a strip. This remark is important because it allows us to only derive the plate problem when studying the generated wave in the plate orientation, but is not surprising in view of equation (1.25).

The coincidence of these two curves is not obvious. Indeed, for a strip in air, the curves do not overlap, and the flexural mode in a plate in air is above the one in a strip in air, by a factor of $2/\sqrt{3}$. But when the plate or the strip is in water, then the dispersion curves are very similar. In fact, if we zoomed in to the very low frequencies, we would notice a gap between the two curves, but this is not measurable in our experiments.

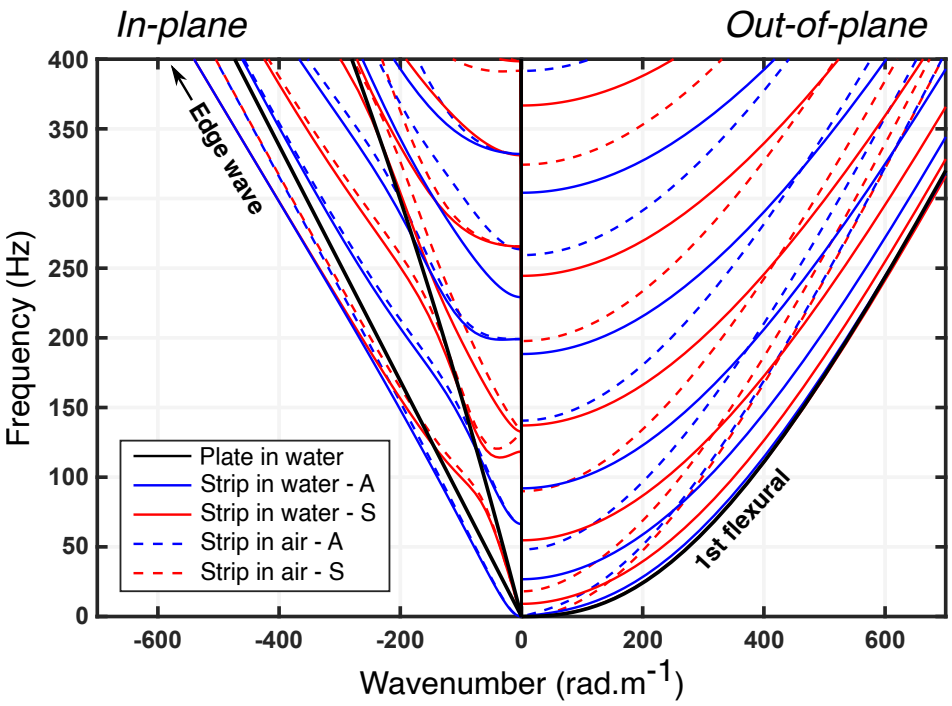

FIGURE 3.21: **Dispersion diagrams for a strip in air and water** — A purely elastic strip is considered with thickness $h = 2.7$ mm, width $b = 4$ cm and transverse velocity $V_T = 5.31$ m/s. Dispersion curves are split in two parts: out-of-plane modes polarized along the thickness axis, and in-plane modes polarized in the plane of the width and propagation axis. Two dispersion diagrams are superimposed: with (full lines) and without (dashed lines) coupling with water.

Chapter 4

Understanding the passive cochlear tonotopy

Objectives

In the cochlea, the organ responsible for the sense of hearing, a guided wave is supported by the strip-shaped basilar membrane. The *cochlear wave* is remarkable because its amplitude reaches a maximum at a position that depends on frequency; this is the so-called tonotopy. In this chapter, we study this tonotopy, alternating between finite element simulations and experiments with a fixed soft strip in a macroscopic model of the cochlea. We start from the problem of a plate immersed in water, right up to the complete waveguide found in the cochlea. We show that the group velocity of the fundamental mode of this waveguide indeed reaches a minimum at a characteristic frequency. This frequency decreases along the basilar membrane and depends on the local cross section of the membrane. The evolution of this local dispersion provides an explanation of the passive cochlear tonotopy, solely based on the physics of elastic waves in a strip. We perform a width gradient and a thickness gradient and show that they enable the observation of amplitude maxima at frequency-dependent positions. Finally, we discuss future experiments with this cochlea model, including the implementation of active elastomers.

- We provide an explanation for the passive cochlear tonotopy, starting from an immersed plate to the full waveguide
- The group velocity of the fundamental mode reaches a minimum at a characteristic frequency that depends on the waveguide cross-section
- A macroscopic model of the cochlea is built and measurements are performed either with a width or a thickness gradient
- Future research will focus in particular on the implementation of active polymers

Contents

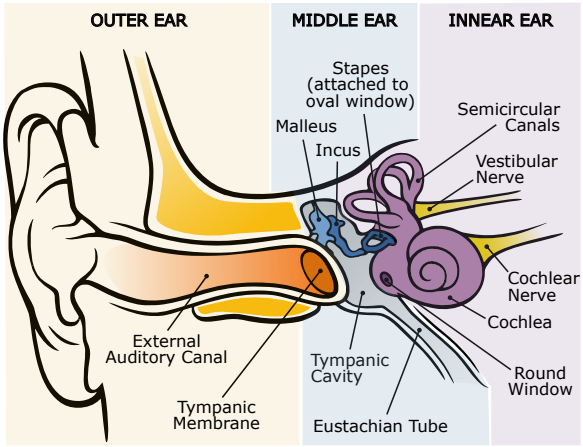

FIGURE 4.1: **General overview of the human ear** – The human ear can be divided into three parts. The outer ear consists of ridged cartilage and a canal leading to the eardrum (or tympanic membrane). The middle ear greatly amplifies sounds using lever effects with three small bones. The inner ear is made of two organs, the vestibular organ for balance, and the cochlea for hearing.
Adapted from CHITTKA and BROCKMANN (2005).

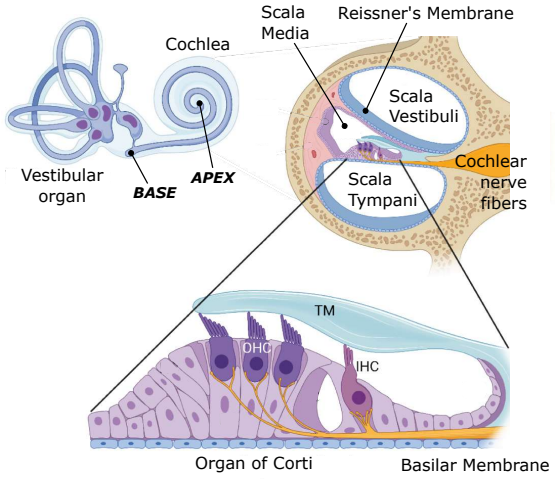

FIGURE 4.2: **Zoom on the human cochlea** – The human cochlea unfoils in a 3 cm-long chamber made of three fluid-filled compartments. The organ of Corti is the central structure for sensory transduction in the cochlea, and it relies on the basilar membrane. It is covered by the tectorial membrane (TM) and contains two types of sensory cells, inner hair cells (IHC) and outer hair cells (OHC).
Adapted from VLAJKOVIC and THORNE (2022).

1 Introduction

As mentioned before, soft elastomers share similarities with biological tissues. We have just described elastography experiments classically used to quantify the elasticity of tissues. In this chapter, we turn to another example on a smaller scale: the cochlea. This organ, present in humans but also in almost all animals, is responsible for the sense of hearing. This cochlea includes a soft strip-shaped membrane, a geometry that we have now mastered.

In this chapter, the presented modeling, simulation and experimental work were carried out jointly with two interns, Sacha GRENIER and Samuel CROQUETTE, during this PhD thesis.

1.1 The human ear

First, we start by giving a general overview of the full human ear. It is illustrated in figure 4.1. Its many functions can be divided into three parts, which are briefly described below.

Outer ear
The outer ear mainly consists of the auricle, ear canal and tympanic membrane (or eardrum). Sound waves are guided through the ear canal. The shape and length of the ear canal do contribute to a small sound amplification (in the frequency range of human speech). Additionally, auricles slightly alter sound waves and they help in sound localisation. When sound reaches the end of the canal, it causes the vibrations of the eardrum. This is a highly stretched membrane, *i.e* an organ of the human body that is subject to large prestresses, as described in the previous chapter, and it lies

between the outer ear and middle ear.

Middle ear
The middle ear is made of three very small ossicles: the malleus (or hammer), the incus (or anvil), and the stapes (or stirrup) which is the smallest bone in the body. When sound waves reach the eardrum, air pressure variations make the eardrum move back and forth, and the ossicles transmit this vibration to the oval window of the inner ear. Its role is to ensure an impedance matching between vibrations in the air and in the water in the inner ear, using different lever actions and area ratio. Without the middle ear, less than 1% of the sound pressure would get to the inner ear.

Inner ear
Finally, the inner ear has two very different functions, which are carried out by two different parts. Firstly, the vestibule organ is composed of three semicircular ducts. These semicircular canals are positioned at angles between each other that ensure dynamic balance of the body. Secondly, the snail-shaped organ in figure 4.1 is the cochlea and is responsible for the sense of hearing. In practice, it performs the so-called mechano-electrical transduction[108,169]. Let us take a closer look at how the cochlea works.

1.2 The cochlea

We uncoil the cochlear duct to identify its main compartments. The total curvilinear length of a human cochlea is around 30 mm, from the base (oval window) to the apex (center of the snail-shape). An enlargement on this organ is shown in figure 4.2.

Global structure
There are three main compartments, surrounded by a bony structure (osseous spiral lamina). Two of them are water-filled: the scala vestibuli and scala tympani. While these canals meet at the apex, the scala vestibuli is connected to the oval window (or stapes) and the scala tympani to the round window (see figure 4.1). Sandwiched between these two compartments, the organ of Corti rests on the basilar membrane. This basilar membrane is strip-shaped and the object of study of this chapter.

The Reissner's membrane also separates the scala vestibuli and the scala media. But its displacement does not serve a mechanical function[24]. That's why we forget about this membrane afterwards. However, it has another very important role in chemical processes, acting as a diffusion barrier for ions and enabling the organ of Corti to function properly.

When the stapes pushes the oval window, an overpressure is generated, water pushes on the basilar membrane and makes it bend. This deforms the organ of Corti, as explained next. But it also works the other way around: once the basilar membrane is deflected, it creates an overpressure on one side, and an underpressure on the other side. The basilar membrane deformation is thus intimately related to water pressure in both compartments. Moreover, the elasticity of the basilar membrane always pulls it back to its initial position.

Organ of Corti
The organ of Corti is detailed in figure 4.2. It is supported by the basilar membrane and is composed of a variety of cells[170]. Its function is to perform the mechano-electrical transduction *i.e.* to convert information carried by the mechanical deformation into an electrical signal, or action potentials.

[108] Robles and Ruggero (2001): "Mechanics of the mammalian cochlea"
[169] Martin (2014): "Physical principles of hearing"
[24] Reichenbach and Hudspeth (2014): "The physics of hearing: fluid mechanics and the active process of the inner ear"
[170] Lim (1986): "Functional structure of the organ of Corti: a review"

Table 4.1: Typical dimensions of the basilar membrane, the Scala Tympani (ST) and the Scala Vestibuli (SV) in a human cochlea.

	width (µm)	thickness (µm)	ST diameter (mm)	SV diameter (mm)
Base	100	75	1.2	1.1
Apex	500	25	0.6	0.7

Another membrane, quite different from the basilar membrane, is also attached to the osseous spiral lamina: the tectorial membrane. It rests on hair cells in the organ of Corti.

Second, hair cells are sensory cells which are connected to nerve fibers: they are central elements to the mechano-electrical transduction. In fact, the tectorial membrane rests on stereocilia, a specific part of the hair cell. The deflection of the stereocilia opens mechanically gated ion channels that allow potassium and calcium (positive ions) to enter the cell[169]. The release of neurotransmitters at the basal end of the cell finally occurs after other undetailed steps.

There are two types of hair cells: inner (IHC) and outer (OHC). Although they look very similar, they have different functions. While IHCs send a nerve signal which is then interpreted by the brain, OHCs are not directly responsible for the sense of hearing but rather act as a local acoustic amplifier thanks to their electromotility[171,172,173,174,175]. In this process, they increase the basilar and tectorial membranes displacements and therefore increase stereocilia deflection in the inner hair cells.

This electromotility is fascinating, but it is not the subject of this work. Instead, we focus on the behavior of elastic waves in the basilar membrane. Just as interestingly, similar hair cells are also found in the above-mentioned vestibular ducts and are responsible for the sense of balance.

Let us sum up how information travel through the ear. First, sound arrives in the form of pressure waves in the air. Then pressure waves are transformed into mechanical waves as the eardrum causes the ossicles to vibrate. These mechanical waves cause the oval window to vibrate, generating pressure waves again, but in water. These pressure waves are then coupled to elastic waves in the basilar membrane. These deflect IHC sterocilia in the organ of Corti, which generate an electrical signal that is finally interpreted by the brain.

The basilar membrane

Let us come back on the properties of the basilar membrane. For now, we have only considered a cross-section of the cochlea, but its properties actually vary from base to apex. An uncoiled representation of a simplified cochlea is presented in figure 4.3. In particular, one can notice how its width increases when progressing towards the apex. On the contrary, although not visible in this figure, its thickness decreases.

Many works are devoted to the imaging of the cochlea to access how its geometry evolves from the base to the apex[176,177,178]. Some orders of magnitude for its dimensions are given in Table 4.1. A remarkable characteristic is the evolution of the aspect ratio. The basilar membrane actually resembles a squared-shaped beam at the base, and a wide slender strip at the apex. One can already guess it behaves very differently at both locations.

[169] Martin (2014): "Physical principles of hearing"
[171] Ryan and Dallos (1975): "Effect of absence of cochlear outer hair cells on behavioural auditory threshold"
[172] Ashmore (1987): "A fast motile response in guinea-pig outer hair cells: the cellular basis of the cochlear amplifier."
[173] Ulfendahl and Flock (1998): "Outer Hair Cells Provide Active Tuning in the Organ of Corti"
[174] Ashmore (2008): "Cochlear Outer Hair Cell Motility"
[175] Dallos (2008): "Cochlear amplification, outer hair cells and prestin"
[176] Rau et al. (2006): "Visualizing soft tissue in the mammalian cochlea with coherent hard X-rays"
[177] Verbist et al. (2010): "Consensus panel on a cochlear coordinate system applicable in histological, physiological and radiological studies of the human cochlea"
[178] Rask-Andersen et al. (2012): "Human Cochlea: Anatomical Characteristics and their Relevance for Cochlear Implantation"

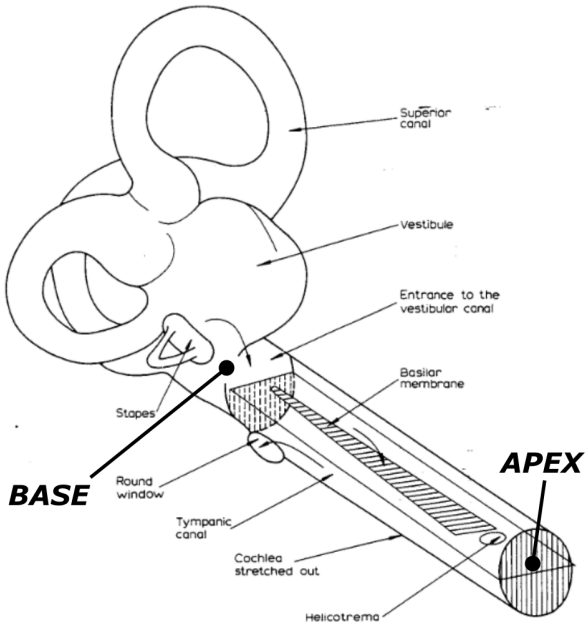

FIGURE 4.3: **Uncoiled cochlea** – The snail-shaped cochlear duct is uncoiled and a simplified basilar membrane is represented.
Adapted from the Nobel Prize Lecture of Georg von Békésy in 1961.

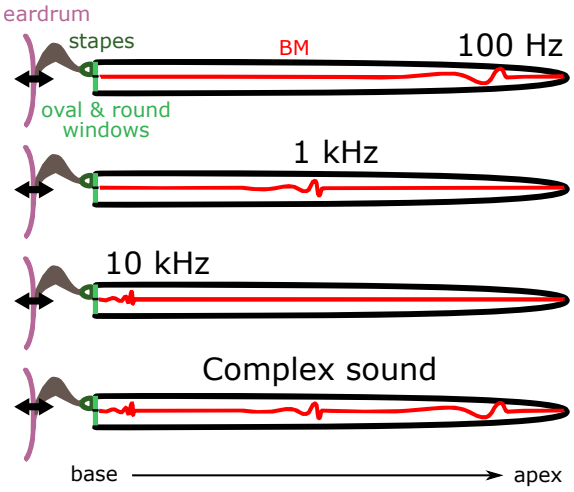

FIGURE 4.4: **Tonotopy** – The vibration of the basilar membrane reaches a maximum at a position depending on the input sound frequency. Low-frequency sounds propagate long distances towards the apex, while high frequencies rather remain close to the base.
Adapted from MARTIN (2014).

1.3 The tonotopy map

The cochlea is full of different gradients. We mentioned in Table 4.1 the most noticeable ones, but there surely are other gradients of mechanical properties of the Organ of Corti. These gradients are at the heart of tonotopy.

In fact, Evolution has selected these gradients because they serve a purpose: to discriminate input frequencies. For now, we just described how sound was reaching the cochlea and how electric signals were created. But the cochlea is made in such a way that a given frequency f will particularly deflect a given position x along the basilar membrane. Therefore, IHCs at this position x generate nerve impulses sent to the brain, which interprets these signals as a sign of the presence of f in the input sound. The basilar membrane acts as an acoustic spectrometer with a spatial discrimination of frequencies along the basilar membrane: this is what we call the tonotopy map. It is illustrated in figure 4.4.

High frequencies are not able to travel far and their corresponding positions are located near the base. On the contrary, low frequencies are able to reach the apex. In the light of these observations, the obvious question is: what is the link between the frequency f and the positions x where the deflection is maximum ?

GREENWOOD (1990)[179] reported several observations for the cochlear frequency-position mapping in different species and found a logarithmic distribution was a good matching, as presented in figure 4.5. From this distribution, we deduce that the higher the frequencies, the closer the

[179] GREENWOOD (1990): "A cochlear frequency-position function for several species—29 years later"

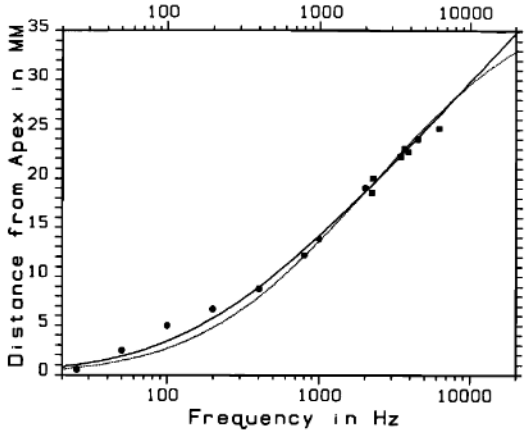

FIGURE 4.5: **Tonotopy from Greenwood** – For each frequency, the position of localisation along the cochlea is plotted and a model provides the full lines.
Adapted from GREENWOOD (1990).

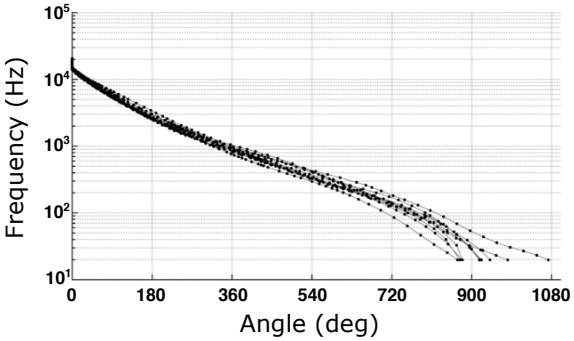

FIGURE 4.6: **Recent measurements for tonotopy** – The frequency is plot as a function of the position along the cochlea, which is itself coded by the angle of the coiled cochlear duct, for ten samples.
Adapted from HELPARD et al. (2021).

corresponding positions. With recent technical progress in imaging[180,181,182,183], it is now easier to make these type of measurements, and to measure patient-specific tonotopic maps. See an example in figure 4.6.

1.4 Modelling the cochlea

The original approach by Helmholtz

A theory initially introduced by Helmholtz[185] suggested that different regions of the basilar membrane act as resonators for tones of different frequency. More precisely, he modeled the basilar membrane as a series of strings whose natural frequencies are distributed over a wide frequency range, omitting water coupling. These strings are narrower and more tensed at the base (near the oval window) but wider and more flexible at the apex.

This theory persisted for almost a century before Békésy used more modern techniques to measure the vibrations of the basilar membrane in the cochlea of several mammals.

The Nobel Prize of Georg von Békésy in 1961

Békésy was awarded the Nobel Prize in Physiology or Medicine in 1961 "for his discoveries of the physical mechanism of stimulation within the cochlea". He developed innovative techniques to study the mechanical responses of the cochlea[186], such as the traveling wave theory[187].

This theory sets up a traveling wave along the basilar membrane, which always progresses from the base to the apex. The basilar membrane is assumed isotropic and to have neither longitudinal or transverse tension in the resting state. Its mains results are that the amplitude of this traveling

[180] ELFARNAWANY et al. (2017): "Micro-CT versus synchrotron radiation phase contrast imaging of human cochlea"
[181] LI et al. (2021): "Three-dimensional tonotopic mapping of the human cochlea based on synchrotron radiation phase-contrast imaging"
[182] SCHURZIG et al. (2021): "A cochlear scaling model for accurate anatomy evaluation and frequency allocation in cochlear implantation"
[183] BREITSPRECHER et al. (2022): "CT imaging-based approaches to cochlear duct length estimation—a human temporal bone study"
[185] HELMHOLTZ (1868): "Die Mechanik der Gehörknöchelchen und des Trommelfells"
[186] BÉKÉSY (1960): *Experiments in Hearing*
[187] BÉKÉSY (1956): "Current Status of Theories of Hearing"

wave reaches a maximum at a position that depends on the incident sound frequency, and that the wavelength shortens during propagation, particularly at this position. One of the systems he used for these demonstrations was that of pendulums coupled together.

A brief overview of the existing mathematical models

In the wake of these measurements by Békésy, there was a huge interest in trying to model mathematically the mechanics of the basilar membrane and the travelling wave. There are too many models to list here, and we simply provide a brief overview.

The simplest approach is to build a 1D model of a uniform beam in a viscous fluid by considering equation 3.8 and adding an external viscous force. Complexity can be added by taking a 2D model of a membrane in a fluid-filled channel. Starting from this 2D model, there has also been a lot of interest in models in which the cochlea acts as a transmission line that filters different frequencies and relies on the representation of the cochlea as a series of interconnected resonators[188,189]. Such models are also referred to as port-Hamiltonian systems. Finally, full 3D models of the cochlea were considered, like box-models, with a solid separating two fluid-filled chambers, and adding geometry gradients[190,191,192]. To avoid excessive computational costs in finite-element simulations, the Wentzel-Kramers-Brillouin (WKB) method was used[193,194]. This method is based on the assumption that the properties of the medium vary very slowly with position compared to phase of the traveling wave.

Numerous experiments were then carried out to provide a better understanding of the active phenomena taking place in the cochlea. Thus, new models[195,196] were developed to factor these properties in. Once again, there are several approaches to successfully model and predict the experimental measurements. To name just two, the active system can be described using, at each position, oscillators that operate at their critical point[197,198,169]. The other approach consists in considering the electromotility of OHC[199,200,174,201] as mentioned above. Recently, some efforts have been made to review the advances in cochlea modeling[202,24] and range from simple passive models to complete models that take the active properties of cochlea into account.

We are not biologists, but we have acquired some expertise in guided waves in membranes and strip, as shown in the first chapters of this thesis. Our idea is to find out if we can add something to the many fluid mechanics models that already exist. In the rest of this chapter, we focus on the deformation of the basilar membrane, a clamped strip separating two water compartments. We study the vibrations of such a strip when it is in air, in water, and then when it separates two water-filled chambers, as in the cochlea.

[188] Zweig et al. (1976): "The cochlear compromise"
[189] Neely (1981): "Finite difference solution of a two-dimensional mathematical model of the cochlea"
[190] Inselberg (1978): "Cochlear Dynamics: The Evolution of a Mathematical Model"
[191] De Boer (1981): "Short waves in three-dimensional cochlea models: Solution for a 'block' model"
[192] Vetešník and Nobili (2006): "The approximate scaling law of the cochlea box model"
[193] Steele and Taber (1979): "Comparison of WKB calculations and experimental results for three-dimensional cochlear models"
[194] Lim and Steele (2002): "A three-dimensional nonlinear active cochlear model analyzed by the WKB-numeric method"
[195] Lighthill (1991): "Biomechanics of Hearing Sensitivity"
[196] Allen and Neely (1992): "Micromechanical Models of the Cochlea"
[197] Duke and Jülicher (2003): "Active Traveling Wave in the Cochlea"
[198] Hudspeth et al. (2010): "A Critique of the Critical Cochlea: Hopf—a Bifurcation—Is Better Than None"
[169] Martin (2014): "Physical principles of hearing"
[199] Kolston and Ashmore (1996): "Finite element micromechanical modeling of the cochlea in three dimensions"
[200] Nobili et al. (1998): "How well do we understand the cochlea?"
[174] Ashmore (2008): "Cochlear Outer Hair Cell Motility"
[201] Ni and Elliott (2018): "Modelling three-dimensional cochlear micromechanics within the guinea pig organ of Corti"
[202] Olson et al. (2012): "Von Békésy and cochlear mechanics"
[24] Reichenbach and Hudspeth (2014): "The physics of hearing: fluid mechanics and the active process of the inner ear"

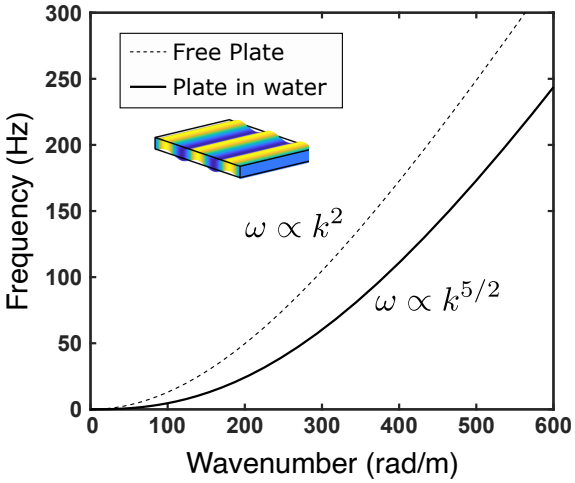

FIGURE 4.7: **Theoretical dispersion curves of A_0 in an immersed plate** – Assuming a purely elastic plate of thickness $h = 2.7$ mm, density 1.07 g/cm^3, longitudinal velocity 1000 m/s and transverse velocity 5.31 m/s, we plot the dispersion curve of the A_0 mode which is mainly flexural. The plate is either free (dashed lines) or immersed in water (full lines) with density 1 g/cm^3 and sound wave velocity 1500 m/s.

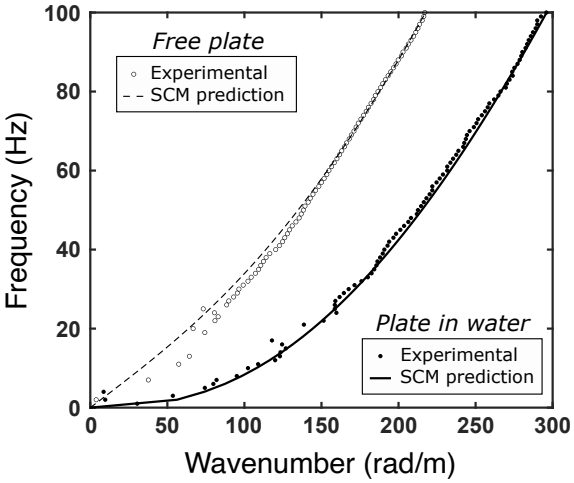

FIGURE 4.8: **Experimental dispersion curves of A_0 in an immersed plate** – Using a line source, we generate flexural plane waves in a plate Ecoflex-0030 with thickness $h = 3.7$ mm. The plate is either free (empty dots) or immersed in water (filled dots). To predict these dispersion curves, one should take into account the deformation due to the weight of the plate itself (∼5% for the free plate), as well as the viscoelasticity.

2 A progressive understanding

A simplified cochlear waveguide, without coiling or active properties, is still quite complex. We first consider a much simpler system: an elastic plate immersed in water. In chapter 1, we discussed guided elastic waves in a free plate and found that three fundamental modes exist in the low frequency regime (much lower compared to the first cut-off frequency). We measured the dispersion curves of these three modes, shown in figure 1.11 and 1.12. While in-plane modes SH_0 and S_0 have been widely studied and discussed in the course of this thesis, this is less the case for out-of-plane modes. However, the basilar membrane displacements are *a priori* mainly out-of-plane. So, we should focus on the first anti-symmetric mode A_0 whose displacements are mostly out-of-plane.

2.1 Flexural waves in a fluid-loaded plate

In chapter 3, we study such a flexural wave using the ultrasound elastography technique. We compare the theoretical dispersion curve of this flexural wave in a free plate and in a plate immersed in water that are presented in figure 4.7. Because there is a certain quantity of fluid to move when bending an elastic plate immersed in water, the dispersion curve is lowered. Let us derive the low frequency dispersion of the A_0 mode in a nearly-incompressible free plate[25] of thickness h. For anti-symmetrical modes, one has the Rayleigh-Lamb equation, as described in equation (1.19) in chapter 1, and it reads:

$$(k^2-q^2)^2 \tan\left(\frac{ph}{2}\right) + 4k^2pq \tan\left(\frac{qh}{2}\right) = 0 \quad \text{with } p = \sqrt{\frac{\omega^2}{V_L^2} - k^2}, \text{and } q = \sqrt{\frac{\omega^2}{V_T^2} - k^2}. \tag{4.1}$$

[25] ROYER and DIEULESAINT (1999): *Elastic waves in solids I: Free and guided propagation*

Assuming $ph \ll 1$ and $qh \ll 1$, one should perform a limited expansion to order 3 of the tangent functions, to finally obtain the dispersion relation associated to an incompressible material:

$$\omega = \frac{V_T}{\sqrt{3}}\, k^2 h. \tag{4.2}$$

Similarly, it is also possible to rewrite the Rayleigh-Lamb equation when the plate is immersed in a fluid[203,164] of density ρ_w and speed of sound c_w:

$$\left(k^2-q^2\right)^2 \tan\left(p\frac{h}{2}\right) + 4k^2pq \tan\left(q\frac{h}{2}\right) + i\frac{\rho_w}{\rho}\frac{\omega^4}{V_T^4}\frac{p}{r} = 0 \quad \text{with } r = \sqrt{\frac{\omega^2}{c_w^2} - k^2}. \tag{4.3}$$

Following similar steps, we obtain the dispersion of the flexural wave propagating in a fluid-loaded plate:

$$\omega = \frac{V_T}{\sqrt{3}} \frac{k^{5/2}h^{3/2}}{\sqrt{kh + \frac{2\rho_w}{\rho}}} \underset{kh\ll 1}{\sim} \frac{V_T}{\sqrt{3}} \sqrt{\frac{\rho}{2\rho_w}}\, k^{5/2}h^{3/2} \tag{4.4}$$

Interestingly, the sound velocity in water does not appear here. In fact, all that is needed is for the sound velocity in the fluid to be very large compared to that of the flexural wave, which led us to consider $r^2 \sim -k^2$ in our previous calculation.

On the contrary, the fluid density plays a fairly important role. For a fluid like air, ρ_w should be replaced by $\rho_a \ll \rho$ and equation (4.4) indeed simplifies into equation (4.2). But a heavy fluid, like water, greatly increases the inertia of the system, and therefore leads to a lowering of the dispersion curve. Here, densities are similar $\rho_w \sim \rho$, so that the coupling with water is in fact manifested by a factor $\sqrt{kh/2}$. Please note that all these comments hold in the low frequency regime, where the wavelength is much larger than the thickness.

The dispersion curve of the flexural mode in a free plate was measured in chapter 1. Using the same experimental method, we do similar measurements on a plate immersed in a water tank with transparent walls. The obtained dispersion curve is plotted in figure 4.8.

Predictions are not straightforward since two factors need to be taken into account. First, when the plate is not immersed in water, it is deformed under its own weight which is not the case when immersed in water since the densities are similar and the plate almost floats. The second factor is the material viscoelasticity. As already discussed several times in this thesis, rather than finding the roots of equation (4.3), we can use the SCM for an immersed plate[166], in combination with the equivalent elasticity tensor $\mathbf{C}^\omega$. Doing so leads to predictions plotted in figure 4.8 where we have considered an elongation of 5% in the free plate due to its own weight. This once again confirms the effectiveness of our material model coupled with the SCM. Note that, again, the velocity of this flexural mode becomes non-zero as soon as a prestress is applied. This can be seen in figure 4.8 where the dashed gray curve exhibits a linear behavior at low frequencies.

One detail remains to be clarified here. Equation (4.4) assumes that the plate is immersed in an infinite quantity of water. However, the water tank used in the experiment is finite (obviously) and we know this has an effect on the dispersion of the flexural wave in a plate. Following the work of Schulkes et al. (1987)[204], equation (4.4) is modified to

$$\omega = \frac{V_T}{\sqrt{3}} \frac{k^{5/2}h^{3/2}}{\sqrt{kh + \frac{2\rho_w}{\rho}\coth\left(kH\right)}} \underset{kh\ll 1}{\sim} \frac{V_T}{\sqrt{3}} \sqrt{\frac{\rho}{2\rho_w}\tanh\left(kH\right)}\, k^{5/2}h^{3/2}, \tag{4.5}$$

[203] Osborne and Hart (1945): "Transmission, Reflection, and Guiding of an Exponential Pulse by a Steel Plate in Water. I. Theory"
[164] Li and Cao (2017): "Mechanics of ultrasound elastography"
[166] Kiefer et al. (2019): "Calculating the full leaky Lamb wave spectrum with exact fluid interaction"
[204] Schulkes et al. (1987): "Waves due to a steadily moving source on a floating ice plate. Part 2"

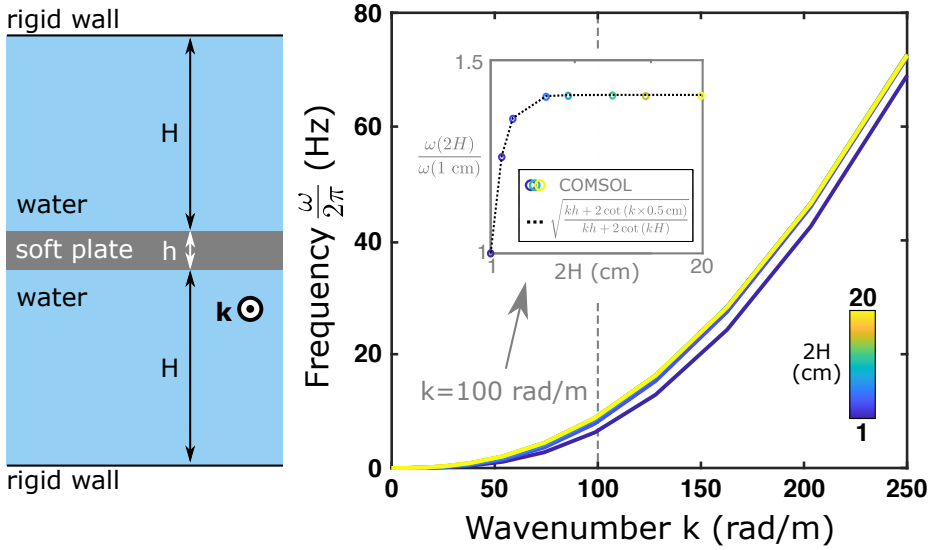

FIGURE 4.9: **Influence of the water height on the plate flexural mode dispersion** – By using COMSOL Multiphysics, we solve for the eigenvalue problem of an immersed plate of thickness $h = 4$ mm with varying water domain sizes $2H$ from 1 cm (blue) to 20 cm (yellow), with rigid boundary conditions. The evolution of frequencies at 100 rad/m are compared with theory in the inset.

with H the height of water immersing the plate (and $2H$ being the total height of the water domain).

We want to check this equation with COMSOL because the SCM assumes an infinite water domain and does not provide the corresponding predictions. Results for a purely elastic plate, of thickness $h = 4$ mm and transverse velocity $V_T = 6$ m/s, are shown in figure 4.9. First, a schematic diagram of the problem is recalled. Upper and lower walls are assumed to be rigid, and we apply periodic Floquet-Bloch conditions between the two normal faces indicated by the wave vector $\mathbf{k}$. Continuity is imposed between right and left faces to ensure the propagation of plane waves in the normal direction. Then, dispersion curves are displayed for various values of the water domain size $2H$, ranging from 1 cm (blue) to 20 cm (yellow). To check the validity of equation (4.5), we plot the obtained frequencies at $k = 100$ rad/m as a function of $2H$. Theoretical predictions for $\omega_{2H}/\omega_{2H=1\text{ cm}}$ are also added in this inset and fits perfectly the results from COMSOL simulations. We note that for $2H = 10$ cm, the dispersion becomes nearly constant with the water domain size. This is the so-called deep-water regime, well known in the water waves community, where the value of H becomes irrelevant, as long as it is much larger than the wavelength. In our experiment, the water tank has a size of $2H = 30$ cm, and everything actually occurs as if the flexural wave sees an infinite water domain.

Now that we understand properly the propagation of this flexural wave in a water-loaded plate, let us investigate the propagation of flexural modes in a water-loaded soft strip.

2.2 Flexural waves in a fluid-loaded strip with fixed edges

As explained in chapter 1, the flexural mode does not couple (or very weakly) to the other fundamental modes (S_0 and SH_0), and are therefore guided independently up to the first cut-off frequency in a plate of same thickness. Here, we present the dispersion curves for guided waves in a fixed strip in figure 4.10. In the ($k > 0$) (respectively $k < 0$) region are presented the out-of-plane (resp. in-plane) guided waves, both for a strip in air (dashed lines) and in water (full lines).

The SCM does not allow (yet) to build predictions for a waveguide with a rectangular cross-

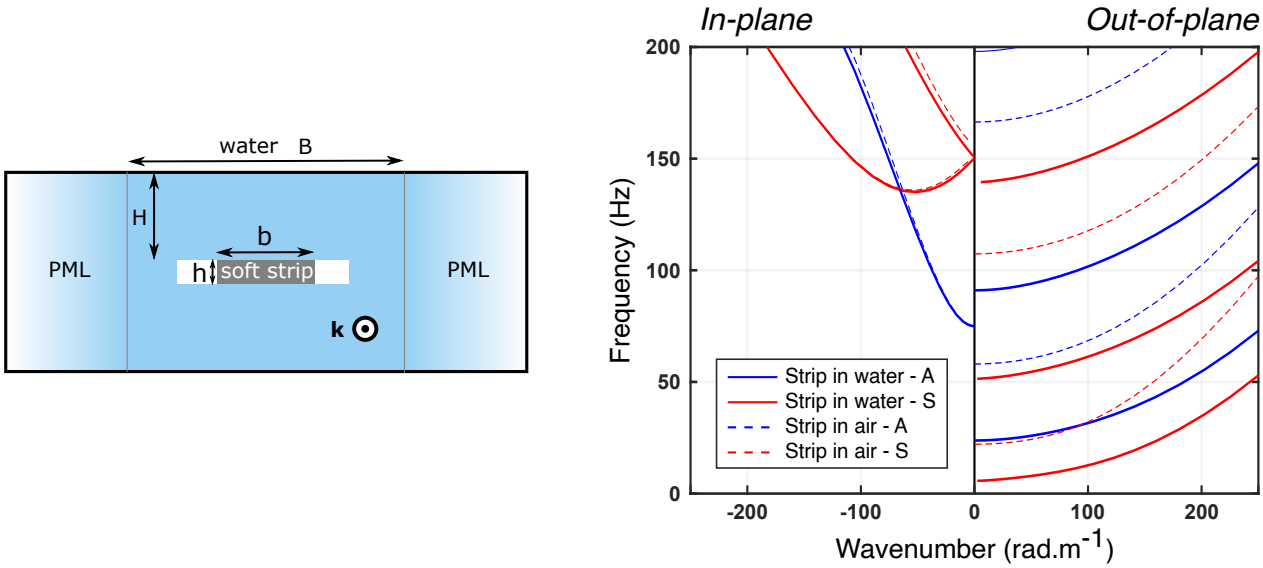

FIGURE 4.10: **Full dispersion curves for an immersed strip with fixed edges** – Calculations are made with a strip of dimensions 60 cm × 2.7 mm × 4 cm with fixed edges, either free or water-loaded. The cross-section is represented and PML are here to mimic an infinite water domain in the x_3 direction. Dispersion curves are obtained using COMSOL Multiphysics ($2H = 30$ cm and $B = 1$ m) and modes are separated upon their main polarisation and symmetry.

section immersed in water. So, to have these theoretical predictions, COMSOL is used again. In practice, we extrude a cross-section to obtain a small thickness and apply periodic Floquet-Bloch conditions between the two faces, as in the case of the immersed plate. A schematic diagram is given in figure 4.10. As discussed previously in figure 4.9, we considered $2H = 30$ cm for the height of water. For the transverse direction, we replace the continuity by a water domain of a certain width $2B$ coupled to Perfectly Matched Layers (PML) which are often used to mimic infinite environments. These PML attenuate the wave over a short distance, avoiding any reflection.

We recover the fact that in-plane guided waves are not really impacted by the presence of water. Their movement only sets in motion a thin layer of water (called boundary layer) of thickness 10 to 100 µm. In contrast, out-of-plane guided modes are significantly affected by the presence of water, just like the flexural mode in a plate, as explained above in figure 4.7.

Again, their typical power-law behaviour is recovered and cut-off frequencies are no longer evenly spaced. Moreover, their values are largely impacted by the presence of water. A zoom on the theoretical dispersion curve of the first flexural mode around its cut-off frequency is presented in figure 4.11. It has a really simple and intuitive displacement. Its transverse profile is roughly that of a string attached at both (lateral) ends.

Again, adding the water coupling significantly lowered the dispersion curve, thus the cut-off frequency, since the mode's inertia has increased. This cut-off frequency is an important feature since it means that no propagation is allowed at lower frequencies. Besides, one should note that the group velocity, *i.e.* the slope of the dispersion curve, is null at the cut-off frequency and remains quite low at higher frequencies: ∼1 m/s at 15 Hz. This remark will prove useful in the next section.

Let us now explore experimentally the dispersion curve of this mode in an Ecoflex strip. Results are presented in figure 4.12, for a strip in air (grey) or in water (black). Observations are coherent with previous discussions, as the coupling with water actually lowered the dispersion curve. To be more consistent, we add predictions for this strip of width $b = 18$ mm and thickness $h = 4$ mm. These predictions are correct but not fully accurate. In previous chapters, viscoelasticity was the key element to consider to fully describe the dispersion of guided waves in such soft media.Thus we

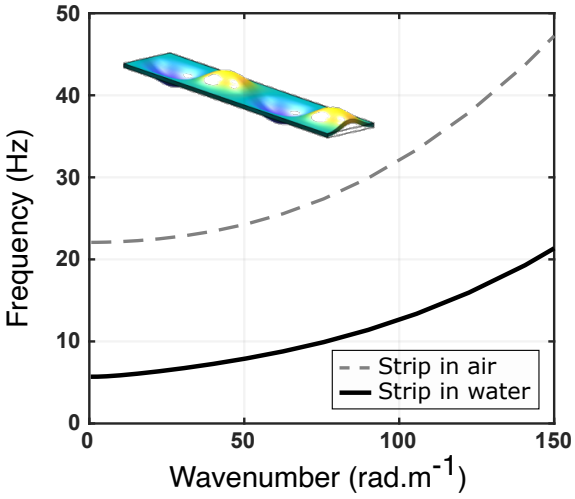

FIGURE 4.11: **Theoretical dispersion curve of the flexural mode in an immersed fixed strip** – Dimensions of the strip are $h = 2.7$ mm, $b = 40$ mm and the transverse velocity is $V_T = 6$ m/s. The first flexural mode is displayed, as well as its dispersion.

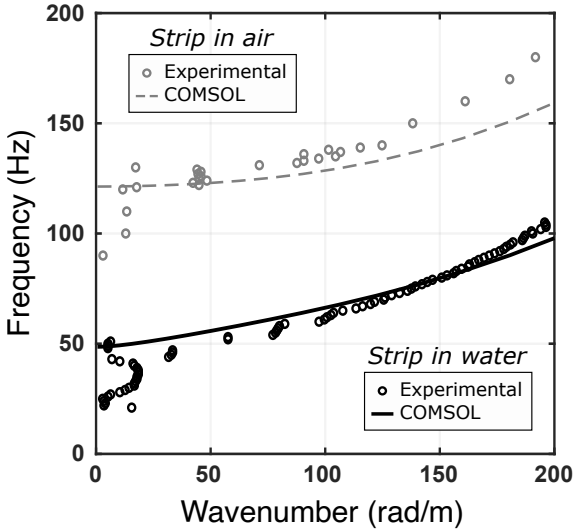

FIGURE 4.12: **Experimental dispersion curve of the flexural mode in an immersed fixed strip** – A point source generates out-of-plane displacement in an Ecoflex strip, with dimensions $h = 4$ mm, $b = 18$ mm when the water tank is empty (in air), and filled (in water).

believe that better predictions are possible by implementing the rheology of the material in these simulations. Moreover, there is also a slight possibility that the strip was initially deformed (with a stretch ratio $1 \leq \lambda \leq 1.05$), but neither this prestress nor the rheology can simply be taken into account in the COMSOL software.

Additionally, we have just seen in the previous chapter that, in a lossless medium, a cutoff-frequency mode has a purely imaginary wavenumber below a certain frequency, that switches to a purely real wavenumber at this frequency. But in a medium with intrinsic losses, the transition is not abrupt and is smoothed, with wavenumbers having both non-zero real and imaginary parts, as illustrated in figure 3.19. Once again, we find this aspect in experimental measurements where non-zero wavelengths are measured below the theoretical cut-off frequencies (50 Hz in air, and 120 Hz in water). Note that these points indeed correspond to highly attenuated waves, that only propagate over short distances.

Last but not least, we examine the pressure distribution in water with COMSOL. While analytically challenging, we can still discuss its evolution in the x_2 direction in the water domain. The transverse velocities in such soft media are of the order of 5 m/s, that is to say much lower compared to the pressure wave velocity in water $c_w = 1500$ m/s. Thus, no pressure wave can propagate in water with the pair (ω, k) and pressure waves must decay exponentially in the x_2 direction. Here, the decay length is generally given by the $1/|r| = c_w/f_c$ at the cut-off frequency f_c and is of the order of 30 m at 50 Hz. This remark points out the difficulties encountered when trying to implement PML with COMSOL, as the PML thickness should be of the order of 10 m but the studied system is of dimensions 1 cm×1 mm. In practice, we chose the width of the water domain B and the PML size to be around 1 m.

Measurements were carried out in a water tank with width $B = 80$ cm. This raises the question of how the predictions change when PMLs are removed while retaining this value for B. Moreover, we might also wonder: how does this dispersion curve evolves when B is reduced, in the same way as we did for the height of water $2H$ in the case of the plate in figure 4.9? Results are shown in

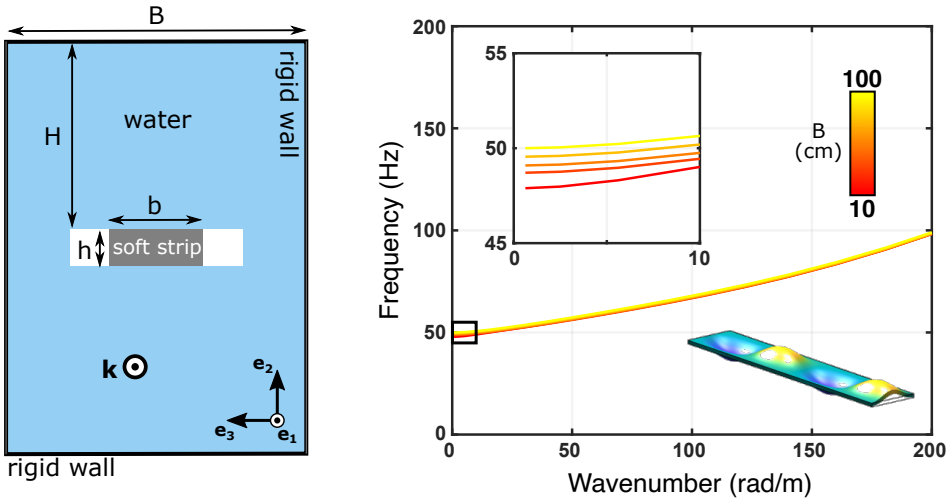

FIGURE 4.13: **Influence of the water domain width on the flexural mode dispersion** – By using COMSOL Multiphysics, we solve for the eigenvalue problem of an immersed strip of thickness $h = 4$ mm and width $b = 18$ mm with varying water domain widths B from 10 cm (blue) to 100 cm (yellow). A zoom in around the cut-off frequency is added in the inset.

figure 4.13.

We see that the dispersion of this mode is only slightly affected by the size of the water domain, including its cut-off frequency. The discussion on the evolution of this cut-off frequency with geometric parameters (h, b) is done later.

In the end, one may argue that considering an infinite water domain is indeed irrelevant in our problem since it is not the case in the cochlear waveguide. In particular, the two water compartments (top and bottom in figure 4.13) are connected in our simulations. However, in the cochlea, compartments are isolated and only join at the apex. So we move on to this waveguide, and start by studying it without any gradient at all.

2.3 The full waveguide

Additional boundary conditions are implemented as illustrated in the schematic diagram in figure 4.14(a). The soft strip is the same as before, assumed fixed at its lateral edges in $x_3 = \pm b/2$. The water compartments have finite sizes and are isolated.

The full dispersion curves of guided waves in this system are obtained using COMSOL by only keeping the top and bottom water domains, and are plotted in figure 4.14(b). A zoom is also performed on the first flexural mode dispersion, and is compared to the case where compartments are connected in figure 4.14(c).

The dispersion curves are indeed similar except for the symmetric out-of-plane modes (red lines in the $(k > 0)$ region), *i.e.* the flexural waves, and in particular in the low frequency regime. This time, there is no cut-off frequency and the fundamental flexural wave propagates even below 50 Hz. In many cases, the existence of a cut-off frequency implies the absence of solution in the static regime (zero frequency). For instance, for a fixed strip in air, it appears because a rigid body motion is forbidden by the boundary conditions. This time, applying a static overpressure in one water compartment statically deforms the strip along its entire length, leading the cut-off frequency to disappear.

Here we have modelled the coupling between an elastic waveguide (a clamped soft strip) and two acoustic waveguides (water compartments), making this system a particularly complex environment to study. Pressure waves propagate at approximately 1500 m/s in water, while the flexural wave

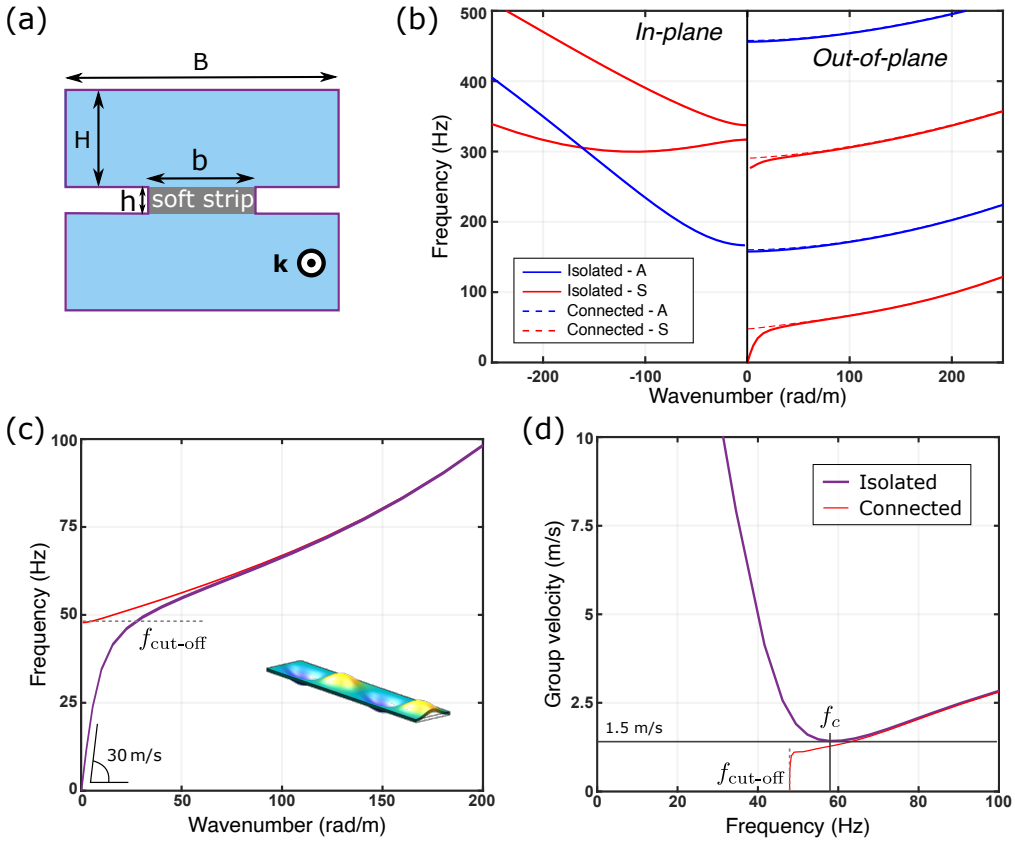

FIGURE 4.14: **Theoretical dispersion curves with two isolated water compartments** – (a) The same fixed strip of thickness $h = 2.7$ mm and width $b = 40$ mm is immersed in water and the top and bottom water compartments are now isolated. The cross-section is represented. (b) Dispersion curves are obtained using COMSOL Multiphysics ($2H = 20$ cm and $B = 10$ cm) and modes are separated upon their main polarisation and symmetry with respect to $x_1 = 0$ axis. (c) Zoom in around the first cut-off frequency. Curves are compared to the case where top and bottom compartments are connected (dashed lines in (a,b) and red lines in (c,d)). (d) Their group velocities $V_g(f)$ are plotted as well.

propagates at 1-2 m/s in the strip. Remarkably in such a complex waveguide, in the low frequency regime the guided wave is weakly dispersive with a velocity of around 30 m/s. This value is between the shear wave velocity in the strip and the sound velocity in water, confirming the importance of the waveguide coupling.

Many questions naturally arise, particularly about the nature and strength of this coupling. Just as important, one may also wonder about the influence of geometrical parameters (b, h). Last but not least, we will obviously be asking what influence the size of the water compartments (B, H) has on this coupling, and in particular on the wave velocity below the cut-off frequency.

2.4 An explanation to passive cochlear tonotopy

Before answering all these questions, one should notice that the group velocity reaches a minimum at a characteristic frequency $f_c \sim 50$ Hz in figure 4.14(d). It is also compared to the case where water compartments are connected.

As expected when a cut-off frequency $f_{\text{cut-off}}$ exists, the group velocity is minimal and equals zero at this frequency. However, when water compartments are isolated, the cut-off frequency disappears

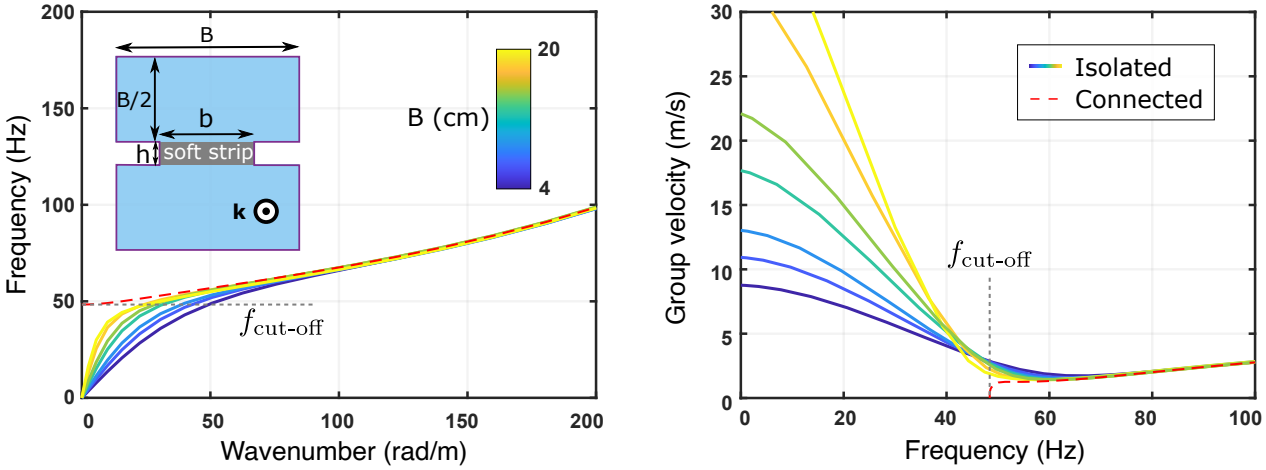

FIGURE 4.15: **Effect of the water domain size B on the group velocity** – The dispersion of the fundamental flexural mode, in a strip of thickness $h = 4$ mm and width $b = 18$ mm, with connected water compartments is recalled for comparison (red dashed line) and its group velocity is plotted as well. Compartments are then isolated and their dispersion are computed for different values of the water compartment size $2H = B$ ranging from 4 to 20 cm.

but the group velocity reaches a minimum at a characteristic frequency $f_c \gtrsim f_{\text{cut-off}}$. Again, of particular interest are the high values of the group velocity V_g for $f < f_{\text{cut-off}}$ where the propagation was previously not possible. Overall, the dispersion of this mode can be roughly simplified into two distinct parts. At frequencies $f < f_c$, the wave is weakly dispersive and propagates at high speed. For $f > f_c$, the wave is quite dispersive and propagates very slowly with an almost constant group velocity.

We now understand that it was unimportant to study the effect of geometrical parameters (b, h) on the cut-off frequency $f_{\text{cut-off}}$. Instead, we now study the characteristic frequency f_c. There are several gradients of properties along the cochlea, but we will only study the simplest ones, as shown in table 4.1. For the sake of simplicity, we can assume ST and SV to have rectangular cross-sections with $B = 2H$ and to be the same size, *i.e.* top and bottom compartments are identical. We can then compute the dispersion of the fundamental mode for several values of (b, h) and B.

Effect of the water compartment size B – The effect of the size B of the water compartments is shown in figure 4.15, with the dispersion curve $f(k)$ and the $V_g(f)$ plots. The conclusion is quite straightforward since only one feature is modified, that is the coupling strength. The larger the water compartments, the more they dictate the physics of this mode in the low frequency regime, *i.e.* the closer the initial group velocity, and the phase velocity, tends towards the sound velocity in water and diverges from the transverse velocity in the material. In fact, in the limit where the water compartments become large enough to become infinite, the acoustic waveguides would disappear and we should recover the physics of an immersed fixed strip in water, as indicated by the dashed red line where water compartments are connected and of size $2H = B = 10$ cm.

As we do not have any theory to model the coupling between the acoustic and elastic waveguides, it is difficult to add predictions about the evolution of this group velocity with B. In addition, we could also ask what the effects of B or H are independently. Is it rather the value of the cross-sectional area that comes into play, or its shape? These questions have not been answered here, but it is clearly a research topic for the future.

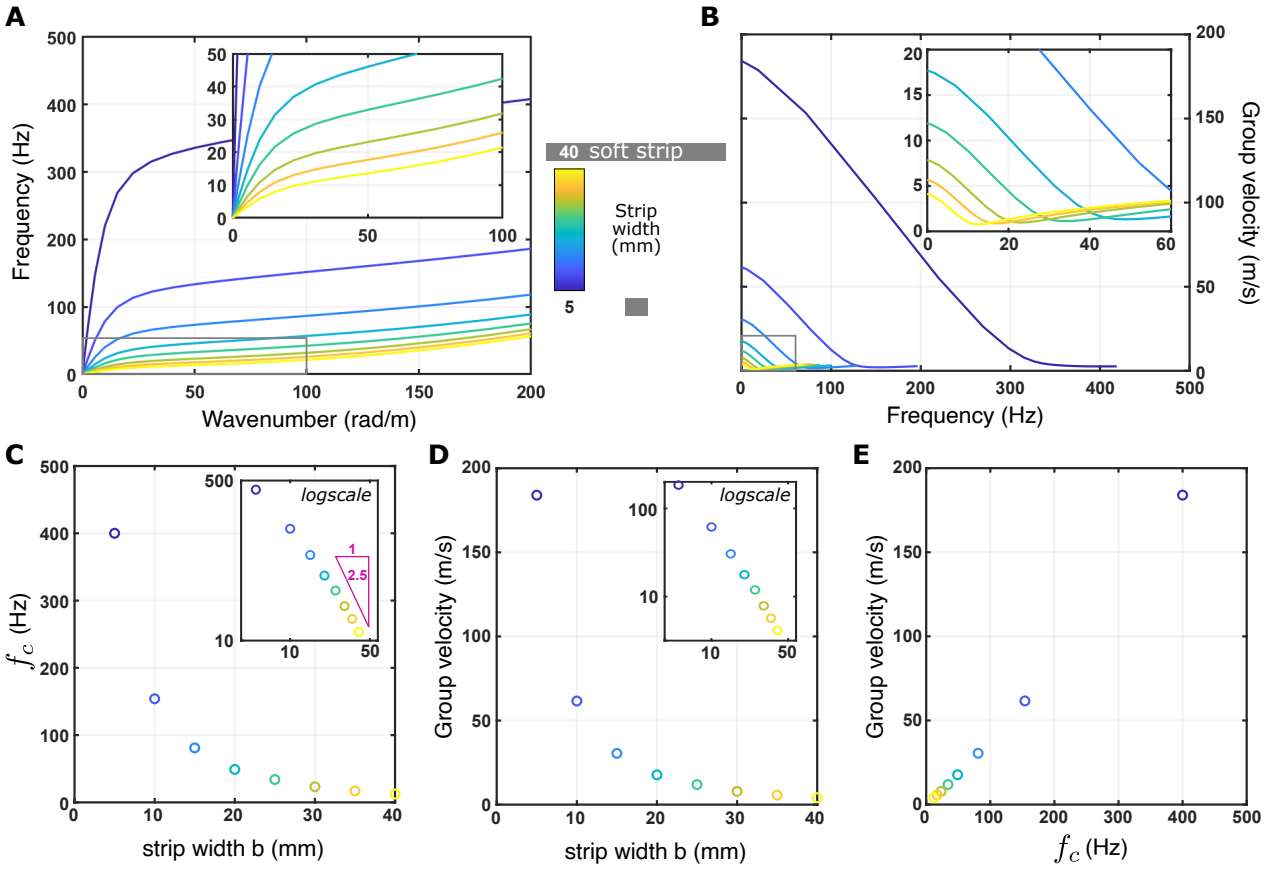

FIGURE 4.16: **Effect of the strip width b on the group velocity** – The dispersion of the fundamental flexural mode, in a strip of thickness $h = 4$ mm and width $b = 18$ mm, is recalled when water up and bottom compartments are connected (red dashed lines) and its group velocities is plotted as well. Compartments are then isolated and are of size $2H = B = 10$ cm. **A-** Dispersion curves are then computed for different values of the strip width b ranging from 5 to 40 mm. A zoom in is performed to reveal the large strip width behavior. **B-** Same for the group velocity. **C-** The characteristic frequency f_c is extracted and plotted as a function of the strip width b. A logarithmic scale is added in the inset. **D-** Similarly, the group velocity at low frequency is also plotted. **E-** Noting their behaviors are quite similar, we also plot this group velocity as a function of the previously assessed characteristic frequency f_c.

Effect of the strip width b and thickness h – In the cochlea, the width of the basilar membrane increases from the base to the apex. We can compute the dispersion curves of the same fundamental mode for increasing values of the strip width b, and the results are shown in figure 4.16A. Here, the dispersion curve is completely modified when changing the strip width b. When increasing b (from blue to yellow), frequencies are largely decreased, including the cut-off frequency that would exist for a similar system with connected compartments, but also the characteristic frequency f_c that minimizes the group velocity. Additionally, the initial slope must follow this decrease in frequency and that is why the group velocity at low frequency largely decreases when increasing the value of b, as indicated in figure 4.16B. To better visualize this effect, we extract the group velocity for $f \to 0$ Hz, as well as f_c, and plot them as a function of the strip width b in figure 4.16C and D.

These two features seem to be quite similar and this is why we plot the extracted group velocity as a function of the characteristic frequency f_c, in figure 4.16E. We note that a strong correlation exists between these two values, meaning the dispersion curves could be superimposed by normalizing each

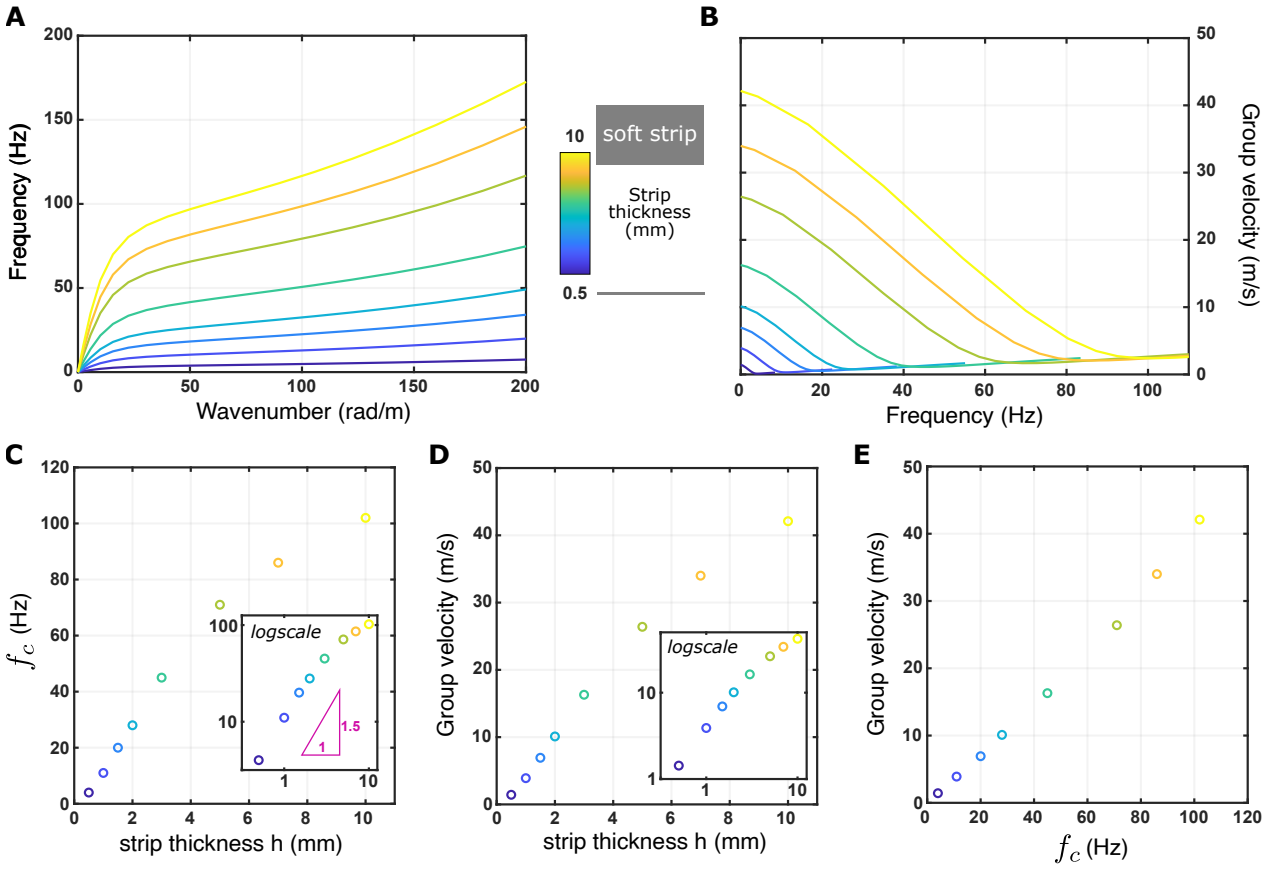

FIGURE 4.17: **Effect of the strip thickness h on the group velocity** – Same as previous figure with varying thickness values h ranging from 0.5 to 10 mm.

by their corresponding characteristic frequency.

Before commenting further these changes, we can perform a similar study with varying strip thickness h, and results are presented in figure 4.17. When the strip thickness h increases, both the characteristic frequency f_c and the group velocity V_g increase. Similarly to the case where the strip width b is varied, the two features of interest are highly correlated in figure 4.17E.

Now may be the adequate time to talk about the observed dependence of f_c with the width b and the thickness h. However, it has already been said that we are currently unable to provide a model for this coupling of the two waveguides. Nevertheless, we note that this characteristic frequency f_c is often quite close to the cut-off frequency $f_{\text{cut-off}}$ that would exist in the same system if the two water compartments were connected. This raises the question of whether we can understand how $f_{\text{cut-off}}$ evolves with the parameters (b, h) of the strip. By using equation (4.4), one may guess $f_{\text{cut-off}}$ by evaluating the function $\omega(k)$ for the plate wavenumber $k = \pi/b$, resulting in the following equation:

$$f_{\text{cut-off}} \propto V_T \, b^{-5/2} h^{3/2} \tag{4.6}$$

This predicts a power-law behavior for $f_{\text{cut-off}}$, and likewise the function $f_c(b, h)$, with both b and h. So, to check the accuracy of this equation, we plot $f_c(b)$ in the inset of figure 4.16C and $f_c(h)$ in 4.17C with logarithmic scales. Plotting them in this way does not produce straight lines, which means they don't actually follow power laws. We also add triangles to give an indication about the predicted slopes for these curves. Predictions in equation (4.6) work well for small thickness h, or large width b. Equation (4.4) is valid in the low frequency regime of a plate *i.e.* for plate wavenumbers $kh \ll 1$. Here, we evaluate $\omega(k)$ for $k = \pi/b$, meaning equation (4.6) holds when $h \ll b$, or

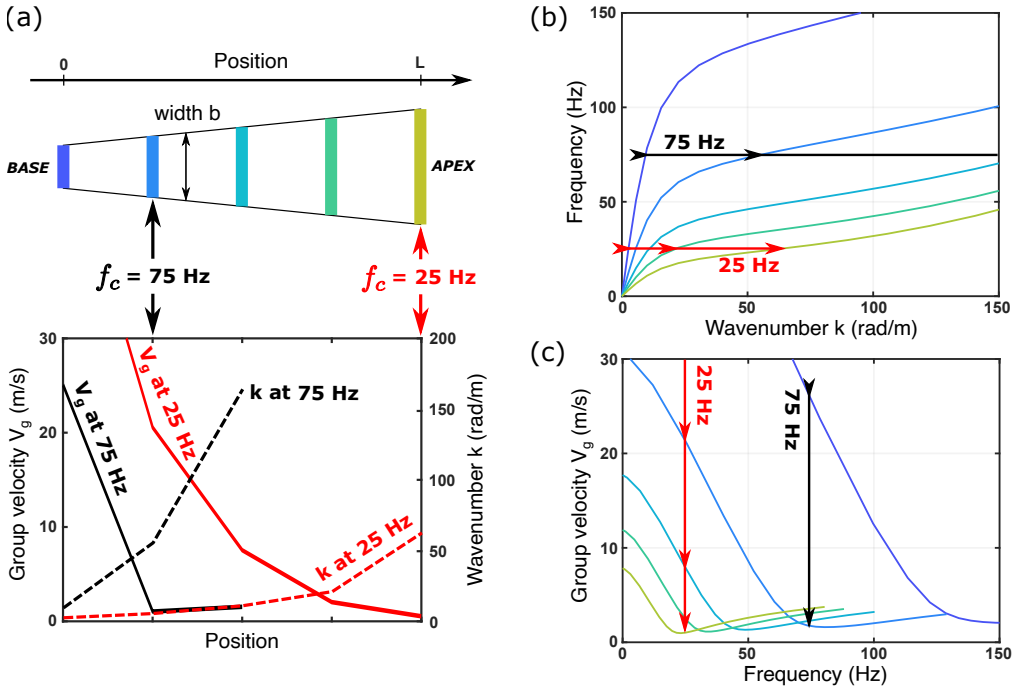

FIGURE 4.18: **Experience of the cochlear wave in the basilar membrane** – (a) A strip with a varying width from 1 to 3 cm is considered. For two frequencies 25 and 75 Hz, we plot the evolution of the group velocity and of the wavenumber as functions of the positions. (b,c) Local dispersion curves and group velocities for each position.

when the studied strip has an important aspect ratio. And in both figures 4.16C and 4.17C, the approximation in equation (4.6) typically works when h is small, or when b is large.

The experience of the cochlear wave along the basilar membrane – Now that we have seen how the parameters vary with the water compartment size B, the strip width b and thickness h, we can understand how the local wave dispersion evolves with position along the basilar membrane. At the cochlear base, b is the smallest, h is the largest and B is also the largest. On the contrary, at the cochlear apex, b is the largest, h the smallest and B also the smallest. As a result, the characteristic frequency f_c is the highest at the base and the lowest at the apex, and similarly the group velocity of this wave is the highest at the base and the lowest at the apex. For an intermediate position, the characteristic frequency is also intermediate, meaning that some frequencies are still propagating very fast, while others have been slowed down. To illustrate the experience of a sound at frequency f, we use an example where we study two waves at frequencies 25 and 75 Hz in a strip with a width gradient (from 1 to 3 cm), as indicated in figure 4.18(a). Each position corresponds to a width b, and therefore a local dispersion as displayed in figure 4.18(b) and (c). As a result, we can plot the evolution of the wavenumber k and the group velocity V_g as a function of the wave's position along the strip.

We retrace the passage of a sound of frequency $f = 25$ Hz in the cochlea. At the base, $f < f_c = 154$ Hz and the wave propagates really fast. But there is more because the wavenumber is also really small, *i.e.* the wavelength is really large. Progressively when propagating along the cochlea, f_c decreases, leading the group velocity (full red line) to progressively decrease, and the wavenumber (red dashed line) to increase. At some point, the wave reaches a position where $f = f_c = 25$ Hz. At this position, the initial wave finds itself slowing down enormously. From this, one expects

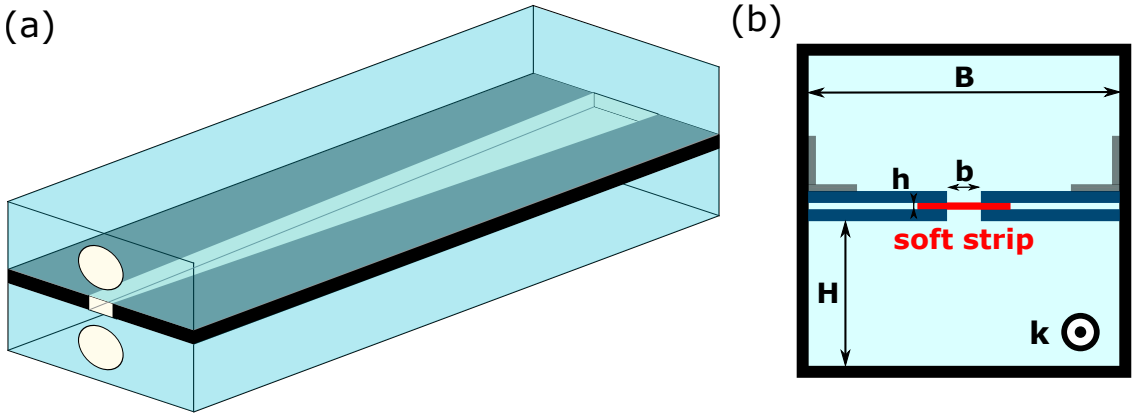

FIGURE 4.19: **Our macroscopic model of the cochlea** – (a) Diagram of the full macroscopic model. (b) A cross-section view of the macroscopic model, with geometrical parameters $b \sim 1$ cm, $h \sim 1$ mm, $H = 5$ cm and $B = 10$ cm.

that the wave amplitude increases at this position. Likewise, the wavenumber rises sharply and the wavelength drops suddenly. Once the wave has passed through this position, it arrives in a portion of the strip where $f > f_c$, so it propagates very slowly with a wavelength that continues to decrease. In practice, the medium has intrinsic losses and the wave is attenuated after having stopped. Clearly, a sound at a different frequency will not slow down at the same position. Namely, for a sound at a higher frequency like 75 Hz (black lines), the amplitude rises at a position closer to the base (remember that f_c is maximal at the base).

To conclude, the amplitude of a sound will suddenly increase as it propagates through the cochlea, at a position that depends on its frequency. We have just found a physical explanation, based on the physics of elastic waves in a soft strip, for the tonotopy observed in the cochlea of many mammals, including humans.

We have seen what we expected in simulations, and we have clearly understood where the tonotopy phenomenon comes from. In particular, we have seen that the gradient with the greatest effect is that of width b, since $f_c(b)$ varies more rapidly than $f_c(h)$. Now let's explore this mode experimentally.

3 Experimental implementation

3.1 The macroscopic model

To obtain a macroscopic model of the cochlea in the laboratory, we first build a rectangular box that does not leak. Then, we insert a strip which divides the box into two compartments. One of the most important point in this step is to make sure that the two compartments are not connected, except at the apex. Otherwise, the waveguide behaves in a completely different manner, as pointed out in figure 4.14. A schematic of this macroscopic model is displayed in figure 4.19. The box is entirely built with PMMA, a transparent engineering thermoplastic. Two circular holes are left on one side of the box. They are covered with silicone (Ecoflex) membranes to mimic the presence of the oval and round windows in the cochlea. Then, the strip is set in this plastic box. Actually, it is prepared with a width larger than b, but is fixed in a way that only the central part, of width b, can move. This clamping process is quite delicate because if we tighten the strip too much, then it swells and can even buckle. But if we do not clamp it enough, then the strip can move as the elastic wave passes, something which we absolutely want to avoid.

As in the cochlea, the wave is generated by the oval window using a shaker attached to it.

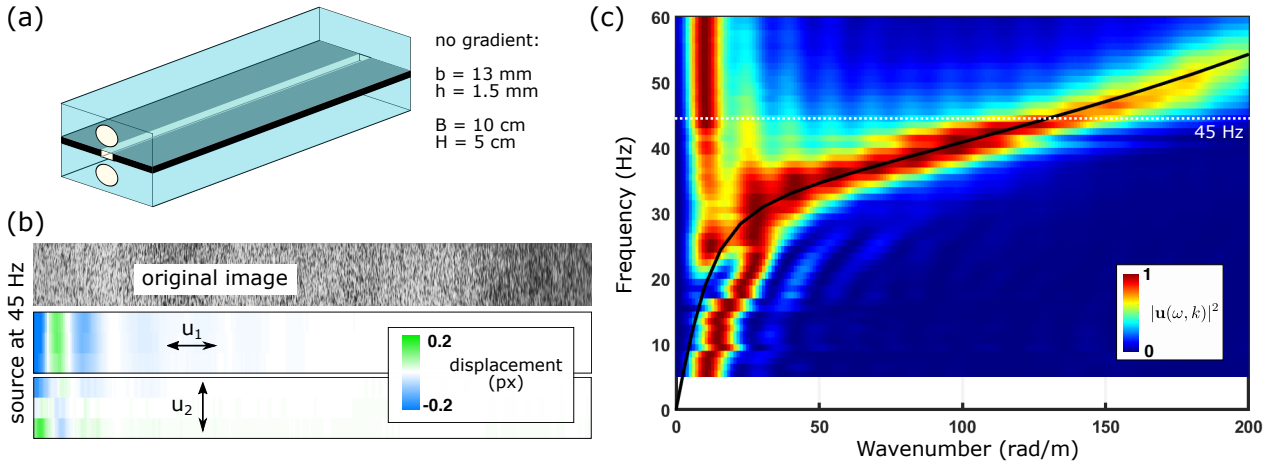

FIGURE 4.20: **Experimental dispersion curve of our cochlear waveguide without any gradient** – (a) Diagram of the full macroscopic model with geometrical parameters values. (b) Typical in-plane displacement maps obtained at 45 Hz. (c) Experimental 2D energy spectrum, normalized at each frequency, and theoretical prediction for the dispersion curve of this mode.

There remains one last subtlety before showing the first results. In previous chapters, we made in-plane wave measurements, where the displacement was mostly in the plane imaged by the camera (up-down and left-right). But here, the main displacement of the fundamental guided mode in this system mostly has an out-of-plane displacement (front-back), as illustrated in figure 4.14. Our method is therefore unable to measure out-of-plane displacements. However, as already mentioned when measuring the A_0 mode in a plate (figure 1.12 in chapter 1), flexural modes have not only an out-of-plane displacement component, but also in-plane components, which are weaker. By generating large enough amplitudes in our system, we can make sure that in-plane components of this mode are measurable.

We then install a strip of width b and thickness h fixed in the box and we measure the dispersion relation of the guided mode.

3.2 Results without gradient

The results are displayed in figure 4.20. First, the diagram of the fixed strip, made of Ecoflex-0030, is recalled and its geometrical parameters are given. Then, a typical acquired image is shown in 4.20(b), as well as the displacement maps at 45 Hz. By exciting a pressure wave in the fluid, we have succeeded in generating displacements in the strip. By performing a Singular Value Decomposition for each frequency, as detailed in figure 1.17, followed by a spatial Fourier transform, we extract the dispersion diagram of this mode in figure 4.20(c). The two regimes are clearly visible. Above $f_c \sim 35$ Hz, the dispersion is rather flat with a low group velocity. For lower frequencies, we are able to measure the propagation of a wave, contrary to what was observed for an immersed fixed strip in figure 4.12. Additionally, the theoretical prediction fits well with the measurements, except for the initial slope. However, one should remember that at these low frequencies, the corresponding wavenumbers are close to the limit of resolution (given by the length of the measured displacement maps), and that the rheology was omitted in this theoretical predictions. Here, a transverse velocity of 6 m/s is assumed but we know that this velocity goes down when decreasing the frequency, thus giving a simple explanation of why the measured curve is indeed below the theoretical prediction.

Lastly, notice there is always a peak at $k \sim 10$ rad/m for frequencies ranging from 20 to 60 Hz. This is in fact an artifact coming from the SVD.

Now that we have been able to probe this dispersion curve, we replace the current fixed strip of

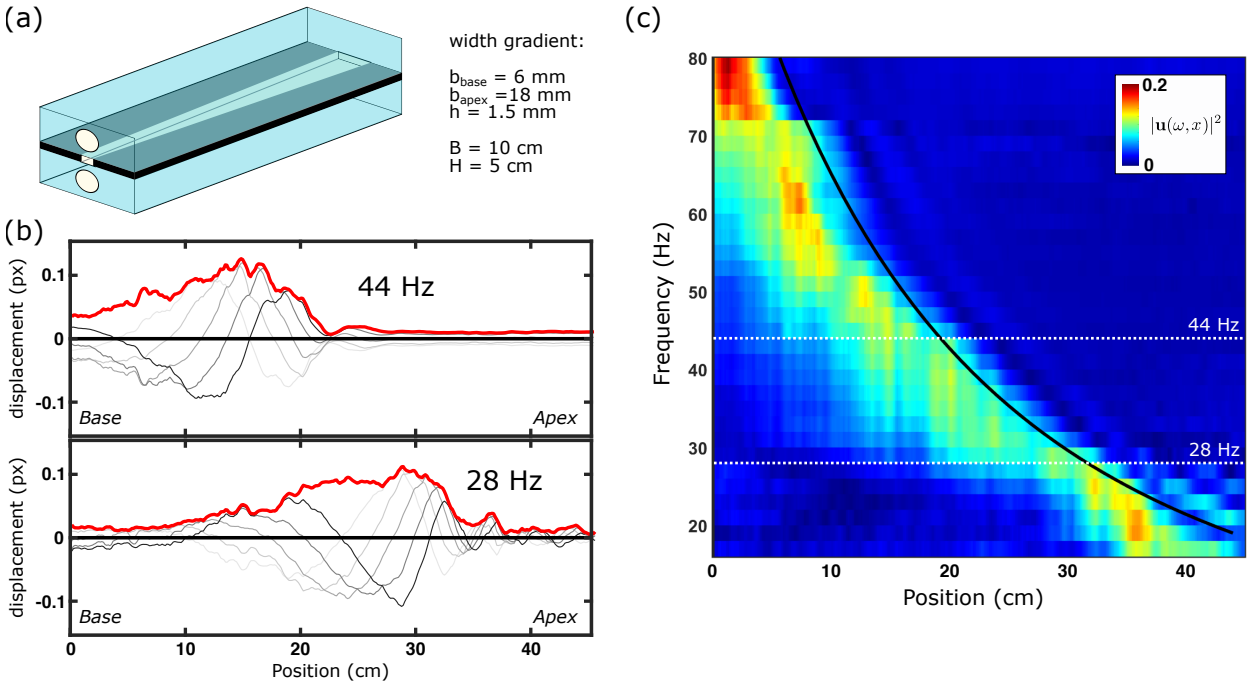

FIGURE 4.21: **Experimental tonotopic map of our cochlear waveguide with a width gradient** – (a) Diagram of the full macroscopic model with geometrical parameters values. (b) Typical displacements for different times, at 44 Hz or 28 Hz. (c) For each frequency, the wave envelope is extracted and plot as a function of the position along the waveguide. Theoretical predictions for the characteristic frequency f_c are added.

constant width b and thickness h by another one where the width gradually increases.

3.3 Results with a linear width-gradient

Here, we follow the same procedure as before, but using a cochlear waveguide with a width gradient. Close to the oval window, the width is set at 6 mm and at the other side of the box, it has increased and the width is set at 18 mm. Results are shown in figure 4.21. Again, the diagram of the macroscopic model is recalled. Then, typical displacement maps are processed and the first singular vector is computed and displayed in figure 4.21B at different times.

On these curves, we see that the amplitude is not constant with the position. It first increases around a certain position, and then decreases. This is expected from all the considerations depicted in figure 4.18, and this is also why the wavelength is greater near the source (or the base) before gradually decreasing along the strip.

By plotting these displacements for two different frequencies, we see that the higher the frequency is, the closer to the base the amplitude rise. To better characterize this link between the excitation frequency and the position of maximum amplitude, we trace the envelope of the wave (red line in 4.21B) $|u(\omega, x)|$ in figure 4.21C. Again, high frequency tones reach a maximum close to the source, while low frequencies propagate all along the waveguide before the amplitude rises. To predict these positions, we compute the local dispersion for each position, and then derive its characteristic frequency, plotted as a thick black line in figure 4.21C. Note that the zero-position corresponds to a distance of ~ 10 cm from the source (*i.e.* the base). Thus, the width varies from 8.2 mm at 0 cm, to 18 mm at 44 cm.

The predictions give a correct trend. At each position, the frequency that stops propagating is always slightly overestimated with f_c. To explain this, we go back to the curves shown in figure 4.16.

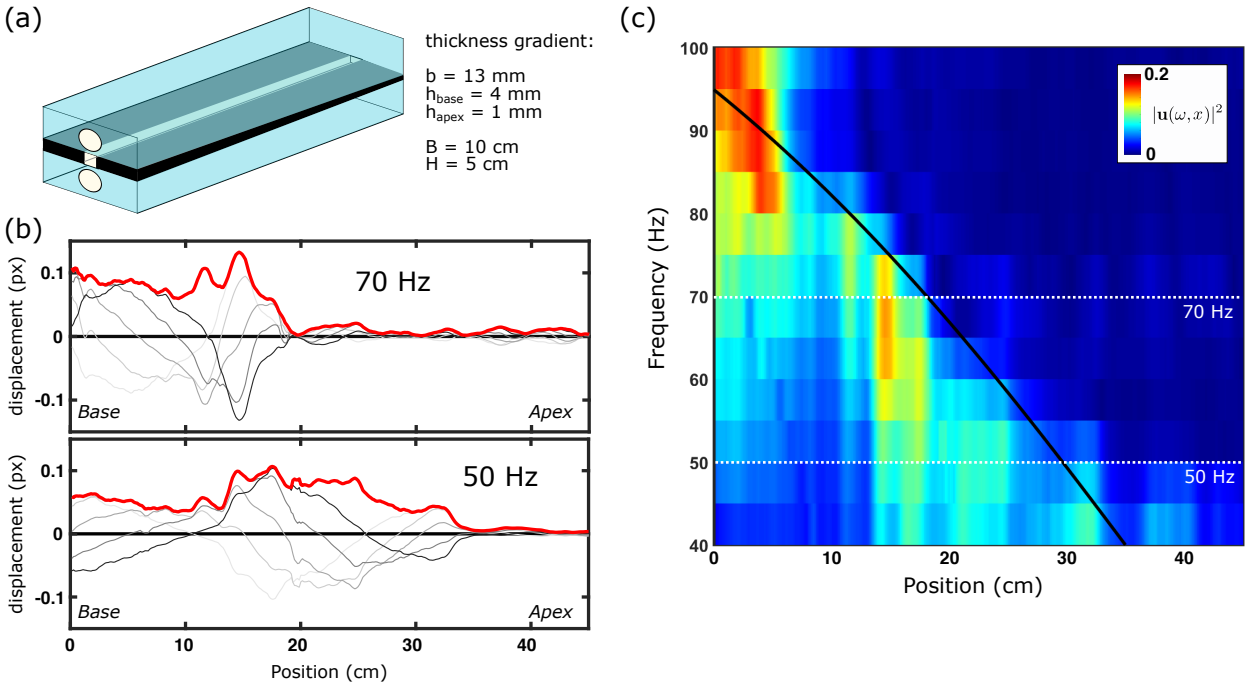

FIGURE 4.22: **Experimental tonotopic map of our cochlear waveguide with a thickness gradient** – (a) Diagram of the full macroscopic model with geometrical parameters values. (b) Typical displacements for different times, at 70 Hz or 50 Hz. (c) For each frequency, the wave envelope is extracted and plot as a function of the position along the waveguide. Theoretical predictions for the characteristic frequency f_c are added.

The frequency f_c is in fact the frequency that minimize the group velocity, but it is already very low for smaller frequencies. We deduce that f_c is the maximum value of frequencies that stop at a given position. This is why the black curve appears above the line formed by the maxima. Once again, the rheology of the material surely plays an important role in determining precisely these positions where the amplitude reaches its maximum. In the end, decreasing the width b by a factor of 2 implies the localisation of frequencies varying by a factor of 4.

As seen in simulations in previous section, the thickness also has a great effect on the characteristic frequency f_c. Let us implement such a thickness gradient.

3.4 Results with a linear thickness-gradient

Here, we again follow the same procedure using a cochlear waveguide with a thickness gradient. The thickness varies from 1 mm close to the round window, to 4 mm at the apex. Results are shown in figure 4.22. Similarly, the diagram of the macroscopic model is recalled and the first singular vector is plotted at different times in figure 4.22B.

Observations are quite similar to the case of the width gradient except that the amplitude rise and the wavelength decrease are not as clear as in figure 4.21B. Still, the wave slows down when reaching the position corresponding its frequency. For each frequency, the wave envelope is extracted and plotted as a function of the position. The image is less contrasted than with a width gradient since amplitude rises are less clear, meaning less significant. However, there is, at each frequency, a position where the wave stops, which is a sign of a significant decrease of the group velocity. High frequencies are still stopped near the base, while low frequencies propagate further. We even note that for frequencies close to ~ 40 Hz, the wave reaches the end of the waveguide without any amplitude increase. This is more likely because the lowest f_c in this waveguide is about 40 Hz. To

check this assumption, we again plot theoretical predictions for the characteristic frequency with the position as a thick black line. The thickness varies from 3.4 mm at 0 cm to 1 mm at 44 cm. The shape is quite different this time, and the curvature is in the other direction. Keep in mind that this experiment is at a preliminary stage, which is why the frequency resolution is low, and the curves presented in figure 4.21B are noisy. There is still a lot of work to be done before we can draw any clear conclusions. In the end, the thickness gradient does not have as much effect as a width gradient, but it does contributes to tonotopy.

4 Conclusion

We implemented both a width gradient and a thickness gradient, and we observed wave localisation at frequency-dependent positions. We explained the link between frequency and position but there is still a lot more to do. For instance, we mentioned and explained the role of the water compartment size in figure 4.15. While it does not seem to have a great effect on the characteristic frequency, an increase in B induces a significant increase in the group velocity at low frequency. This was not discussed but it could have an impact in the increase in amplitude we experimentally observed.

The next step will be to combine the width and the thickness gradient simultaneously. But, in fact, there are many other things to study in this macroscopic model of the cochlea. For instance, understanding more precisely the velocity distribution in the water compartments could lead to breakthroughs of capital importance in medicine with applications in drug delivery[205,206,207,208,209]. For that study, we imagine that techniques such as Particle Image Velocimetry (PIV) to probe water flows along the waveguide would be useful.

Last but not least, as briefly discussed in this chapter's introduction, the cochlea is a living organ with active properties crucial to the sense of hearing[210]. These active properties greatly increase our sensitivity. Thus, one may think of a way to make our sample active. Actually, there is some ongoing research about soft piezoelectric materials where an electric field is able to modulate the elastic properties of the material. Other electroactive samples already exist and we have even prepared one during this PhD thesis but so far, the experiments have not been fruitful. Another way to make elastomers active is to use iron particles, which are fixed in the elastomeric matrix and make the sample sensitive to magnetic fields; they are said to be magneto-active. Again, there is quite a rich literature on the subject for static modulations, but progress remains slow and is therefore rarely implemented experimentally.

Whether or not we succeed in creating these active materials to improve our macroscopic model of the cochlea, this work is still very promising for other applications. Such a waveguide is capable of separating very different frequencies over relatively short distances. Remember that a sound at 50 Hz has a wavelength of 30 m in water. By coupling our waveguide to a multitude of more efficient absorbers, but with a reduced bandwidth, we can create a highly efficient absorbing system over a very wide frequency band. This could prove particularly interesting for water ultrasonics applications.

This brings us to the end of this chapter, motivated by the need to better understand the cochlear tonotopy, the key phenomenon for the sense of hearing. The next chapter has nothing to do with this motivation, but digs a little deeper into the physics of guided waves in strips. Rather than using an electric or magnetic field to actively modulate the properties of the material, we induce a modulation by a varying axial stress.

[205] Anderson et al. (2019): "Local Delivery of Therapeutics to the Inner Ear: The State of the Science"
[206] Mittal et al. (2019): "Nanoparticle-based drug delivery in the inner ear: current challenges, limitations and opportunities"
[207] Rybak et al. (2019): "Local Drug Delivery for Prevention of Hearing Loss"
[208] Hao and Li (2019): "Inner ear drug delivery: Recent advances, challenges, and perspective"
[209] Szeto et al. (2020): "Inner ear delivery: Challenges and opportunities"
[210] Ashmore et al. (2010): "The remarkable cochlear amplifier"

Chapter 5

A space-time interface in a soft strip

Objectives

When the deformation is static, the behaviour of fundamental modes in a highly-deformed soft strip is well understood. In particular, flexural modes are highly dependent on predeformation and their velocities, in the low-frequency regime, are given by the applied stress. In this chapter, we propose a novel experimental setup to apply an increasing stress in the soft strip to enable a time modulation for these fundamental modes. Surprisingly, the induced deformation does not grow linearly as expected, but propagates as a step function. Once this step has been passed, the strip not only is deformed, but also translates at a constant speed. After properly characterizing this phenomenon, we understood that we could use it as a space-time interface. We therefore observed the passage of flexural waves through this space-time interface and measured frequency and wavenumber changes. The case of a superluminal interface is also investigated, promising very interesting observations in terms of wave manipulation. Finally, we speculate that this work will enable the observation of exotic phenomena and analogies with astrophysics in the future.

- An experimental setup is introduced to allow for time modulation of flexural waves
- A deformation wavefront is observed, leading to a deformed and moving strip
- The travelling wave separates 2 media and corresponds to a space-time interface
- Frequency and wavenumber jumps are measured for flexural waves crossing the interface, or being caught up by it
- Other wave manipulations are theoretically explored

Contents

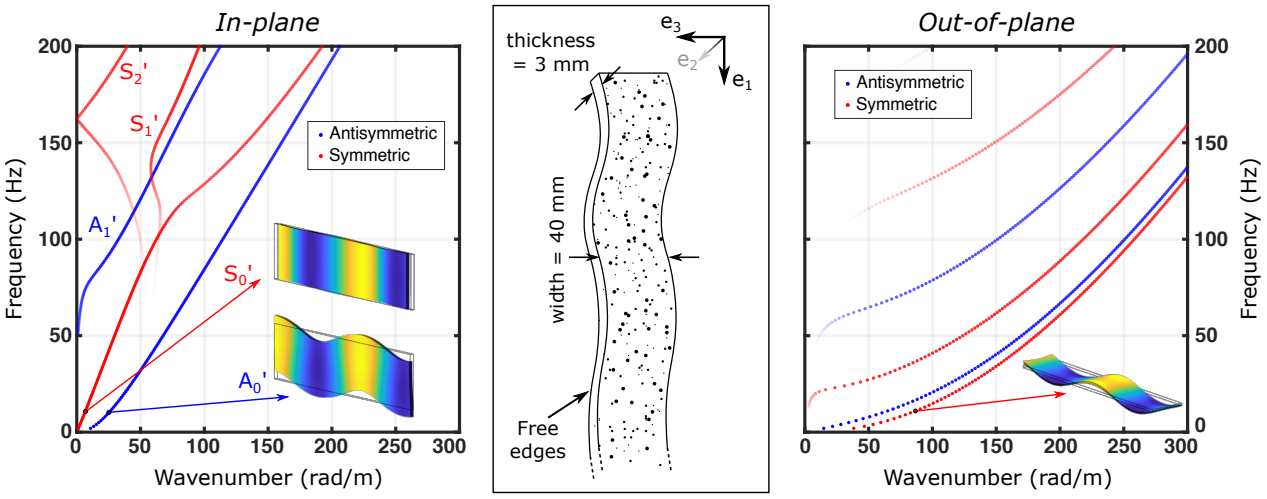

FIGURE 5.1: **Dispersion curves in a free strip** – Guided elastic waves in a strip of geometry 60 cm × 3 mm × 4 cm in (x_1, x_2, x_3) coordinate system with free boundary conditions. The material is assumed isotropic and viscoelastic. Modes are classified according to their polarization and symmetry.

1 An original idea: the expanding media

1.1 Reminder about guided waves in a strip with free edge

Throughout this thesis, we have studied guided elastic waves in strips and here, we provide a quick summary. First, let us start by sketching out the problem, as illustrated in figure 5.1. The propagation axis is still set as x_1 while the thickness $h = 3$ mm and width $b = 4$ cm are again along x_2 and x_3. Free boundary conditions are also considered everywhere. The equation of motion and the material model are unchanged (see chapters 2 and 3). The dispersion curves in such a strip are computed using the Spectral Collocation Method (SCM), and are displayed in figure 5.1. Guided waves are split into two families depending on their polarization (either in-plane or out-of-plane), and each family is again split into two families depending on their symmetry with respect to the $(x_3 = 0)$-plane. Three fundamental modes coexist. The first flexural mode (bending in the (x_1, x_2)-plane) and the first two in-plane guided waves S_0' (compression) and A_0' (bending in the (x_1, x_3)-plane) which are symmetrical and anti-symmetrical with respect to the $(x_3 = 0)$-plane, respectively. Their asymptotic dispersions are given in chapter 3, as well as their displacement profiles that are recalled in figure 5.1.

1.2 The effect of prestress on the fundamental modes

In chapter 3, we investigated the effect of a static prestress on the guided waves in a strip and we recall here, the results obtained for the fundamental modes. The zero-frequency limit for the velocities of the fundamental modes reads $\rho V^2 = \sigma$ for flexural waves, and $\rho V^2 = \tilde{E}$ for the compression mode S_0', $\tilde{E}$ being the equivalent Young modulus given by ZHAO and CHANG (2021)[110] and detailed in equation (3.2) when the viscoelasticity is omitted.

Results are shown in figure 5.2. First, dispersion curves are plotted for frequencies ranging from 0 to 200 Hz for $\lambda = 1$ or 2. Thin light colored lines corresponds to the undeformed strip ($\lambda = 1$). On the other side, thick dark colored lines corresponds to the deformed strip ($\lambda = 2$). To compare these results with analytical predictions described previously, phase velocities are computed at 10 Hz

[110] ZHAO and CHANG (2021): "Elastic wave velocities in finitely pre-stretched soft fibers"

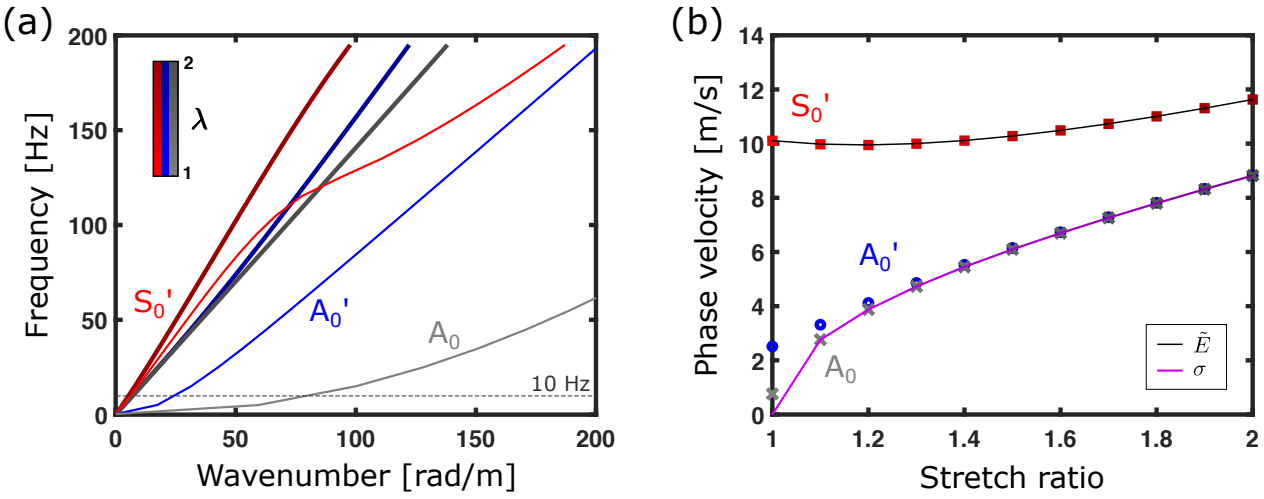

FIGURE 5.2: **The effect of prestress on fundamental modes** – The strip of dimensions 60 cm × 3 mm × 4 cm with free boundary conditions, is submitted to a uniaxial tension. (a) Dispersion curves (given by the SCM) are plotted for an undeformed (thin light lines) and a deformed strip with ($\lambda = 2$) (thick dark lines). (b) Phase velocities are computed at 10 Hz and compared to analytical predictions.

(low frequency) and plotted as a function of the stretch ratio. These analytical predictions perfectly depict the evolution of flexural mode velocities with the applied tension. Differences may appear at low stretch ratios because flexural modes have non-zero velocities at the considered frequency of 10 Hz, which by definition does not correspond to the zero-frequency limit. Overall, differences in phase velocities are huge and doubling the stretch ratio leads to quadrupling the velocities of the flexural modes. The combination of the equivalent elasticity tensor $\mathbf{C}^{\omega}$ together with the equivalent Young's modulus formula[110] provides an exact prediction for the velocity of the compression mode, still in the low frequency regime. This equivalent elasticity tensor (derived from our material model) is once again the key item to understand wave propagation in a prestressed strip. In the following, we stick to our visco-hyperelastic model combined with the SCM so that we can work at higher frequencies and not suffer too much from the zero-frequency limit from these analytical predictions.

So far, we mainly focused on the effect of a static prestress on guided waves. We saw that the applied stress can have a significant effect on the velocities of flexural waves. We now wonder what happens if this large prestress varies in time.

1.3 Creating a time-varying medium

For a long time, we have been using media with spatial variations to manipulate waves. A waveguide geometry is an example of this type of medium, where spatial interfaces not only force the propagation of a wave in one direction, but also greatly enrich the physics involved.

Time-varying media are less common but have recently been used to control waves in optics or electromagnetism. What is special about these environments is that, unlike spatial structures, they no longer conserve the frequency ω. They first appeared in the 1970s with theoretical works from FELSEN and WHITMAN (1970)[211] and FANTE (1971)[212] and quickly found applications in plasma physics[213]. Theoretical work did not stop here, and everything that was known about spatial

[110] ZHAO and CHANG (2021): "Elastic wave velocities in finitely pre-stretched soft fibers"
[211] FELSEN and WHITMAN (1970): "Wave propagation in time-varying media"
[212] FANTE (1971): "Transmission of electromagnetic waves into time-varying media"
[213] KALLURI (2010): *Electromagnetics of Time Varying Complex Media: Frequency and Polarization Transformer, 2nd Edition*

modulations was used as an inspiration to study time-varying media, such as interactions with one or more time interfaces[214,215]. With this motivation, interest has also grown in time crystals, which can be seen as periodic temporal modulation of the wave velocity[216,217,218,219,220,221].

This notion quickly conquered the field of metamaterials[222], where time t appeared as a new degree of freedom to dramatically increase the possible wave manipulations[223,224]. An exhaustive state of the art on these applications is beyond the scope of this chapter but recent reviews can be found in Galiffi et al. (2022)[225] or Pacheco-Peña et al. (2022)[226]. The concept of time-varying media has also been exported to other fields than optics and electromagnetics, such as quantum physics[227], underwater acoustics[228], acoustics[229], elasticity[230] or water waves[231,232].

From the above reminders, we know that a prestress results in a significant increase in the velocity of flexural waves, so it is a great way to control the wave. The idea here is to generate a flexural wave in an undeformed strip, let it propagate a few centimeters, and then apply an increasing uniaxial stress in the strip, so that a wave packet would propagate in a time-varying strip.

If we ever manage to create this kind of time-varying media, we should be able to perform huge frequency conversions. Additional questions logically arise, such as: What happens when you increase the uniaxial stress quickly or slowly compared to the initial wave velocity? What happens the other way around if you start with a prestressed strip that you let go back to its initial undeformed shape, *i.e.* in a medium that shrinks over time?

1.4 Space and time interfaces

Before detailing the experiment, we compare the interactions of a wave with a space or a time interface.

Crossing a space interface The case of a wave crossing a space interface is well-known but notations need to be introduced. We consider a 1D problem with space coordinates x_1. A system with a space interface in $x_1 = 0$ is assumed time-invariant: the material properties are not changing in time. This invariance directly leads to the conservation of the angular frequency ω, accordingly to Noether's theorem. Rather than writing general relations for the evolution of wavenumbers in such a system, we can graphically represent them for a given mode (A_0' for example) in figure 5.3(a). Knowing that the angular frequency ω is conserved, and that the pair (k, ω) must remain on the corresponding dispersion curves, the crossing of a space interface induces a conversion represented by the horizontal black arrow. Space interface is now well understood so we consider its time counterpart.

Crossing a time interface Space and time are essentially symmetric in the framework of propagative waves, via the phase $\phi = k_1 x_1 - \omega t$. In this last expression, we see that x_1 and t play interchangeable functions. When the system is varying in space and invariant in time, the angular frequency ω is conserved. Similarly, when the system is varying in time and invariant in space, the wavenumber k_1 is conserved. Using this property, it is possible to guess how the conversion is made

[214] Mendonça and Shukla (2002): "Time Refraction and Time Reflection: Two Basic Concepts"
[215] Mendonça et al. (2003): "Temporal beam splitter and temporal interference"
[216] Else et al. (2016): "Floquet Time Crystals"
[217] Choi et al. (2017): "Observation of discrete time-crystalline order in a disordered dipolar many-body system"
[218] Zhang et al. (2017): "Observation of a discrete time crystal"
[219] Milton and Mattei (2017): "Field patterns: a new mathematical object"
[220] Sacha and Zakrzewski (2017): "Time crystals: a review"
[221] Apffel et al. (2022): "Experimental Implementation of Wave Propagation in Disordered Time-Varying Media"
[222] Ramaccia et al. (2021): "Temporal multilayer structures for designing higher-order transfer functions using time-varying

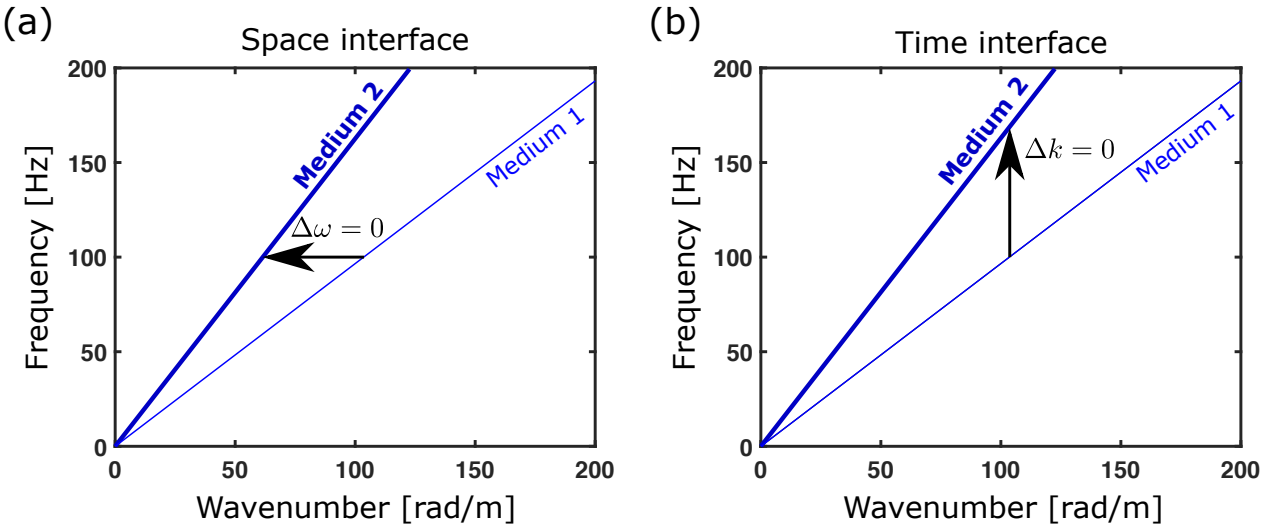

FIGURE 5.3: **Crossing a space or a time interface** – Assuming a non-dispersive propagation in media 1 and 2, the crossing of a space (a) or a time (b) interface are illustrated by horizontal ($\Delta\omega = 0$) or vertical ($\Delta k = 0$) jumps from a dispersion curve to another.

i.e. with a vertical black arrow, as represented in figure 5.3. When the wave of interest is non-dispersive, the velocity change does not depend on the interface but the pairs (k, ω) after conversion are different. In a dispersive medium, the velocities after conversion depend on the nature of the interface. For example, APFFEL and FORT (2022)[232] used successive space and time interfaces to achieve large frequency conversions of water waves.

2 Dynamic stretching of the strip

2.1 Experimental setup

Contrary to experiments carried out in chapters 2 and 3, we need a way to automatically control the strip deformation. To do so, we modified the experimental setup presented in figure 1.16 and the new one is introduced in figure 5.4. A motor is used to drive and control the pulling of an initially loosen rope, at a velocity V_{pulling}. A three-phase asynchronous motor with an integrated variable speed drive (Varmeca VMA31M) is used, in combination with an homemade electronic assembly. This electronic assembly is made of an Arduino board (Circuit Playground Express, Adafruit), power relays and a digital potentiometer. Its many functions are: controlling the motor rotation speed using the digital potentiometer and integrated variable speed drive, controlling the direction of rotation, switching on and off the motor using a power relay. Last but not least, motion detectors are also created by facing a red LED with a simple photodiode. The photodiode signal is monitored

metamaterials"
[223] HUANG and ZHOU (2019): "A time-varying mass metamaterial for non-reciprocal wave propagation"
[224] ENGHETA (2021): "Metamaterials with high degrees of freedom: space, time, and more"
[225] GALIFFI et al. (2022): "Photonics of time-varying media"
[226] PACHECO-PEÑA et al. (2022): "Time-varying electromagnetic media: opinion"
[227] DODONOV et al. (1993): "Quantum phenomena in nonstationary media"
[228] JOSSO et al. (2010): "Time-varying wideband underwater acoustic channel estimation for OFDM communications"
[229] WANG et al. (2015): "Acoustic asymmetric transmission based on time-dependent dynamical scattering"
[230] NASSAR et al. (2020): "Nonreciprocity in acoustic and elastic materials"
[231] D'HARDEMARE et al. (2020): "Probing Floquet modes in a time periodic system with time defects using Faraday instability"
[232] APFFEL and FORT (2022): "Frequency Conversion Cascade by Crossing Multiple Space and Time Interfaces"
[232] APFFEL and FORT (2022): "Frequency Conversion Cascade by Crossing Multiple Space and Time Interfaces"

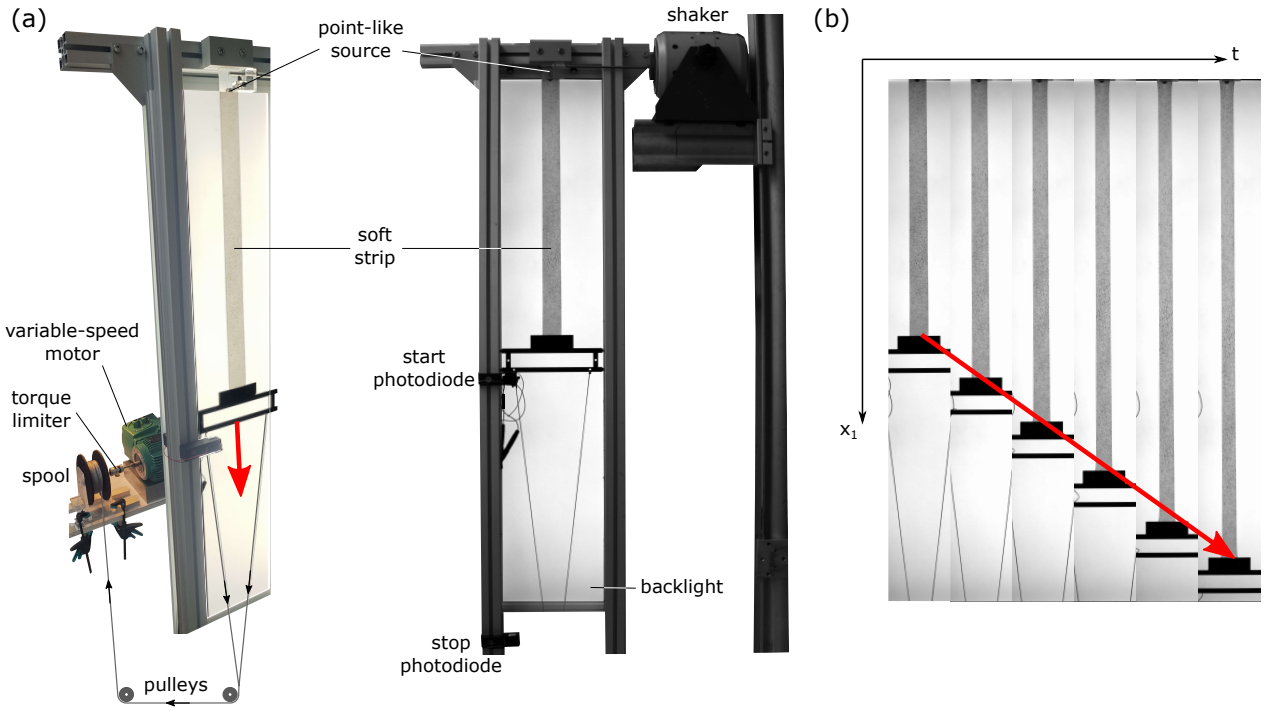

FIGURE 5.4: **Experimental setup to study guided waves in a time-varying strip** – The setup is improved to allow for an automatic control of the prestress in the strip. (a) The combination of the motor and a spool pulls the rope at a given linear pulling velocity V_{pulling}. Triggering is handled via a photodiode-based motion detector "start photodiode". (b) Example of acquired frames using this setup. The bottom of the strip is pulled at a constant velocity V_{pulling}, indicated by the red arrow.

by the board and triggers both the camera and the signal generator supplying the shaker, *i.e.* the wave packet emission.

Let us go through the different steps of this experimental method. The rope is initially loose since the motor needs some time before reaching its final rotating speed, see Appendix A for more details. Then, the motor is switched on, the rope wraps around the spool and when it is no longer loose, it pulls on the bottom of the strip at a constant velocity V_{pulling}. At this time, the wave packet is emitted and the recording begins. The stroboscopy, initially implemented to overcome the camera limited acquisition framerate, is no longer possible. However, by largely reducing the field of view to a few lines (around 50), 255 frames are recorded at a frame rate of 1000 Hz, enabling good tracking of the strip. Furthermore, a 25-mm lens is used to get a large distance along x_1, as you can see in figure 5.4(b). In a fraction of a second, the strip length doubles and the bottom of the strip reaches the "stop photodiode". At this point, the signal suddenly changes and the board switches off the motor.

2.2 Post-processing

Once the recording stopped, the first step of the post-processing is to use an enhanced version of the DIC that we called the iterative Digital Image Correlation (iDIC). The objective is to gather the displacement u_1 in a single matrix $u_1(X_1^0, t)$ (same for u_3). However, it is not possible to use the first image as a reference of the whole movie since images are then too different and classical DIC fails. Therefore, we apply the DIC between successive images, as is often done in Particle Image Velocity algorithms.

First, we apply the DIC to the first two images to get the displacement $\mathbf{u}\left(X_1^0, X_3^0, t_0\right)$, where $X_1^0 = X_1(t_0), X_3^0 = X_3(t_0)$ are the in-plane coordinates in the undeformed strip. Then, the DIC is applied to the second and third images. A new displacement is obtained $\mathbf{u}\left(X_1(t_1), X_3(t_1), t_1\right)$ where $\left(X_1(t_1), X_3(t_1)\right) \neq \left(X_1^0, X_3^0\right)$ since the DIC uses a new reference image and thus creates a new grid at t_1, which is different from the first one. To find back $\mathbf{u}\left(X_1^0, X_3^0, t_1\right)$, we deform the initial grid $\left(X_1^0, X_2^0\right)$ using the previous displacement: $X_1^0 + u_1\left(X_1^0, X_3^0, t_0\right), X_3^0 + u_3\left(X_1^0, X_3^0, t_0\right)$ and we interpolate the newly obtained displacement $\mathbf{u}\left(X_1(t_1), X_3(t_1), t_1\right)$ on this deformed grid. Doing so gives $\mathbf{u}\left(X_1^0, X_3^0, t_1\right)$ which is the displacement between times t_0 and t_1 expressed in the reference configuration using in-plane coordinates of the undeformed strip. To have the displacement between the first and third images, one should compute $\mathbf{u}\left(X_1^0, X_3^0, t_0\right) + \mathbf{u}\left(X_1^0, X_3^0, t_1\right)$.
At step $i+1$, $\mathbf{u}\left(X_1(t_i), X_3(t_i), t_i\right)$ is obtained and interpolated on the deformed grid of the previous iteration:

$$\begin{cases} X_1^0 + \displaystyle\sum_{k=0}^{i-1} u_1\left(X_1^0, X_3^0, t_k\right) \\ X_3^0 + \displaystyle\sum_{k=0}^{i-1} u_3\left(X_1^0, X_3^0, t_k\right) \end{cases} \tag{5.1}$$

and the displacement at each time t_i is expressed in the reference coordinates $\left(X_1^0, X_3^0\right)$:

$$\begin{cases} u_1^{\text{tot}}\left(X_1^0, X_3^0, t_i\right) = \displaystyle\sum_{k=0}^{i-1} u_1\left(X_1^0, X_3^0, t_k\right) \\ u_3^{\text{tot}}\left(X_1^0, X_3^0, t_i\right) = \displaystyle\sum_{k=0}^{i-1} u_3\left(X_1^0, X_3^0, t_k\right) \end{cases} \tag{5.2}$$

In practice, as we apply a uniaxial stress, we have reduced the number of lines (X_3 direction) such that the displacement $\mathbf{u}$ is only measured as a function of X_1^0, but displacement u_3 is still measured. Finally, two maps representing the displacement along the strip axis $u_1^{\text{tot}}\left(X_1^0, t_i\right)$ and transversely to it $u_3^{\text{tot}}\left(X_1^0, t_i\right)$ are obtained.

2.3 Evidence of a transition wave

We can display maps as a function of the reference coordinate X_1^0 and time t, but we can also display them as a function of the deformed coordinate $X_1^0 + u_1^{\text{tot}}\left(X_1^0, t\right)$ and time t. Both are performed and discussed in the following.

We first study the evolution of u_1^{tot} in space and time. We plot successive frames of the recorded movie in figure 5.5. It clearly appears that the bottom edge goes down with a constant velocity $V_{\text{pulling}} = 2.05$ m/s. The displacement u_1^{tot} is extracted, and the contours of the corresponding colored surface are plotted using deformed coordinates. These contours help visualize these maps: the closer the lines, the higher the changes. The first blue line starting at ($t = 0$ ms, $x = 50$ cm) corresponds to points that have just started moving.

Then, for each time, we compute the gradient of u_1^{tot} with respect to undeformed coordinates X_1^0 giving us the local stretch ratio:

$$\lambda_1 = 1 + \frac{\partial u_1^{\text{tot}}}{\partial X_1^0}.$$

Again, we plot the stretch ratio using deformed coordinates.

Contrary to the naive belief that the pulling will create a uniform stretching in the strip, this map exhibits a very different behavior. The deformation is neither homogeneous in space, nor increasing linearly with time. Instead, a wavefront separating an undeformed ($\lambda_1 = 1$) and a stretched portion of the strip travels from the bottom to the top at early times. This is visible in the displacement

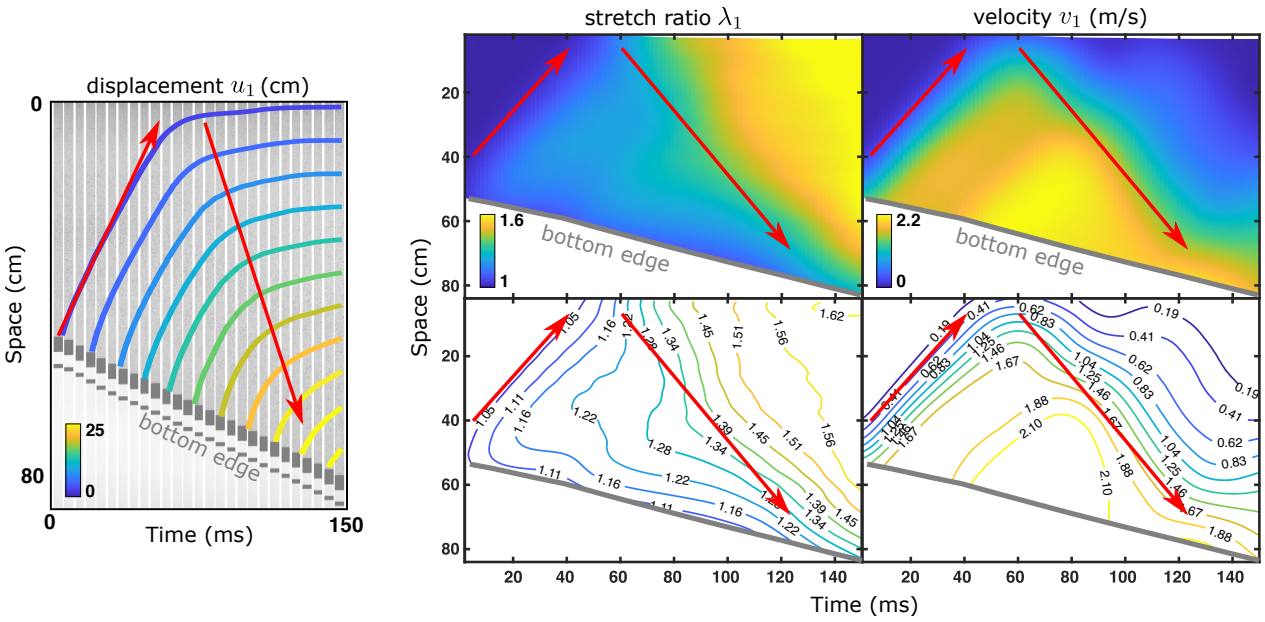

FIGURE 5.5: **First observation of the transition wave** – The displacement u_1^{tot} is extracted from the recorded movie. The stretch ratio λ_1 and the particle velocity v_1 are plotted using deformed coordinates. To help visualize these maps, contours of these colored surfaces are also plotted. Red arrows represent the observed deformation wavefront.

map, where the blue line goes up. The wave actually carries information about the deformation taking place at the bottom of the strip. A given area remains at rest until the wave reaches it, and only then does it deform. This is known as a transition wave. Note that a reflection occurs at the top edge (not visible on acquired frames), but we will come back on this point in the last section of this chapter.

This transition wave is all the more remarkable on the contours drawn in the bottom of figure 5.5, and its propagation is indicated by red arrows. The question then arises: what is the nature of this wave and what governs its velocity? A rough estimate is 10 m/s, and this value should ring a bell because it is approximately the S_0' velocity.

To get a more precise value, the stretch ratio map is saturated as presented in figure 5.6(a) and we now want to extract the slope of this blue-yellow interface. At each deformed coordinate x_1, we look for the time when the stretch ratio exceeds a given threshold (1.02 for example). Thus, space-time coordinates (x_1, t) of this blue-yellow interface are extracted and plotted in figure 5.6(b). The slope of the linear regression gives the interface velocity $V_{\text{interface}} = 9.77$ m/s. This information propagates along x_1 and the related deformation is mainly in this same direction, leading us to the conclusion that this transition wave is in fact the compression mode propagating in a strip, namely the S_0' mode discussed in chapter 3.

These first observations lead us to the conclusion that our initial idea of a time-varying medium was indeed naive. Fortunately, this transition wave will prove to be very promising for enriched physics.

2.4 Characterizing the post-transition medium

To sum up, when pulling the strip edge, the bottom end starts being deformed and this deformation propagates as a transition wave, carrying information that we want to characterize. To start, we look into the value of the stretch ratio once the wave has travelled.

A simple derivation consists in considering a small portion $[X; X + \mathrm{d}X]$ of the strip. At time t_0,

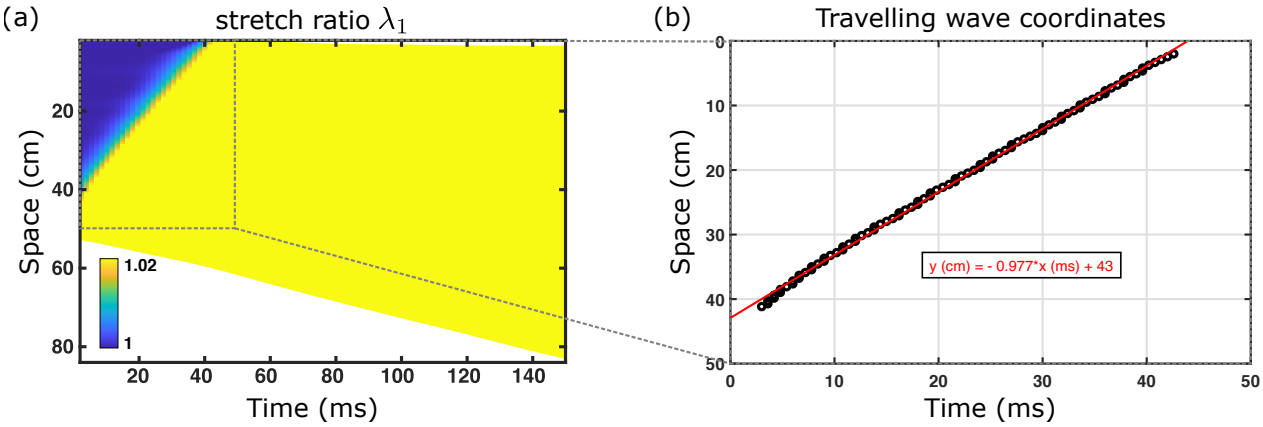

FIGURE 5.6: **Extraction of the transition wave velocity** – (a) The stretch ratio map is saturated so that every value above a given threshold of $\lambda_1 = 1.02$ appears yellow (and blue for values below). Red arrows still represent the deformation wavefront. (b) Space-time coordinates (x_1, t) of the interface are plotted and a transition wave velocity of 9.77 m/s is measured.

the transition wave arrives at coordinate $X + \mathrm{d}X$ (given the representation in figure 5.4b), and at $t_0 + \mathrm{d}t$, it went up and reached the coordinate X. Using the transition wave velocity $V_{\text{interface}}$, it is easy to derive $\mathrm{d}t = \dfrac{\mathrm{d}X}{V_{\text{interface}}}$. During this time, the material at coordinate X has not moved since the information has not arrived yet, but the material at $X + \mathrm{d}X$ has moved at a velocity V_{pulling}. Thus, at time $t + \mathrm{d}t$, the new material length is $\mathrm{d}X + V_{\text{pulling}}\mathrm{d}t$. Replacing $\mathrm{d}t$, one gets the stretch ratio:

$$\lambda_1 = 1 + \frac{V_{\text{pulling}}}{V_{\text{interface}}} \tag{5.3}$$

Although we were surprised to see this transition wave, it has in fact already been observed and studied in a rubber band[233] or a slinky[234]. Equation (5.3) is consistent with these works.

Let's check that this relationship holds for other acquisitions with various V_{pulling}. Results are shown in figure 5.7, where we added the prediction using equation (5.3) and the value for $V_{\text{interface}} = 7.9$ m/s. The agreement with the prediction is quite good as long as the interface speed is set to 7.9 m/s which is a little different from 9.77 m/s measured in figure 5.6. The nature of this transition wave is not in question, but it would seem that equation (5.3) is too simplistic. To improve this model, and as seen many times along this thesis, it would certainly be necessary to take into account the viscoelasticity of the material, but it is complex to deal with a fractional time derivative when it is not in a harmonic regime.

There is another physical component. The material is not only deformed after the transition wave passed by, but it also gains a drift velocity. This is particularly noticeable when plotting the particle velocity $v_1 = \dfrac{\partial u_1}{\partial t}$ as a function of the deformed coordinate x_1 in figure 5.5. According to figure 5.5, once deformed, the material has a velocity of 2.2 m/s, which is in good agreement with the pulling velocity of the bottom edge at 2.05 m/s. Using equation (5.3), a stretch of ratio of 1.22 should be obtained, and this is confirmed by the contour plot in figure 5.5.

To sum up, by pulling the bottom strip edge at a constant velocity V_{pulling}, a transition wave is emitted in the material and carries both the information about deformation in the material, but also the acquired velocity. This transition wave separates two media. Above, the material is undeformed and static. Below, the material is uniformly stretched and moving at a constant speed. Against

[233] VERMOREL et al. (2006): "Rubber band recoil"
[234] CROSS and WHEATLAND (2012): "Modeling a falling slinky"

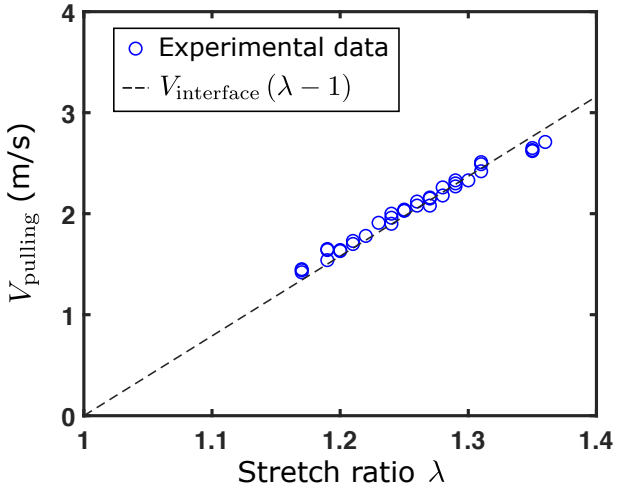

FIGURE 5.7: **Stretch ratio as a function of the particle velocity** – For each experiment, both the stretch ratio and particle velocity are extracted just after the transition wave has passed. A prediction using equation (5.3) and $V_{\text{interface}} = 7.9$ m/s is added.

the odds, we have created a moving interface. Thus, we expect great effect for flexural waves when crossing this interface, as will be seen in figure 5.8.

3 Elastic waves in a space-time-varying medium

3.1 Dispersion curves for each medium

We need to adapt what we have seen in figure 5.2 for fundamental modes in a strip which is not only deformed but also moving at a constant speed. We can certainly neglect relativistic effects and apply a simple additive law for phase velocities. This can be implemented in two ways depending on the choice to either change frequencies or wavenumbers in the dispersion diagram:

$$\omega' = \omega + V_{\text{pulling}} k \quad \text{or} \quad k' = \frac{\frac{\omega}{k}}{\frac{\omega}{k} + V_{\text{pulling}}} k \tag{5.4}$$

The choice seems arbitrary and we decide to change wavenumbers. Using equation (5.3) and (5.4), one can plot the dispersion curves for flexural waves in a strip which is both deformed and moving at a constant velocity, presented in figure 5.8. Just like for figure 5.2, we plot the dispersion curves of flexural modes in a stationary undeformed strip (thin light lines), in a stationary deformed strip (light dashed lines) and also in a deformed strip ($\lambda_1 = 1.3$) moving at a constant speed $V_{\text{pulling}} = V_{\text{interface}}\,(\lambda_1 - 1)$ (thick dark lines). However, it is noteworthy that the symmetry $k_1 \leftrightarrow -k_1$ is now lost and this is why we plot branches for propagation in x_1 and $-x_1$ directions. Waves in a moving medium are not so common in optics or electromagnetism and are often associated with theoretical difficulties due to relativistic effects. Nevertheless, properties for waves in these media can be very interesting and have been exploited for the last two decades or so in the water wave community to build fascinating analogies with cosmological objects and phenomena[235,236,237,238,239,240]. We will

[235] ROUSSEAUX et al. (2008): "Observation of negative-frequency waves in a water tank: a classical analogue to the Hawking effect?"
[236] BARCELÓ et al. (2011): "Analogue Gravity"
[237] FACCIO et al. (2013): *Analogue Gravity Phenomenology: Analogue Spacetimes and Horizons, from Theory to Experiment*
[238] PELOQUIN et al. (2016): "Analog wormholes and black hole laser effects in hydrodynamics"
[239] DAS et al. (2018): "Dynamics of flexural gravity waves: from sea ice to Hawking radiation and analogue gravity"
[240] EUVÉ et al. (2020): "Scattering of Co-Current Surface Waves on an Analogue Black Hole"

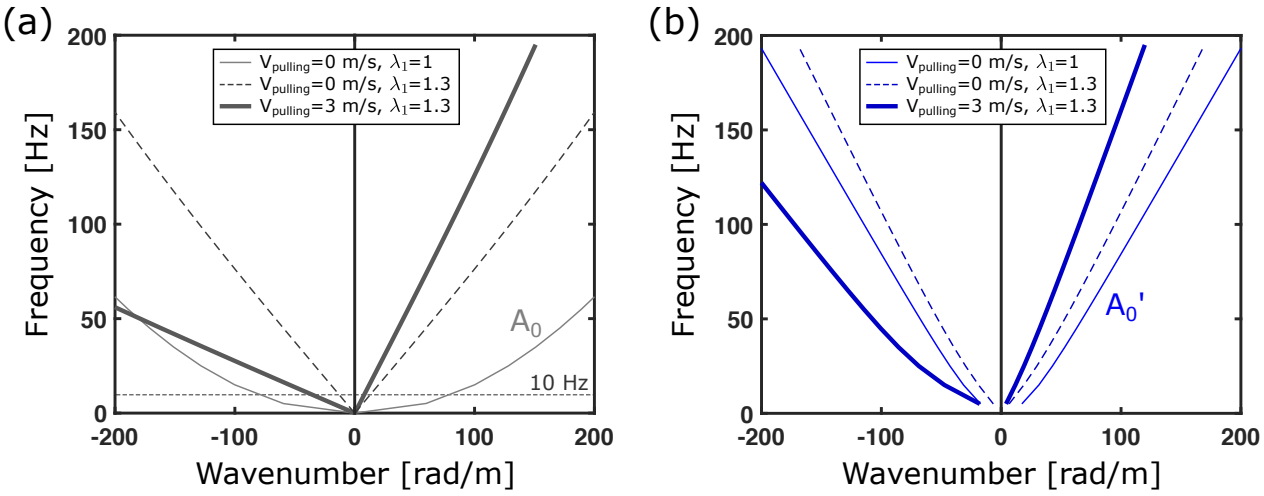

FIGURE 5.8: **Dispersion curves are modified in a moving deformed strip** – A strip of dimensions 60 cm × 3 mm × 4 cm with free boundary conditions, is deformed and moving at a constant velocity $V_{\text{pulling}} = V_{\text{interface}}\,(\lambda_1 - 1)$ where $V_{\text{interface}} = 10$ m/s is approximated. Dispersion curves of the flexural wave along the thickness (a) and along the width (b) are plotted for a stationary undeformed (thin light lines), stationary deformed (thin dashed lines) and a moving deformed strip with $(\lambda = 1.3, V_{\text{pulling}} = 3$ m/s) (thick dark lines). The symmetry $k_1 \leftrightarrow -k_1$ is now broken.

come back on this point at the very end of this chapter.

3.2 Crossing a space-time interface

In a previous section, we mentioned the advantages of working with time-varying media. Here, we go even further, because the properties change not only over time, but also in space. In fact, when the community realised that time metamaterials could be produced, enormous interest quickly arose in space-time metamaterials, where a classic metamaterial also sees its properties vary in time, making 4D modulation possible[241,242,224,243,244]. From then on, there was a lot of theoretical work on the subject, but experiments were rarer. Thus we realised that our experiment could serve as an analogue for visualising and studying this physics. The simplest modulation is probably the interface. In fact, this is also what other physicists have decided to start with[245,242]. Note that it was already a center of interest 50 years ago[246,247]. It seems that the literature on these questions is still fairly sparse, and it is currently quite difficult to bring together the communities that have studied a moving interface, even though it seems to be appearing in several areas of physics. There is probably still work to be done on this point.

To finish this thesis, we first describe the main features of such a space-time interface, but we do not discuss the transmission and reflection coefficients of such moving interfaces. Then, we implement it experimentally in two possible configurations. The wave and interface either propagate in opposite directions or in the same direction.

[241] HUIDOBRO et al. (2019): "Fresnel drag in space–time-modulated metamaterials"
[242] CALOZ and DECK-LEGER (2020): "Spacetime Metamaterials - Part I: General Concepts"
[224] ENGHETA (2021): "Metamaterials with high degrees of freedom: space, time, and more"
[243] CHEN et al. (2021): "Efficient nonreciprocal mode transitions in spatiotemporally modulated acoustic metamaterials"
[244] WEN et al. (2022): "Unidirectional amplification with acoustic non-Hermitian space-time varying metamaterial"
[245] GAAFAR et al. (2019): "Front-induced transitions"
[242] CALOZ and DECK-LEGER (2020): "Spacetime Metamaterials - Part I: General Concepts"
[246] LAMPE et al. (1978): "Interaction of electromagnetic waves with a moving ionization front"
[247] TSAI and AULD (1967): "Wave Interactions with Moving Boundaries"

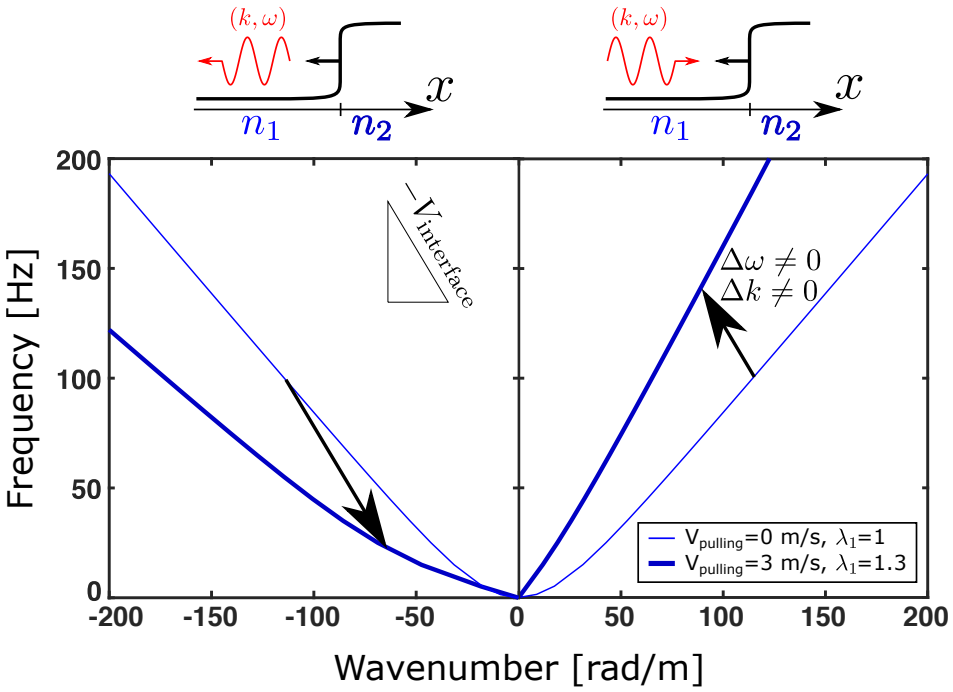

FIGURE 5.9: **Crossing a space-time interface** – Using dispersion curves of the in-plane flexural mode A_0' in figure 5.8, the crossing of a moving interface is illustrated by a tilted ($\Delta\omega/\Delta k = -V_{\text{interface}}$) jump from a dispersion curve to another. Depending on the interface propagation direction, different conversions are expected.

Crossing a moving interface The frequency or wavenumber conversions presented in figure 5.3 should be adapted when considering a moving interface, *i.e.* a space-time interface. In that case, there are no space or time invariance anymore, so that neither the angular frequency ω nor the wavenumber k_1 are conserved. The conversion can no longer be represented by a horizontal or vertical black arrow, but rather a tilted one. By ensuring the phase continuity at the interface, elementary derivations provide:

$$\frac{\Delta\omega}{\Delta k} = V_{\text{interface}} \tag{5.5}$$

or $-V_{\text{interface}}$ if the wave and interface propagate in opposite directions.
Let's take a look at limit cases. When $V_{\text{interface}} \to 0$, the interface is not moving (space interface), and equation (5.5) provides $\Delta\omega = 0$ which is consistent with figure 5.3(a). When $V_{\text{interface}} \to \infty$, the interface propagates much faster compared to the wave of interest. In that case, the medium sees a very fast variation in time which looks the same for all points in the medium, it is a time interface. Equation (5.5) then provides $\Delta k = 0$. This is again consistent with figure 5.3(b).

Now that we have discussed these limit cases, let's represent the conversion in figure 5.9. As in the first experiment, the interface and the wave are propagating in opposite directions so that we need to consider $-V_{\text{interface}}$ in equation (5.5).

3.3 Frequency and wavenumbers shift when meeting in opposite directions

The two media being fully characterized, we generate a flexural wave. To get started, we select the A_0' mode because its measurement is fairly easy when using the u_3 displacement component.

Raw displacement maps The in-plane flexural mode A_0' is generated by the shaker at the top edge of the strip ($x_1 = 0$) and propagates toward the bottom of the strip ($k_1 > 0$). The generated

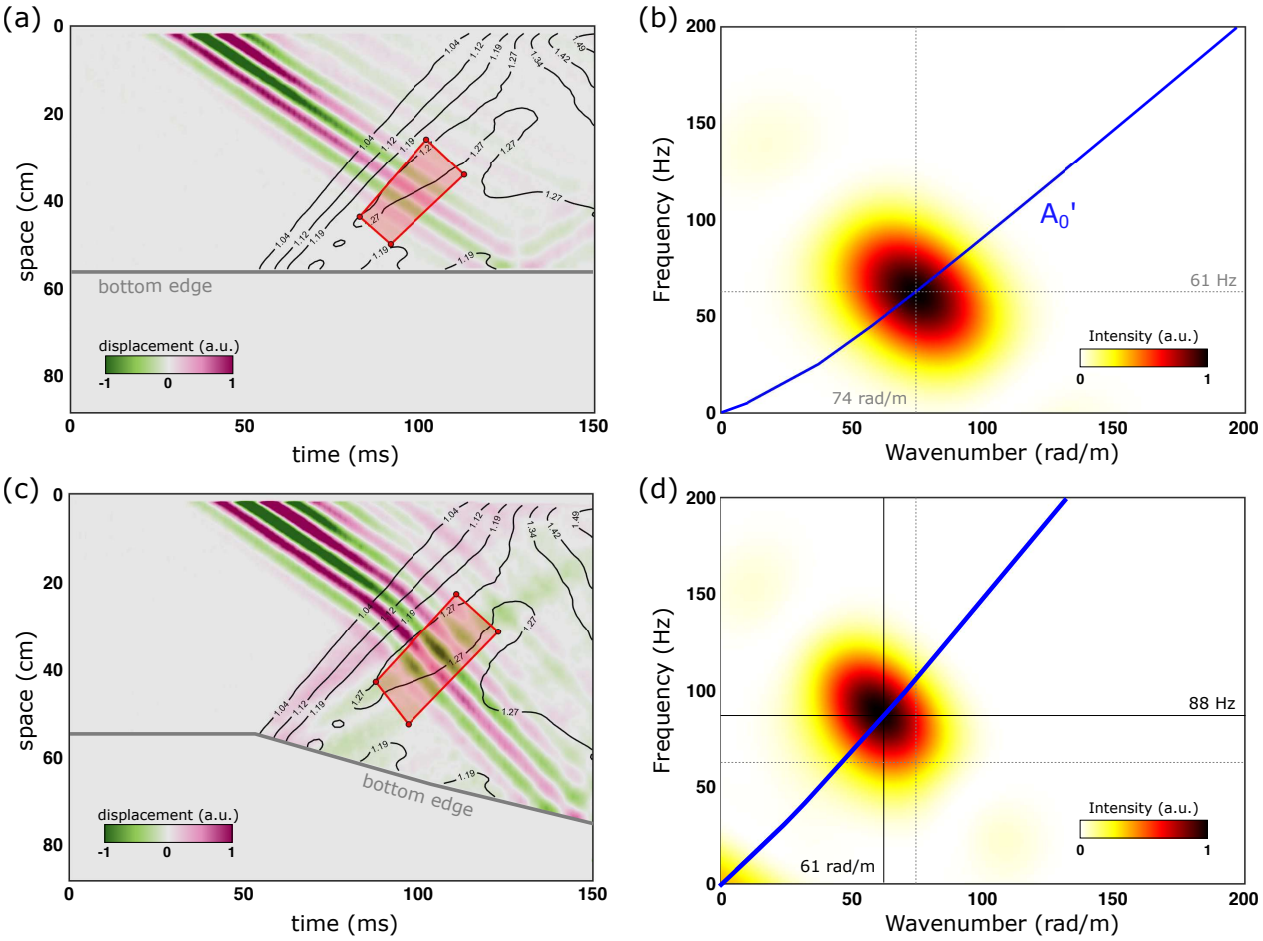

FIGURE 5.10: **Experimental observation of a flexural wave crossing the moving interface** – (a,c) The space-time diagram of the transverse displacement is plot with (c) or without (a) pulling. Contours representing the stretch ratio are extracted in (c) and then added in (a) to facilitate the red area positions. (b,d) 2D Fourier transforms are performed in red areas, and predictions are added in (b) for an undeformed strip and (d) for a deformed strip $\lambda_1 = 1.27$ moving at $V_{\text{pulling}} = 2.18$ m/s.

wave packet is an Hann function composed of 4 cycles at 70 Hz. To visualize the effect of this moving interface, we compare the propagation of the A_0' mode both in the case of an undeformed strip and in the case of the moving interface.

To offer more versatility in the wave packet emission, we also install a mechanical delay. The updated experimental setup is used to get the full space-time displacements maps, displayed in figure 5.10(a) and (c). Looking at stretch ratio contours in figure 5.10(a) and repeated in 5.10(c), one can notice a 50 ms mechanical delay with this updated setup. Moreover, this improvement was also accompanied by a user-defined 10 ms electronic delay in the wave packet emission. This delay allows the wave to cross the interface and arrive in a medium with a given stretch ratio $\lambda_1 = 1.27$ and velocity $V_{\text{pulling}} = 2.18$ m/s. The generated wave packet crosses the moving interface around the point ($t = 90$ ms, $x_1 = 30$ cm). We clearly see the velocity, given by the slope in figure 5.10(c), changes abruptly at this point.

Although the time and space invariance are broken in this system, the 2D Fourier Transform still provides valuable information about the spectral content of the A_0' mode both before and after crossing the moving interface. To select the appropriate signal, this Fourier transform is applied to the red region, which is also used to average stretch ratios and particle velocities to get $\lambda_1 = 1.27$ and

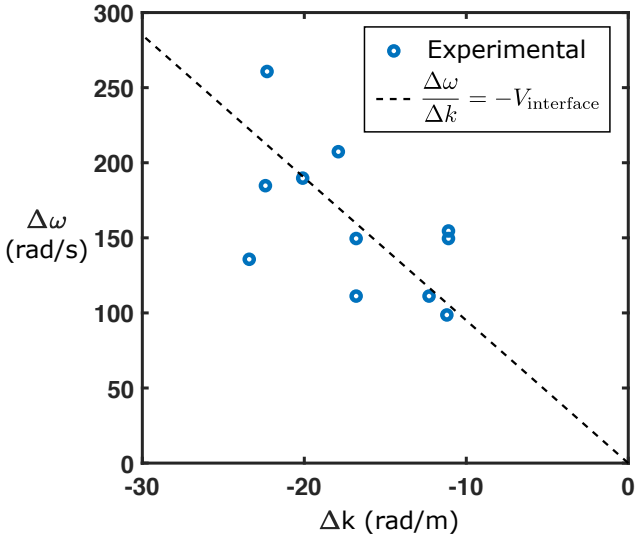

FIGURE 5.11: **Experimental results for frequency and wavenumber jumps** – The frequency and wavenumber of the A_0' mode are measured after the interface and compared to the case without interface. Changes in frequency and wavenumbers are confronted to theoretical predictions from equation (5.5) with $V_{\text{interface}} = 9.5$ m/s.

$V_{\text{pulling}} = 2.18$ m/s. Results are shown in figure 5.10(b) and (d). We can see that (k, f) coordinates of the main spot are different: the frequency increased while the wavenumber decreased.

Before discussing those variations, and because we can probe with a certain accuracy both the stretch ratio and particle velocity, we add theoretical predictions for the dispersion curves (blue lines). Please note that, in this experiment, the strip is initially stretched by 15%. This small amount of prestress keeps the strip aligned and avoids unwanted movements when the motor starts pulling. Main spots are indeed centered on the theoretical predictions curves, confirming that we have properly characterized the two media of interest. We now come back on the quantification of frequency and wavenumber changes.

Repeating this experiment for different frequencies and pulling velocities To check the validity of these measurements, we repeat them by varying the pulling velocity from 1.5 to 3.5 m/s and the initial wave packet frequency. It is difficult to make these measurements at low frequency because the wave packet temporal spread becomes too important and the whole wave packet does not necessarily experience the same thing. On the other hand, at high frequencies, the shaker is limited and the attenuation is very high. For these reasons, we stick to frequencies ranging from 60 to 130 Hz. On the whole, the trend is quite good, but observed variations do not follow theoretical predictions well, as can be seen in figure 5.11. To explain this, we can put forward some hypotheses. Firstly, the attenuation due to viscoelasticity leads to a measurement bias, which we compensated for as best we could, but it leads us to perform the 2D Fourier transform in small regions (red areas in figure 5.10) which result in wide spots. Secondly, there are some uncertainties in our measurements. For example, the deformed coordinate x_1 is deduced from the measured displacement u_1, and errors in this displacement pile up over the iterative DIC.

Theoretically, this was not discussed but one could expect a wave reflection on such a moving interface[242]. Here, no reflection is visible in figure 5.10. Similar observations were done by APFFEL and FORT (2022)[232] who did not see any reflection for water waves encountering a time interface and

[242] CALOZ and DECK-LEGER (2020): "Spacetime Metamaterials - Part I: General Concepts"
[232] APFFEL and FORT (2022): "Frequency Conversion Cascade by Crossing Multiple Space and Time Interfaces"

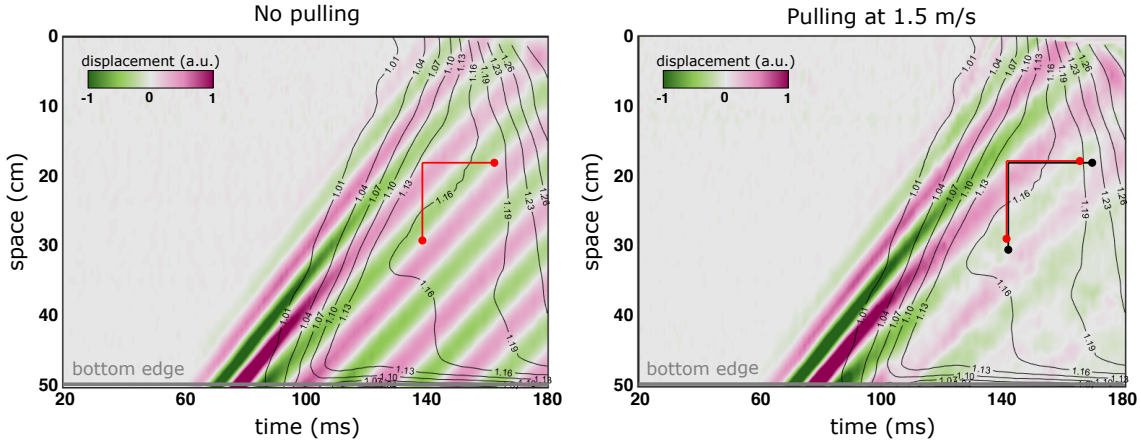

FIGURE 5.12: **Observation of a superluminal interface** – The space-time diagram of the transverse displacement is plot with (right) or without (left) pulling. Contours representing the stretch ratio are extracted when there is an interface (right), and superimposed on both diagrams. An indication of the period and wavelength are given by red lines (left) and should be compared to black lines (right).

assumed it originates from the inherent impedance matching when using water waves. We believe a similar assumption can be made in our case since the very definition of impedance for the A_0' mode (and more generally elastic guided waves) could not be found in the literature.

3.4 A superluminal interface catches up the wave

We have already demonstrated that the interface propagates faster, $V_{\text{interface}} \sim 10$ m/s, than the A_0' mode, $\omega/k \sim 5$ m/s. One could thus wonder what happens when the interface catches up with the wave, *i.e.* when the interface and wave propagate in the same direction. This superluminal case was studied by CALOZ and DECK-LEGER (2020)[242] for optics who took relativistic effects into account. Here, such effects can be neglected and predictions are much easier to implement.

Before explaining how to update the current experimental setup, we build these predictions in the ($k < 0$) region in figure 5.9. The interface still propagates from the bottom edge of the strip towards the top, but the wave is emitted in direction $-x_1$ and that is why we consider negative wavenumbers. The lowest medium is a stationary undeformed strip and the upper one is a deformed one moving opposite to the propagation direction. The equivalent conversion is again plotted as a tilted black arrow.

In figure 5.8 and figure 5.11, frequencies and wavelengths increased once the wave crossed the moving interface. However, in this configuration, while the wavelength are still expected to increase, frequencies should decrease.

Experimental demonstration We employ the same experimental setup but we lower the shaker to generate the wave packet near the strip bottom edge. Typical displacements maps are presented in figure 5.12. On the left part, there is no pulling; while on the right part, the motor is pulling at $\sim$1.5 m/s. This time, the change in slope is not very clear, but it can still be seen at the point with coordinates ($t = 100$ms, $x = 30$cm). What is more visible is the increase in both the wavelength and the time period, *i.e.* a decrease in both the wavenumber k and frequency ω. To understand the very small velocity change, we plot the dispersion curves as in figure 5.8, but with $V_{\text{pulling}} = 1.5$ m/s and $\lambda = 1.16$. A slight decrease in phase velocities (20%) is expected. This is indeed a measurable

[242] CALOZ and DECK-LEGER (2020): "Spacetime Metamaterials - Part I: General Concepts"

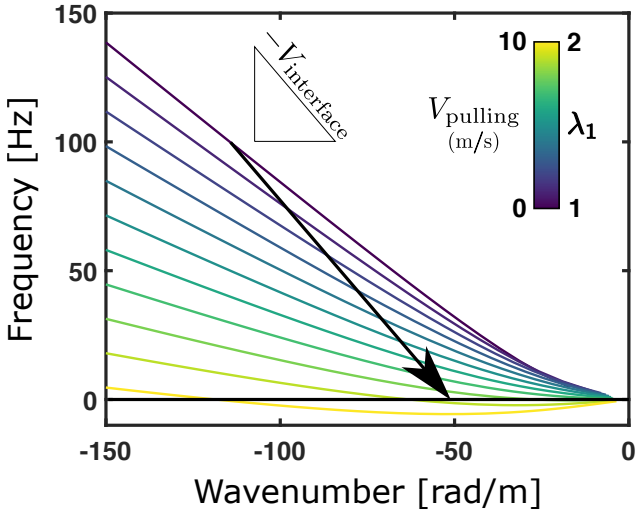

FIGURE 5.13: **Freezing the wave by increasing V_{pulling}** – Dispersion curves of the A_0' mode propagating along $-x_1$ are plotted for different pulling velocities V_{pulling} *i.e.* stretch ratios. Again, the interface is assumed to propagate along $-x_1$ and the black arrow represents the conversion when the wave crosses the moving interface. Here, a pulling velocity $V_{\text{pulling}} \sim 9$ m/s allows freezing the wave.

difference, but as we can see in figure 5.12, it's difficult to clearly define a region where the wave has fully crossed the interface. Quickly, both the wave and the interface have reached the top edge of the strip. Another limit also comes from the temporal spreading of the interface. It is quite smooth and spread over 25 ms, which is larger than the wave time period. For the moment, we have not modeled the shape of this moving interface, but it is clearly something we will be working on in the near future.

3.5 To go beyond

Even though the results obtained in this configuration are not completely satisfying because of the aforementioned limits, there is room for improvement and fascinating ideas. This last part is here to introduce them and explain why we have not been able to implement them yet.

Freezing the wave Despite the fact that velocity changes are not very important in our experiments (figure 5.10), an intriguing idea comes up when we see figures 5.8 and 5.9. Is there a way to pull faster on the strip so that the branch of the A_0' (or A_0) mode reaches or goes below the $\omega = 0$ axis ?

By carefully choosing the pulling velocity V_{pulling}, there should be a way to obtain a wave packet with $\omega = 0$ after crossing the interface. Let's still assume that λ_1 and V_{pulling} are related by equation (5.3). Dispersion curves of the A_0' mode for different stretch ratios $1 \leq \lambda_1 \leq 2$ are displayed in figure 5.13. The light green curve, at $V_{\text{pulling}} \sim 9$ m/s, reaches the $\omega = 0$ axis. The phase velocity then also goes to zero so the phase does not propagate anymore. The wave is thus frozen. Just as interesting, when the curve goes below the $\omega = 0$ axis, the phase velocity switches from positive to negative meaning the phase now propagates along x_1, in opposite direction compared to the initial wave. This is a so-called time-reversal operation. While it was already predicted for the reflection on a well chosen superluminal interface[242], this time-reversal operation appears here in transmission.

[242] CALOZ and DECK-LEGER (2020): "Spacetime Metamaterials - Part I: General Concepts"

We have tested this experiment by pushing the motor and our experimental facilities at their best and a velocity V_{pulling} of around 9 m/s was reached. Although we manage to measure a speed of around 9 m/s, we obtain a stretch ratio of 2.4, which is strangely no longer given by equation (5.3). This reveals an obstacle for two reasons. First, the higher the stretch ratio, the higher the pulling velocity needs to be to time-reverse the initial wave, and we are experimentally limited to this value of around 9 m/s. Second, at such a high stretch ratio, we know that our material model fails, as detailed at the end of chapter 2, in figure 2.9.
To achieve the above-mentioned regime, a redesign of the experimental set-up is probably needed, along with a smarter choice for the material and geometrical parameters.

Last but not least, a zero-group velocity point appears in a moving strip because of the flexural wave quadratic dispersion. We have already mentioned such points earlier in this thesis. A zero-group velocity mode is characterized by a wave packet energy that does not propagate *i.e.* remains located where it was generated. We can also notice that its phase velocity is also non-zero and positive, meaning that the phase actually propagates along x_1 but the envelope does not. Interestingly, in this configuration, the wave packet would indeed propagate until it crosses the moving interface. By carefully setting initial delays, it is thus possible to stop the energy at a precise location, which could be valuable for future applications.

Allowing the strip to shrink For now, we have only increase the deformation in the strip by pulling on it. We can imagine a whole range of other measurements in which a wave (such as the A_0' mode) is emitted in a stationary deformed strip, which is then allowed to retract. In this configuration, an interface again propagates along $-x_1$, but the information is different. Before the interface passes, the strip is stationary and deformed, but after it passes, the strip is undeformed and moving with a constant velocity along $-x_1$. The initial deformation λ_1 also sets the retracting velocity:

$$V_{\text{retracting}} = \left(1 - \frac{1}{\lambda_1^{\text{initial}}}\right) V_{S_0'}\left(\lambda_1^{\text{initial}}\right) \tag{5.6}$$

With this simple idea, let's display a similar graphical representation of frequency and wavenumber conversions when crossing the interface. The conversion is represented in figure 5.14(a), where $k_1 < 0$ corresponds to a wave emitted from the bottom, *i.e.* a superluminal configuration. When the interface velocity $V_{\text{interface}}$ is close to the wave velocity ω/k (thin line), great changes in frequency and wavenumber are expected, as noticeable in the superluminal case in figure 5.14.
Moreover, we can increase the initial stretch ratio, and thus the value for $V_{\text{retracting}}$, and plot corresponding dispersion curves in figure 5.14(b). When $V_{\text{retracting}}$ becomes large, around 6 m/s, it is possible to freeze a wave emitted from the top. Nevertheless, this is different from the freezing discussed in the previous paragraph since it was in the superluminal case. In fact, we could have guessed this value of around 6 m/s since it is approximately the A_0' phase velocity in an undeformed strip.

Playing with the multiple passages of the transition wave There is one feature we have left out for the moment: the multiple passes of the transition wave. We have clearly seen in figure 5.5 that the moving interface is reflected at the top edge. This reflection occurs since this top edge is fixed and a new information must propagate, about its zero moving velocity and larger deformation. The information propagates again in the form of a transition wave, but in a medium that is already deformed and moving at constant speed. This reflected wave also propagates faster. So, on the second pass, the material reaches a stationary but further deformed state, as observed

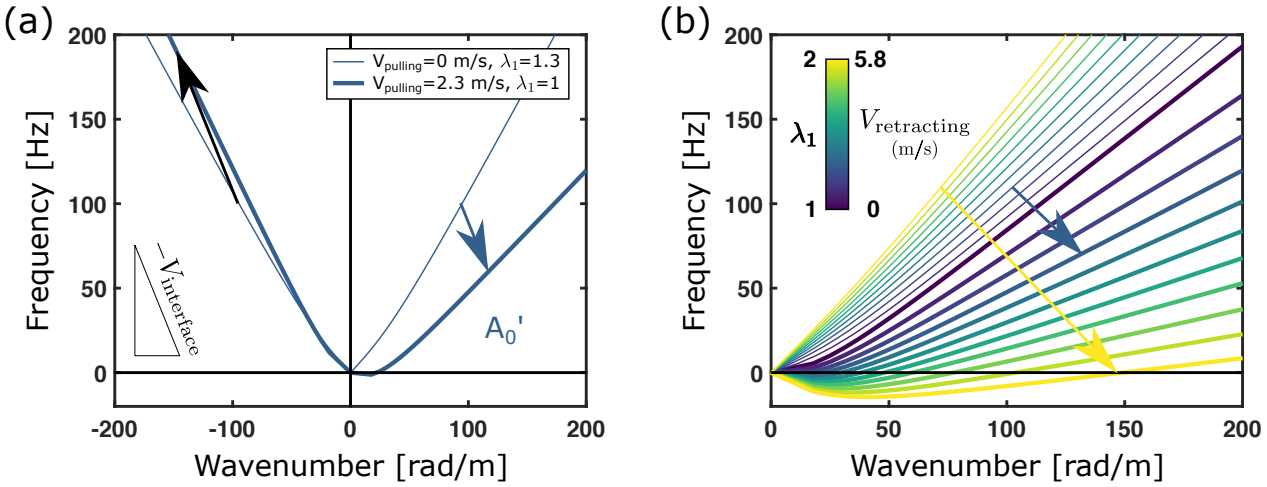

FIGURE 5.14: **Moving interface in a retracting strip** – (a) Dispersion curves of the A_0' mode are plotted either for a stationary and initially deformed $\lambda_1 = 1.3$ strip, either for an undeformed $\lambda_1 = 1$ and moving at constant velocity $V_{\text{retracting}}$ in direction $-x_1$. (b) Similar plot as in (a) but for various starting stretch ratios, and thus retracting velocities $V_{\text{retracting}}$. Frequency and wavenumber conversions are represented using arrows, and one should note that the interface velocity slightly depends on the initial stretch ratio (see figure 5.2).

experimentally in figure 5.5. Using equation (5.3), we can determine the new stretch ratio:

$$\lambda_1 = \lambda_1^{\text{pre}} \left(1 + \frac{V_{\text{pulling}}}{V_{S_0'}(\lambda_1 = \lambda_1^{\text{pre}})} \right) \quad \text{with} \quad \lambda_1^{\text{pre}} = 1 + \frac{V_{\text{pulling}}}{V_{S_0'}\,(\lambda_1 = 1)} \tag{5.7}$$

We can of course repeat this reasoning to understand what happens during the third pass, etc...

Using this same reasoning, the stretch ratio is determined and presented in equation (5.7) and the solid no longer moves. We imagine the strip is long enough to enable multiple crossing of the moving interface, being reflected at the edges. The first medium is a stationary undeformed strip ($\lambda_1 = 1, V = 0$). The second one is deformed and moving at constant velocity ($\lambda_1 = \lambda_1^{\text{first pass}}, V = V_{\text{pulling}}$). The third one is more deformed and stationary ($\lambda_1 = \lambda_1^{\text{second pass}}, V = 0$). The fourth one is even more deformed and moving at constant velocity ($\lambda_1 = \lambda_1^{\text{third pass}}, V = V_{\text{pulling}}$). Let's display in figure 5.15 the different dispersion curves for a wave emitted at the top edge, and the corresponding conversions when crossing the moving interface multiple times. Globally, a wavenumber cascade is observed but not a frequency one. This makes sense because the strip is progressively stretched with the passes of the interface while the strip velocity does not increase but alternates between V_{pulling} and 0 m/s. No frequency cascade could be efficiently implemented with such a configuration.

A double interface transition wave Inspired from the work of BACOT et al. (2016)[248], who used an acceleration pulse as a time mirror for water waves, we could perform a deformation pulse by pulling the strip for a few milliseconds before stopping it. In that case, a first interface is generated and separates a static undeformed and a moving deformed strip. Then, a second interface is generated as well and separates the moving deformed strip and a static deformed strip. We may wonder whether it is really any different from what we have seen above with the multiple passages in previous paragraph. Actually, it is different because the interfaces propagate in the same direction here. And what happens is pretty straightforward, since there is an equivalent moving interface

[248] BACOT et al. (2016): "Time reversal and holography with spacetime transformations"

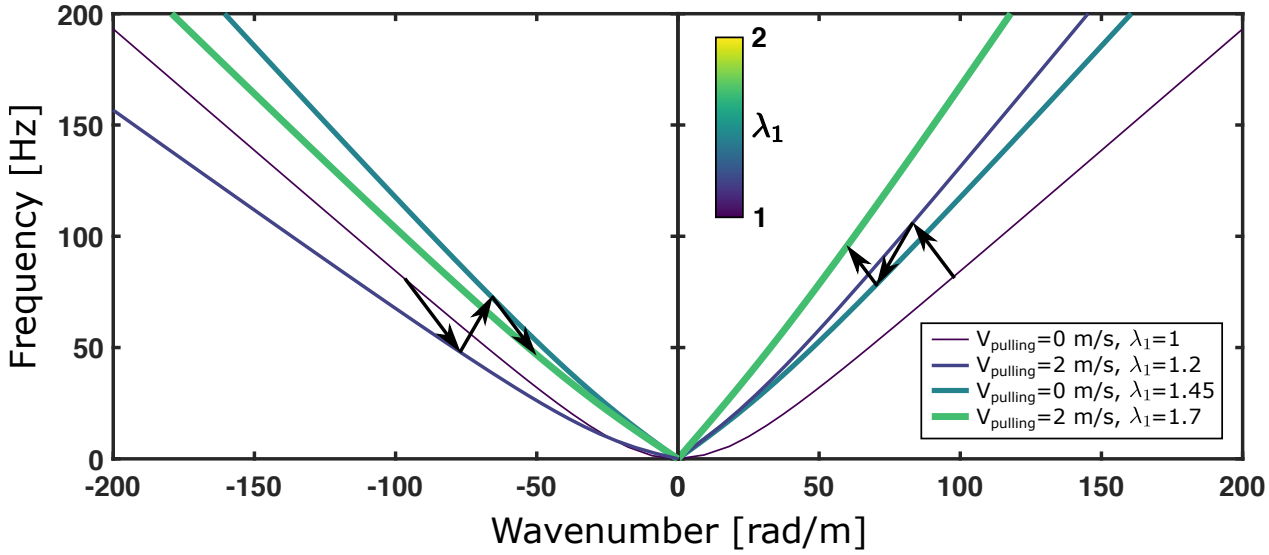

FIGURE 5.15: **Crossing the moving interface multiple times** – Dispersion curves of the A_0' mode are plotted for different media. Frequency and wavenumber conversions are represented using arrows, and one should note that the interface velocity depends (slightly) on the initial stretch ratio (see figure 5.2) but also on the solid velocity.

separating a static undeformed strip and a static deformed strip, so that previous methods still work but with adequate dispersion curves.

Accelerated modulation Going back to the original idea, we started with an experimental set-up that induced a velocity V_{pulling} that increases over time as a result of the free fall of a weight. In fact, this is a situation where the speed is not constant, but the acceleration is constant. This has recently been studied for electromagnetic waves[249]. What we can now conjecture is that in such a situation, a wave would cross a continuum of space-time interfaces. This time, the conversion illustrated in figure 5.9 by a black arrow would no longer be a straight line but a curve. This is because, at each "elementary" crossing, the interface velocity $V_{\text{interface}}$ (still in the laboratory reference frame) decreases as a result of velocity additivity, and because the material moves in the opposite direction.

Building analogies with other fields of physics Everything that has been discussed in this last section is possible because the media is moving. There are some works devoted to the handling of water waves propagating at the surface of water flows. These works are particularly interesting because a full analogy with black hole physics is presented and applied to understand and explore difficult-to-assess physics[238], such as Hawking's radiation[235,239]. Such waves are then a great way to implement analogies with another field of physics[236,237]. Similarly, other recent works were devoted to use optics as a guideline to explore fancy aspects of using space interfaces with water

[249] BAHRAMI et al. (2023): "Electrodynamics of Accelerated-Modulation Space-Time Metamaterials"
[238] PELOQUIN et al. (2016): "Analog wormholes and black hole laser effects in hydrodynamics"
[235] ROUSSEAUX et al. (2008): "Observation of negative-frequency waves in a water tank: a classical analogue to the Hawking effect?"
[239] DAS et al. (2018): "Dynamics of flexural gravity waves: from sea ice to Hawking radiation and analogue gravity"
[236] BARCELÓ et al. (2011): "Analogue Gravity"
[237] FACCIO et al. (2013): *Analogue Gravity Phenomenology: Analogue Spacetimes and Horizons, from Theory to Experiment*

waves[250]. Initially investigated by Catheline et al. (2022)[251], elastic membranes are also a great experimental platform to explore exotic phenomena. Here, we believe that a soft strip could also be used as a playground, since it allows metric deformation and measurements in both the reference and deformed configurations.

[250] Mouet et al. (2023): "Comprehensive refractive manipulation of water waves using electrostriction"
[251] Catheline et al. (2022): "Gravitational lens effect of membrane waves"

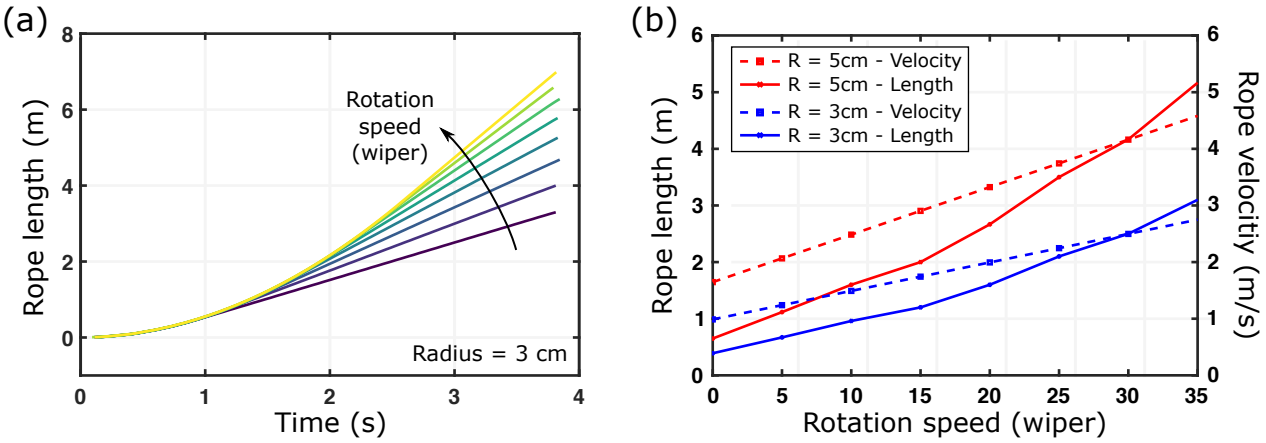

FIGURE 5.16: **Calibration of the motor speed and rope length to loosen** – A lateral camera is used to record a movie of the early moments of the rotating motor. The unrolled length and velocity of the rope are deduced for different values of `wiper` *i.e.* the variable controlling the motor speed (min= 0, max= 127).

Appendix A

A calibration is needed for the amount of rope to loosen and the motor speed. A lateral camera is used to record a movie of the early moments of the rotating motor. The electronic assembly uses a `wiper` variable, controlling the digital potentiometer value, thus the rotation speed, $0 \leq$ `wiper` $\leq$ 127. The length of unrolled rope is first plotted in figure 5.16(a) for different values of `wiper`. Every curve starts the same way and reaches a linear behaviour after a few seconds. When it does, the length is measured and the slope, giving the pulling velocity, is derived. The results are shown in figure 5.16(b) for two values of the spool radius. To get a given velocity, we first deduce the corresponding `wiper` value and then read the length of rope to loosen. Generally, if the same velocity can be achieved using a higher radius, this is set up to reduce the length of rope to loosen.

Mechanical delay – That consists in the same "start photodiode" motion detector system but is placed where the rope is loosen. A small rope loop is placed and slightly trapped in a plastic cylinder. At one entry, the rope loop comes in. At the other entry, the rope loop slightly sticks out and is positioned between the LED and the photodiode. When the motor has pulled all the rest of the rope, it starts pulling on this loop. At this point, the photodiode signal changes and the trigger signal is sent. However, the bottom edge of the strip has not yet been pulled, as there is still a length of rope to be pulled (roughly twice the cylinder size), and this corresponds to a mechanical delay. By adjusting the position of the motion detector system, one can tune the delay. Now that we achieved to add this delay, we can adjust the electronic delay on the wave packet emission as well.

Conclusion and Perspectives

In the course of this thesis, we have fully described guided waves in soft solids. We began with a reminder of Lamb's problem and first measurements in a plate. We then obtained dispersion diagrams for in-plane waves in a soft strip, which we were able to explain quantitatively, provided we took the material viscoelasticity into account.

We then subjected these soft materials to large static deformations. The acoustoelastic theory which predicts how wave velocities change with the applied stress was introduced. In our case, we developed a material model combing acoustoelastic theory and material viscoelasticity, including a fractional time derivative, and it has enabled correct theoretical predictions in a stretched plate.

Once done, we were able to validate our model by following dispersion curves in a free or clamped strip, and compared them with the predictions from SCM, our semi-analytical method.

This thesis, based on experimental measurements, led to a better understanding of the acoustoelastic effect for soft solids. To go further, note that a generalization of our method to compute the velocities of guided waves in plates and strips is accessible to other hyperelastic (*e.g.* Gent), and rheological models (*e.g.* generalized Maxwell) by adjusting the stress tensor. Then, a generalization to other guiding geometry (*e.g.* cylinders, tubes) can also be performed. Even intrinsically anisotropic media can be investigated by using appropriate constitutive laws and invariants.

Then, in our material model, the constitutive law contains a term that depends jointly on frequency and prestress. To the best of our knowledge, this interdependence of variables is rarely discussed in the literature. A systematic analysis of several different materials (silicone, polyurethane, hydrogels, food, etc...) could help guiding current micromechanics research.

Next, we applied our understanding of elastic guided waves in a strip directly to the problem of elastography. Waveguiding, viscoelasticity and prestress are well-known challenges to the reliability and quantitativity of this medical imaging technique.

Using elastography experiments, we presented a method to measure and predict dispersion curves in a viscoelastic medium, with a waveguiding geometry and possibly prestress. This paves the way for robust quantitative elastography. The next step is the implementation of an inverse problem based on the measurement of these dispersion curves to enable the characterization of both the hyperelastic and viscoelastic properties of biological tissues. Moreover, we saw in Chapter 2 that stress can be probed in the medium using a material-independent quantity. This would apply particularly well to measurements in the musculoskeletal system.

Our initial motivation being the similarities between soft solids and biological tissues, we then

discussed the case of the basilar membrane in the cochlea which supports the *cochlear wave*. We succeeded in reproducing such a wave with a macroscopic model, and provided an understanding of the spatial discrimination of frequencies observed in the cochlea.

From there, the pressure distribution in the water compartments is still to be assessed, as well as multiple gradients. A last topic that could be discussed is the shape of the *cochlear wave* amplitude. We can probably derive a model for this amplitude using only the local dispersion of the basilar membrane.

Finally, we used prestress as a modulation tool to create time-varying media. A space-time interface was observed and exploited to achieve frequency and wavenumber jumps. Even if measurements in the case of a superluminal interface are not yet completely satisfactory, we have already imagined all the possible wave manipulations with such an experimental platform.

The thesis not only provides a way for harnessing guided elastic waves in dynamic environments, but it also opens opportunities for building analogies with astrophysics for future exploration.

Thus, this thesis has opened up a number of horizons, and we can think of more global perspectives, still centered around guided waves in soft solids, but with new systems.

One of the original objective of this thesis was to have a modulable medium. We have seen that prestress can be used to modulate the speed of elastic waves, but we can also concive using other materials such as electro-active or magneto-active polymers. From there, such materials could be coupled with gradients as described above for the cochlea. This would enable the investigation of local feedback loops in such a system, as well as new time and space modulations during the propagation of guided waves.

We have also seen on several occasions (elastography, cochlea) that coupling with a fluid has significant impacts. Here the fluid remained static. By adding flows, non-reciprocal effects should appear, that are particularly interesting for wave manipulation. On top of that, this additional phenomenon directly applies to the case of the artery.

Finally, only homogeneous media were considered here, and microstructuring the strip, which is easy to mold, would undoubtedly bring new amazing effects. Periodic and/or bistable designs are not only interesting for wave physics, but microstructuring should provide links with biological tissues which are generally multi-scale.

Bibliography

[1] Josephson (1993): "Contraction dynamics and power output of skeletal muscle", *Annual review of physiology*, vol. 55, no. 1, pp. 527–546, DOI: 10.1146/annurev.ph.55.030193.002523.

[2] Huffard et al. (2005): "Underwater bipedal locomotion by octopuses in disguise", *Science*, vol. 307, no. 5717, pp. 1927–1927, DOI: 10.1126/science.1109616.

[3] Dervaux and Amar (2008): "Morphogenesis of growing soft tissues", *Physical review letters*, vol. 101, no. 6, p. 068101, DOI: 10.1103/PhysRevLett.101.068101.

[4] Heisenberg and Bellaïche (2013): "Forces in tissue morphogenesis and patterning", *Cell*, vol. 153, no. 5, pp. 948–962, DOI: 10.1016/j.cell.2013.05.008.

[5] Liang and Mahadevan (2011): "Growth, geometry, and mechanics of a blooming lily", *Proceedings of the National Academy of Sciences*, vol. 108, no. 14, pp. 5516–5521, DOI: 10.1073/pnas.1007808108.

[6] Goriely (2017): "The mathematics and mechanics of biological growth", Springer.

[7] Moulia et al. (2021): "Fluctuations shape plants through proprioception", *Science*, vol. 372, no. 6540, eabc6868, DOI: doi/10.1126/science.abc6868.

[8] Levental et al. (2007): "Soft biological materials and their impact on cell function", *Soft Matter*, vol. 3, no. 3, pp. 299–306, DOI: 10.1039/B610522J.

[9] Wozniak and Chen (2009): "Mechanotransduction in development: a growing role for contractility", *Nature reviews Molecular cell biology*, vol. 10, no. 1, p. 34, DOI: 10.1038/nrm2592.

[10] Kumar and Weaver (2009): "Mechanics, malignancy, and metastasis: the force journey of a tumor cell", *Cancer and Metastasis Reviews*, vol. 28, no. 1-2, pp. 113–127, DOI: 10.1007/s10555-008-9173-4.

[11] Kalita and Schaefer (2008): "Mechanical models of artery walls", *Archives of Computational Methods in Engineering*, vol. 15, no. 1, pp. 1–36, DOI: 10.1007/s11831-007-9015-5.

[12] Kaspar et al. (2021): "The rise of intelligent matter", *Nature*, vol. 594, no. 7863, pp. 345–355, DOI: 10.1038/s41586-021-03453-y.

[13] Zhao et al. (2021): "Soft materials by design: unconventional polymer networks give extreme properties", *Chemical Reviews*, vol. 121, no. 8, pp. 4309–4372, DOI: 10.1021/acs.chemrev.0c01088.

[14] Murray and Thomson (2011): "Synthetic, multi-layer, self-oscillating vocal fold model fabrication", *JoVE (Journal of Visualized Experiments)*, no. 58, e3498, DOI: 10.3791/3498.

[15] Vannelli et al. (2015): "*'Dynamic heart phantom with functional mitral and aortic valves'*", *Medical Imaging 2015: Image-Guided Procedures, Robotic Interventions, and Modeling*, International Society for Optics and Photonics, 2015, vol. 9415, p. 941503, DOI: 10.1117/12.2082277.

[16] Smith et al. (2023): "Soft devices in neurological surgery", *Nature Reviews Materials*, pp. 1–3, DOI: 10.1038/s41578-023-00565-x.

[17] Marechal et al. (2021): "Toward a common framework and database of materials for soft robotics", *Soft Robotics*, vol. 8, no. 3, pp. 284–297, DOI: 10.1089/soro.2019.0115.

[18] Siéfert et al. (2019): "Bio-inspired pneumatic shape-morphing elastomers", *Nature Mater*, vol. 18, no. 1, pp. 24–28, DOI: 10.1038/s41563-018-0219-x.

[19] Sandrin et al. (2003): "Transient elastography: a new noninvasive method for assessment of hepatic fibrosis", *Ultrasound in Medicine & Biology*, vol. 29, no. 12, pp. 1705–1713, DOI: 10.1016/j.ultrasmedbio.2003.07.001.

[20] Gennisson et al. (2010): "Viscoelastic and Anisotropic Mechanical Properties of in vivo Muscle Tissue Assessed by Supersonic Shear Imaging", *Ultrasound in Medicine & Biology*, vol. 36, no. 5, pp. 789–801, DOI: 10.1016/j.ultrasmedbio.2010.02.013.

[21] Deffieux et al. (2015): "Investigating liver stiffness and viscosity for fibrosis, steatosis and activity staging using shear wave elastography", *Journal of Hepatology*, vol. 62, no. 2, pp. 317–324, DOI: 10.1016/j.jhep.2014.09.020.

[22] Griesbauer et al. (2012): "Propagation of 2D Pressure Pulses in Lipid Monolayers and Its Possible Implications for Biology", *Phys. Rev. Lett.*, vol. 108, p. 198103, DOI: 10.1103/PhysRevLett.108.198103.

[23] Hirano (1974): "Morphological structure of the vocal cord as a vibrator and its variations", *Folia Phoniatrica et Logopaedica*, vol. 26, no. 2, pp. 89–94, DOI: 10.1159/000263771.

[24] Reichenbach and Hudspeth (2014): "The physics of hearing: fluid mechanics and the active process of the inner ear", *Reports on Progress in Physics*, vol. 77, no. 7, p. 076601, DOI: 10.1088/0034-4885/77/7/076601.

[25] Royer and Dieulesaint (1999): "Elastic waves in solids I: Free and guided propagation", Springer Science & Business Media.

[26] Su et al. (2006): "Guided Lamb waves for identification of damage in composite structures: A review", *Journal of sound and vibration*, vol. 295, no. 3-5, pp. 753–780, DOI: 10.1016/j.jsv.2006.01.020.

[27] Gennisson et al. (2007): "Acoustoelasticity in soft solids: Assessment of the nonlinear shear modulus with the acoustic radiation force", *The Journal of the Acoustical Society of America*, vol. 122, no. 6, pp. 3211–3219, DOI: 10.1121/1.2793605.

[28] Biot (1940): "The Influence of Initial Stress on Elastic Waves", *Journal of Applied Physics*, vol. 11, no. 8, pp. 522–530, DOI: 10.1063/1.1712807.

[29] Destrade and Saccomandi (2007): "Waves in Nonlinear Pre-Stressed Materials", Springer Wien New York.

[30] Delory et al. (2022): "Soft elastomers: A playground for guided waves", *The Journal of the Acoustical Society of America*, vol. 151, no. 5, pp. 3343–3358, DOI: 10.1121/10.0011391.

[31] Auld (1973): "Acoustic Fields and Waves in Solids", John Wiley & Sons Inc.

[32] Hooke (1678): “Lectures de potentia restitutiva, or of spring, explaining the power of springing bodies”, Martin, John.

[33] Landau et al. (1986): “Theory of elasticity: volume 7”, Elsevier.

[34] Lamb (1917): “On waves in an elastic plate”, *Proceedings of the Royal Society of London. Series A, Containing Papers of a Mathematical and Physical Character*, vol. 93, no. 648, pp. 114–128, doi: 10.1098/rspa.1917.0008.

[35] Muller (1956): “A method for solving algebraic equations using an automatic computer”, *Mathematics of Computation*, vol. 10, pp. 208–215, doi: 10.1090/S0025-5718-1956-0083822-0.

[36] Pavlakovic et al. (1997): “Disperse: A General Purpose Program for Creating Dispersion Curves” in: *Review of Progress in Quantitative Nondestructive Evaluation: Volume 16A*, Springer US, Boston, MA, pp. 185–192.

[37] Kiefer (2022): “GEW dispersion script”, doi: 10.5281/zenodo.7050790.

[38] Kiefer (2022): “Elastodynamic quasi-guided waves for transit-time ultrasonic flow metering”, FAU University Press.

[39] Shannon (1949): “Communication in the Presence of Noise”, *Proceedings of the IRE*, vol. 37, no. 1, pp. 10–21, doi: 10.1109/JRPROC.1949.232969.

[40] Wildeman (2018): “Real-time quantitative Schlieren imaging by fast Fourier demodulation of a checkered backdrop”, *Experiments in Fluids*, vol. 59, no. 6, p. 97, doi: 10.1007/s00348-018-2553-9.

[41] Wildeman (2021): “DICflow”, url: https://github.com/swildeman/dicflow.

[42] Lanoy et al. (2020): “Dirac cones and chiral selection of elastic waves in a soft strip”, *Proc Natl Acad Sci USA*, vol. 117, no. 48, pp. 30186–30190, doi: 10.1073/pnas.2010812117.

[43] Krushynska and Meleshko (2011): “Normal waves in elastic bars of rectangular cross section”, *The Journal of the Acoustical Society of America*, vol. 129, no. 3, pp. 1324–1335, doi: 10.1121/1.3531800.

[44] Cross and Lifshitz (2001): “Elastic wave transmission at an abrupt junction in a thin plate with application to heat transport and vibrations in mesoscopic systems”, *Physical Review B*, vol. 64, p. 085324, doi: 10.1103/PhysRevB.64.085324.

[45] Laurent et al. (2020): “In-plane backward and Zero-Group-Velocity guided modes in rigid and soft strips”, *The Journal of the Acoustical Society of America*, vol. 147, doi: 10.1121/10.0000760.

[46] Ugural and Fenster (2003): “Advanced strength and applied elasticity”, Pearson education.

[47] Mindlin (2006): “An Introduction to the Mathematical Theory of Vibrations of Elastic Plates”, J. Yang (Ed.), World Scientific, Singapore.

[48] Stobbe and Murray (2017): “Conical dispersion of Lamb waves in elastic plates”, *Physical Review B*, vol. 96, no. 14, p. 144101, doi: 10.1103/PhysRevB.96.144101.

[49] Maznev (2014): “Dirac cone dispersion of acoustic waves in plates without phononic crystals”, *The Journal of the Acoustical Society of America*, vol. 135, no. 2, pp. 577–580, doi: 10.1121/1.4861234.

[50] Huang et al. (2011): “Dirac cones induced by accidental degeneracy in photonic crystals and zero-refractive-index materials”, *Nature materials*, vol. 10, no. 8, p. 582, doi: 10.1038/nmat3030.

[51] Mindlin and Medick (1959): "Extensional Vibrations of Elastic Plates", *Journal of Applied Mechanics*, vol. 26, no. 4, pp. 561–569, doi: 10.1115/1.4012112.

[52] Prada et al. (2005): "Laser-based ultrasonic generation and detection of zero-group velocity Lamb waves in thin plates", *Applied Physics Letters*, vol. 87, no. 19, p. 194109, doi: 10.1063/1.2128063.

[53] Philippe et al. (2015): "Focusing on plates: controlling guided waves using negative refraction", *Scientific reports*, vol. 5, p. 11112, doi: 10.1038/srep11112.

[54] Gérardin et al. (2016): "Negative reflection of Lamb waves at a free edge: Tunable focusing and mimicking phase conjugation", *The Journal of the Acoustical Society of America*, vol. 140, no. 1, pp. 591–600, doi: 10.1121/1.4959024.

[55] Meral et al. (2009): "Surface response of a fractional order viscoelastic halfspace to surface and subsurface sources", *The Journal of the Acoustical Society of America*, vol. 126, no. 6, pp. 3278–3285, doi: 10.1121/1.3242351.

[56] Kearney et al. (2015): "Dynamic viscoelastic models of human skin using optical elastography", *Physics in Medicine & Biology*, vol. 60, no. 17, p. 6975, doi: 10.1088/0031-9155/60/17/6975.

[57] Rolley et al. (2019): "A flexible rheometer design to measure the visco-elastic response of soft solids over a wide range of frequency", *Review of scientific instruments*, vol. 90, no. 2, p. 023906, doi: 10.1063/1.5064599.

[58] Yasar et al. (2013): "Wideband MR elastography for viscoelasticity model identification", *Magnetic Resonance in Medicine*, vol. 70, no. 2, pp. 479–489, doi: 10.1002/mrm.24495.

[59] Liu et al. (2014): "Ultra wideband (0.5–16 kHz) MR elastography for robust shear viscoelasticity model identification", *Physics in Medicine & Biology*, vol. 59, no. 24, p. 7717, doi: 10.1088/0031-9155/59/24/7717.

[60] Mainardi (2010): "Fractional Calculus and Waves in Linear Viscoelasticity", Imperial College Press.

[61] Machado et al. (2011): "Recent history of fractional calculus", *Communications in Nonlinear Science and Numerical Simulation*, vol. 16, no. 3, pp. 1140–1153, doi: 10.1016/j.cnsns.2010.05.027.

[62] Meral et al. (2010): "Fractional calculus in viscoelasticity: An experimental study", *Communications in Nonlinear Science and Numerical Simulation*, vol. 15, no. 4, pp. 939–945, doi: 10.1016/j.cnsns.2009.05.004.

[63] Sharma et al. (2023): "Characterizing Viscoelastic Polyvinyl Alcohol Phantoms for Ultrasound Elastography", *Ultrasound in Medicine and Biology*, vol. 49, no. 2, pp. 497–511, doi: 10.1016/j.ultrasmedbio.2022.09.019.

[64] Parker et al. (2019): "Towards a consensus on rheological models for elastography in soft tissues", *Physics in Medicine & Biology*, vol. 64, no. 21, p. 215012, doi: 10.1088/1361-6560/ab453d.

[65] Delory et al. (2023): "Guided elastic waves in stretched viscoelastic strip", *Submitted to Pys. Rev. X*.

[66] Simonetti and Lowe (2005): "On the meaning of Lamb mode nonpropagating branches", *The Journal of the Acoustical Society of America*, vol. 118, no. 1, pp. 186–192, doi: 10.1121/1.1938528.

[67] Trefethen (2000): "Spectral Methods in MATLAB", Society for Industrial and Applied Mathematics.

[68] Weideman and Reddy (2000): "A MATLAB Differentiation Matrix Suite", *ACM Trans. Math. Softw.*, vol. 26, no. 4, pp. 465–519, DOI: 10.1145/365723.365727.

[69] Adamou and Craster (2004): "Spectral methods for modelling guided waves in elastic media", *The Journal of the Acoustical Society of America*, vol. 116, no. 3, pp. 1524–1535, DOI: 10.1121/1.1777871.

[70] Kiefer et al. (2023): "Computing zero-group-velocity points in anisotropic elastic waveguides: Globally and locally convergent methods", *The Journal of the Acoustical Society of America*, vol. 153, no. 2, pp. 1386–1398, DOI: 10.1121/10.0017252.

[71] Toupin and Bernstein (1961): "Sound Waves in Deformed Perfectly Elastic Materials. Acoustoelastic Effect", *The Journal of the Acoustical Society of America*, vol. 33, no. 2, pp. 216–225, DOI: 10.1121/1.1908623.

[72] Rogerson and Fu (1995): "An asymptotic analysis of the dispersion relation of a prestressed incompressible elastic plate", *Acta Mechanica*, vol. 111, no. 1-2, pp. 59–74, DOI: 10.1007/BF01187727.

[73] Nolde et al. (2004): "Dispersion of Small Amplitude Waves in a Pre-Stressed, Compressible Elastic Plate", *Journal of Elasticity*, vol. 75, no. 1, pp. 1–29, DOI: 10.1023/B:ELAS.0000039920.67766.d3.

[74] Rogerson and Prikazchikova (2009): "Generalisations of long wave theories for prestressed compressible elastic plates", *International Journal of Non-Linear Mechanics*, vol. 44, no. 5, pp. 520–529, DOI: 10.1016/j.ijnonlinmec.2008.11.002.

[75] Li et al. (2022): "Non-destructive mapping of stress and strain in soft thin films through sound waves", *Communications Physics*, vol. 5, no. 231, DOI: 10.1038/s42005-022-01000-3.

[76] Delory et al. (2023): "Guided elastic waves in a highly-stretched soft plate", *Extreme Mechanics Letters*, p. 102018, DOI: https://doi.org/10.1016/j.eml.2023.102018.

[77] Ogden (1997): "Non-Linear Elastic Deformations", Dover Publications.

[78] Saccomandi and Ogden (2004): "Mechanics and Thermomechanics of Rubberlike Solids", Springer Vienna.

[79] Mihai and Goriely (2017): "How to characterize a nonlinear elastic material? A review on nonlinear constitutive parameters in isotropic finite elasticity", *Proceedings of the Royal Society A: Mathematical, Physical and Engineering Sciences*, vol. 473, no. 2207, p. 20170607, DOI: 10.1098/rspa.2017.0607.

[80] Destrade et al. (2010): "Third- and fourth-order constants of incompressible soft solids and the acousto-elastic effect", *The Journal of the Acoustical Society of America*, vol. 127, no. 5, pp. 2759–2763, DOI: 10.1121/1.3372624.

[81] Destrade et al. (2012): "Large Acoustoelastic Effect", *Wave Motion*, vol. 49, no. 2, pp. 364–374, DOI: 10.1016/j.wavemoti.2011.12.002.

[82] Balzani et al. (2006): "A polyconvex framework for soft biological tissues. Adjustment to experimental data", *International Journal of Solids and Structures*, vol. 43, no. 20, pp. 6052–6070, DOI: 10.1016/j.ijsolstr.2005.07.048.

[83] Peyraut et al. (2010): "A closed form solution for the uniaxial tension test of biological soft tissues", *International Journal of Non-Linear Mechanics*, vol. 45, no. 5, pp. 535–541, DOI: 10.1016/j.ijnonlinmec.2010.02.003.

[84] Mukherjee et al. (2022): "Representing the stress and strain energy of elastic solids with initial stress and transverse texture anisotropy", *Proceedings of the Royal Society A: Mathematical, Physical and Engineering Sciences*, vol. 478, no. 2266, p. 20220255, DOI: 10.1098/rspa.2022.0255.

[85] Wex et al. (2015): "Isotropic incompressible hyperelastic models for modelling the mechanical behaviour of biological tissues: a review", *Biomedical Engineering*, vol. 60, no. 6, DOI: 10.1515/bmt-2014-0146.

[86] Chagnon et al. (2015): "Hyperelastic Energy Densities for Soft Biological Tissues: A Review", *Journal of Elasticity*, vol. 120, pp. 129–160, DOI: 10.1007/s10659-014-9508-z.

[87] Treloar (2005): "The Physics of Rubber Elasticity", Third Edition, Third Edition, Oxford University Press.

[88] Rivlin (1948): "Large elastic deformations of isotropic materials IV. Further developments of the general theory", *Philosophical transactions of the royal society of London. Series A, Mathematical and physical sciences*, vol. 241, no. 835, pp. 379–397.

[89] Anssari-Benam et al. (2021): "On the central role of the invariant I_2 in nonlinear elasticity", *International Journal of Engineering Science*, vol. 163, p. 103486, DOI: 10.1016/j.ijengsci.2021.103486.

[90] Fung (1993): "Biomechanics", 2nd ed.

[91] Gent (1958): "On the relation between indentation hardness and Young's modulus", *Rubber Chemistry and Technology*, vol. 31, no. 4, pp. 896–906, DOI: 10.5254/1.3542351.

[92] Boyce and Arruda (2000): "Constitutive Models of Rubber Elasticity: A Review", *Rubber Chemistry and Technology*, vol. 73, no. 3, pp. 504–523, DOI: 10.5254/1.3547602.

[93] Marckmann and Verron (2006): "Comparison of hyperelastic models for rubber-like materials", *Rubber Chemistry and Technology*, vol. 79, no. 5, pp. 835–858, DOI: 10.5254/1.3547969.

[94] Pence and Gou (2015): "On compressible versions of the incompressible neo-Hookean material", *Mathematics and Mechanics of Solids*, vol. 20, no. 2, pp. 157–182, DOI: 10.1177/1081286514544258.

[95] Blatz and Ko (1962): "Application of Finite Elastic Theory to the Deformation of Rubbery Materials", *Transactions of The Society of Rheology*, vol. 6, no. 1, pp. 223–252, DOI: 10.1122/1.548937.

[96] Wolfram Research (2021): "Mathematica 12.2.0.0", URL: https://www.wolfram.com.

[97] Zhang et al. (2023): "Noninvasive measurement of local stress inside soft materials with programmed shear waves", *Science Advances*, vol. 9, no. 10, eadd4082, DOI: 10.1126/sciadv.add4082.

[98] Antman (2004): "Nonlinear Problems of Elasticity", 2nd ed, Springer.

[99] Destrade et al. (2009): "Small amplitude waves and stability for a pre-stressed viscoelastic solid", *Zeitschrift für angewandte Mathematik und Physik*, vol. 60, no. 3, pp. 511–528, DOI: 10.1007/s00033-008-7147-6.

[100] Zhang et al. (2022): "Propagation and attenuation of Lamb waves in functionally graded fractional viscoelastic soft plates with a pre-deformation", *Composite Structures*, vol. 293, p. 115727, DOI: 10.1016/j.compstruct.2022.115727.

[101] Berjamin and Destrade (2023): "Models of fractional viscous stresses for incompressible materials", arXiv: 2305.01934.

[102] Nenadic et al. (2011): "Lamb wave dispersion ultrasound vibrometry (LDUV) method for quantifying mechanical properties of viscoelastic solids", *Physics in Medicine & Biology*, vol. 56, no. 7, p. 2245, DOI: 10.1088/0031-9155/56/7/021=.

[103] Liou et al. (2019): "Nondestructive characterization of soft materials and biofilms by measurement of guided elastic wave propagation using optical coherence elastography", *Soft matter*, vol. 15, no. 4, pp. 575–586, DOI: 10.1039/C8SM01902A.

[104] Couade et al. (2010): "Quantitative assessment of arterial wall biomechanical properties using shear wave imaging", *Ultrasound in medicine & biology*, vol. 36, no. 10, pp. 1662–1676, DOI: 10.1016/j.ultrasmedbio.2010.07.004.

[105] Astaneh et al. (2017): "Arterial waveguide model for shear wave elastography: implementation and in vitro validation", *Physics in Medicine & Biology*, vol. 62, no. 13, p. 5473, DOI: 10.1088/1361-6560/aa6ee3.

[106] Maksuti et al. (2017): "Influence of wall thickness and diameter on arterial shear wave elastography: a phantom and finite element study", *Physics in Medicine & Biology*, vol. 62, no. 7, p. 2694, DOI: 10.1088/1361-6560/aa591d.

[107] Brum et al. (2014): "In vivo evaluation of the elastic anisotropy of the human Achilles tendon using shear wave dispersion analysis", *Physics in Medicine & Biology*, vol. 59, no. 3, p. 505, DOI: 10.1088/0031-9155/59/3/505.

[108] Robles and Ruggero (2001): "Mechanics of the mammalian cochlea", *Physiological reviews*, vol. 81, no. 3, pp. 1305–1352, DOI: 10.1152/physrev.2001.81.3.1305.

[109] Delory et al. (2023): "Exploring the limits to quantitative elastography: supersonic shear imaging in stretched soft strips", *To be submitted to Physics in Medicine and Biology*.

[110] Zhao and Chang (2021): "Elastic wave velocities in finitely pre-stretched soft fibers", *International Journal of Solids and Structures*, vol. 233, p. 111208, DOI: 10.1016/j.ijsolstr.2021.111208.

[111] Doyle (1989): "Wave propagation in structures", Springer.

[112] Melde (1860): "Ueber die Erregung stehender Wellen eines fadenförmigen Körpers", *Annalen der Physik*, vol. 185, no. 2, pp. 193–215, DOI: 10.1002/andp.18601850202, URL: https://onlinelibrary.wiley.com/doi/abs/10.1002/andp.18601850202.

[113] Avicenna (1025): "The Canon of Medicine".

[114] Sandrin et al. (2002): "Shear modulus imaging with 2-D transient elastography", *IEEE Transactions on Ultrasonics, Ferroelectrics, and Frequency Control*, vol. 49, no. 4, pp. 426–435, DOI: 10.1109/58.996560.

[115] Asbach et al. (2010): "Viscoelasticity-based Staging of Hepatic Fibrosis with Multifrequency MR Elastography", *Radiology*, vol. 257, no. 1, pp. 80–86, DOI: 10.1148/radiol.10092489.

[116] Kennedy et al. (2018): "Quantitative Elastography Methods in Liver Disease: Current Evidence and Future Directions", *Radiology*, vol. 286, no. 3, pp. 738–763, DOI: 10.1148/radiol.2018170601.

[117] Bercoff et al. (2003): "In vivo breast tumor detection using transient elastography", *Ultrasound in Medicine & Biology*, vol. 29, no. 10, pp. 1387–1396, DOI: https://doi.org/10.1016/S0301-5629(03)00978-5.

[118] Sinkus et al. (2005): "Viscoelastic shear properties of in vivo breast lesions measured by MR elastography", *Magnetic Resonance Imaging*, vol. 23, no. 2, pp. 159–165, DOI: 10.1016/j.mri.2004.11.060.

[119] Barr and Zhang (2012): "Effects of Precompression on Elasticity Imaging of the Breast", *Journal of Ultrasound in Medicine*, vol. 31, no. 6, pp. 895–902, DOI: 10.7863/jum.2012.31.6.895.

[120] Barr (2019): "Future of breast elastography", *Ultrasonography*, vol. 38, no. 2, pp. 93–105, DOI: 10.14366/usg.18053.

[121] Correas et al. (2013): "Ultrasound elastography of the prostate: State of the art", *Diagnostic and Interventional Imaging*, vol. 94, no. 5, pp. 551–560, DOI: 10.1016/j.diii.2013.01.017.

[122] Cantisani et al. (2015): "Strain US Elastography for the Characterization of Thyroid Nodules: Advantages and Limitation", *International Journal of Endocrinology*, vol. 2015, e908575, DOI: 10.1155/2015/908575.

[123] Elgeti and Sack (2014): "Magnetic Resonance Elastography of the Heart", *Current Cardiovascular Imaging Reports*, vol. 7, no. 2, p. 9247, DOI: 10.1007/s12410-013-9247-8.

[124] Sinkus (2014): "Elasticity of the Heart, Problems and Potentials", *Current Cardiovascular Imaging Reports*, vol. 7, no. 9, p. 9288, DOI: 10.1007/s12410-014-9288-7.

[125] Hansen et al. (2015): " *'Shear wave elastography for lipid content detection in transverse arterial cross-sections'*", *2015 IEEE International Ultrasonics Symposium (IUS)*, 2015, pp. 1–4, DOI: 10.1109/ULTSYM.2015.0001.

[126] Khan et al. (2018): "Cardiovascular magnetic resonance elastography: A review", *NMR in Biomedicine*, vol. 31, no. 10, e3853, DOI: 10.1002/nbm.3853.

[127] Pruijssen et al. (2020): "Vascular Shear Wave Elastography in Atherosclerotic Arteries: A Systematic Review", *Ultrasound in Medicine & Biology*, vol. 46, no. 9, pp. 2145–2163, DOI: 10.1016/j.ultrasmedbio.2020.05.013.

[128] Prado-Costa et al. (2018): "Ultrasound elastography: compression elastography and shear-wave elastography in the assessment of tendon injury", *Insights into Imaging*, vol. 9, no. 5, pp. 791–814, DOI: 10.1007/s13244-018-0642-1.

[129] Farron et al. (2009): "Measurement of Tendon Strain During Muscle Twitch Contractions Using Ultrasound Elastography", *IEEE transactions on ultrasonics, ferroelectrics, and frequency control*, vol. 56, no. 1, pp. 27–35, DOI: 10.1109/TUFFC.2009.1002.

[130] Mifsud et al. (2023): "Elastography in the assessment of the Achilles tendon: a systematic review of measurement properties", *Journal of Foot and Ankle Research*, vol. 16, no. 1, p. 23, DOI: 10.1186/s13047-023-00623-1.

[131] Winn et al. (2016): "Sonoelastography in the musculoskeletal system: Current role and future directions", *World Journal of Radiology*, vol. 8, no. 11, pp. 868–879, DOI: 10.4329/wjr.v8.i11.868.

[132] Paluch et al. (2016): "Use of Ultrasound Elastography in the Assessment of the Musculoskeletal System", *Polish Journal of Radiology*, vol. 81, pp. 240–246, DOI: 10.12659/PJR.896099.

[133] Taljanovic et al. (2017): "Shear-Wave Elastography: Basic Physics and Musculoskeletal Applications", *RadioGraphics*, DOI: 10.1148/rg.2017160116.

[134] Davis et al. (2019): "Clinical utilization of shear wave elastography in the musculoskeletal system", *Ultrasonography*, vol. 38, no. 1, pp. 2–12, DOI: 10.14366/usg.18039.

[135] Sandrin et al. (2011): "Non-Invasive Assessment of Liver Fibrosis by Vibration-Controlled Transient Elastography (Fibroscan)" in: *Liver Biopsy*, IntechOpen, Rijeka.

[136] Ormachea and Parker (2020): "Elastography imaging: the 30 year perspective", *Physics in Medicine & Biology*, vol. 65, no. 24, 24TR06, DOI: 10.1088/1361-6560/abca00.

[137] Gennisson et al. (2013): "Ultrasound elastography: principles and techniques", *Diagnostic and interventional imaging*, vol. 94, no. 5, pp. 487–495, DOI: 10.1016/j.diii.2013.01.022.

[138] Shiina (2014): "Ultrasound elastography: Development of novel technologies and standardization", *Japanese Journal of Applied Physics*, vol. 53, no. 7S, 07KA02, DOI: 10.7567/JJAP.53.07KA02.

[139] Sigrist et al. (2017): "Ultrasound Elastography: Review of Techniques and Clinical Applications", *Theranostics*, vol. 7, no. 5, pp. 1303–1329, DOI: 10.7150/thno.18650.

[140] Doherty et al. (2013): "Acoustic radiation force elasticity imaging in diagnostic ultrasound", *IEEE Transactions on Ultrasonics, Ferroelectrics and Frequency Control*, vol. 60, no. 4, pp. 685–701, DOI: 10.1109/TUFFC.2013.2617.

[141] Bercoff et al. (2004): "Supersonic shear imaging: a new technique for soft tissue elasticity mapping", *IEEE Transactions on Ultrasonics, Ferroelectrics and Frequency Control*, vol. 51, no. 4, pp. 396–409, DOI: 10.1109/TUFFC.2004.1295425.

[142] T. Deffieux, "Palpation par force de radiation ultrasonore et échographie ultrarapide : Applications à la caractérisation tissulaire in vivo", Thèse de doctorat, Institut Langevin: Université Paris 7 - Paris Diderot, 2008, URL: https://www.theses.fr/2008PA077181.

[143] Zvietcovich and Larin (2022): "Wave-based optical coherence elastography: the 10-year perspective", *Progress in Biomedical Engineering*, vol. 4, no. 1, p. 012007, DOI: 10.1088/2516-1091/ac4512.

[144] Leartprapun and Adie (2023): "Recent advances in optical elastography and emerging opportunities in the basic sciences and translational medicine [Invited]", *Biomedical Optics Express*, vol. 14, no. 1, pp. 208–248, DOI: 10.1364/BOE.468932.

[145] Kirby et al. (2017): "Optical coherence elastography in ophthalmology", *Journal of Biomedical Optics*, vol. 22, no. 12, p. 121720, DOI: 10.1117/1.JBO.22.12.121720.

[146] Lan et al. (2023): "In vivo corneal elastography: A topical review of challenges and opportunities", *Computational and Structural Biotechnology Journal*, vol. 21, pp. 2664–2687, DOI: 10.1016/j.csbj.2023.04.009.

[147] Low et al. (2016): "General review of magnetic resonance elastography", *World Journal of Radiology*, vol. 8, no. 1, pp. 59–72, DOI: 10.4329/wjr.v8.i1.59.

[148] Sack (2023): "Magnetic resonance elastography from fundamental soft-tissue mechanics to diagnostic imaging", *Nature Reviews Physics*, vol. 5, no. 1, pp. 25–42, DOI: 10.1038/s42254-022-00543-2.

[149] Marlevi et al. (2020): "Combined spatiotemporal and frequency-dependent shear wave elastography enables detection of vulnerable carotid plaques as validated by MRI", *Scientific Reports*, vol. 10, no. 1, p. 403, DOI: 10.1038/s41598-019-57317-7.

[150] Hiscox et al. (2016): "Magnetic resonance elastography (MRE) of the human brain: technique, findings and clinical applications", *Physics in Medicine & Biology*, vol. 61, no. 24, R401, DOI: 10.1088/0031-9155/61/24/R401.

[151] Kennedy et al. (2014): "A Review of Optical Coherence Elastography: Fundamentals, Techniques and Prospects", *IEEE Journal of Selected Topics in Quantum Electronics*, vol. 20, no. 2, pp. 272–288, DOI: 10.1109/JSTQE.2013.2291445.

[152] Pelivanov et al. (2019): "Does group velocity always reflect elastic modulus in shear wave elastography?", *Journal of Biomedical Optics*, vol. 24, no. 7, p. 076003, doi: 10.1117/1.JBO.24.7.076003.

[153] Ramier et al. (2019): "Measuring mechanical wave speed, dispersion, and viscoelastic modulus of the cornea using optical coherence elastography", *Optics Express*, vol. 27, no. 12, p. 16635, doi: 10.1364/OE.27.016635.

[154] Li et al. (2017): "Guided waves in pre-stressed hyperelastic plates and tubes: Application to the ultrasound elastography of thin-walled soft materials", *Journal of the Mechanics and Physics of Solids*, vol. 102, pp. 67–79, doi: 10.1016/j.jmps.2017.02.008.

[155] Bilston (2018): "Soft tissue rheology and its implications for elastography: Challenges and opportunities", *NMR in Biomedicine*, vol. 31, no. 10, doi: 10.1002/nbm.3832.

[156] Caenen et al. (2022): "Assessing cardiac stiffness using ultrasound shear wave elastography", *Physics in Medicine & Biology*, vol. 67, no. 2, 02TR01, doi: 10.1088/1361-6560/ac404d.

[157] Crutison et al. (2022): "The combined importance of finite dimensions, anisotropy, and prestress in acoustoelastography", *The Journal of the Acoustical Society of America*, vol. 151, no. 4, pp. 2403–2413, doi: 10.1121/10.0010110.

[158] Zampini et al. (2021): "Measuring viscoelastic parameters in Magnetic Resonance Elastography: a comparison at high and low magnetic field intensity", *Journal of the Mechanical Behavior of Biomedical Materials*, vol. 120, p. 104587, doi: 10.1016/j.jmbbm.2021.104587.

[159] Jugé et al. (2023): "Ex vivo bovine liver nonlinear viscoelastic properties: MR elastography and rheological measurements", *Journal of the Mechanical Behavior of Biomedical Materials*, vol. 138, p. 105638, doi: 10.1016/j.jmbbm.2022.105638.

[160] Caenen et al. (2015): "A versatile and experimentally validated finite element model to assess the accuracy of shear wave elastography in a bounded viscoelastic medium", *IEEE Transactions on Ultrasonics, Ferroelectrics, and Frequency Control*, vol. 62, no. 3, pp. 439–450, doi: 10.1109/TUFFC.2014.006682.

[161] Marais et al. (2019): "Arterial Stiffness Assessment by Shear Wave Elastography and Ultrafast Pulse Wave Imaging: Comparison with Reference Techniques in Normotensives and Hypertensives", *Ultrasound in Medicine & Biology*, vol. 45, no. 3, pp. 758–772, doi: https://doi.org/10.1016/j.ultrasmedbio.2018.10.032.

[162] Thu-Mai Nguyen et al. (2011): "Assessment of viscous and elastic properties of subwavelength layered soft tissues using shear wave spectroscopy: Theoretical framework and in vitro experimental validation", *IEEE Transactions on Ultrasonics, Ferroelectrics and Frequency Control*, vol. 58, no. 11, pp. 2305–2315, doi: 10.1109/TUFFC.2011.2088.

[163] Catheline et al. (2003): "Measurement of elastic nonlinearity of soft solid with transient elastography", *The Journal of the Acoustical Society of America*, vol. 114, no. 6, pp. 3087–3091, doi: 10.1121/1.1610457.

[164] Li and Cao (2017): "Mechanics of ultrasound elastography", *Proceedings of the Royal Society A: Mathematical, Physical and Engineering Sciences*, vol. 473, no. 2199, Publisher: Royal Society, p. 20160841, doi: 10.1098/rspa.2016.0841.

[165] Deffieux et al. (2009): "Shear Wave Spectroscopy for In Vivo Quantification of Human Soft Tissues Visco-Elasticity", *IEEE Transactions on Medical Imaging*, vol. 28, no. 3, pp. 313–322, doi: 10.1109/TMI.2008.925077.

[166] Kiefer et al. (2019): "Calculating the full leaky Lamb wave spectrum with exact fluid interaction", *The Journal of the Acoustical Society of America*, vol. 145, no. 6, pp. 3341–3350, doi: 10.1121/1.5109399.

[167] Chittka and Brockmann (2005): "Perception Space—The Final Frontier", *PLOS Biology*, vol. 3, no. 4, null, DOI: 10.1371/journal.pbio.0030137.

[168] Vlajkovic and Thorne (2022): "Purinergic Signalling in the Cochlea", *International Journal of Molecular Sciences*, vol. 23, no. 23, p. 14874, DOI: 10.3390/ijms232314874.

[169] Martin (2014): "Physical principles of hearing" in: *Physics and Biology : from molecules to life*, World Scientific, pp. 127–147.

[170] Lim (1986): "Functional structure of the organ of Corti: a review", *Hearing Research*, vol. 22, no. 1, pp. 117–146, DOI: https://doi.org/10.1016/0378-5955(86)90089-4.

[171] Ryan and Dallos (1975): "Effect of absence of cochlear outer hair cells on behavioural auditory threshold", *Nature*, vol. 253, no. 5486, pp. 44–46, DOI: 10.1038/253044a0.

[172] Ashmore (1987): "A fast motile response in guinea-pig outer hair cells: the cellular basis of the cochlear amplifier.", *The Journal of Physiology*, vol. 388, no. 1, pp. 323–347, DOI: https://doi.org/10.1113/jphysiol.1987.sp016617.

[173] Ulfendahl and Flock (1998): "Outer Hair Cells Provide Active Tuning in the Organ of Corti", *Physiology*, vol. 13, no. 3, pp. 107–111, DOI: 10.1152/physiologyonline.1998.13.3.107.

[174] Ashmore (2008): "Cochlear Outer Hair Cell Motility", *Physiological Reviews*, vol. 88, no. 1, pp. 173–210, DOI: 10.1152/physrev.00044.2006.

[175] Dallos (2008): "Cochlear amplification, outer hair cells and prestin", *Current Opinion in Neurobiology*, vol. 18, no. 4, pp. 370–376, DOI: 10.1016/j.conb.2008.08.016.

[176] Rau et al. (2006): "Visualizing soft tissue in the mammalian cochlea with coherent hard X-rays", *Microscopy Research and Technique*, vol. 69, no. 8, pp. 660–665, DOI: 10.1002/jemt.20336.

[177] Verbist et al. (2010): "Consensus panel on a cochlear coordinate system applicable in histological, physiological and radiological studies of the human cochlea", *Otology & neurotology : official publication of the American Otological Society, American Neurotology Society [and] European Academy of Otology and Neurotology*, vol. 31, no. 5, pp. 722–730, DOI: 10.1097/MAO.0b013e3181d279e0.

[178] Rask-Andersen et al. (2012): "Human Cochlea: Anatomical Characteristics and their Relevance for Cochlear Implantation", *The Anatomical Record*, vol. 295, no. 11, pp. 1791–1811, DOI: 10.1002/ar.22599.

[179] Greenwood (1990): "A cochlear frequency-position function for several species—29 years later", *The Journal of the Acoustical Society of America*, vol. 87, no. 6, pp. 2592–2605, DOI: 10.1121/1.399052.

[180] Elfarnawany et al. (2017): "Micro-CT versus synchrotron radiation phase contrast imaging of human cochlea", *Journal of Microscopy*, vol. 265, no. 3, pp. 349–357, DOI: 10.1111/jmi.12507.

[181] Li et al. (2021): "Three-dimensional tonotopic mapping of the human cochlea based on synchrotron radiation phase-contrast imaging", *Scientific Reports*, vol. 11, no. 1, p. 4437, DOI: 10.1038/s41598-021-83225-w.

[182] Schurzig et al. (2021): "A cochlear scaling model for accurate anatomy evaluation and frequency allocation in cochlear implantation", *Hearing Research*, vol. 403, p. 108166, DOI: 10.1016/j.heares.2020.108166.

[183] Breitsprecher et al. (2022): "CT imaging-based approaches to cochlear duct length estimation—a human temporal bone study", *European Radiology*, vol. 32, no. 2, pp. 1014–1023, doi: 10.1007/s00330-021-08189-x.

[184] Helpard et al. (2021): "An Approach for Individualized Cochlear Frequency Mapping Determined From 3D Synchrotron Radiation Phase-Contrast Imaging", *IEEE Transactions on Biomedical Engineering*, vol. 68, no. 12, pp. 3602–3611, doi: 10.1109/TBME.2021.3080116.

[185] Helmholtz (1868): "Die Mechanik der Gehörknöchelchen und des Trommelfells", *Archiv für die gesamte Physiologie des Menschen und der Tiere*, vol. 1, no. 1, pp. 1–60, doi: 10.1007/BF01640310.

[186] Békésy (1960): "Experiments in Hearing", McGraw-Hill Book Company, Inc.

[187] Békésy (1956): "Current Status of Theories of Hearing", *Science*, vol. 123, no. 3201, pp. 779–783, doi: 10.1126/science.123.3201.779.

[188] Zweig et al. (1976): "The cochlear compromise", *The Journal of the Acoustical Society of America*, vol. 59, no. 4, pp. 975–982, doi: 10.1121/1.380956.

[189] Neely (1981): "Finite difference solution of a two-dimensional mathematical model of the cochlea", *The Journal of the Acoustical Society of America*, vol. 69, no. 5, pp. 1386–1393, doi: 10.1121/1.385820.

[190] Inselberg (1978): "Cochlear Dynamics: The Evolution of a Mathematical Model", *SIAM Review*, vol. 20, no. 2, pp. 301–351.

[191] De Boer (1981): "Short waves in three-dimensional cochlea models: Solution for a 'block' model", *Hearing Research*, vol. 4, no. 1, pp. 53–77, doi: https://doi.org/10.1016/0378-5955(81)90036-8.

[192] Vetešník and Nobili (2006): "The approximate scaling law of the cochlea box model", *Hearing Research*, vol. 222, no. 1, pp. 43–53, doi: https://doi.org/10.1016/j.heares.2006.08.012.

[193] Steele and Taber (1979): "Comparison of WKB calculations and experimental results for three-dimensional cochlear models", *The Journal of the Acoustical Society of America*, vol. 65, no. 4, pp. 1007–1018, doi: 10.1121/1.382570.

[194] Lim and Steele (2002): "A three-dimensional nonlinear active cochlear model analyzed by the WKB-numeric method", *Hearing Research*, vol. 170, no. 1, pp. 190–205, doi: 10.1016/S0378-5955(02)00491-4.

[195] Lighthill (1991): "Biomechanics of Hearing Sensitivity", *Journal of Vibration and Acoustics*, vol. 113, no. 1, pp. 1–13, doi: 10.1115/1.2930149.

[196] Allen and Neely (1992): "Micromechanical Models of the Cochlea", *Physics Today*, vol. 45, no. 7, pp. 40–47, doi: 10.1063/1.881349.

[197] Duke and Jülicher (2003): "Active Traveling Wave in the Cochlea", *Physical Review Letters*, vol. 90, no. 15, p. 158101, doi: 10.1103/PhysRevLett.90.158101.

[198] Hudspeth et al. (2010): "A Critique of the Critical Cochlea: Hopf—a Bifurcation—Is Better Than None", *Journal of Neurophysiology*, vol. 104, no. 3, pp. 1219–1229, doi: 10.1152/jn.00437.2010.

[199] Kolston and Ashmore (1996): "Finite element micromechanical modeling of the cochlea in three dimensions", *The Journal of the Acoustical Society of America*, vol. 99, no. 1, pp. 455–467, doi: 10.1121/1.414557.

[200] Nobili et al. (1998): "How well do we understand the cochlea?", *Trends in Neurosciences*, vol. 21, no. 4, pp. 159–167, doi: https://doi.org/10.1016/S0166-2236(97)01192-2.

[201] Ni and Elliott (2018): "Modelling three-dimensional cochlear micromechanics within the guinea pig organ of Corti", *AIP Conference Proceedings*, vol. 1965, no. 1, p. 140005, doi: 10.1063/1.5038525.

[202] Olson et al. (2012): "Von Békésy and cochlear mechanics", *Hearing Research*, vol. 293, no. 1, pp. 31–43, doi: https://doi.org/10.1016/j.heares.2012.04.017.

[203] Osborne and Hart (1945): "Transmission, Reflection, and Guiding of an Exponential Pulse by a Steel Plate in Water. I. Theory", *The Journal of the Acoustical Society of America*, vol. 17, no. 1, pp. 1–18, doi: 10.1121/1.1916293.

[204] Schulkes et al. (1987): "Waves due to a steadily moving source on a floating ice plate. Part 2", *Journal of Fluid Mechanics*, vol. 180, Publisher: Cambridge University Press, pp. 297–318, doi: 10.1017/S0022112087001812.

[205] Anderson et al. (2019): "Local Delivery of Therapeutics to the Inner Ear: The State of the Science", *Frontiers in Cellular Neuroscience*, vol. 13.

[206] Mittal et al. (2019): "Nanoparticle-based drug delivery in the inner ear: current challenges, limitations and opportunities", *Artificial Cells, Nanomedicine, and Biotechnology*, vol. 47, no. 1, pp. 1312–1320, doi: 10.1080/21691401.2019.1573182.

[207] Rybak et al. (2019): "Local Drug Delivery for Prevention of Hearing Loss", *Frontiers in Cellular Neuroscience*, vol. 13.

[208] Hao and Li (2019): "Inner ear drug delivery: Recent advances, challenges, and perspective", *European Journal of Pharmaceutical Sciences*, Advanced Drug Delivery Approaches for Inner Ear Therapeutics, vol. 126, pp. 82–92, doi: 10.1016/j.ejps.2018.05.020.

[209] Szeto et al. (2020): "Inner ear delivery: Challenges and opportunities", *Laryngoscope Investigative Otolaryngology*, vol. 5, no. 1, pp. 122–131, doi: 10.1002/lio2.336.

[210] Ashmore et al. (2010): "The remarkable cochlear amplifier", *Hearing Research*, vol. 266, no. 1, pp. 1–17, doi: https://doi.org/10.1016/j.heares.2010.05.001.

[211] Felsen and Whitman (1970): "Wave propagation in time-varying media", *IEEE Transactions on Antennas and Propagation*, vol. 18, no. 2, pp. 242–253, doi: 10.1109/TAP.1970.1139657.

[212] Fante (1971): "Transmission of electromagnetic waves into time-varying media", *IEEE Transactions on Antennas and Propagation*, vol. 19, no. 3, pp. 417–424, doi: 10.1109/TAP.1971.1139931.

[213] Kalluri (2010): "Electromagnetics of Time Varying Complex Media: Frequency and Polarization Transformer, 2nd Edition", 2nd ed., CRC Press.

[214] Mendonça and Shukla (2002): "Time Refraction and Time Reflection: Two Basic Concepts", *Physica Scripta*, vol. 65, no. 2, p. 160, doi: 10.1238/Physica.Regular.065a00160.

[215] Mendonça et al. (2003): "Temporal beam splitter and temporal interference", *Phys. Rev. A*, vol. 68, p. 043801, doi: 10.1103/PhysRevA.68.043801.

[216] Else et al. (2016): "Floquet Time Crystals", *Phys. Rev. Lett.*, vol. 117, p. 090402, doi: 10.1103/PhysRevLett.117.090402.

[217] Choi et al. (2017): "Observation of discrete time-crystalline order in a disordered dipolar many-body system", *Nature*, vol. 543, no. 7644, pp. 221–225, doi: 10.1038/nature21426.

[218] Zhang et al. (2017): "Observation of a discrete time crystal", *Nature*, vol. 543, no. 7644, pp. 217–220, DOI: 10.1038/nature21413.

[219] Milton and Mattei (2017): "Field patterns: a new mathematical object", *Proceedings of the Royal Society A: Mathematical, Physical and Engineering Sciences*, vol. 473, no. 2198, p. 20160819, DOI: 10.1098/rspa.2016.0819.

[220] Sacha and Zakrzewski (2017): "Time crystals: a review", *Reports on Progress in Physics*, vol. 81, no. 1, p. 016401, DOI: 10.1088/1361-6633/aa8b38.

[221] Apffel et al. (2022): "Experimental Implementation of Wave Propagation in Disordered Time-Varying Media", *Phys. Rev. Lett.*, vol. 128, p. 094503, DOI: 10.1103/PhysRevLett.128.094503.

[222] Ramaccia et al. (2021): "Temporal multilayer structures for designing higher-order transfer functions using time-varying metamaterials", *Applied Physics Letters*, vol. 118, no. 10, p. 101901, DOI: 10.1063/5.0042567.

[223] Huang and Zhou (2019): "A time-varying mass metamaterial for non-reciprocal wave propagation", *International Journal of Solids and Structures*, vol. 164, pp. 25–36, DOI: 10.1016/j.ijsolstr.2018.12.029.

[224] Engheta (2021): "Metamaterials with high degrees of freedom: space, time, and more", *Nanophotonics*, vol. 10, no. 1, pp. 639–642, DOI: 10.1515/nanoph-2020-0414.

[225] Galiffi et al. (2022): "Photonics of time-varying media", *Advanced Photonics*, vol. 4, no. 1, p. 014002, DOI: 10.1117/1.AP.4.1.014002.

[226] Pacheco-Peña et al. (2022): "Time-varying electromagnetic media: opinion", *Optical Materials Express*, vol. 12, no. 10, Publisher: Optica Publishing Group, pp. 3829–3836, DOI: 10.1364/OME.471007.

[227] Dodonov et al. (1993): "Quantum phenomena in nonstationary media", *Phys. Rev. A*, vol. 47, pp. 4422–4429, DOI: 10.1103/PhysRevA.47.4422.

[228] Josso et al. (2010): "*'Time-varying wideband underwater acoustic channel estimation for OFDM communications'*", *2010 IEEE International Conference on Acoustics, Speech and Signal Processing*, 2010, pp. 5626–5629, DOI: 10.1109/ICASSP.2010.5495257.

[229] Wang et al. (2015): "Acoustic asymmetric transmission based on time-dependent dynamical scattering", *Scientific Reports*, vol. 5, no. 1, p. 10880, DOI: 10.1038/srep10880.

[230] Nassar et al. (2020): "Nonreciprocity in acoustic and elastic materials", *Nature Reviews Materials*, vol. 5, no. 9, pp. 667–685, DOI: 10.1038/s41578-020-0206-0.

[231] d'Hardemare et al. (2020): "Probing Floquet modes in a time periodic system with time defects using Faraday instability", *Europhysics Letters*, vol. 131, no. 2, p. 24007, DOI: 10.1209/0295-5075/131/24007.

[232] Apffel and Fort (2022): "Frequency Conversion Cascade by Crossing Multiple Space and Time Interfaces", *Physical Review Letters*, vol. 128, no. 6, p. 064501, DOI: 10.1103/PhysRevLett.128.064501.

[233] Vermorel et al. (2006): "Rubber band recoil", *Proceedings of the Royal Society A: Mathematical, Physical and Engineering Sciences*, vol. 463, no. 2079, pp. 641–658, DOI: 10.1098/rspa.2006.1781.

[234] Cross and Wheatland (2012): "Modeling a falling slinky", *American Journal of Physics*, vol. 80, no. 12, pp. 1051–1060, DOI: 10.1119/1.4750489.

[235] Rousseaux et al. (2008): "Observation of negative-frequency waves in a water tank: a classical analogue to the Hawking effect?", *New Journal of Physics*, vol. 10, no. 5, p. 053015, DOI: 10.1088/1367-2630/10/5/053015.

[236] Barceló et al. (2011): "Analogue Gravity", *Living Reviews in Relativity*, vol. 14, no. 1, p. 3, DOI: 10.12942/lrr-2011-3.

[237] Faccio et al. (2013): "Analogue Gravity Phenomenology: Analogue Spacetimes and Horizons, from Theory to Experiment", Springer International Publishing.

[238] Peloquin et al. (2016): "Analog wormholes and black hole laser effects in hydrodynamics", *Physical Review D*, vol. 93, no. 8, p. 084032, DOI: 10.1103/PhysRevD.93.084032.

[239] Das et al. (2018): "Dynamics of flexural gravity waves: from sea ice to Hawking radiation and analogue gravity", *Proceedings of the Royal Society A: Mathematical, Physical and Engineering Sciences*, vol. 474, no. 2209, p. 20170223, DOI: 10.1098/rspa.2017.0223.

[240] Euvé et al. (2020): "Scattering of Co-Current Surface Waves on an Analogue Black Hole", *Physical Review Letters*, vol. 124, no. 14, p. 141101, DOI: 10.1103/PhysRevLett.124.141101.

[241] Huidobro et al. (2019): "Fresnel drag in space–time-modulated metamaterials", *Proceedings of the National Academy of Sciences*, vol. 116, no. 50, pp. 24943–24948, DOI: 10.1073/pnas.1915027116.

[242] Caloz and Deck-Leger (2020): "Spacetime Metamaterials - Part I: General Concepts", *IEEE Transactions on Antennas and Propagation*, vol. 68, no. 3, pp. 1569–1582, DOI: 10.1109/TAP.2019.2944225.

[243] Chen et al. (2021): "Efficient nonreciprocal mode transitions in spatiotemporally modulated acoustic metamaterials", *Science Advances*, vol. 7, no. 45, eabj1198, DOI: 10.1126/sciadv.abj1198.

[244] Wen et al. (2022): "Unidirectional amplification with acoustic non-Hermitian space-time varying metamaterial", *Communications Physics*, vol. 5, no. 1, pp. 1–7, DOI: 10.1038/s42005-021-00790-2.

[245] Gaafar et al. (2019): "Front-induced transitions", *Nature Photonics*, vol. 13, no. 11, pp. 737–748, DOI: 10.1038/s41566-019-0511-6.

[246] Lampe et al. (1978): "Interaction of electromagnetic waves with a moving ionization front", *The Physics of Fluids*, vol. 21, no. 1, pp. 42–54, DOI: 10.1063/1.862069.

[247] Tsai and Auld (1967): "Wave Interactions with Moving Boundaries", *Journal of Applied Physics*, vol. 38, no. 5, pp. 2106–2115, DOI: 10.1063/1.1709838.

[248] Bacot et al. (2016): "Time reversal and holography with spacetime transformations", *Nature Physics*, vol. 12, no. 10, pp. 972–977, DOI: 10.1038/nphys3810.

[249] Bahrami et al. (2023): "Electrodynamics of Accelerated-Modulation Space-Time Metamaterials", *Physical Review Applied*, vol. 19, no. 5, p. 054044, DOI: 10.1103/PhysRevApplied.19.054044.

[250] Mouet et al. (2023): "Comprehensive refractive manipulation of water waves using electrostriction", *Proceedings of the National Academy of Sciences*, vol. 120, no. 6, e2216828120, DOI: 10.1073/pnas.2216828120.

[251] Catheline et al. (2022): "*'Gravitational lens effect of membrane waves'*", *16ème Congrès Français d'Acoustique, CFA2022*, Société Française d'Acoustique and Laboratoire de Mécanique et d'Acoustique, Marseille, France, 2022.

RÉSUMÉ

Cette thèse de doctorat explore les ondes élastiques guidées dans les matériaux mous, en particulier les élastomères synthétiques comme l'Ecoflex qui imitent les propriétés des tissus humains. Elle vise à comprendre l'impact de la précontrainte sur les ondes guidées et ses implications plus large dans les processus physiologiques. Cette thèse couvre la mécanique, la vitesse des ondes élastiques et les diagrammes de dispersion dans des plaques et rubans mous. La rhéologie des matériaux est implémentée à l'aide d'une méthode semi-analytique, permettant d'aligner les prédictions théoriques sur les résultats expérimentaux. La théorie acoustoélastique et la viscoélasticité sont combinées pour quantifier l'anisotropie induite dans une plaque fortement étirée et les courbes de dispersion des ondes guidées "in-plane" dans des rubans déformés. L'application en élastographie par ondes de cisaillement est étudiée pour améliorer la robustesse de cette technique d'imagerie médicale, en particulier pour les tissus allongés. Cette thèse permet d'établir un lien entre les matériaux mous et les tissus biologiques en examinant notamment les vibrations de la membrane basilaire dans la cochlée. En modélisant cette membrane comme un ruban fin, nous expliquons la discrimination de fréquence, *i.e.* la tonotopie, en évaluant la dispersion locale le long de la membrane. Dans le dernier chapitre, une interface spatio-temporelle est créée en appliquant une contrainte axiale croissante dans le temps, conduisant à des sauts de fréquence et de nombre d'ondes pour l'onde de flexion qui la rencontre. Cette recherche a donc des applications dans la manipulation des ondes. En résumé, cette thèse de doctorat se penche sur la propagation d'ondes élastiques guidées dans les matériaux mous, couvrant la théorie, les expériences et les applications pratiques dans divers domaines tels que l'imagerie médicale et la biologie.

MOTS CLÉS

Ondes élastiques guidées, milieux mous, viscoélasticité, acoustoélasticité, onde cochléaire, interface spatio-temporelle

ABSTRACT

This PhD thesis explores guided elastic waves in soft materials, particularly synthetic elastomers like Ecoflex that mimic human tissue properties. It aims to understand the impact of prestress on guided waves and its broader implications in physiological processes. The thesis covers mechanics, elastic wave velocities, and dispersion diagrams in soft plates and strips. Material rheology is addressed through a semi-analytical method, aligning theoretical predictions with experimental findings. The acoustoelastic effect and viscoelasticity are combined to quantify the induced anisotropy in a highly-stretched plate and the dispersion curves of in-plane guided waves in prestressed strips. The application of shear wave elastography is explored to improve medical imaging, especially for elongated tissues. The thesis further establishes connections between soft materials and biological tissues by examining the vibrations of the basilar membrane in the cochlea. Modeling this membrane as a thin strip, this thesis explains the frequency discrimination, *i.e.* the tonotopy, by evaluating the local dispersion along the strip. In the last chapter, a space-time interface is created by applying an increasing axial stress, leading to frequency and wavenumber changes for the flexural wave that crosses it. This research has applications in wave manipulation. In summary, this PhD thesis delves into guided elastic wave propagation in soft materials, covering theory, experiments, and practical applications in diverse fields such as medical imaging and biology.

KEYWORDS

Guided elastic waves, soft solids, viscoelasticity, acoustoelastic, cochlear wave, space-time interface